Conference Proceedings of the Society for Experimental Mechanics Series

Steven Mates
Veronica Eliasson *Editors*

Dynamic Behavior of Materials, Volume 1

Proceedings of the 2021 Annual Conference and Exposition on Experimental and Applied Mechanics

SEM

Springer

Conference Proceedings of the Society for Experimental Mechanics Series

Series Editor

Kristin B. Zimmerman
Society for Experimental Mechanics, Inc.,
Bethel, CT, USA

The Conference Proceedings of the Society for Experimental Mechanics Series presents early findings and case studies from a wide range of fundamental and applied work across the broad range of fields that comprise Experimental Mechanics. Series volumes follow the principle tracks or focus topics featured in each of the Society's two annual conferences: IMAC, A Conference and Exposition on Structural Dynamics, and the Society's Annual Conference & Exposition and will address critical areas of interest to researchers and design engineers working in all areas of Structural Dynamics, Solid Mechanics and Materials Research.

More information about this series at http://www.springer.com/series/8922

Steven Mates • Veronica Eliasson
Editors

Dynamic Behavior of Materials, Volume 1

Proceedings of the 2021 Annual Conference and Exposition on Experimental and Applied Mechanics

Springer

Editors

Steven Mates
National Institute of Standards and Tech
Gaithersburg, MD, USA

Veronica Eliasson
Colorado School of Mines
Golden, CO, USA

ISSN 2191-5644 ISSN 2191-5652 (electronic)
Conference Proceedings of the Society for Experimental Mechanics Series
ISBN 978-3-030-86561-0 ISBN 978-3-030-86562-7 (eBook)
https://doi.org/10.1007/978-3-030-86562-7

© The Society for Experimental Mechanics, Inc. 2022
This work is subject to copyright. All rights are solely and exclusively licensed by the Publisher, whether the whole or part of the material is concerned, specifically the rights of translation, reprinting, reuse of illustrations, recitation, broadcasting, reproduction on microfilms or in any other physical way, and transmission or information storage and retrieval, electronic adaptation, computer software, or by similar or dissimilar methodology now known or hereafter developed.
The use of general descriptive names, registered names, trademarks, service marks, etc. in this publication does not imply, even in the absence of a specific statement, that such names are exempt from the relevant protective laws and regulations and therefore free for general use.
The publisher, the authors and the editors are safe to assume that the advice and information in this book are believed to be true and accurate at the date of publication. Neither the publisher nor the authors or the editors give a warranty, expressed or implied, with respect to the material contained herein or for any errors or omissions that may have been made. The publisher remains neutral with regard to jurisdictional claims in published maps and institutional affiliations.

This Springer imprint is published by the registered company Springer Nature Switzerland AG
The registered company address is: Gewerbestrasse 11, 6330 Cham, Switzerland

Preface

Dynamic Behavior of Materials represents one of four volumes of technical papers to be presented at the 2021 SEM Annual Conference & Exposition on Experimental and Applied Mechanics organized by the Society for Experimental Mechanics scheduled to be held June 14–17, 2021. The complete proceedings also include volumes on: *Challenges In Mechanics of Time-Dependent Materials, Mechanics of Biological Systems and Materials, and Micro-and Nanomechanics; Mechanics of Composite, Hybrid & Multifunctional Materials, and Fracture, Fatigue, Failure and Damage Evolution; and Thermomechanics & Infrared Imaging, Inverse Problem Methodologies, Mechanics of Additive & Advanced Manufactured Materials, and Advancement of Optical Methods & Digital Image Correlation.*

Each collection presents early findings from experimental and computational investigations on an important area within Experimental Mechanics. Dynamic Behavior of Materials is one of these areas.

The Dynamic Behavior of Materials track was initiated in 2005 and reflects our efforts to bring together researchers interested in the dynamic behavior of materials and structures, and to provide a forum to facilitate technical interaction and exchange. Over the years, this track has been representing the ever-growing interests in dynamic behavior to the SEM community, working towards expanding synergy with other tracks and topics, and improving diversity and inclusivity, as evidenced by the increasing number and diversity of papers and attendance.

The contributed papers span numerous technical divisions within SEM, demonstrating its relevance not only in the dynamic behavior of materials community, but also in the mechanics of materials community as a whole. The track organizers thank the authors, presenters, organizers and session chairs for their participation, support, and contribution to this track. The SEM support staff is also acknowledged for their devoted efforts in accommodating the large number of paper submissions this year, making the 2021 Dynamic Behavior of Materials Track a success.

Gaithersburg, MD	Steven Mates
Golden, CO	Veronica Eliasson

Contents

Chapter 1
Crack Branching in Soda-Lime Glass: Optical Measurement of Precursors Using Digital Gradient Sensing

S. Dondeti and H. V. Tippur

Abstract The dynamic fracture of soda-lime glass (SLG) involves crack branching, underlying mechanics of which is not yet fully understood. Addressing this issue using full-field optical techniques is challenging due to severe spatio-temporal requirements as crack speeds in this material reach 1500 m/s or more and is accompanied by highly localized nanoscale deformations. Recent work by the authors have shown that transmission-mode Digital Gradient Sensing (DGS) method is capable of overcoming these challenges to visualize crack-tip fields over large regions of interest and quantify fracture parameters associated with each of the phases of crack growth event in SLG plates. In this work, time-resolved stress gradient measurements of two different SLG geometries subjected to dynamic wedge-loading are performed to quantitatively visualize single and cascading branch formations. The precursors of crack branching event are identified from the optical measurements leading up to the first and/or successive branch formations. These precursors are based on crack velocity, stress intensity factors, higher order coefficients of the asymptotic crack tip fields, and a non-dimensional parameter involving a combination of these measured quantities.

Key words Dynamic fracture · Soda-lime glass · Crack branching · Digital gradient sensing · Transparent structures

1.1 Introduction

Investigating fast fracture in soda-lime glass using full-field optical methods pose unique challenges due to high crack speeds (>1500 m/s) and highly localized nanoscale (<100 nm CTOD) crack tip deformations. Furthermore, the dynamic fracture in these materials typically involves crack branching, which is yet to be fully understood from a mechanics perspective. In light of these experimental challenges, earlier investigations generally resorted to using amorphous brittle polymers instead even though they are viscoelastic and prone microscopic non-homogeneity issues. Dally [1] reported dynamic fracture of Homalite-100 using photoelasticity and noted that crack branching occurs when mode-I stress intensity factor reaches the so-called crack branching toughness. Ramulu and Kobayashi [2] also investigated crack branching in Homalite-100 photoelastically and proposed a necessary condition based on a critical dynamic stress intensity factor and a sufficient condition of minimum characteristic distance for crack curving. Theocaris et al. [3] proposed crack branching based on macroscopic fracture energy criteria and applying it to the branch crack tips to determine the expected angle of crack propagation. Sundaram and Tippur [4] were the first to investigate dynamic fracture of SLG using a full-field optical method called DGS method in conjunction with ultrahigh-speed digital photography. The present work is in pursuit of these studies [4, 5] to identify potential precursors of crack branching in two different SLG specimen geometries where single and cascading crack branching events are achieved.

1.2 Experimental Details

In this work, the dynamic fracture of V-notched specimens (Fig. 1.1) leading crack branching is studied using transmission-mode DGS method. Two planar SLG specimen geometries—100 mm × 150 mm and 150 mm × 150 mm—are cut from a 5.7 mm thick sheet and a V-notch is machined into an edge and extended by 8 mm, as shown, by a diamond saw. A schematic of the experimental setup used for the optical investigation is shown in Fig. 1.2. It consists of an ultrahigh-speed camera, a pair

---

S. Dondeti (✉) · H. V. Tippur
Department of Mechanical Engineering, Auburn University, Auburn, AL, USA
e-mail: szd0057@auburn.edu; tippuhv@auburn.edu

S. Mates, V. Eliasson (eds.), *Dynamic Behavior of Materials, Volume 1*, Conference Proceedings of the Society for Experimental Mechanics Series, https://doi.org/10.1007/978-3-030-86562-7_1

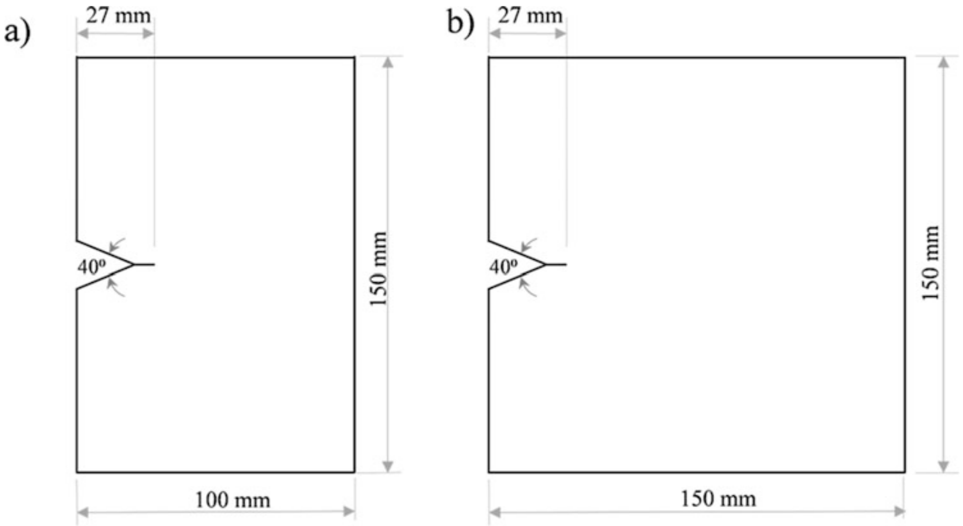

Fig. 1.1 V-notched soda-lime glass specimen geometries: (**a**) 100 mm × 150 mm and (**b**) 150 mm × 150 mm

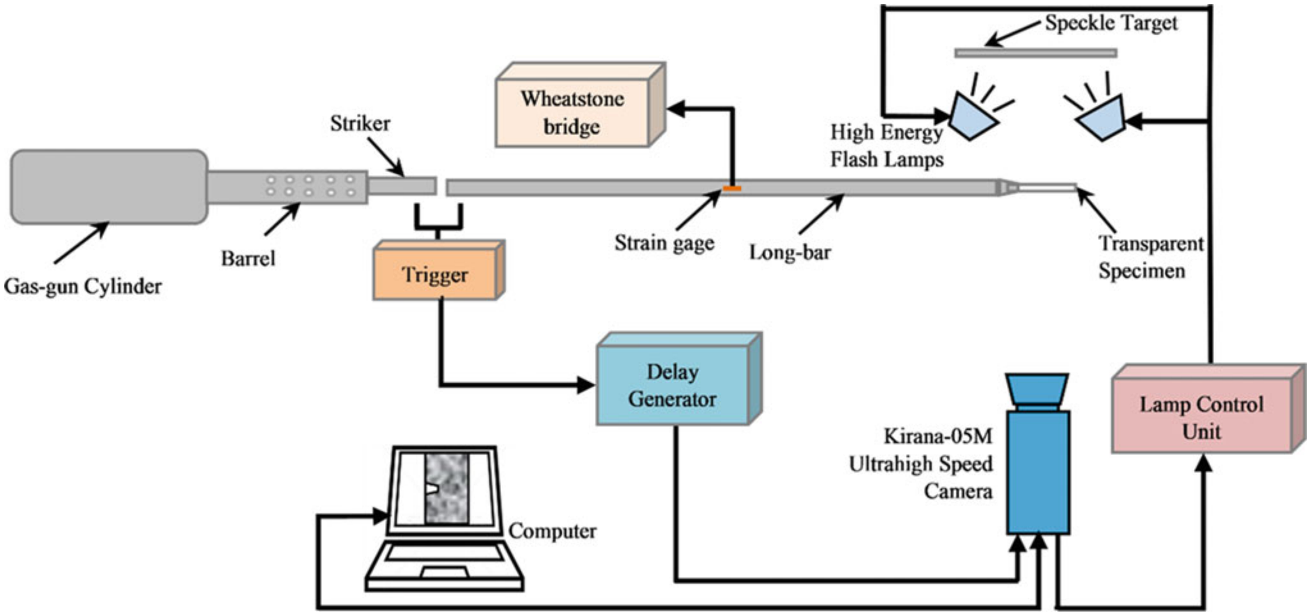

Fig. 1.2 Experimental setup to study dynamic fracture of glass using DGS

of high energy flash lamps, and a gas-gun to launch a striker, and a tapered-tip Hopkinson bar (long-bar) matching the V-notch to load the specimen dynamically. Both the long-bar (1830 mm long, 25.4 mm diameter) and the striker (305 mm long, 25.4 mm diameter) are made of maraging steel. The impact of the striker causes a compressive stress wave to travel the length of the long-bar and load the specimen. Simultaneously, a trigger pulse is also generated to initiate the camera to capture images. A random black and white speckle target placed behind the specimen at a known distance is photographed through the transparent specimen using a Kirana-05 M single sensor (924 × 768 pixels) camera capable of recording up to 180 full resolution images and at up to five million fps.

1.3 Optical Measurements

The optical method of transmission DGS measures angular deflections of light rays due to combined refractive index and specimen thickness changes due to the local state of stress in the region of interest (ROI). They are obtained by correlating the speckle images in the deformed and reference states of the specimen. The measured angular deflections in the two orthogonal planes are proportional to spatial gradients of in-plane normal stress ($\sigma_x + \sigma_y$) in the x- and y-directions. The details of the method are avoided here for brevity but can be found in Ref. [6]. First, the optical measurements are performed in the 100 mm × 150 mm specimen (ROI = 83 mm × 72 mm) and the resulting crack growth pattern is evident from the fractured specimen photograph shown in Fig. 1.3a. Figure 1.4 shows a representative pair of contour plots of orthogonal angular deflections of light rays in the post-branching phase at a select time instant of $\tau = 9$ μs in this geometry. Here, time $\tau = 0$ corresponds to when the mode-I mother crack branches. The contours have a lobed structure and they converge to the crack tip due to the singular nature of the two orthogonal stress gradient fields. (Tracking the crack tip location is relatively simpler in DGS when compared to non-singular displacements measured from DIC [5].) The successive solid white dots superposed on the contours in Fig. 1.4 represent the measured crack tip location histories of the growing mode-I and mixed-mode daughter cracks during the fracture event in 1 μs intervals.

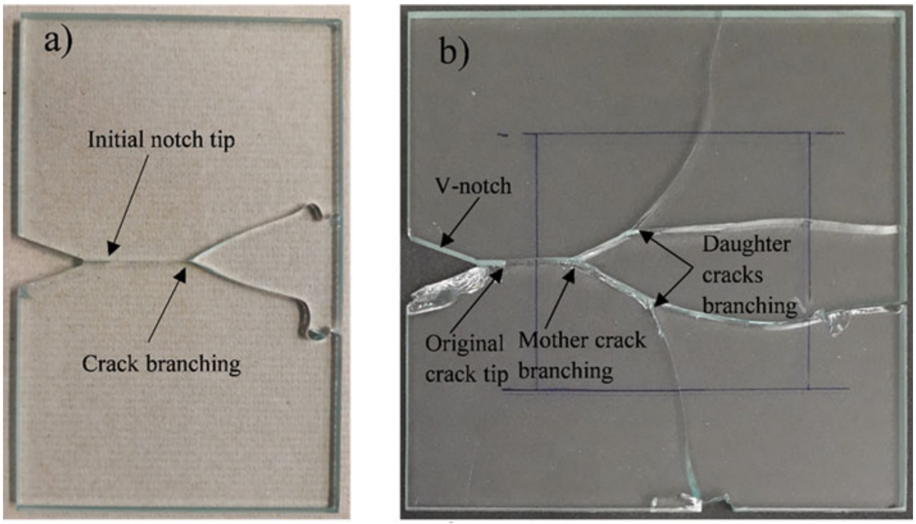

Fig. 1.3 Fractured SLG specimens of (**a**) 100 mm × 150 mm and (**b**) 150 mm × 150 mm geometry

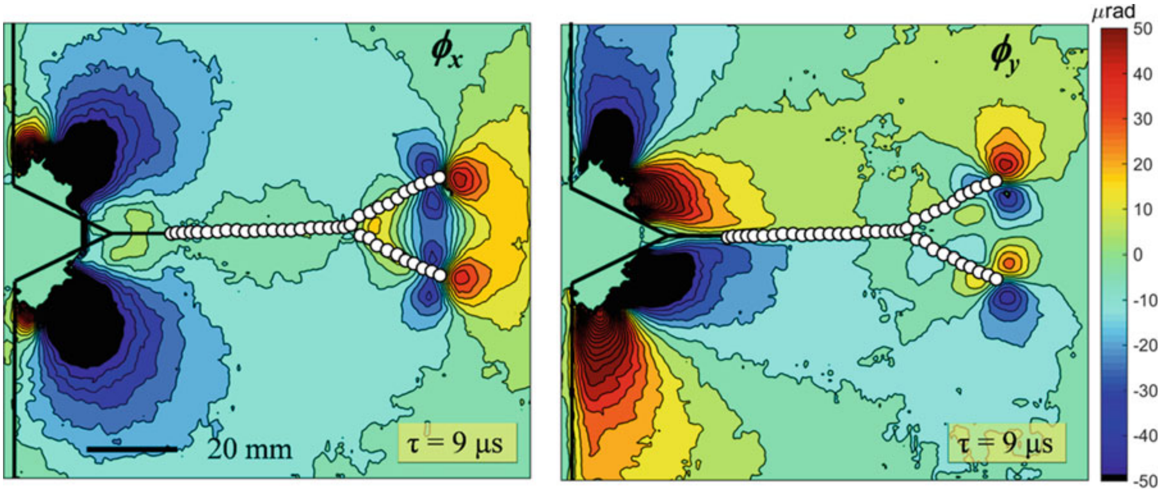

Fig. 1.4 Angular deflection contours proportional to stress-gradients in the x- and y-directions. (Time, $\tau = 0$ corresponds to crack branching)

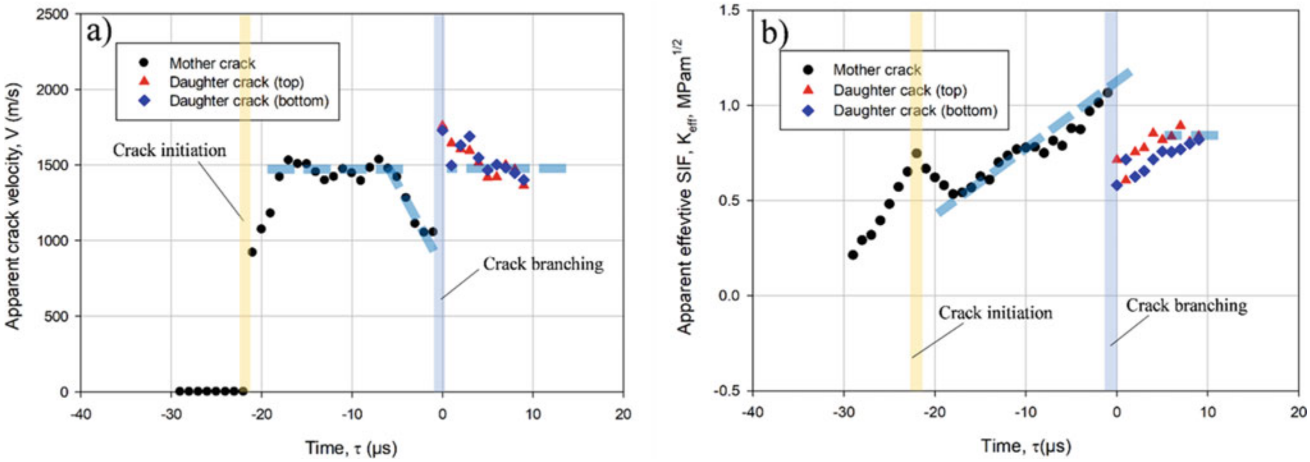

Fig. 1.5 Fracture parameter histories: (**a**) crack velocity and (**b**) effective stress intensity factors

Figure 1.5a shows crack velocity history obtained using DGS contours such as the ones shown in Fig. 1.4. The crack velocity increases rapidly to ~1500 m/s after crack initiation from the initial notch tip. Subsequently, the crack propagates self-similarly (mode-I mother crack) in the range of 1450–1550 m/s for the next ~11 μs as suggested by the broken blue line. Following that, the crack velocity gradually decreases to ~1050 m/s over the next 5 μs or so before it bifurcates. This drop in the crack speed, as suggested by the broken blue line, is a consistent precursor for the crack branching event, consistent with the previous reports [4, 5]. Once the crack bifurcates into two globally symmetric mixed-mode daughter cracks, a sudden increase in crack velocity (to ~1700 m/s) occurs. The velocity of the two daughter cracks decrease back to a steady value of ~1500 m/s over ~5 μs and travel the rest of the observation window without any noticeable drop in crack speed and no further crack bifurcations.

Using an over-deterministic least-squares analysis of DGS measurements, the effective stress intensity factor, K_{eff} $\left(= \sqrt{K_I^2 + K_{II}^2}\right)$, history is evaluated, see Fig. 1.5b. The K_{eff} increases in the pre-initiation phase to ~0.75 MPa√m when the mode-I crack initiates from the notch tip. Subsequently, K_{eff}dips to ~0.6 MPa√m over ~2 μs before increasing to approx. Twice the value or ~1.1 MPa√m prior to branching event (denoted by time, $\tau = 0$). The increase in K_{eff} by two fold, as represented by a thick blue dashed line could be considered another precursor in addition to the crack speed reduction noted earlier. Soon after branching, both daughter cracks decelerate instantaneously to an average K_{eff}value of 0.6–0.7 MPa√m. Subsequently, K_{eff}values increase to an average value of 0.75–0.9 MPa√m over the next 5 μs or so and continue until the end of the observation window. Both daughter cracks propagate in a mixed-mode fashion without any further branching as the K_{eff} values of each remain below twice the lowest value seen after initiation (= ~0.6 MPa√m) of the mother crack.

Besides K_{eff}, coefficients of higher order terms in the asymptotic stress field, namely A_3 and D_3 are also evaluated from DGS and are shown in Fig. 1.6a. (Note that A_2 and D_2 are absent in the asymptotic expressions for stress gradients.) Evidently, $|A_3|$ increases monotonically until crack initiation to ~230 MPa/√m. After initiation, its value decreases modestly to ~210 MPa/√m and then on remains steady for ~11 μs, matching the behavior of the velocity history. Subsequently, the $|A_3|$ increases steadily to a local peak value of ~240 MPa/√m before starting to decrease to ~210 MPa/√m at branching. The coefficient D_3 remains nearly zero during this period until crack branching at $\tau = 0$. Excluding the transient effects after branching, both daughter cracks propagate with nearly constant A_3 and D_3 until the end of the observation window. Based on these trends, the drop in $|A_3|$ (represented with a broken blue line) in the pre-branching phase can be treated as another precursor of the crack branching event.

A non-dimensional parameter based on K_{eff}, V, and A_3, namely $\widehat{K} = \left(\frac{K_{\text{eff}}}{A_3 V}\right)\left(\frac{C_L}{W}\right)$ is also identified as a potential precursor of the crack branching event. Here, C_L is the longitudinal wave speed of SLG, W is width of the specimen, and a is the instantaneous crack length. The history of $\widehat{K}$ is shown in Fig. 1.6b for the 100 mm × 150 mm geometry. After initiation, $|\widehat{K}|$ remains approx. Constant relative to a steep descent over ~5 μs before the crack branching event. This descent as marked by the broken blue line of Fig. 1.6b also stands out as a potential precursor of crack branching.

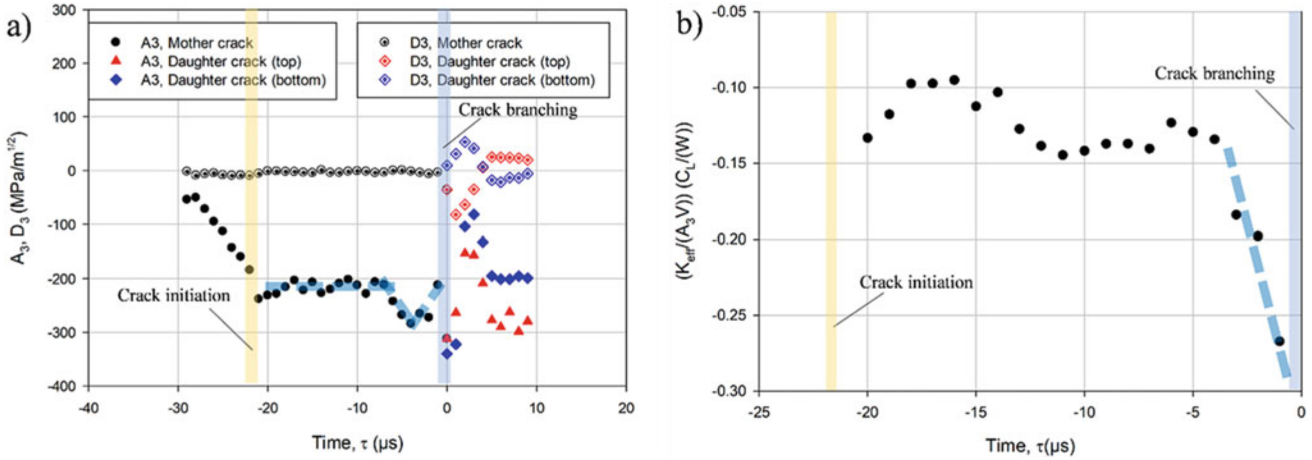

Fig. 1.6 Fracture parameter histories: (**a**) Higher order coefficients A_3, D_3 and (**b**) Non-dimensional parameter $\widehat{K}$

1.4 Work-In-Progress

The study of sequential/cascading crack branching observed in a larger SLG specimen geometry with 150 mm × 150 mm dimensions, shown in Fig. 1.3b, is currently in progress. All the dynamic fracture parameters including crack velocity histories (V), effective stress intensity factor histories K_{eff}, and higher order coefficients A_3 and D_3 are being evaluated to assess their consistency with those from the 100 mm × 150 mm geometry. Additionally, fractography is being performed for both the geometries and the relationship of those results with the fracture parameters, if any, are being examined.

1.5 Summary

Dynamic fracture of SLG plate with 100 mm × 150 mm geometry using DGS has resulted in the following notable precursors for crack branching/bifurcation. The drop in the macroscale crack velocity V from a steady ~1500 m/s to ~1000 m/s is a precursor of crack branching event. The monotonic increase of the effective stress intensity factor K_{eff} by twice its value after initiation is a second notable precursor of crack bifurcation. The increase of higher order coefficient $|A_3|$ before branching is a third notable precursor of branching. These precursors can be lumped into a non-dimensional parameter $\widehat{K}$ that shows a steep drop ahead of the observed crack branching event. Quantification of fractographic features via post-mortem analysis as well as analysis of DGS data for 150 mm × 150 mm geometry resulting in sequential/cascading branching phenomena currently underway is expected to add further insight into these precursors of crack branching in SLG.

References

1. Dally, J.W.: Dynamic photoelastic studies of fracture. Exp. Mech. **19**(10), 349–361 (1979)
2. Ramulu, M., Kobayashi, A.S.: Mechanics of crack curving and branching - a dynamic fracture analysis. Dyn. Fract., 61–75 (1985)
3. Theocaris, P., Andrianopoulos, N., Kourkoulis, S.: Crack branching: a "twin-crack" model based on macroscopic energy fracture criteria. Eng. Fract. Mech. **34**(5–6), 1097–1107 (1989)
4. Sundaram, B.M., Tippur, H.V.: Dynamic fracture of soda-lime glass: a full-field optical investigation of crack initiation, propagation and branching. J. Mech. Phys. Solids. **120**, 132–153 (2018)
5. Dondeti, S., Tippur, H.V.: A comparative study of dynamic fracture of soda-lime glass using Photoelasticity, digital image correlation and digital gradient sensing techniques. Exp. Mech. **60**(2), 217–233 (2019). https://doi.org/10.1007/s11340-019-00549-5
6. Periasamy, C., Tippur, H.V.: Full-field digital gradient sensing method for evaluating stress gradients in transparent solids. Appl. Opt. **51**(12), 2088 (2012)

Chapter 2
Investigation of the Discrepancy Between Contact Force and Measured Force in a Hopkinson Tube

Troy Lyons

Abstract Hopkinson tubes can be used similarly to Hopkinson bars and undergo larger deformation than a solid Hopkinson bar of equal outer diameter. This is advantageous for loading that is small in magnitude, where the resulting strain in the bar may be too small to be measured with strain gages. The challenge with using Hopkinson tubes is that the force determined from the traveling stress wave in many cases does not match the contact force causing the deformation. This is due to the relatively complicated dynamics of the Hopkinson tube in comparison to the Hopkinson bar. In this work, simulations of the dynamics due to an impulse hammer striking a Hopkinson tube are used to investigate why the force measured from the impulse hammer does not match the force derived from measurements on the tube. Simulations are first validated with experimental data, and then used to demonstrate that the inertia of the end cap and tube length caused the significant force discrepancies in the experiment.

Key words Hopkinson bar · LS-DYNA · Wave propagation · Explicit time integration

2.1 Introduction

Deformation at high strain rate is somewhat common within aerospace engineering, and accurate modeling of these events often requires material data that was also determined under such conditions. These material properties are often determined from experimental testing using Hopkinson bars. In some circumstances, material data can be calculated by directly shooting the specimen into a Hopkinson bar. A couple examples of this include studying birds [1] and gelatin bird surrogates [2]. Many soft materials cause somewhat small deformation within the bar upon impact, which can be difficult to measure experimentally. To overcome this issue, Annett and Pereira [2], and Seidt et al. [3] used instrumented tubes (referred to as "Hopkinson tubes" in this work) to measure the deformation. The advantage with the tubes over the Hopkinson bars was that the tubes have a significantly smaller cross-sectional area, and thus a given contact force would create larger deformation that would be easier to measure. A key challenge in working with Hopkinson tube tests is that the measured force often poorly matches the contact force caused by impact with the specimen [2, 4]. Hopkinson bars and tubes are commonly fitted with strain gages to measure the deformation, where each gage gives the transient strain at the location where it is attached. If the traveling stress wave is uniform through the thickness, the strain gage, along with the cross-sectional area, and elastic constants, can be used to determine the contact force from the specimen.

In this work, a finite element model of the Hopkinson tube used by Annett and Pereira [4, 5] is created with the commercially available finite element software LS-DYNA. Simulations apply a time-dependent force on the nodes of the end cap, and the resulting deformation is calculated with explicit time integration. The forcing being applied to the Hopkinson tube was measured experimentally with an impulse hammer [4]. The finite element model is validated by comparing simulated results to the force determined experimentally with strain gages. After the validation simulation, considerations about tube length, cap inertia, and cap deformation are investigated to determine why the contact force and tube-derived force disagree from the experiment.

T. Lyons (✉)
Department of Mechanical and Aerospace Engineering, College of Engineering, The Ohio State University, Columbus, OH, USA

S. Mates, V. Eliasson (eds.), *Dynamic Behavior of Materials, Volume 1*, Conference Proceedings of the Society for Experimental Mechanics Series, https://doi.org/10.1007/978-3-030-86562-7_2

2.2 Methodology

Dimensions of the tube were given by Annett and Pereira [2] and Pereira et al. [4]. The tube was made of aluminum, was modeled with an isotropic, linear-elastic material model, with 68.95 GPa for Young's modulus, 0.33 for Poisson's ratio, and 2768.0 $\frac{\text{kg}}{\text{m}^3}$ for the density. Dimensions of the tube are shown in Fig. 2.1.

The finite element model of the tube used constant stress elements and stiffness-based Flanagan-Belytschko [3] hourglass control. The end cap and tube were meshed separately and held together with a tied contact. The tied contact was constraint based for simulations where the end cap was deformable, and a penalty based when the end cap was rigid. The difference in tied contact type did not produce significantly different results when checked on the deformable end cap. Engineering strain was measured on the tube 15.24 cm (6 in.) past the transition between the tube and end cap. The engineering strain in the axial direction was calculated by comparing the length separating two nodes in the mesh and how it varied in time. The force measured in the tube can be related from these strain measurements:

$$F(t) = -A\sigma(t) = -AE\varepsilon(t)$$

where *F(t)* is the measured force, *A* is the cross-sectional area of the tube, *σ(t)* is the normal stress in the axial direction, *E* is Young's modulus, and *ε(t)* is the time-dependent engineering strain in the axial direction.

A mesh refinement study was conducted on the finite element model of the Hopkinson tube. Meshes with two, three, four, five, and six elements in the thickness were created. Refinement along the circumference and length of the tube was determined by requiring the aspect ratio stay below 3.0 for all tube elements. Separate studies using forcing in the axial direction were conducted; the first with nodes being forced uniformly by their radial position, and a second study used a radial dependent forcing pattern. The case of uniform forcing (shown in Fig. 2.2) gave strong agreement in the calculated force vs. time for all meshes. The case of radial dependent forcing also had good agreement among the various meshes, but there was noticeable improvement from two to three elements in the tube thickness. Thus, the mesh adopted for the Hopkinson tubes in the simulation of the bird validation experiment had three elements in the thickness.

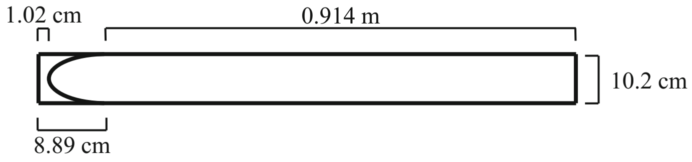

Fig. 2.1 A cross section showing the dimensions of the Hopkinson tube used in the experiments [4, 5]. The end cap is 8.89 cm long and is shown on the left. The wall thickness for the tube was 1.5875 mm

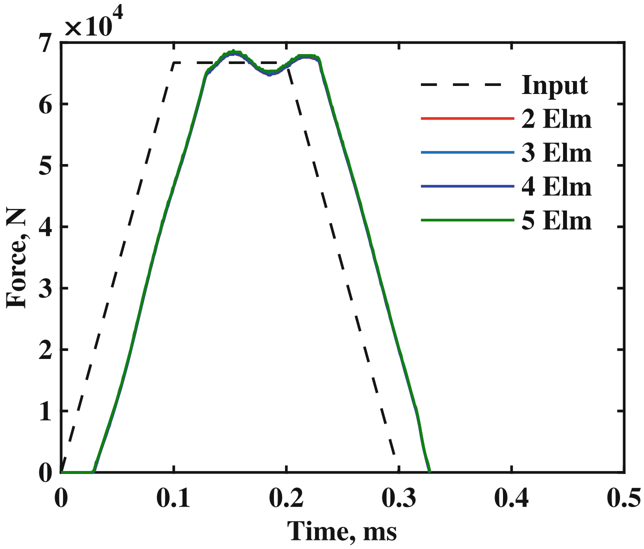

Fig. 2.2 Mesh refinement study comparing results from simulations using two through five elements through the tube thickness, with spatially uniform forcing. Nodes on the end of the tube were forced equally in the axial direction, and the end cap of the tube was omitted

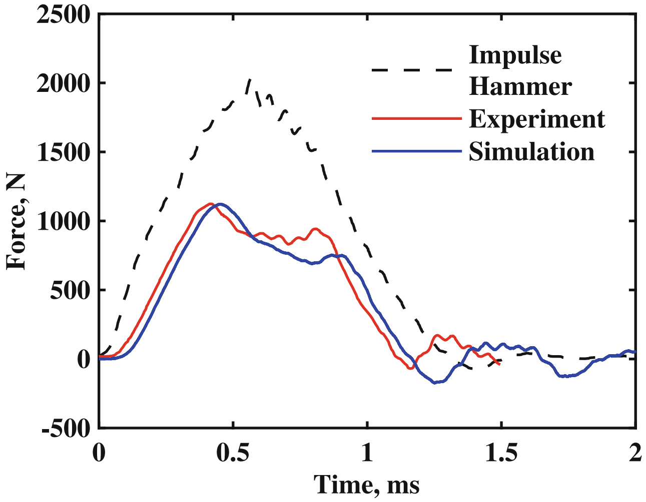

Fig. 2.3 The comparison of experimental and simulated force derived from strain gage measurements. The foam that was placed between the opposite end of the tube and the wall was not simulated

To validate the Hopkinson tube finite element model, the force measured from an impulse hammer strike [4] was simulated. In the simulations, the force measured from the impulse hammer was applied uniformly over the end cap. This created a stress wave that propagated down the bar, past nodes being used to simulate strain gages. Results from both the experiment, and the simulation, are shown in Fig. 2.3. In the experiment, foam was placed behind the opposite end of the Hopkinson tube. In the simulations, the opposite end was unrestricted. This was based off preliminary simulations comparing the free and fixed (zero displacement) boundary conditions, which found that the free boundary condition was a much better approximation for the foam in the experiment than a fixed boundary condition.

2.3 Results

Upon reaching the end of the bar, the stress wave rebounds and begins to return towards the impacted end. Typically, Hopkinson bars and tubes are designed such that the stress wave has finished passing the strain gages prior to the beginning of the wavefront returning to the measurement location. Forcing occurring over longer time durations requires longer Hopkinson bars (or tubes) to avoid superposition of waves at the measurement locations. A compression wave that propagates down the bar will return as a compression wave if the opposite end of the bar is fixed, or as a tension wave if the opposite end is free from constraint [6].

To calculate the necessary length of the Hopkinson tube, consider a “strength of materials” type equation [6] for the wave propagation within the tube:

$$E\frac{\partial^2 w}{\partial z^2} = \rho\frac{\partial^2 w}{\partial t^2}$$

Where w is the displacement in the axial direction. This equation approximates the deformation of the Hopkinson tube, as it assumes that the wave traveling is one dimensional. It predicts a wave propagation speed, which we will call the “strength of materials velocity,” of

$$v_{\text{som}} = \sqrt{\frac{E}{\rho_0}}$$

The strength of materials velocity is intermediate in comparison to the dilatational v_d and shear, v_s velocities. The dilational wave speed is

$$v_d = \sqrt{\frac{\lambda + 2\mu}{\rho_0}}$$

Where λ amd μ are Lamé's constants, which can be related to Young's modulus and Poisson's ratio, where $\lambda = \frac{\nu E}{(1+\nu)(1-2\nu)}$, and $\mu = \frac{E}{2(1+\nu)}$. The shear wave velocity can also be of interest for certain problems, but is not used in this work. It is given here for convienience:

$$v_s = \sqrt{\frac{\mu}{\rho_0}}$$

For materials with Poisson's ratio in the range $0 < \nu < 0.5$, the dilatational velocity is the fastest, followed by the strength of materials velocity and shear velocity, $v_d > v_{som} > v_s$. Using the elastic constants from this work, namely 68.95 GPa for Young's modulus, 0.33 for Poisson's ratio, and 2768.0 $\frac{kg}{m^3}$ for the density, the wave speeds can be calculated. The corresponding dilatational and strength of materials velocity is 6084 m/s and 4998 m/s, respectively. The strength of materials velocity predicts that the wave in the Hopkinson bar will take about 0.3 ms to traverse from the strain gages, to the opposite tube end, and back. To achieve a target time of 1.5 ms of force measurement without superposition with the rebounding signal, the tube was extended by an additional 3.8 m, and the new dimensions are given in Fig. 2.4. This new length was calculated with the dilatational velocity, which is faster than the strength of materials velocity, to be conservative.

Simulations with the extended Hopkinson tube avoided the superposition of original (compression) and rebounding (tension) waves until after the target time of 1.5 ms. An image of the compression wave passing through the cap-tube connection, and strain gage location is shown in Fig. 2.5.

The force derived from the strain gage, using the elastic cap, is shown in Fig. 2.6. The results from the simulation with the elastic cap show considerable improvement over the shorter tube shown in Fig. 2.3. Despite the significant improvement with the extended tube, there are still noticeable differences between the contact force and measured force from the tube. This comparison is shown in Fig. 2.6. Deformation of the cap was also investigated as a potential cause for the discrepancy. Figure 2.6 also shows a simulation if the cap were modeled as a rigid body. This was done to offer a comparison between results from an elastic cap and one that did not deform. The resulting force from the elastic cap closely matches that from the rigid cap.

The simulations shown in Fig. 2.6 were also checked for whether the stress wave within the tube varied through the tube thickness. This can occur [3], particularly when the contact loading causes large deflections in the end cap. Such conditions create bending of the cap and cause the tube to bend inward radially. The corresponding axial stress wave from such a situation would likely be tensile on the outside of the tube and compressive on the inner wall of the tube. Figure 2.7 shows the

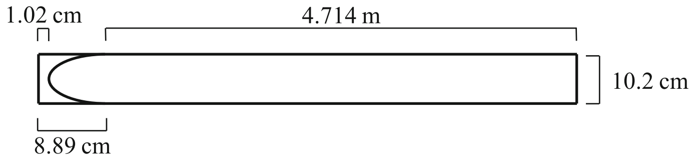

Fig. 2.4 Cross section and dimensions of the extended Hopkinson tube, which is 3.8 m longer than the one from the experiments [4, 5], which is shown in Fig. 2.1

Fig. 2.5 Normal stress in the axial direction is shown 0.8 ms into the simulation. Elements having stress in the range of −3.58 to −3.35 MPa are shown in color. Elements with the axial stress outside that range are shown in grey

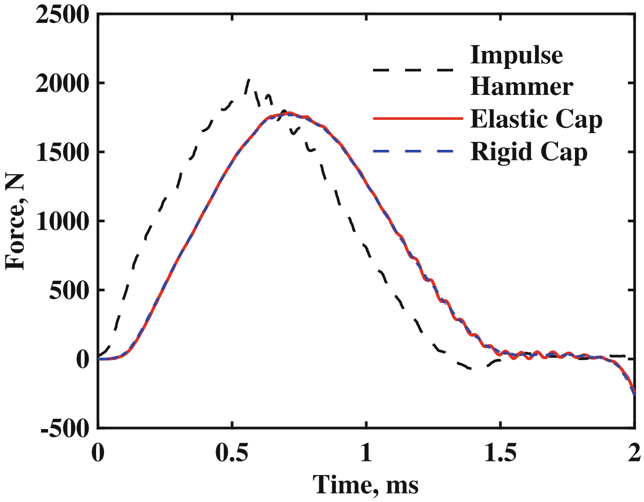

Fig. 2.6 Force measured from the extended tube improved agreement relative to the original tube. Separate simulations, one with the end cap elastic, the other with it rigid, produced very similar results

axial stress calculated for three elements at the cap-tube connection, as well as the virtual strain gage location (see Fig. 2.5). In each plot, the element labeled R_1 is on the inner wall of the tube, followed by a mid-thickness element labeled R_2, and finally an element labeled R_3 on the outer wall. The axial stresses shown in Fig. 2.7 are uniform by the time they reach the virtual strain gages, which supports the one-dimensional wave assumption used to calculate the force from the tube.

Up to this point, the simulations have shown the motion of the end cap is dominated by rigid body motion, and not deformation of the end cap. The momentum equation for a rigid cap would be:

$$m\ddot{z}_{\text{cap}} = F_{\text{h}}(t) - F_{\text{c}}(t)$$

Where m is the mass of the cap, $F_h(t)$ is the force applied by the impulse hammer, and $F_{\text{c}}(t)$ is the force from the connection, with the positive sense taken to be in the opposite direction as the contact force from the hammer, $F_{\text{h}}(t)$. The resultant force across the connection, $F_{\text{c}}(t)$, is given in Fig. 2.8.

If the mass of the rigid cap were to be negligible, the momentum equation for the cap suggests the tube-cap connection force would be approximately equal to the contact force from the impulse hammer. Figure 2.9 shows simulations where the mass of the cap was altered by reducing the density within the rigid material model used. With the cap's reduced inertia, simulations with one-tenth and one-hundredth the mass create stress waves that closely reproduce the contact force applied to the cap.

To test if the reduced inertia would also improve agreement with the deformable end caps, two additional simulations were run with elastic aluminum material models for the end cap, and results are shown in Fig. 2.10. A simulation with an elastic end cap with the density scaled to one-tenth the original value (Young's modulus and Poisson's ratio were unaltered) showed close agreement with the contact force, close to what was seen in the rigid cap cases of Fig. 2.9. Fewer cases were run with the deformable cap of scaled density than the rigid cases. This is because reducing density also requires reducing the time-step in the simulation for numerical stability, and thus increases the computational cost.

The considerations represented in Fig. 2.10, as well as Fig. 2.7, collectively give important design guidelines to make the measured force in Hopkinson tubes closely match the contact force. In a tube that is sufficiently long for the stress wave to not have time to propagate back, the cap should deform minimally to produce a stress wave that is uniform through the tube's thickness, but also be sufficiently light, otherwise the added inertia can also influence results.

2.4 Conclusions

It was found the causes for the discrepancy in contact and measured force were predominantly due to the tube's length, and the large mass of the end cap relative to the tube. Experimental data from previous work was used to validate the computational models used here, where simulations using the forcing measured from an impulse hammer successfully predicted the force

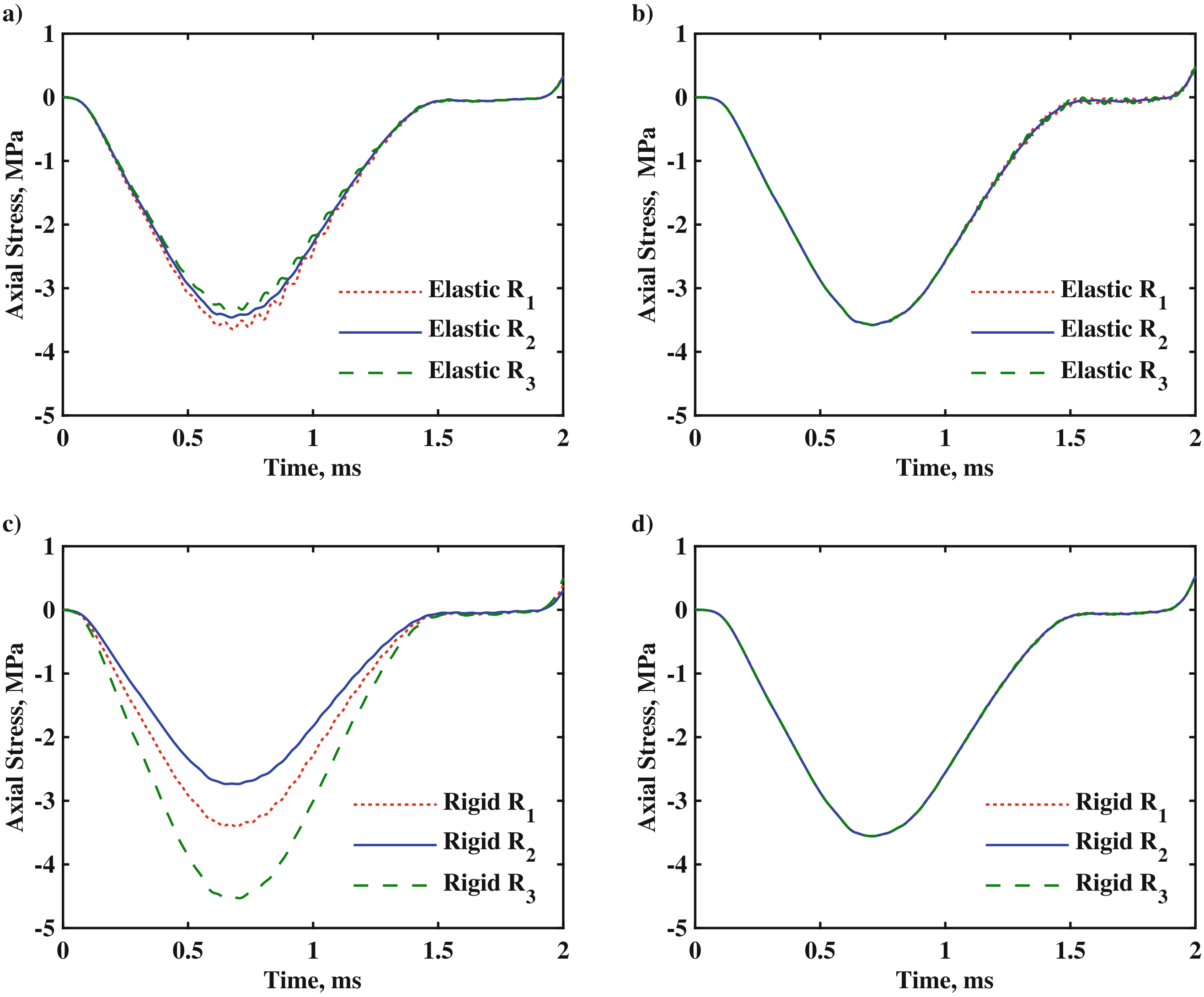

Fig. 2.7 Two separate simulations were used to calculate the normal stress in the axial direction, with one simulation having an elastic end cap and the other having a rigid end cap. Each plot gives the axial stress for each of the three elements through the tube's thickness at either the cap-tube connection or virtual strain gage location. (**a**) Simulation using an elastic end cap, with the stress measured at the cap-tube connection. (**b**) Simulation using an elastic end cap, with the stress measured at the virtual strain gage location. (**c**) Simulation using a rigid end cap, with the stress measured at the cap-tube connection. (**d**) Simulation using a rigid end cap, with the stress measured at the virtual strain gage location

derived from the strain gages. In the experiment, the traveling stress wave was in a state of compression when first passing the strain gages, rebounded from the opposite end, and due to the boundary condition, was tensile when returning to the strain gages. This superposition of the tensile and compressive waves created artificially small force measurements. It was found that to measure contact forcing occurring for time intervals longer than 0.3 ms, the tube would need to be lengthened. Subsequent simulations featured an extra 3.8 m of tube to increase the allowed forcing time duration beyond 1.5 ms.

Switching from elastic to rigid material models for the aluminum cap created little difference in the measurements by the strain gages. This suggests the deformation within the end cap is small, and not a significant cause of discrepancy between the force measurements. However, the mass of the end cap did have significant influence over the force measurement discrepancy. The end cap was significantly heavier than a portion of the tube of equal length. Simulation of the density of the end cap being reduced, with the bar lengthened, showed far better agreement with the contact force. Future work using a Hopkinson tube could feature determining an end cap design that balances both being lightweight to reduce inertial effects on results and still sufficiently strong to resist excess deformation that could also potentially occur.

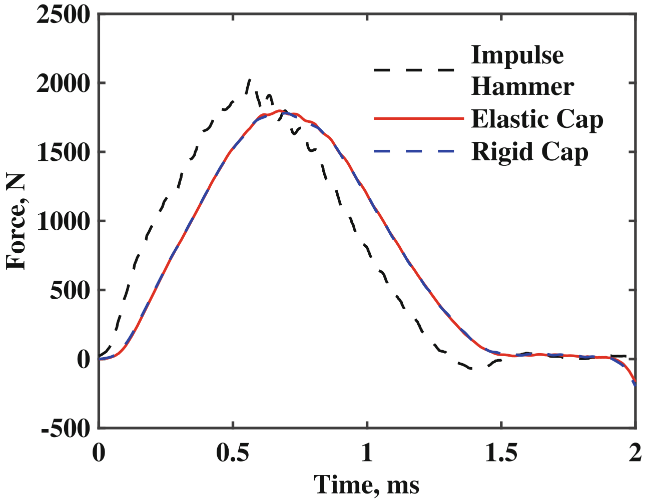

Fig. 2.8 The resultant force, $F_c(t)$, across the cap-tube connection (location shown in Fig. 2.5), which closely resembles the force calculated from the Hopkinson tube, shown in Fig. 2.6

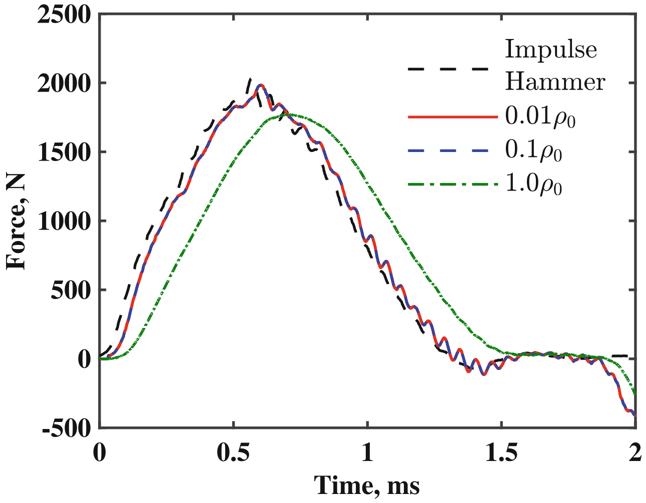

Fig. 2.9 Simulations using a rigid end cap of one-tenth and one-hundredth of aluminum's density showed agreement with the contact force. The density of the tube was not altered in any of the simulations

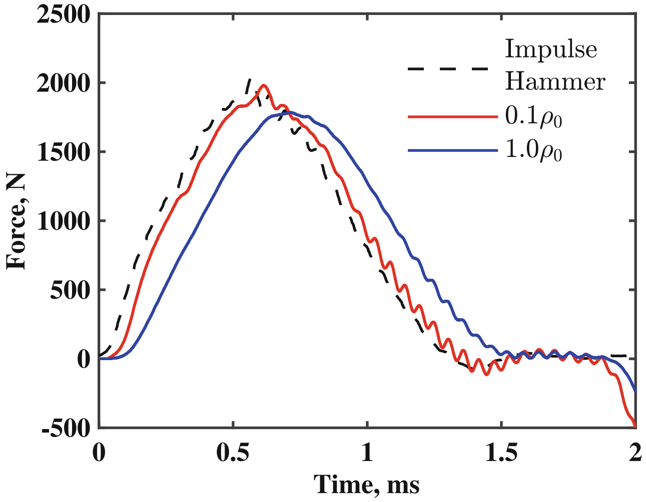

Fig. 2.10 Simulations using an elastic end cap of one-tenth aluminum's density showed good agreement with the contact force, which was also the case with the rigid caps shown in Fig. 2.9. The density of the tube was not altered in any of the simulations

Acknowledgements The author would like to thank Chuck Ruggeri, Mike Pereira, and Duane Revilock from NASA Glenn Research Center and Martin Annett from NASA Langley Research Center, for the discussions that supported this work. The author would also like to thank the members of the Gas Turbine Laboratory at Ohio State, including Dushyanth Sirivolu and Kiran D'Souza, for some interesting discussions during this work.

References

1. Barber, J. P., Taylor, H. R., Wilbeck, J. S.: Bird impact forces and pressures on rigid and compliant targets. Tech. rep., Airforce Flight Dynamics Laboratory (1978)
2. Seidt, J., Pereira, J., Hammer, J., Gilat, A., Ruggeri, C.: Dynamics load measurements of ballistic gelatin impact using an instrumented tube. Tech. rep., NASA Glenn Research Center, The Ohio State University. (2012)
3. Flanagan, D., Belytschko, T.: A uniform strain hexahedron and quadrilateral with orthogonal hourglass control. Int. J. Numer. Methods Eng. **17** (5), 679–706 (1981)
4. Pereira, J. M., Annett, M. S., Luquin, V., Ruggeri, C. R.: Experimental and computational simulation of bird impacts on flat and sharp objects. Presentation, Aerospace Structural Impact Dynamics International Conference (2018)
5. Annett, M., Pereira, M.: Sensitivity analysis of bird strike on low noise rotor blade sections. In: AHS International 74th Annual Forum & Technology Display (2018)
6. Graff, K.F.: Wave Motion in Elastic Solids. Oxford University Press, London (1975)

Chapter 3
Evaluation of Constitutive Behavior of Aluminum Alloy AA6063-T6

Sanjay Kumar, Anoop Kumar Pandouria, Purnashis Chakraborty, Kuldeep Yadav, Amit Kumar, and Vikrant Tiwari

Abstract In this chapter, an effort has been made to investigate the constitutive behavior of aluminum alloy AA6063-T6 under different temperatures. Spectroscopy of the alloy is performed to get the chemical composition and weight percentage of elements in AA6063-T6. The quasi-static experiments under different strain rates at room (25 °C) and elevated temperatures (25 °C, 50 °C, 100 °C, 150 °C, and 200 °C) are performed. The tensile tests at high strain rates are performed using split Hopkinson tensile bar. It is observed that the flow stresses increase with an increase of strain rates, whereas flow stresses decrease at higher temperature experiment. Using these results, the constants of Johnson-Cook plasticity are evaluated by fitting the experimental data. These Johnson-Cook plasticity parameters are used as input parameters for finite element simulation.

Key words AA6063-T6 · spectroscopy · Johnson-Cook plasticity parameters · Hopkinson tensile bar

3.1 Introduction

Aluminum alloy of AA6xxx series is magnesium- and silicon-based alloy and possesses good strength to weight ratio with good machinability. Magnesium is used to increase its strength whereas the silicon reduces its melting temperature [1]. The heat treatment (T6) of aluminum alloy of grade AA6063-T6 represents solution heat treated with artificially aged. Due to light weight of aluminum alloy, it is preferred in automobiles and light trucks. AA6063-T6 has good weldability properties, so that it is used in vehicle chassis. Due to the use of aluminum alloys instead of steel, the weight may be saved up to 47% and it saves fuels, produces less pollution. Aluminum alloys are easily recyclable [2].

It has been seen through literatures that many authors obtained Johnson-Cook plasticity and Johnson-Cook failures model parameters for different alloys of aluminum, but few are available related to evaluation of dynamic properties of AA6063-T6. Johnson et al. [3], Lesuer [4], and Teng [5] obtained the constitutive model of AA2024-T351 whereas Sharma et al. [6] obtained constitutive model and failure model parameters of AA2014-T652. Giglio et al. [7] and Dabboussi et al. [8] evaluated parameters of constitutive model of AA6061-T6. Fracture model parameters of different aluminum alloys AA5083-H116 and AA7075-T651 were obtained by authors Clausen et al. [9] and Brar et al. [10], respectively.

3.2 Johnson-Cook Plasticity Model

Johnson-Cook plasticity model [11] relates the flow stress of metal with three independent parameters strain, strain rates, and temperature. The model includes five material constants (A, B, n, C, and m) as shown in Eq. (3.1)

S. Kumar (✉)
Applied Mechanics Department, Indian Institute of Technology, Delhi, New Delhi, India

Assistant Professor at Mechanical Engg, Deptt. at Delhi Technological university, Delhi, India

A. K. Pandouria · P. Chakraborty · K. Yadav · A. Kumar · V. Tiwari
Applied Mechanics Department, Indian Institute of Technology, Delhi, New Delhi, India

S. Mates, V. Eliasson (eds.), *Dynamic Behavior of Materials, Volume 1*, Conference Proceedings of the Society for Experimental Mechanics Series, https://doi.org/10.1007/978-3-030-86562-7_3

$$\sigma = [A + B\varepsilon^{n}]\left[1 + C\ln\frac{\dot{\varepsilon}}{\dot{\varepsilon}_{o}}\right][1 - (T^{*})^{m}] \tag{3.1}$$

where plastic strain is denoted byε, the strain rate is $\dot{\varepsilon}$, and the reference strain rate is $\dot{\varepsilon}_o$ whose value is $10^{-3}\ \mathrm{s}^{-1}$. "*A*" is the true yield stress of the material at a strain rate of $10^{-3}\ \mathrm{s}^{-1}$, corresponding to 0.2% offset strain. B and n represent the effect of strain hardening on the material. The parameter "*C*" is also known as strain rate sensitivity parameter, controls the effect of strain rate. The thermal softening fraction is denoted by "*m*" and T^{*} is the homologous temperature $\left(T^{*} = \frac{T - T_0}{T_m - T_0}\right)$, T_o is the room temperature while T_m is the melting temperature of the material.

3.3 Experimental Procedures

3.3.1 Material

Aluminum alloys AA6063-T6 is a Al-Si-Mg alloys which weight percentage of different elements is obtained with spectroscopy shown in Table 3.1. Tensile specimens for quasi-static and high strain rates are directly machined from a circular bar of 13 mm diameter using lathe machine. Specimen used for quasi-static experiment with dimensions is shown in Fig. 3.2 whereas fractured specimens at different strain rates are shown in Fig. 3.5.

3.3.2 Mechanical Testing

The quasi-static experiments were performed on universal testing machine of 100kN capacity procured with Zwick Company, whereas high strain rate tests were performed on tensile split Hopkinson bar (TSHB). The schematic diagram of TSHB is shown in Fig. 3.1 which consists hollow striker tube, end cap, incident, and transmitted bar. When striker impacts end cap, the tensile pulses are induced in bar and propagated towards specimen. When the propagated tensile waves pass through specimen, the tensile tests at high strain rates are supposed to conducted at high strain rates. The strain–stress properties at high strain rates are obtained using measured reflected and transmitted tensile strain on incident and transmitted bar, respectively.

Table 3.1 The chemical composition of AA6063-T6

Elements	Al	Cr	Cu	Fe	Mg	Mn	Si	Ti	Zn	Sn
% weight (wt%)	98.71	0.0016	0.0038	0.163	0.5476	0.0139	0.504	0.0213	0.0087	<0.001

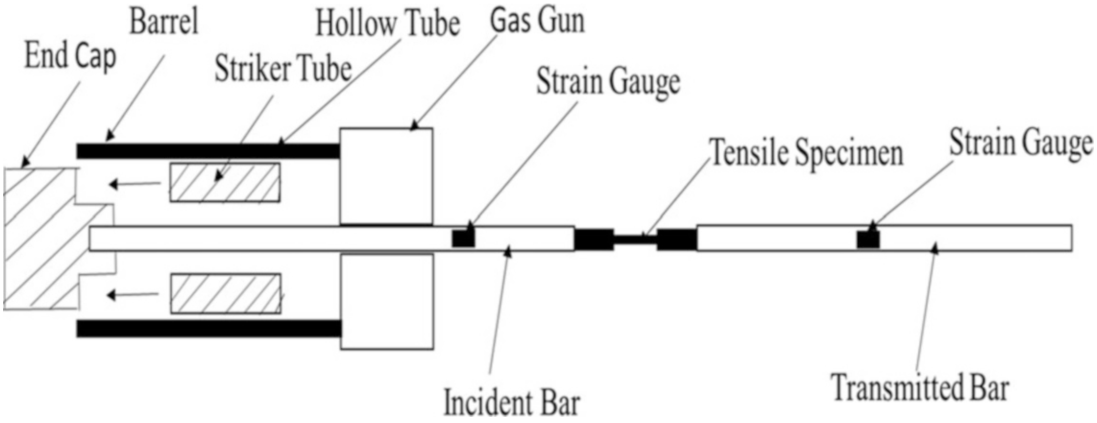

Fig. 3.1 Schematic of a tensile split Hopkinson pressure bar

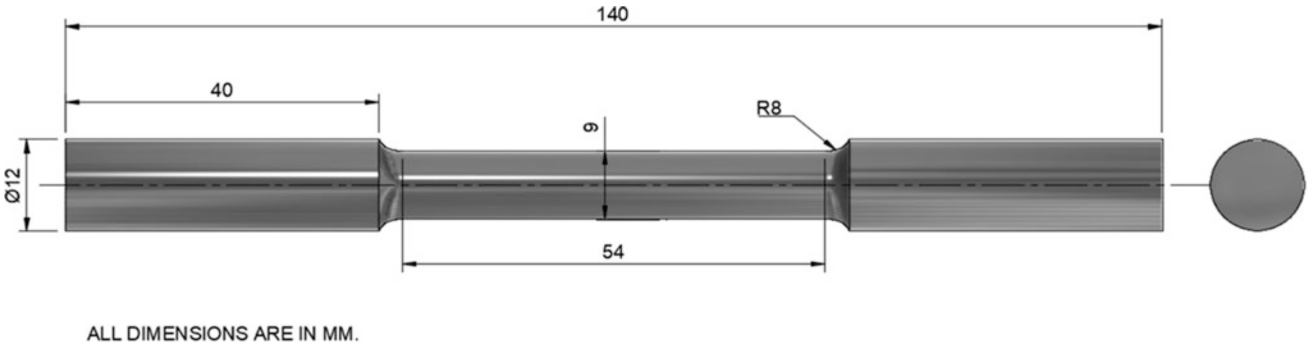

Fig. 3.2 Dimensions used for tensile test specimens of AA6063-T6

3.4 Results and Discussions

The specimen shown in Fig. 3.2, used for quasi-static tests at strain rates from 10^{-4} to 10^{-1}/s, had a gauge diameter of 9 mm, and the length of the reduced section is 54 mm, whereas the gauge length measured was 45 mm. The total length of the specimen, including gripping length (40 mm at each side), was140 mm, while portion used for gripping had 12 mm diameter according to standard E8M.

Figure 3.3 shows the true stress–strain curve for AA6063-T6 at different strain rates. The quasi-static experiments performed at strain rates 10^{-4}, 10^{-3}, 10^{-2}, to 10^{-1}/s are shown in Figs. 3.3a, b, c, d, respectively, and corresponding yield stress obtained with 0.2% offset method are 271.85, 278.17, 282.37, and 294.46 MPa. Tensile test at strain rate 410/s was performed on tensile Hopkinson pressure bar setup shown in Fig. 3.1. The true stress–strain curve is shown in Fig. 3.3e, and the yield strength measured corresponding to the strain rate is 346.07 MPa.

The parameter A of Johnson-Cook for AA6063-T6 is obtained from Fig. 3.3b, which shows the initial part of stress–strain curve and a 0.2% offset strain method is used to find yield stress for the AA6063-T6. In this method, a line parallel to the elastic region and 0.2% offset is drawn, which intersects the true stress–strain curve at a point. The intersection point, which is considered the yield stress for AA60632-T6, is 278.17 MPa, which denotes the parameter A of the Johnson-Cook constitutive model which is presented in Table 3.2.

The strain hardening parameters (B and n) for AA6063-T6 are obtained from the curve drawn between log plastic stress versus log plastic strain (Fig. 3.4). The linear fit line slope is the value of n, whereas the intercept with the y-axis provides ln (B), which is used to obtain the value of B. The values of strain hardening parameters n and B obtained from Fig. 3.4 are 0.9632 and 527.55 MPa, respectively, which are presented in Table 3.2. The photographs of the fractured specimen at different strain rates are shown in Fig. 3.5.

For the evaluation of strain rate parameter C, the experiments are performed at different strain rates, and fractured specimens with different strain rates are shown in Fig. 3.5. The strain rate hardening parameter C is obtained from Fig. 3.6, where the ratio of dynamic stress to static stress is drawn on the y-axis, whereas the logarithm of strain rate multiplied with thousand is represented on the x-axis. The linear fit line is drawn over the experimental curve, and the slope of the line gives the value of C, which is 0.0132, and is represented in Table 3.2.

To obtain thermal softening parameter m, some experiments are performed at different temperatures at strain rate 0.001/s. The true stress–strain diagram of tensile specimens at different temperatures are shown in Fig. 3.7. From these curves, shown in the figure, the yield points at different temperatures are obtained. It can be seen in the figure that yield stresses decrease with temperatures. It is also observed that a curve at temperature 150 °C becomes flat, and the aluminum alloy behaves perfectly plastic. After getting yield stresses at different temperatures, the flow stresses at higher temperatures are divided with flow stress at room temperature. Figure 3.8 is drawn, which shows a graph between flow stress ratio and homologous temperature (T^{*}) on a log-log scale. The strain rate sensitivity parameter (m) is obtained with the slope of this curve and presented in Table 3.2.

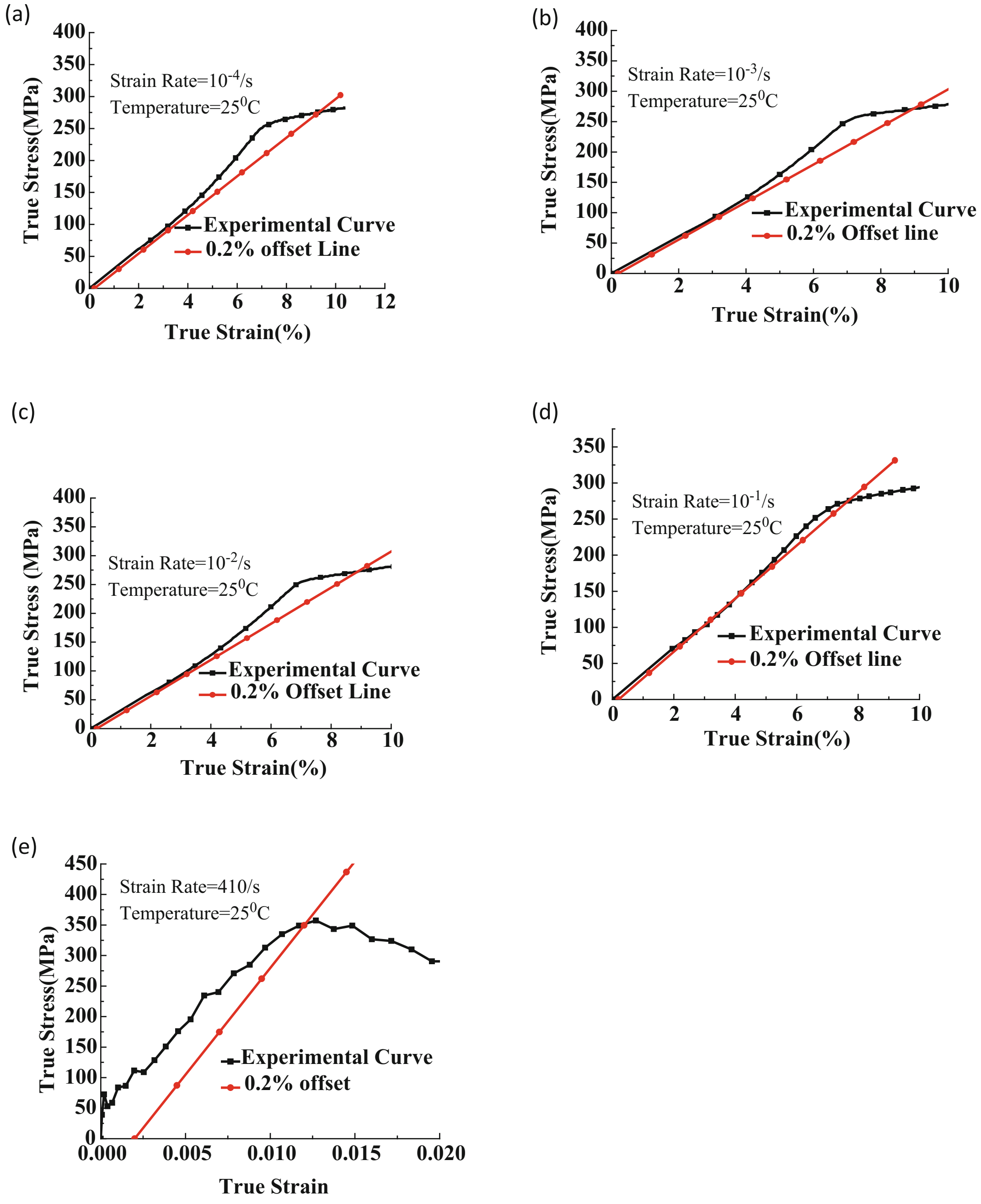

Fig. 3.3 True stress-strain curve for AA6063-T6 at different strain rates (25 °C temp) (**a**)10^{-4}/s (**b**)10^{-3}/s (**c**)10^{-2}/s (**d**)10^{-1}/s (**e**) 410/s

Table 3.2 Johnson-Cook Constitutive model parameters for AA6063-T6

A (MPa)	*B* (MPa)	*n*	*C*	*m*
278.17	527.55	0.9632	0.0132	1.246

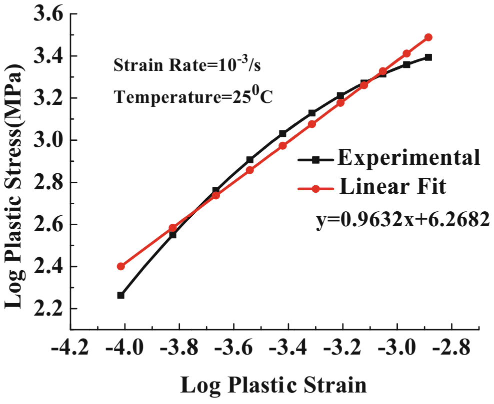

Fig. 3.4 Determination of strain hardening parameter for AA6063-T6

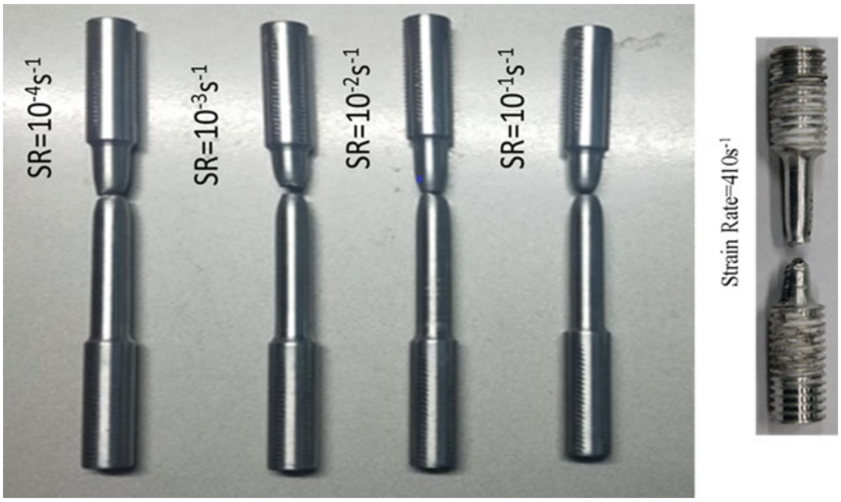

Fig. 3.5 Fractured Tensile specimens at different strain rates

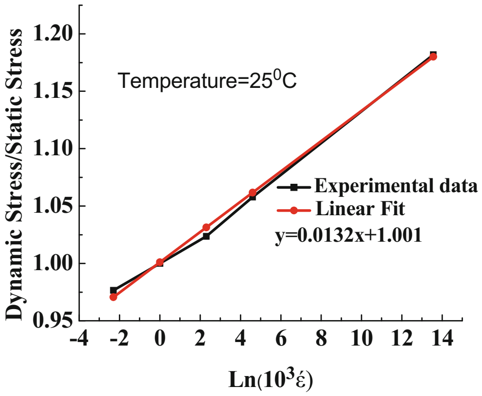

Fig. 3.6 Determination of strain rate sensitivity parameter (*C*) for AA6063-T6

3.5 Conclusions

This chapter reports the effect of strain rate and temperature on flow stress of aluminum alloy AA6063-T6. The uniaxial tensile tests in quasi-static conditions and dynamic tests at high strain rates were performed at universal testing machine and tensile split Hopkinson perrssure bar, respectively. The experimental results obtained were used to calibrate constitutive

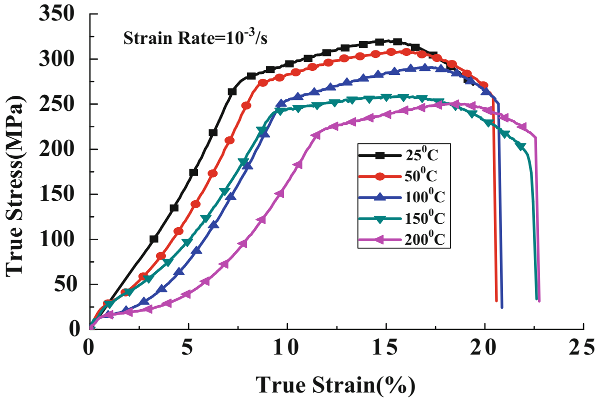

Fig. 3.7 True stress-strain curves at various temperatures for AA6063-T6 (strain rates 10^{-3} s^{-1})

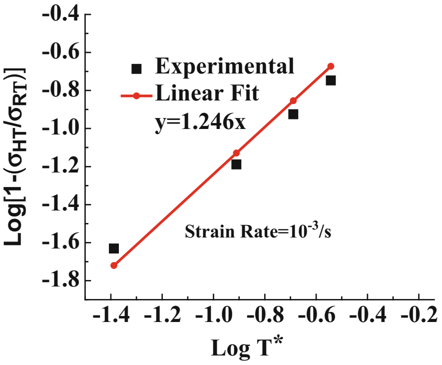

Fig. 3.8 Determination of thermal sensitivity parameter(m) AA6063-T6 (strain rates 10^{-3} s^{-1})

model of Johnson-Cook. It was also observed that AA6063-T6 exhibited positive strain rate sensitivity but flow stresses decreased with temperature. It was also observed that stress–strain curve at temperature 150 °C became flat, and the aluminum alloy behaved perfectly plastic.

References

1. KalpakJian, S., Schmid, S.R.: Manufacturing Engineering and Technology. Seventh Edition Pearson Education (2014)
2. Smerd, R., Winkler, S., Salisbury, C., Worswick, M., Lloyd, D., Finn, M.: High strain rate tensile testing of automotive aluminum alloy sheet. Int. J. Impact Eng. **32**, 541–560 (2005)
3. Johnson, G.R., Cook W. H.: A Constitutive Model and Data for Metals Subjected to Large Strains, High Strain Rates, and High TemperaturesProceedings 7th International Symposium on Ballistics, (1983)
4. Lesuer, D.R.: Experimental investigations of material models for Ti6Al4V titanium and 2024-T3 aluminum. Faa. **DOT/FAA/AR**, 1–41 (2000)
5. Teng, X.: High velocity impact fracture. Ph.D. Thesis. (1), 330–2005 (1994)
6. Sharma, P., Chandel, P., Bhardwaj, V., Singh, M., Mahajan, P.: Ballistic impact response of high strength aluminium alloy 2014-T652 subjected to rigid and deformable projectiles. Thin-Walled Struct. **126**, 205–219 (2018)
7. Giglio, A., Giilioli, M., Manes, A.: Mechanical Behaviour of Al 6061-T6 Aluminium Alloy Under Large Strain and Failure. Numerical Modeling of Materials Under Extreme Conditions, pp. 143–171. Springer (2014)
8. Dabboussi, W., Nemes, J.A.Ã.: Modeling of ductile fracture using the dynamic punch test. Int. J. Mech Sci. **47**, 1282–1299 (2005)
9. Clausen, A.H., Børvik, T., Hopperstad, O.S., Benallal, A.: Flow and fracture characteristics of aluminium alloy AA5083-H116 as function of strain rate, temperature and triaxiality. Mater. Sci. Eng. A. **364**(1–2), 260–272 (2004)
10. Brar, N.S., Joshi, V.S., Harris, B.W.: Constitutive model constants for Al7075-T651 and Al7075-T6. AIP Conf. Proc. **1195**(1), 945–948 (2009)
11. Johnson, G.R., Cook, W.H.: A constitutive model and data for metals subjected to large strain, high strain rates and high pressures. Seventh Int. Symp. Ballist., 541–547 (1983)

Chapter 4
Effect of Equal Energy Impact on CFRP in Arctic Conditions

Arnob Banik and Kwek-Tze Tan

Abstract In this study, the impact response and damage mechanisms of carbon fiber-reinforced polymer (CFRP) under equal impact energy but different mass-velocity combinations are investigated. CFRP samples are also subjected to impact at room temperature (23 °C) and low-temperature (−70 °C) conditions with the aim to understand composite behavior in cold Arctic environment. Furthermore, this study explores the effect of ice formed on substrate surface, so as to elucidate the influence of surface ice on impact damage. Results show longer test duration for large mass impactor case, whereas smaller impact mass causes shorter impact duration. Moreover, different damage modes are detected by X-ray micro-computed tomography for different mass-velocity configurations. Initial oscillations from force-time curves indicate that low-mass–high-velocity cases create substantial surface damage. Specimens at −70 °C show less damage than samples at 23 °C due to enhanced stiffness at lower temperature. This study reveals that the presence of surface ice has negligible effect due to the brittleness of ice and small fracture energy compared to the CFRP substrate. This research provides understanding on the dynamic behavior of CFRPs when deployed in low-temperature icy conditions.

Key words Woven CFRP · Arctic condition · Delamination · Surface ice · Micro-computed tomography

4.1 Introduction

Global warming issues for the last few decades have caused a greater amount of shrinkage in ice-covered areas in the polar regions. So, new shipping routes have been discovered for quick transportation in the arctic areas [1]. To operate in those extremely low-temperature environments and avoid potential structural damages from any possible collision with ice, the naval vessels must be uniquely designed. Structural design with composite structures has been increasingly used in various engineering applications such as aerospace exterior surfaces, turbine blades, and arctic naval ships. The involvement of composite structures in such industrial applications is due to their superior flexural stiffness and ultra-lightweight [2]. But still, high-velocity impacts may cause severe structural damage [3–6]. Even low-velocity impacts are found to be responsible for the barely visible impact damage (BVID), where impact velocity stays less than 10 m/s [7]. BVID can exist in marine structures when a collision occurs between ice objects and loadbearing composite sandwich structures of the vessels [8]. So, it is essential to investigate the low-velocity impact on composites.

Furthermore, a low-temperature condition in the arctic region can significantly influence the mechanical properties of the composites and thus alter the impact performance. The dynamic behavior of composite laminates in low-temperature environments was analyzed in few studies. Im et al. [9] analyzed the impact performance of CF/EPOXY laminates at low temperatures and found that the delamination area significantly increased at lower temperatures. A comparison in the impact performance of stitched and unstitched composites at room and low-temperature conditions was presented by Elamin et al. [2]. Though both material systems showed greater matrix damage at—70 °C than room temperature, unstitched CFRP woven laminates were found to be more sensitive to the change in the damage behavior from BVID to visible complicated damage than the stitched polyimide composites. Gómez-del Rıo et al. [10] investigated the impact damage behavior of CF/3502–6 epoxy laminates and observed the existence of damages in the form of larger matrix cracks, greater delamination, deeper penetration, severe fiber-matrix debonding as well as fiber fracture at low temperatures (−150 °C). Jia et al. [11] identified enhanced flexural strength and energy absorption in CFRP composites at lower temperatures (−60 °C, −100 °C) while they became stronger and tougher. Many studies show that the overall impact performance of the CFRP laminates at

---

A. Banik (✉) · K.-T. Tan
Department of Mechanical Engineering, College of Engineering and Polymer Science, The University of Akron, Akron, OH, USA
e-mail: ab353@zips.uakron.edu

S. Mates, V. Eliasson (eds.), *Dynamic Behavior of Materials, Volume 1*, Conference Proceedings of the Society for Experimental Mechanics Series, https://doi.org/10.1007/978-3-030-86562-7_4

low-temperature environments is reduced. But Castellanos et al. [12] found less degree of damage in woven carbon composites at −50 °C than at room temperature. Some studies [13, 14]] focused on the impact behavior of thermosetting (TS)) composites by lowering the temperatures and mentioned less impact resistance as well as lower energy absorption in TS composite due to matrix contraction. Though the above studies have discussed how low-temperature conditions can modify the damage mechanism characteristics of composites from low-velocity impact, the presence of ice on the impact specimen has not been considered. So, it is yet to be explored the significance of the ice thickness on the impact behavior of composite specimens at the arctic condition.

Furthermore, impact responses can be different on composites at the same impact energy but varying the mass and velocity combinations of the impactors. Zabala et al. [15] investigated the influence of equienergetic (4 J & 8 J) impact loads on the woven CFRP specimens and attributed larger velocity responsible for greater delamination area on the specimens. Another research from Artero-Guerrero et al. [16] did not observe any significant influence of mass-velocity combinations on the CFRP samples at a specific impact energy level irrespective of damage mechanism. Though Yang et al. [17] discussed interlaminar and intralaminar damage of woven CFRP from low-velocity impact at different impact energies, how lowering the temperature might vary the damage mechanism was not mentioned. Feraboli et al. [18] discussed the low-velocity impact behavior of composite structure by doubling the impactor mass (9.9 kg and 20.4 kg) on AS4/NCT301 prepreg tape material and found higher critical forces and energy for higher masses. Studies from Prasad et al. [19] found that smaller mass impactors with higher impact velocity generated more damage with higher contact duration than larger mass impactors for specific impact energy on the quasi-isotropic laminated composite plates. But none of the above studies have investigated the equienergetic low-velocity impact at low-temperature conditions on the composites, let alone with ice.

In this study, the impact performance and the damage behavior in woven CFRP laminates are studied at three environmental conditions. The study aims to analyze the impact damage response and characterize the impact damage mechanisms under equienergetic low-velocity impact with different mass-velocity combinations of the impactors at 23 °C (RT), − 70 °C (LT) without ice, and −70 °C with ice (LT_Ice). The impact performances are compared from each condition at two different energy levels and the influence of the existence of ice is discussed. Instron CEAST impact test machine with an environmental chamber is employed to perform the impact tests. Force/energy/displacement-time history data will be analyzed to identify critical damage forces, panel displacement, and absorbed energy. Micro-computed tomography is utilized to observe the internal complex damage modes at RT, LT, and LT_Ice scenarios.

4.2 Experimental Details

4.2.1 Materials and Specimens Preparation

The woven CFRP composites were comprised of 0°/90° woven carbon fiber/epoxy layers and 8552 epoxy that accounted for 50% of the composition. All the specimens are cut into a standard size of 100 mm × 100 mm from panels using an electric diamond saw (Fig. 4.1).

The specimens had nominal thicknesses of 4.63 mm for the CFRP laminates. For specimens that are to be tested at −70 °C (LT), they are first kept in a low-temperature freezer at −12 °C for 48 h, and then conditioned at their test temperature −70 °C for 15 min before impact and during impact using a liquid nitrogen tank. Preparation of the ice face sheets involved using the custom-designed molds for the sample. The mold was made from flexible Tango black material. The whole combination of mold, sample, and water were kept in the freezer at −12 °C for 24 h. So, a 3 mm thick ice layer was created on the impact face

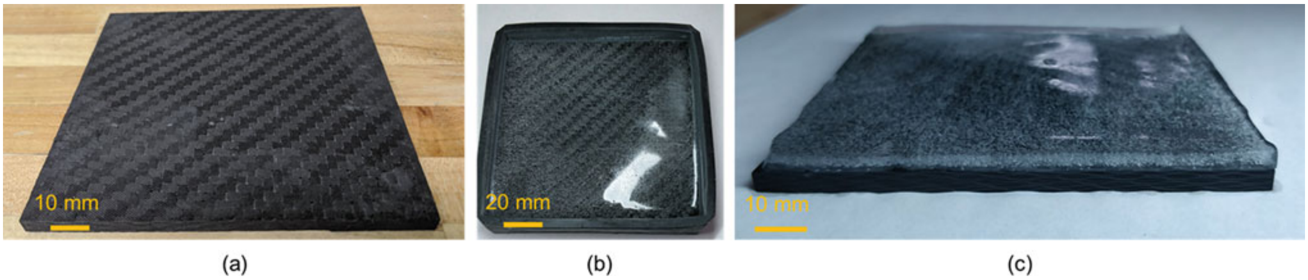

Fig. 4.1 (**a**) Woven CFRP specimen; (**b**) CFRP specimen inside the mold; (**c**) Ice layer on the CFRP sample

of the specimen. Before testing, the sample with ice face sheet was removed from the mold and conditioned at −70 °C (LT_Ice) for 15 min with nitrogen gas.

4.2.2 *Impact Testing Setup*

Instron CEAST 9350 drop tower testing machine equipped with an environmental chamber as shown in Fig. 4.2 was employed to conduct the low-velocity impact testing. A 16 mm diameter hemispherical indentor was attached to the strain gauge tub and tub holder. Anti-rebound catches were kept inactive during the tests. The masses available for the Instron machine were 2.482 kg and 12.482 kg for the low mass and high mass, respectively.

Using the kinetic and potential energy equations, the velocities and heights of impact could be determined when setting up the impact tests. For low-mass impacts at 31 Joules (ASTM D7136/D7136M-15), the corresponding height and velocity of impact were 1.273 m and 4.998 m/s. Whereas, for high-mass impacts at 31 Joules, the corresponding height and velocity of impact were 0.253 m and 2.229 m/s. Though 4.998 m/s from 31 J is considered as high velocities in comparison to the other velocity, they all are well below the criteria for low-velocity impact range (10-100 m/s). The DAS64K was used to acquire the data with a sampling frequency of 500 kHz measured at 1500 points.

4.2.3 *Damage Characterization Technique*

In this study, X-ray micro-computed tomography (μCT) scanning (Nikon XT H 320) was used to investigate the potential internal damages of the composite specimens after low-velocity ice impact testing. The tomographic radiographs were transmitted with an accelerating voltage of 125 keV and a current beam of 35 μA. Finally, VG Studio Max 2.0 software was utilized in post-processing and analyzing the scans.

Fig. 4.2 Instron CEAST 9350 drop tower testing machine

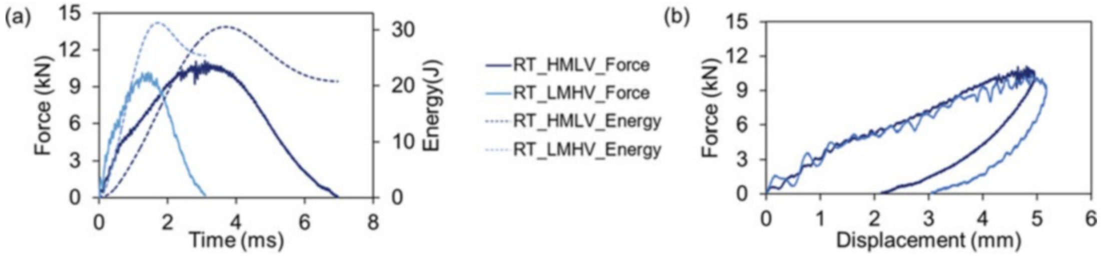

Fig. 4.3 (**a**) Force/energy-time curves; and (**b**)Force/energy-displacement curves for the CFRP specimens impacted at 31 J

4.3 Analysis

4.3.1 Effect of Different Mass-Velocity Combinations

Impact history curves are analyzed to understand the dynamic response and impact behavior of woven CFRP samples from different impactor mass-velocity combinations under similar energy. Representative force/energy/displacement versus time curves in room temperature are presented in Fig. 4.3a, b for 31 J of impact energy.

Impacts on the composites produced the characteristic response of an initial rise in load until a drop occurs at the very early stage of the impact event. This point is defined as the damage initiation force (DIF) which is responsible for the onset of matrix crack followed by delamination. Later, the reloading phase may occur up to a certain maximum point if enough residual potential energy is stored in the impactor during impact. This maximum point is defined as the highest peak force (HPF). Under 31 J impact energy, higher DIF was observed from the LMHV incident. Because higher velocity caused greater damage creation on the specimen which is supported by the initial higher load drop than the HMLV case. But, a higher value of HPF was noticed in the HMLV case. A greater amount of initial matrix crack and delamination damage from the LMHV incident reduced the stiffness of the composite. Moreover, shear crack-induced delamination is unstable, whereas bending crack-induced delamination grows in a stable way [15]. Initial higher oscillation in the force-time curve for the LMHV condition indicates the unstable delamination characteristics, whereas the HMLV scenario produced a smoother curve with bending crack-dominated delamination. Furthermore, contact time for high-velocity impact events is shorter than low-velocity impact. So, LMHV created a mixture of localized damage with a short impact duration. Whereas HMLV was responsible for widespread distal face damage due to a longer contact between the impactor and specimen.

The dotted lines in Fig. 4.3a represent the energy-time relation from the impact events. A higher amount of energy was absorbed from the higher velocity with a lower mass impactor. As such, more permanent displacement (Fig. 4.3b) was noticed from the LMHV incident. So, the higher velocity with a low-mass impactor became more detrimental to the specimen under 31 J energy. A similar trend of impact responses from different mass-velocity combinations was observed from low temperature without and with ice conditions.

However, Fig. 4.4 shows that a higher amount of energy was absorbed from the LMHV condition for 31 J impact energy in all environmental conditions and thus caused greater damage in the CFRP samples than HMLV impactors. Low-mass high-velocity impacts are sensitive to higher strain rate which results in greater tensile and compressive stress on the specimens [16]. Thus, more damage occurred from LMHV on the composites independent of the environmental conditions.

4.3.2 Effect of Environmental Condition

Figure 4.5 shows the micro-CT images of the CFRP specimens from 31 J impact in every environmental condition under LMHV impacts. A higher amount of matrix crack and delamination on the impact face, as well as fiber breakage on the distal face, were observed from LMHV impact than HMLV impact at room temperature (Fig. 4.5a).

Unlike the HMLV condition from the low-temperature condition, a little fiber failure was found on the distal face in the low temperature-LMHV condition (Fig. 4.5b). CFRP sample from LT_Ice condition with LMHV also showed fiber breakage on the distal face (Fig. 4.5c). But when there was ice on the impact face of the sample, (Fig. 4.5c), distal face fiber failure was slightly higher than the LT condition (Fig. 4.5b). It is also supported by Fig. 4.4 where absorbed energy for LT_Ice was found a bit higher than low temperature without ice. It was mostly because of the presence of water beneath the distal face during the preparation of ice in the freezer. The presence of moisture reduces the strength of a CFRP specimen.

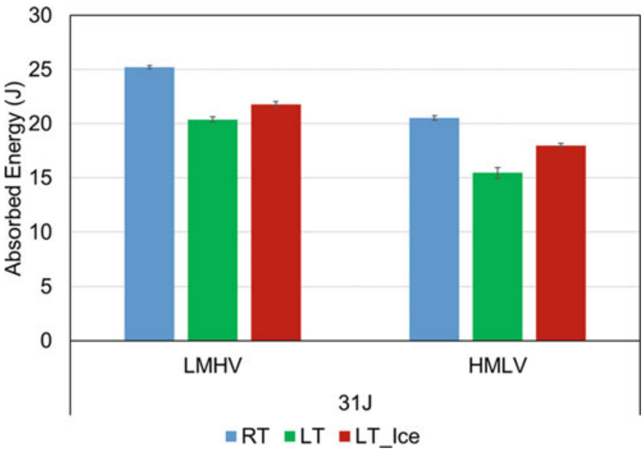

Fig 4.4 Influence of different mass-velocity combinations on absorbed energy

Fig. 4.5 Damage mechanism analysis from micro-CT images at 31 J LMHV in different environmental conditions

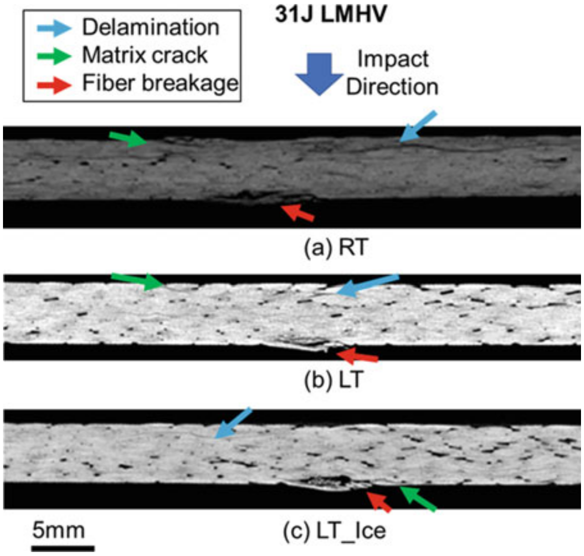

Though matrix cracks and delamination were also spotted on the samples from LT and LT_Ice condition at LMHV, the intensity of interlaminar damage was less than the room temperature sample. At low temperatures, polymer chain mobility is reduced in the CFRP. As such, binding forces between the molecules increase and therefore, the material strength [20]. Overall, at 31 J, all the samples are mostly dominated by interlaminar damage (matrix crack and delamination) at both room and low-temperature conditions.

4.4 Conclusion

This study investigated the low-velocity impact at 31 J varying the impactor mass at three different environmental conditions. The higher velocity with the lower mass of the impactor caused greater damage on the CFRP specimens at all temperatures. Greater strain rate sensitivity from higher velocity was found responsible for a greater amount of interlaminar damage than the impacts from higher mass impactors. Furthermore, less damage was observed at both mass-velocity combinations in low-temperature conditions than at room temperature impacts. Increased strength of CFRP epoxy matrix with lowering temperature assisted to improve impact resistance. The presence of surface ice on the composite specimen absorbed more energy than in low-temperature without ice condition. The existence of moisture during the preparation of ice probably weakened the strength of CFRP under this circumstance.

Acknowledgments The authors would like to acknowledge the support of this work through the research grant N00014-18-1-2546 provided by the United States Office of Naval Research (ONR Program Manager: Dr. Yapa Rajapakse).

References

1. Vihma, T.: Effects of Arctic Sea ice decline on weather and climate: a review. Surv. Geophys. **35**(5), 1175–1214 (2014)
2. Elamin, M., Li, B., Tan, K.T.: Impact performance of stitched and unstitched composites in extreme low temperature Arctic conditions. J. Dyn. Behav. Mater. **4**, 317–327 (2018)
3. Pernas-Sánchez, J., Pedroche, D.A., Varas, D., López-Puente, J., Zaera, R.: Numerical modeling of ice behavior under high velocity impacts. Int. J. Solids Struct. **49**(14), 1919–1927 (2012)
4. Pernas-Sanchez, J., Artero-Guerrero, J.A., Varas, D., Lopez-Puente, J.: Analysis of ice impact process at high velocity. Exp. Mech. **55**, 1669–1679 (2015)
5. Kim, H., Welch, D.A., Kedward, K.T.: Experimental investigation of high velocity ice impacts on woven carbon/epoxy composite panels. Compos. Part A Appl. Sci. Manuf. **34**(1), 25–41 (2003)
6. Coles, L.A., Roya, A., Sazhenkovb, N., Voronovb, L., Nikhamkinb, M., Silberschmidt, V.V.: Ice vs. steel: ballistic impact of woven carbon/epoxy composites. Part I – deformation and damage behaviour. Eng. Fract. Mech. **225**, 106270 (2018)
7. Cantwell, W., Morton, J.: The impact resistance of composite materials-a review. Composites. **22**(5), 347–362 (1991)
8. Elamin, M., Li, B., Tan, K.T.: Impact damage of composite sandwich structures in arctic condition. Compos. Struct. **192**, 422–433 (2018)
9. Im, K.H., Cha, C.S., Kim, S.K., Yang, I.Y.: Effects of temperature on impact damages in CFRP composite laminates. Compos. Part B. **32**(8), 669–682 (2001)
10. Gómez-del Rıo, T., Zaera, R., Barbero, E., Navarro, C.: Damage in CFRPs due to low velocity impact at low temperature. Compos. Part B Eng. **36**(41–50), 2005 (2005)
11. Jia, Z., Li, T., Chiang, F.P., Wang, L.: An experimental investigation of the temperature effect on the mechanics of carbon fiber reinforced polymer composites. Compos. Sci. Technol. **154**, 53–63 (2018)
12. Castellanos, A.G., Cinar, K., Guven, I., Prabhakar, P.: Low-velocity impact response of woven carbon composites in arctic conditions. J. Dyn. Behav. Mater. **4**, 308–316 (2018)
13. Benli, S., Sayman, O.: The effects of temperature and thermal stresses on impact damage in laminated composites. Math. Comput. Appl. **16**, 392–403 (2011)
14. Shah, S.Z.H., Karuppanan, S., Megat-Yusoff, P.S.M., Sajid, Z.: Impact resistance and damage tolerance of fiber reinforced composites: a review. Compos. Struct. **217**, 100–121 (2019)
15. Zabala, H., Aretxabaleta, L., Castillo, G., Urien, J., Aurrekoetxea, J.: Impact velocity effect on the delamination of woven carbon–epoxy plates subjected to low-velocity equienergetic impact loads. Compos. Sci. Technol. **94**, 48–53 (2014)
16. Artero-Guerrero, J.A., Pernas-Sánchez, J., López-Puente, J., Varas, D.: Experimental study of the impactor mass effect on the low velocity impact of carbon/epoxy woven laminates. Compos. Struct. **133**, 774–781 (2015)
17. Yang, B., Chen, Y., Lee, J., Fu, K., Li, Y.: In-plane compression response of woven CFRP composite after low-velocity impact: Modelling and experiment. Thin-Walled Struct. Compos. Part B Eng. **158**, 107186 (2021)
18. Feraboli, P., Kedward, K.T.: A new composite structure impact performance assessment program. Compos. Sci. Technol. **66**, 1336–1347 (2006)
19. Prasad, C.B., Ambur, D.R., Starnes, J.H.: Response of laminated composite plates to low speed impact by different impactors. AIAA J. **32**(6), 1270–1277 (1994)
20. Zsombor Sápi, Z., Richard, B.R.: Properties of cryogenic and low temperature composite materials – a review. Cryogenics. **111**, 103190 (2020)

Chapter 5
Kolsky Bar Tensile Gripping Methods for Structural Adhesives

Evan L. Breedlove

Abstract Structural adhesives are cured thermoset polymers which are employed in a wide range of industrial, transportation, and consumer applications to provide structural joining. Structural adhesives are particularly valuable for joining dissimilar materials, bonding composite materials, and light-weighting structures in transportation in order to minimize energy consumption. These applications also require structural adhesive bonds to provide satisfactory toughness and bond integrity under high strain rate conditions, such as car crash. Direct tensile characterization of structural adhesives at relevant strain rates is therefore critical for engineering design. However, the Kolsky tension bar grip design has not been systematically evaluated to determine what effects gripping may have on results. Grips may alter the stress state near the clamping area and introduce spurious failure modes. Furthermore, gripping methods can influence specimen alignment and efficiency of loading specimens. In this study, the effects of different grip designs on measured stress–strain response and location of failure are evaluated. Three different wedge grip designs are employed along with shoulder grips and clevis grips. Recommendations for tensile grip design and selection are discussed.

Key words Structural adhesives · Kolsky tension bar · Tensile gripping methods · Grip design · Polymer testing

5.1 Introduction

Structural adhesives are widely used for structural joining applications in industries including automotive, aerospace, and consumer electronics, where high-rate behavior is often critical in these applications. Classical split Hopkinson pressure bar (SHPB)/Kolsky bar methods are easily adapted to perform high-rate compression tests on adhesives; however, high-rate tensile failure data is often necessary to determine failure criteria. Furthermore, many industrial structural adhesives contain filler in quantities that can lead to pressure-dependent yield behavior [1, 2], meaning that both tensile and compressive high-rate data are needed to adequately characterize a high-rate yield criterion.

Few Kolsky tension bar experiments on structural adhesives have been conducted. Several studies cast cylindrical dumbbell specimens and threaded them directly into female threads on the bars [3–5]. More recent work by Trimiño et al. studied both toughened and untoughened epoxy using dogbone specimens mounted in a clevis [6]. Outside of structural adhesives, many Kolsky tension bar studies have been conducted on materials ranging from bone to steel with a variety of different test geometries and fixtures [7]. Preferences for methods include factors such as impedance matching to allow for strain calculation [3], mitigating interface-induced force spikes [8], and obtaining stress equilibrium [9].

Although it is well understood that grip design can influence Kolsky tension bar measurements, studies typically only employ a single gripping method. A comparison of different gripping methods has not been conducted on the same material in order to investigate the influence of grips on measured behavior. Furthermore, grip design can affect cost, ease of use, versatility, sensitivity to misalignment, and the ability to accommodate a wide range of materials. While these factors are not directly related to the resultant data, they have a substantial influence on the overall cost, in time and money, of Kolsky tension bar testing, thus influencing the availability of such data to enhance engineering design. In this study, a variety of wedge grip designs along with clevis and shoulder grips were evaluated with respect to resulting data as well as usability when employed for structural adhesive tensile testing.

E. L. Breedlove (✉)
Corporate Research Materials Laboratory, 3M Company, Maplewood, MN, USA
e-mail: elbreedlove@mmm.com

S. Mates, V. Eliasson (eds.), *Dynamic Behavior of Materials, Volume 1*, Conference Proceedings of the Society for Experimental Mechanics Series, https://doi.org/10.1007/978-3-030-86562-7_5

5.2 Methods

Material: Testing was conducted on a 3 M toughened epoxy material. This material is a relatively rubbery structural adhesive and was selected to highlight potential issues with testing that might not be suitable for softer or more complex adhesives. Note that it was not possible to machine this material to create threaded dumbbell specimens. Therefore, adhesive was coated in plaques approximately 2 mm thick and cured. Dogbones 6.35 mm wide and 12.7 mm long were then water-jetted from the plaques and conditioned under controlled temperature and humidity (23 °C/50% RH) for at least 3 days. Sample thickness in the neck region was measured with a drop gage for each sample.

Bar Apparatus: Testing was conducted on a Kolsky tension bar apparatus designed and built by REL Inc. (Calumet, MI). Incident and transmission bars consisted of 19 mm diameter 7075 aluminum, each 3.66 m long. The incident bar was actuated with a 61 cm long concentric 7075 aluminum striker bar, fired from a pneumatic gun, which struck a flange at the end of the incident bar (Fig. 5.1). An ABS pulse shaper was used. Bar strains were recorded by strain gages placed at the midpoint of the bars and recorded at 80 MHz. Strain gages were shunt calibrated prior to testing. Additionally, sample strains were measured in the neck of the dogbone using digital image correlation. Images were collected at 250,000 fps with a Shimadzu HPV-X2 camera.

5.2.1 *Gripping Methods*

Five gripping methods were evaluated, which were connected to the bars through threaded attachments (Fig. 5.2). Because focus was given to an adhesive which could not be easily machined, all gripping methods employed here were suited to testing dogbone specimens. In general, machining threaded dumbbell specimens can be challenging for many polymeric materials, making the dogbone geometry more versatile. Three of the gripping methods were variations on a wedge grip design, employing different wedge types which were press-fit into a collet. The toothed wedges and collet were developed by REL Inc. The flat and line-type wedges were designed and fabricated by the author for this study and paired with the REL collets. For the line-type wedges, a single line-type wedge was mated with a flat wedge for each grip. The shoulder and clevis grips were designed to accept the dogbone geometry. Because specimen strains were measured directly by DIC, impedance matching was not a focus.

5.2.2 *Data Processing*

Data were processed using the REL SurePulse software, version 1.22.0. The SurePulse software incorporates NCORR for digital image correlation [10]. Lagrangian strains were computed using a subregion radius of 5 pixels. Stresses were computed from the transmission bar strain. Data were smoothed with a low pass filter of 10 kHz or spline fitting, as appropriate to the signal.

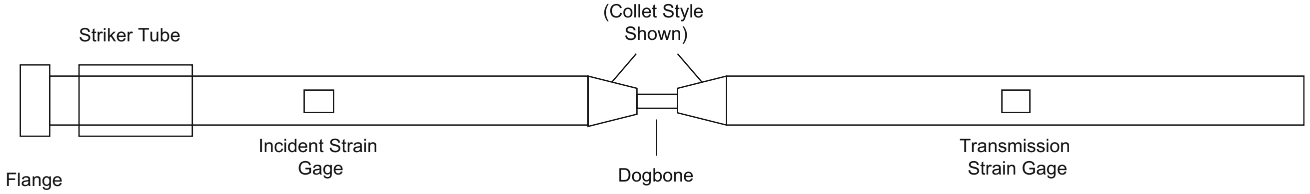

Fig. 5.1 Kolsky tension bar apparatus showing collet-style fixtures, which housed wedge (i.e., flat, line, and toothed) grips

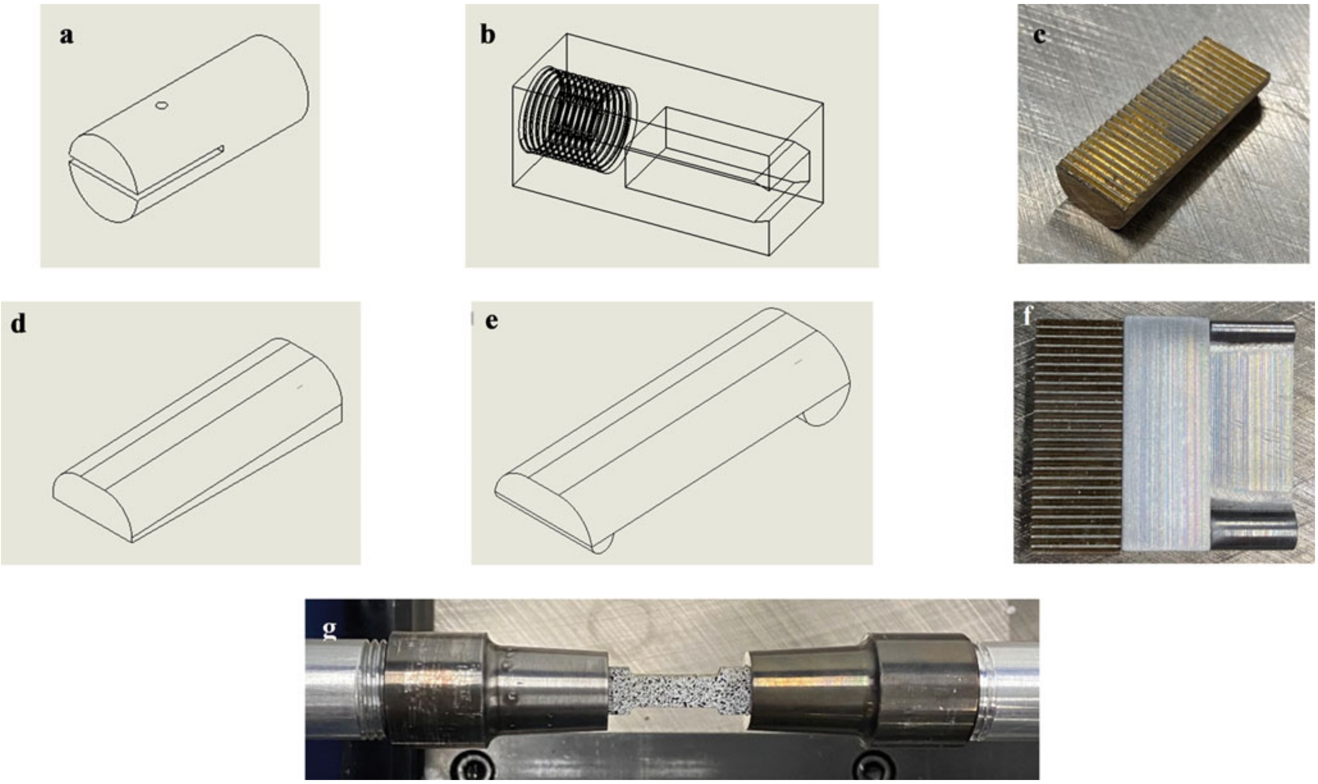

Fig. 5.2 Five gripping methods were evaluated: (**a**) clevis grip, (**b**) shoulder grip, (**c**) toothed wedge, (**d**) flat wedge, and (**e**) line-type. (**f**) All wedges were scaled to the same dimensions. (**g**) The wedge grips (**c**)–(**e**) were press fitted in a collet

5.3 Results

Five replicates were tested for each gripping method. All tests were conducted with the same striker, sample dimensions, and gun pressure, resulting in consistent strain rates of approximately 300 /s. Data for the shoulder grip are shown for completeness; however, the results were generally invalid as the dogbone consistently distorted and twisted out of the shoulder grip cavity. Strain uniformity was observed through the test for all gripping methods except the shoulder grip (Fig. 5.3). Other than for the shoulder grip, stress–strain curves were reasonably similar for all gripping methods (Fig. 5.4). Greater variability was observed for the clevis grip. Toothed grip results appear slightly less stiff than the other wedge grip results.

Dogbone failure was only observed during the first loading pulse for some of the tests. Nevertheless, failure mode was documented since it reflects the homogeneity of the stress state in the dogbone. None of the gripping methods were able to reproducibly cause failure in the middle (Fig. 5.5). The shoulder grip did not cause failure because the samples twisted out of the fixture. The majority of the clevis samples experienced a tear-out failure, where the tab of the dogbone ripped out of the fixture and the neck of the dogbone did not fail.

5.4 Discussion

Multiple gripping methods were evaluated for Kolsky tension bar characterization of a structural adhesive. The grips were all created to hold identical dogbones. Additionally, the experiments were conducted such that bar strain was only used to compute sample stress; therefore, grip impedance matching was not a concern since the reflected wave was not utilized in the analysis. Results indicated that gripping methods influenced the measured stress–strain response of the material; however, the wedge-type grips yielded very similar results. In fact, the clevis grips exhibited similar behavior as well at small strains; although, premature tear-out failure in the tabs occurred, resulting in an artificially low strain at break.

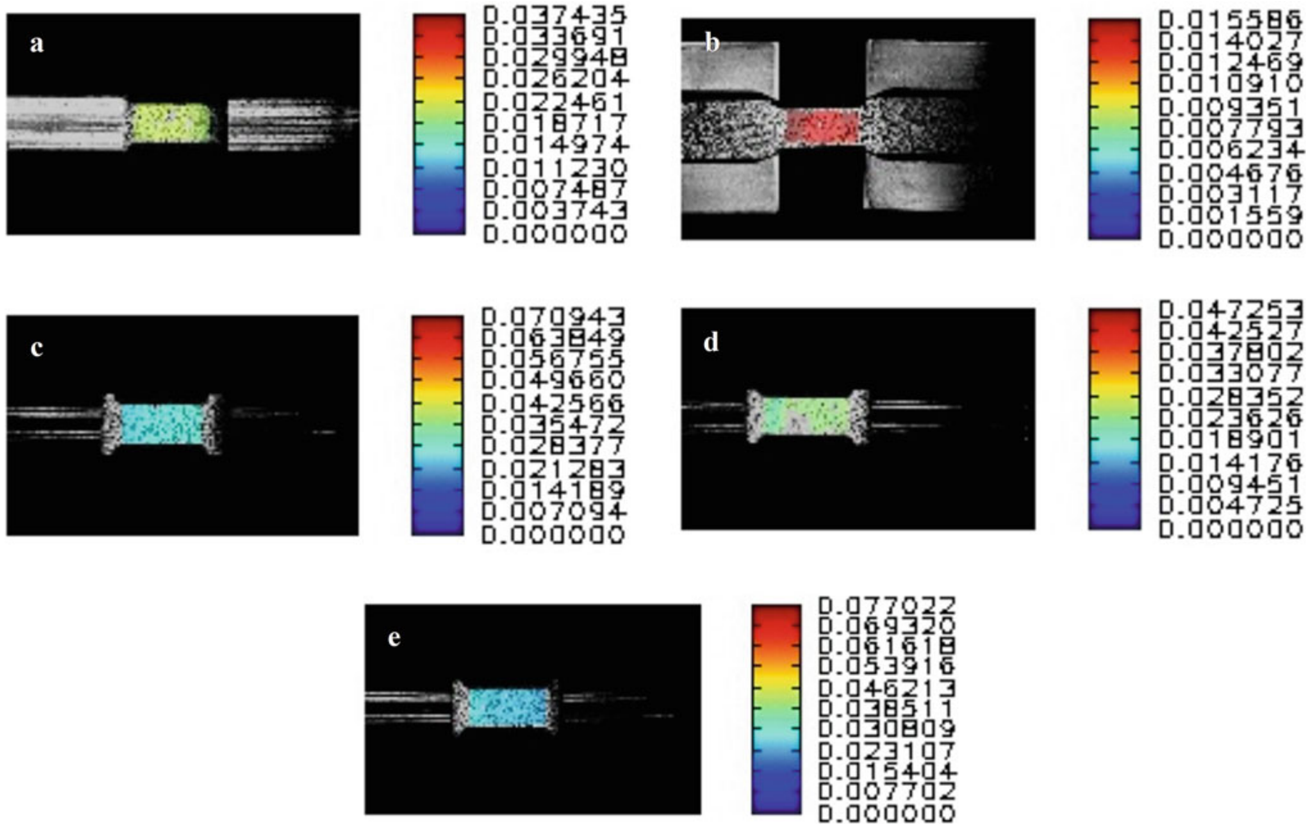

Fig. 5.3 Representative DIC images showing axial engineering strain. Images demonstrate uniform strain throughout neck of dogbone for (**a**) clevis, (**b**) shoulder, (**c**) toothed, (**d**) line, and (**e**) flat grips. All images are shown at approximately 2.5% strain, except for the (**b**) shoulder grip, which is shown at 1.5% strain because 2.5% strain was not achieved before pop-out

It is notable that DIC data indicated a uniform state of strain for all grips. Ideally, the grips themselves should not be a factor in achieving stress equilibrium; however, the grips do limit sample geometry, which does have a direct influence on stress equilibrium. The tested structural adhesive is relatively soft compared to other epoxy materials, meaning wave propagation through the dogbone is particularly slow. Consequently, stiffer structural adhesives will have even less difficulty with attaining stress equilibrium. Therefore, results suggest that this dogbone geometry and the evaluated grip designs are generally suitable for structural adhesives, at least with respect to stress equilibrium.

The applied strain pulse generated a maximum strain of approximately 8%. For approximately half of the samples, this was an insufficient strain to induce failure; although the distribution of failures suggests that the true failure strain is only slightly larger than 8%. Even though not all samples failed during the first loading pulse, it is interesting to consider the distribution of failure locations. Each of the wedge-style grips were able to induce a single failure in the middle of the dogbone. The line-type grip also generated a “blowout” failure, in which the neck of the dogbone fully fractured near both the incident and transmission sides of the sample, causing the entire neck to separate from the tabs. The majority of other failures occurred at the transmission side of the neck near the transition region. Additional experiments (not shown) were conducted to assess whether the sequence with which the sample was threaded onto the bars (e.g., incident side first or transmission side first) had any effect on the sidedness of failure, but no pattern was observed. Similarly, no effect was seen from whether the first collet attached was threaded onto the incident or the transmission bar. In contrast, the clevis grip produced either middle failures or tear-out failures, with no dogbone neck failures preferring one side or the other. This suggests that some feature of the wedge grips in contrast to the clevis grip causes a preference for failure closer to the grips. It was observed that the waterjet cutting left some defects in the edge quality of the dogbones. Furthermore, it was not straightforward to ensure that the collet was perfectly coaxial with the center axis of the dogbone. Even with perfectly aligned bars, any misalignment between the collets and the dogbone would lead to some bending. It is hypothesized that this bending, coupled with any imperfections in the dogbone edges near the neck transition region, would lead to preferential failure closer to the grips. Considering the difficulties with perfectly aligning the collets and the dogbone, it seems unlikely that middle failures can be consistently obtained without developing a more complex fixturing jig for attaching the grips to the dogbone.

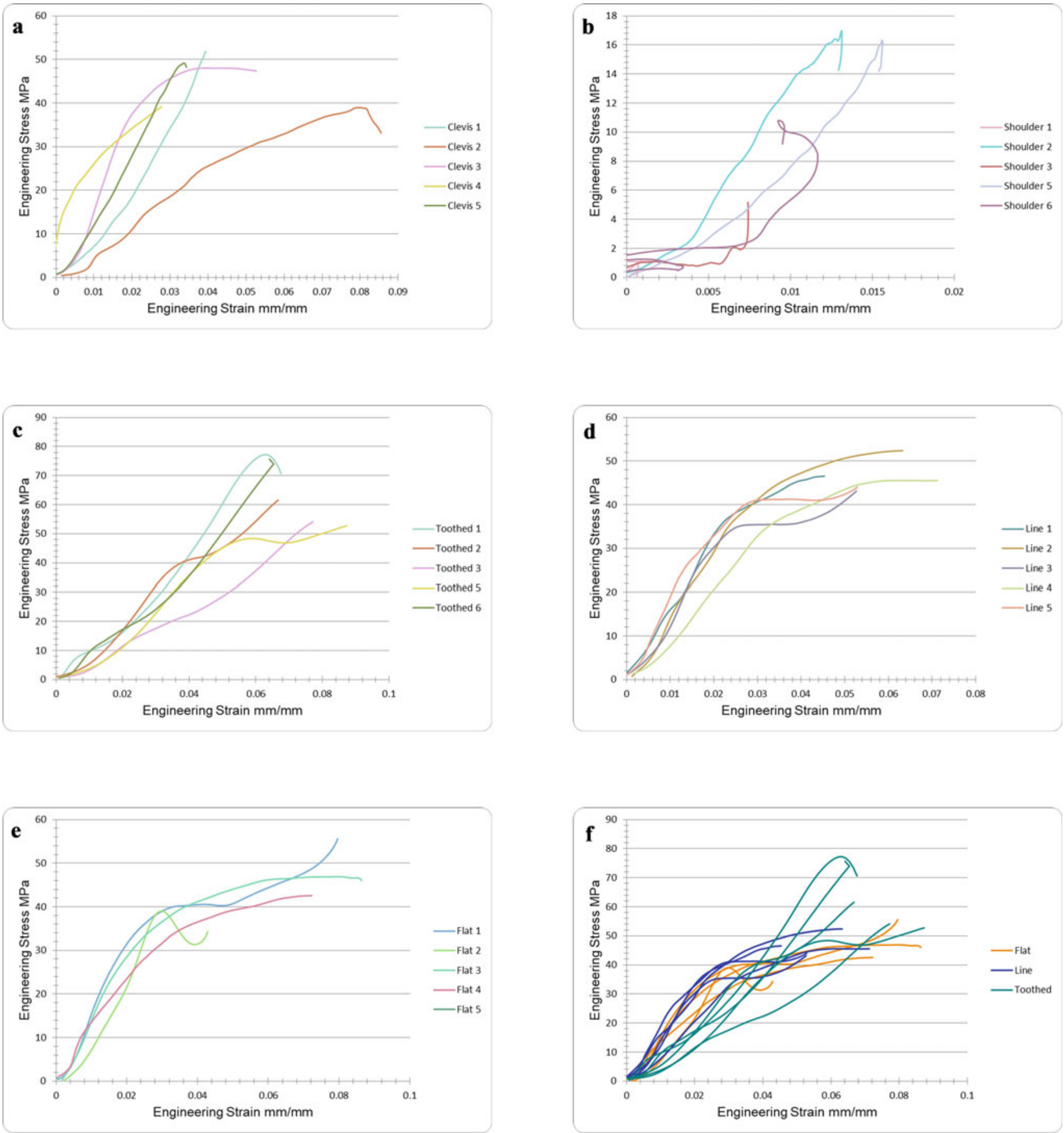

Fig. 5.4 Stress–strain curves for (**a**) clevis, (**b**) shoulder, (**c**) toothed, (**d**) line, and (**e**) flat grips. Large variability was observed for the clevis and shoulder grips. (**f**) Results from the collet type grips (toothed, line, and flat) were also compared

Collectively, the data indicate that any tensile grip design can yield accurate results, provided that several constraints are met. First, the Kolsky bar experiment must be conducted using DIC or some other direct method for strain measurement so that impedance matching is not a factor. Second, the gripping method must retain the sample for the duration of the test. Finally, the gripping method should not induce any secondary loads on the sample that would lead to failure outside the neck region.

The suitability of multiple gripping methods suggests that grips may be selected for non-technical reasons such as ease of use, cost, versatility, and the ability to accommodate multiple thicknesses of materials. These considerations are particularly

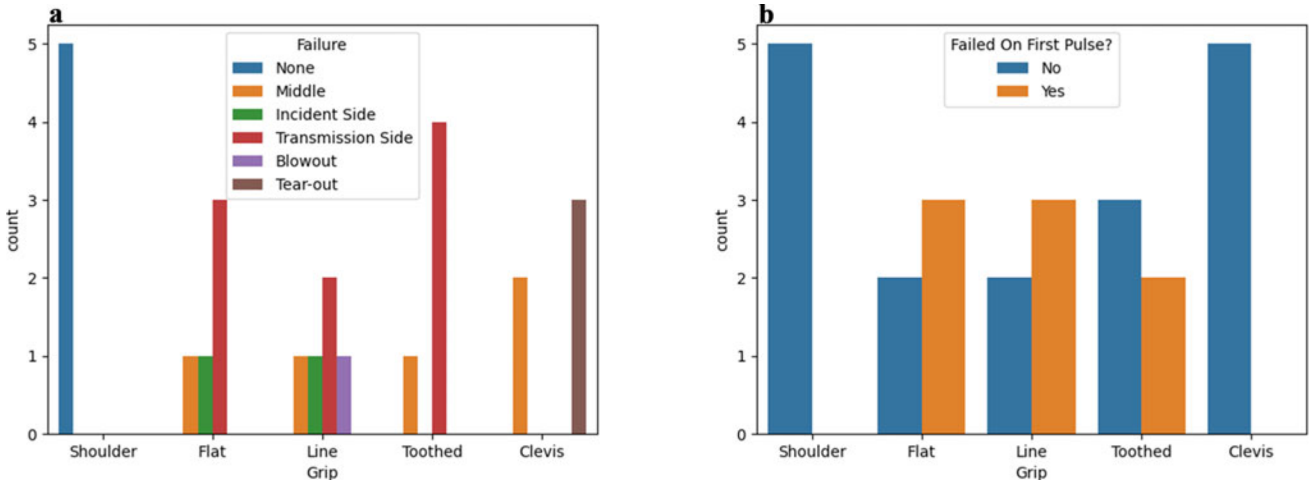

Fig. 5.5 Summary of failure modes showing (**a**) the location of failure and (**b**) whether failure occurred on the first pulse

Table 5.1 Qualitative performance factors assessed for each of the gripping methods

	Performance factors				
Grip	Thickness variation	Misalignment insensitivity	Ease of use	Cost	Material versatility
Shoulder	++	+	++	+	–
Clevis	+	++	+	++	+
Flat	–	–	–	–	+
Line	+	–	–	–	++
Toothed	–	–	–	–	–

important if high-rate test methods are to become accessible to a larger selection of test labs. For instance, the wedge-type grips are designed to accept a specific thickness sample. For a lab where material thickness cannot be easily controlled, this requires creation of a set of wedges of many different thicknesses, which in turn increases cost. Conversely, while the shoulder grips are easy to use, this study demonstrates that they are not suitable for more rubbery materials. Finally, while the toothed grip demonstrated similar performance to the flat and line-type wedges for these experiments, prior testing indicated that the teeth cutting into some structural adhesives can cause failure in the grips, making them less versatile for rubbery materials. These qualitative performance factors are summarized in Table 5.1.

A key limitation of this study was that grip designs were not optimized or revised based on test results. It is possible and even likely that shoulder grips could be redesigned to work with the material tested. Similarly, a redesign of the dogbone geometry would likely resolve the tear-out issue with clevis grips. Future work could provide design guidelines for these different grip types. Nevertheless, it is notable that the wedge-type grips did not require design optimization. Additionally, this study only considered a single material at a single strain rate. Inertia effects could become more pronounced at higher strain rates [11], and misalignment may be less of a concern for materials whose bending stiffness is comparable to or greater than the bending stiffness of the bars.

5.5 Conclusion

Kolsky tension bar testing for structural adhesives is important for many industrial applications. This systematic study suggests that data can be reliably captured using many different gripping methods provided they obey key constraints.

Acknowledgments Special thanks to Derek Edmunds for his assistance with drafting the grip designs.

References

1. Jousset, P., Rachik, M.: Pressure-dependent plasticity for structural adhesive constitutive modeling. J. Adhes. Sci. Technol. **24**(11–12), 1995–2010 (2010)
2. Wang, C.H., Chalkley, P.: Plastic yielding of a film adhesive under multiaxial stresses. J. Adhes. Adhes. **20**(2), 155–164 (2000)
3. Chen, W., Lu, F., Cheng, M.: Tension & compression tests under quasi-static & dynamic loading. Polym. Test. **21**(2), 113–121 (2002)
4. Gilat, A., Goldberg, R.K., Roberts, G.D.: Strain rate sensitivity of epoxy resin in tensile and shear loading. J. Aerosp. Eng. **20**(2), 75–89 (2007)
5. Goglio, L., Peroni, L., Peroni, M., Rossetto, M.: High strain-rate compression and tension behaviour of an epoxy bi-component adhesive. Int. J. Adhes. Adhes. **28**(7), 329–339 (2008)
6. Trimiño, L.F., Cronin, D.S.: Evaluation of numerical methods to model structural adhesive response and failure in tension and shear loading. J. Dyn. Behav. Mater. **2**(1), 122–137 (2016)
7. Chen, W., Song, B.: Split hopkinson (Kolsky) bar. Springer Science, New York (2011)
8. Song, B., Wakeland, P.E., Furnish, M.: Dynamic Tensile Characterization of Vascomax® Maraging C250 and C300 Alloys. J. Dyn. Behav. Mater. **1**(2), 153–161 (2015)
9. Nie, X., Song, B., Ge, Y., Chen, W.W., Weerasooriya, T.: Dynamic tensile testing of soft materials. Exp. Mech. **49**(4), 451–458 (2009)
10. Blaber, J., Adair, B., Antoniou, A.: Ncorr: open-source 2D digital image correlation matlab software. Exp. Mech. **55**(6), 1105–1122 (2015)
11. Song, B., Antoun, B.R., Jin, H.: Dynamic tensile characterization of a 4330-V steel with kolsky bar techniques. Exp. Mech. **53**(9), 1519–1529 (2013)

Chapter 6
An Initial Study of Ultraordnance Impact Experiments on Concrete

George H. Vankirk, Jesse A. Sherburn, William F. Heard, and Erik M. Chappell

Abstract Concrete is the most widely used building material in the world by volume and has historically be an integral component of the construction of US military assets. These assets have the requirement to protect against extreme events such as blast and penetration. Conventional ordnance impacts involving concrete materials at velocities on the order of 500 to 1300 m/s has been studied for many decades. One area that has received little study is in the area of ultraordnance impacts on concrete in which impact velocities exceed 1300 m/s. In this velocity range, material strength becomes less of a factor in the overall impact and penetration process. Due to the lack of relevant experimental data, a newly acquired two-stage light gas gun will be used in this study to perform ultraordnance impact experiments against concrete. Specifically, spherical projectiles will be fired against concrete targets at velocities ranging between 1 km/s and 7 km/s. The experimental data will help identify trends in this velocity range where little data exist in the literature for concrete. The experiments will also provide excellent validation data for computational methods that will model this type of extreme loading condition.

Key words Concrete · High-velocity impact · Two-stage light gas gun · Projectile penetration

6.1 Introduction

The design of structures intended to protect against various weapon threats relies on an understanding of the dynamic response of materials. Since World War II a major focus of research has centered on the penetration of materials subjected to high velocity impact of projectiles. This research includes the study of various materials at various ranges and velocities with the bulk of the early work involving empirical data with limited analytical tools. Numerous review articles have been published documenting large amounts of penetration data at various impact velocities [1–7]. The US Army Engineer Research and Development Center (ERDC) is keenly focused in response to concrete subjected to shock and penetration loading produced by impacts extending into the ultraordnance range and above. Ultraordnance impact velocities, as defined by Backman and Goldsmith [3], range between 1300 m/s and 3000 m/s. Impacts beyond 3000 m/s are considered hypervelocity impacts.

The purpose of this work is to perform some of the first comprehensive experiments of projectiles impacting concrete materials at velocities exceeding 1300 m/s. This data set will be critical for understanding the response of concrete subjected to impacts at increased velocities. The data will also provide for a parallel computational modeling effort that seeks to challenge material models and numerical methods that have very few validation points at increased impact velocities.

G. H. Vankirk (✉) · J. A. Sherburn · E. M. Chappell
Geotechnical Structures Laboratory, Survivability Engineering Branch, U.S. Army Engineer Research and Development Center, Vicksburg, MS, USA
e-mail: george.h.vankirk@erdc.dren.mil

W. F. Heard
Geotechnical Structures Laboratory, Geosciences and Structures Division, U.S. Army Engineer Research and Development Center, Vicksburg, MS, USA

S. Mates, V. Eliasson (eds.), *Dynamic Behavior of Materials, Volume 1*, Conference Proceedings of the Society for Experimental Mechanics Series, https://doi.org/10.1007/978-3-030-86562-7_6

6.2 Background

Little research exists in the literature concerning impact velocities exceeding to and beyond 1300 m/s on concrete and concrete-like materials. Some research does exist for shape charge penetration of concrete; however, those will not be considered in this overview. A brief overview of the literature relevant to this effort is covered in this section. Some of the first high velocity impacts of concrete was performed by Capoccioni et al. [8] where concrete-like spheres and ellipsoids were impacted by 1 g aluminum spheres at velocities around 10 km/s. Forrestal et al. [9] performed experiments with a 1.6 kg steel ogive penetrator at velocities between 1200 and 1400 m/s into semi-infinite concrete targets. Zielinski and Silsby [10] impacted aluminum rods with mass between 42 and 92 g at velocities ranging from 1400 to 2200 m/s into thin reinforced concrete targets. Dawson et al. [11] impacted 51.5 g tungsten rods with initial velocity of 2200 m/s into reinforced concrete targets. Mu and Zhang [12] studied the projectile erosion rates of a 26 g ogive steel penetrator for nominal impact velocities between 600 and 1500 m/s. Atou et al. [13] impacted steel spheres into reinforced concrete columns with mass 0.44–28.13 g at impact velocities ranging from 500 to 1700 m/s. Guo et al. [14] tested 3.8 kg ogive steel projectiles impacts into semi-infinite concrete targets to study the microscopic effects of erosion on the steel projective at velocities between 800 and 1400 m/s. He et al. [15] performed experiments investigating novel projectile design using a 1.4 kg steel penetrator impacting at velocities ranging from 1000 to 1400 m/s into multiple thick concrete targets. Kong et al. [16] quantified the erosion rates of steel projectiles under various impact velocities using 6.58 g steel rods impacting at velocities between 600 and 1800 m/s into semi-infinite concrete targets. The literature covered in this overview represents impacts over a large kinetic energy range of approximately 0.000055–3.7 MJ.

6.3 Analysis

For this study, a spherical 8.4 g S2 tool steel sphere with a diameter of 12.7 mm will be used as the projectile. In order to properly characterize the effects of a sphere impacting concrete at velocities beyond 1300 m/s a properly sized cylindrical concrete target must be used. A recent numerical study was conducted in order to accomplish this goal. Sherburn et al. [17] performed a number of computational simulations to determine an appropriately sized concrete target. The Holmquist-Johnson-Cook (HJC) material model [18] was used to model concrete with appropriate material constants for a conventional strength concrete. The calculations were run in the finite element code EPIC. The results of the exploratory study found that the diameter of the concrete cylinder should be at least 30 times the diameter of the projectile, and the depth of the cylinder should be between 20 and 30 times the projectile diameter. A snapshot of the damage contours of the computational results are shown in Fig. 6.1.

The ERDC has the capability to launch projectiles at velocity ranges below 1000 m/s and extending up to 7.5 km/s. In order to achieve impact velocities below 2000 m/s, a traditional fixed bore powder gun system will be used. When conducting experiments using the traditional fixed bore powder gun, two chronographs and a Phantom V710 high speed camera are used.

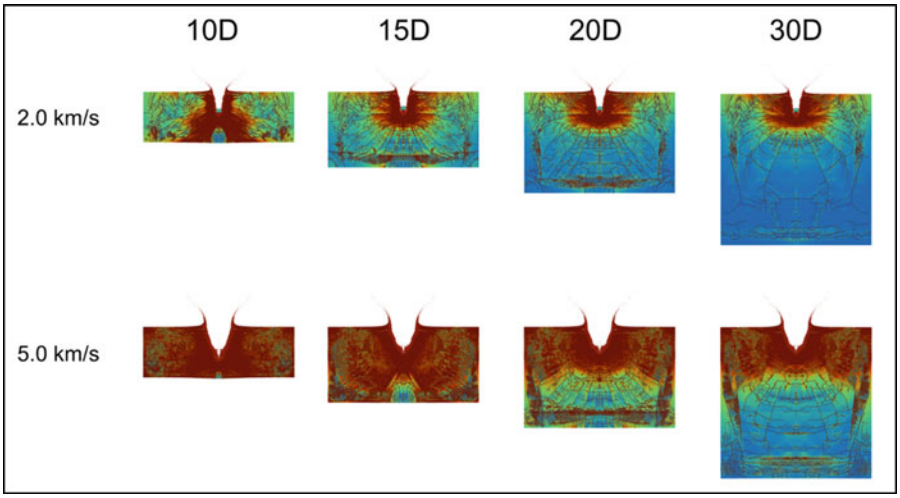

Fig. 6.1 Computational modeling effort to determine optimum depth of concrete target. Color contours represent predicted damage due to impact

Fig. 6.2 ERDC 25 mm two-stage light gas gun (2LSGG)

Table 6.1 Proposed velocity parametric study to be performed out on concrete

Impact velocity (m/s)	Impact energy (MJ)	Testing method
1000	0.0042	Powder gun
1500	0.0095	Powder gun
2000	0.0168	2SLGG
3000	0.0378	2SLGG
4000	0.0672	2SLGG
5000	0.1050	2SLGG
6000	0.1512	2SLGG
7000	0.2058	2SLGG

In order to achieve velocities above 2000 m/s, the ERDC has recently acquired a 25 mm two-stage light gas gun (2SLGG) shown in Fig. 6.2. The velocity of impacts generated by the 2SLGG will be captured by two laser curtains and the impact face will be recorded using a Specialized Imaging Kirana 5 M ultra-high speed video camera. The proposed parametric experimental test matrix is shown in Table 6.1. The test matrix covers a velocity range between 1000 m/s and 7000 m/s and a kinetic energy range of 0.0042–0.2058 MJ. The experimental results will be presented at the conference.

6.4 Conclusion

The study of impact velocities at velocity ranges of ultraordnance and beyond are of great importance to the U S Army. This effort focuses on the terminal effects of impacts on concrete material in velocity regimes that have previously had very little attention in the open literature. The experimental data set produced in this study is expected to aide in the design of protective structures that are exposed to extreme loading conditions as well as provide a valuable challenge to material models and numerical methods at elevated impact velocities.

Acknowledgements Permission to publish was granted by Director, Geotechnical and Structures Laboratory.

References

1. White, M.P.: Effects of Impact and Explosion. Office of Scientific Research and Development, Washington, DC (1946)
2. Kennedy, R.P.: A review of procedures for the analysis and design of concrete structures to resist missile impact effects. Nucl. Eng. neering Des. **37**, 183–203 (1976)
3. Backman, M.E., Goldsmith, W.: The mechanics of penetration of projectiles into targets. Int. J. Eng. Sci. **16**, 1–99 (1978)
4. Wilkins, M.L.: Mechanics of penetration and perforation. Int. J. Eng. Sci. **16**, 793–807 (1978)
5. Jonas, G.H., Zukas, J.A.: Mechanics of penetration: analysis and experiment. Int. J. Eng. Sci. **16**, 879–903 (1978)
6. Aptukov, V.N.: Penetration: mechanical aspects and mathematical modeling (review). Strength Mater. **22**, 230–240 (1990)

7. Ben-Dor, G., Dubinsky, A., Elperin, T.: Recent advances in analytical modeling of plate penetration dynamics – a review. Appl. Mech. Rev. **58** (6), 355–371 (2005)
8. Capaccioni, F., Cerroni, P., Coradini, M., Di Martino, M., Farinella, P., Flamini, E., Martelli, G., Paolicchi, P., Smith, P.N., Woodward, A., Zappala, V.: Asteroidal catastrophic collisions simulated by hypervelocity impact experiments. Icarus. **66**, 487–514 (1986)
9. Forrestal, M.J., Frew, D.J., Hanchak, S.J., Brar, N.S.: Penetration of grout and concrete targets with ogive-nose steel projectiles. Int. J. Impact Eng. **18**(5), 465–476 (1996)
10. Zielinski, A.E., Silsby, G.F.: Hypervelocity Penetration Impacts in Concrete Targets. ARL-TR-2038. September 1999
11. Dawson, A., Bless, S., Levinson, S., Pedersen, B., Satapathy, S.: Hypervelocity penetration of concrete. Int. J. Impact Eng. **35**, 1484–1489 (2008)
12. Mu, Z., Zhang, W.: An investigation on mass loss of ogival projectiles penetrating concrete targets. Int. J. Impact Eng. **38**, 770–778 (2011)
13. Atou, T., Sano, Y., Katayama, M., Hayashi, S.: Damage evaluation of reinforced concrete columns by hypervelocity impact. Procedia Eng. **58**, 348–354 (2013)
14. Guo, L., He, Y., Zhang, X.F., Pang, C.X., Qiao, L., Guan, Z.W.: Study mass loss at microscopic scale for a projectile penetration into concrete. Int. J Impact Eng. **72**, 17–25 (2014)
15. He, L.L., Chen, X.W., Wang, Z.H.: Study on the penetration performance of concept projectile for high-speed penetration (CPHP). Int. J. Impact Eng. **94**, 1–12 (2016)
16. Kong, X., Wu, H., Fang, Q., Zhang, W., Xiao, Y.K.: Projectile penetration into mortar targets with a broad range of striking velocities: test and analyses. Int. J. Impact Eng. **106**, 18–29 (2017)
17. Sherburn, J.A., Rios-Estremera, D.H., Crosby, Z.K., Heard, W.F.: A Modeling Exploration of Ultraordnance Impacts on Concrete. 15th U.S. National Congress on Computational Mechanics, Austin, TX: July 28 – Aug 1, 2019
18. Holmquist, T.J., Johnson, G.R., Cook, W.H.: A Computational Constitutive Model for Concrete Subjected to Large Strains, High Strain Rates, and High Pressures. Proceedings of the 14th International Symposium on Ballistics, Quebec City, Canada, 26–29 September 1993

Chapter 7
Dynamic Damage Evolution in Shale in the Presence of Pre-Existing Microcracks

Ali Fahad Fahem and Raman P. Singh

Abstract Shales are the primary resource to produce unconventional oil and gas using hydraulic fracturing. Thus, understanding and evaluating the evolution of damage in shale materials under dynamic loading conditions will support the development and improve current extraction techniques. An experimental–analytical approach was developed in this work to observe microcrack growth under dynamic stress loading conditions. The developed method was used to measure the local damage across the in-plane of a circular disk (Brazilian disk) subjected to a compressive stress waves. Experimentally, circular disk specimens are prepared from Anadarko basin, Oklahoma, USA and tested with different bedding stacking orientations. The Split Hopkinson pressure bar (SHPB) was used to generate a compressive stress wave. The localized strain and damage initiation as a function of time are monitored using digital image correlation. The experimental data was used as input to the macro-damage (time-depend macro-damage) model. The experimental setup, specimen preparation was presented, as well as a critical local damage-initiation related to the orientation of the layers and cracking density were discussed.

Key words Microcrack · Macro-damage · Full-field data · Heterogeneous · SHPB · Brazilian disk

7.1 Introduction

Damage mechanics of materials is divided into two terms: (i) Physical damage and (ii) Mechanical damage. The growth of existing microcracks or micro-porosity inside the representative volume element (RVE) is referred to as physical damage in a micro-scale. However, the RVE is considered as a continuous material at a macro-scale level. Mechanical damage is related to the effect of physical damage (micro-damage) on the mechanical properties of materials (macro-behavior) like fracture toughness, modulus of elasticity. Usually, the physical-mechanical damage relation is non-linear in most cases [1–3].

Shale is classified as a porosity material since it is composite of fine-grained laminates by clay and compacted into rocks [4]. Thus, the understanding of dynamic damage mechanism of shale (cavities and porosity damage) is important because it is related to the Oil and Gas industry.

The damage area can grow in shale by growth of microcracks from the pre-cavities, holes, surface scratches, microcracks, or other defects in a microstructure scale [5].

In general, there are three different approaches used to solve the damage model: (i) Total strain approach, Costin [6]; (ii) Stress at damage initiation approach, Ashby, 1990 [7]; (iii) The local kinetic energy of motion approach [8–12]. From the public literature review, there is extensive information about the analysis of damage mechanics of shale as a numerical modeling and experimental testing. For example, Grady and Kipp developed the continuous model to simulate the dynamic fracture and fragmentation size of the rock that has pre-microcrack. Depending on the Weibull distribution formula, they show that the absorbed energy to develop new crack surface is one order of magnitude less than the total energy absorbed by specimen volume [13]. Lee et al. treated the rock as brittle-continuous material and developed dynamic damage model as a

---

A. F. Fahem (✉)
Department of Mechanical Engineering, Al-Qadisiyah University, Ad Dīwānīyah, Iraq

Department of Materials Science and Engineering, College of Engineering, Architecture, and Technology, Oklahoma State University-Tulsa, Tulsa, OK, USA
e-mail: afahem@okstate.edu; ali.fahem@qu.edu.iq

R. P. Singh
School of Mechanical and Aerospace Engineering, Oklahoma State University, Tulsa, OK, USA

Department of Materials Science and Engineering, College of Engineering, Architecture, and Technology, Oklahoma State University-Tulsa, Tulsa, OK, USA

S. Mates, V. Eliasson (eds.), *Dynamic Behavior of Materials, Volume 1*, Conference Proceedings of the Society for Experimental Mechanics Series, https://doi.org/10.1007/978-3-030-86562-7_7

function of elastic modulus, Poisson ratio, and fracture toughness of rock. They show that the accumulation of damage is reflected on the materials properties degradation, $D = f(E$, \nu, $K_{\mathrm{Ic}})$ [14].

Thus, the dynamic shale failure process usually occurs very quickly without permanent deformation that can be noted at macro-scale (brittle fracture). However, at the micro-scale level, the failure process develops with the permanent deformation (quasi-brittle behavior).

In this work, measuring the dynamic behavior of shale and dynamic physical damage at high strain rate experimentally and developing a framework related to the microscopic damage by using gradient in macroscopic mechanical properties.

7.2 Experimental Approach

7.2.1 Material and Specimen Preparation

The shale material that was used in this work was collected from the Anadarko Basin in Oklahoma, USA. The shale is provided as a cylindrical core with $D = 100$ mm in diameter and $H = 200$ mm in length. As shown in Fig. 7.1, the Brazilian dick specimens were machine with the final dimensions of $d = 16$ mm in diameter and the thickness is $t = 5$ mm.

7.2.2 Experimental Setup

A traditional Split Hopkinson Pressure Bar (SHPB) apparatus, [15] was used to subject the specimen to elastic compression stress waves. A full-field stress–strain hysteric behavior was obtained by using the 1D-elastic wave propagation theory and digital image correlating method.

In general, the apparatus consists of incident, transmitter, and striker bars. The bars are made of 25.4 mm diameter of high-strength aluminum 7075-T651. The bars are supported in a horizontal plane. The circle disk specimen (Brazilian disk) was sandwiched between the bars (Incident and Transmitted), Fig. 7.2. The assembly is used to load the specimen at the strain rate around 1500/s.

Full-field stress: Linear strain gauges were used to measure the strain waves of incident and transmitted bars (Quarter Wheatstone Bridge). In equilibrium conditions, and no inertia effect, the input and output loading waves are calculated as follows, Eq. (7.1):

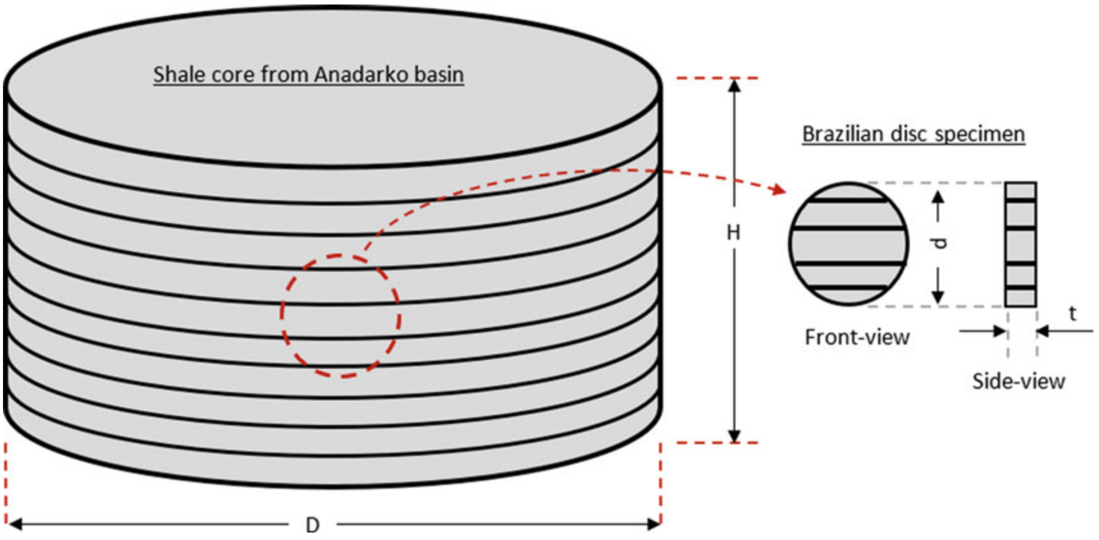

Fig. 7.1 Schematic of shale and specimen preparation

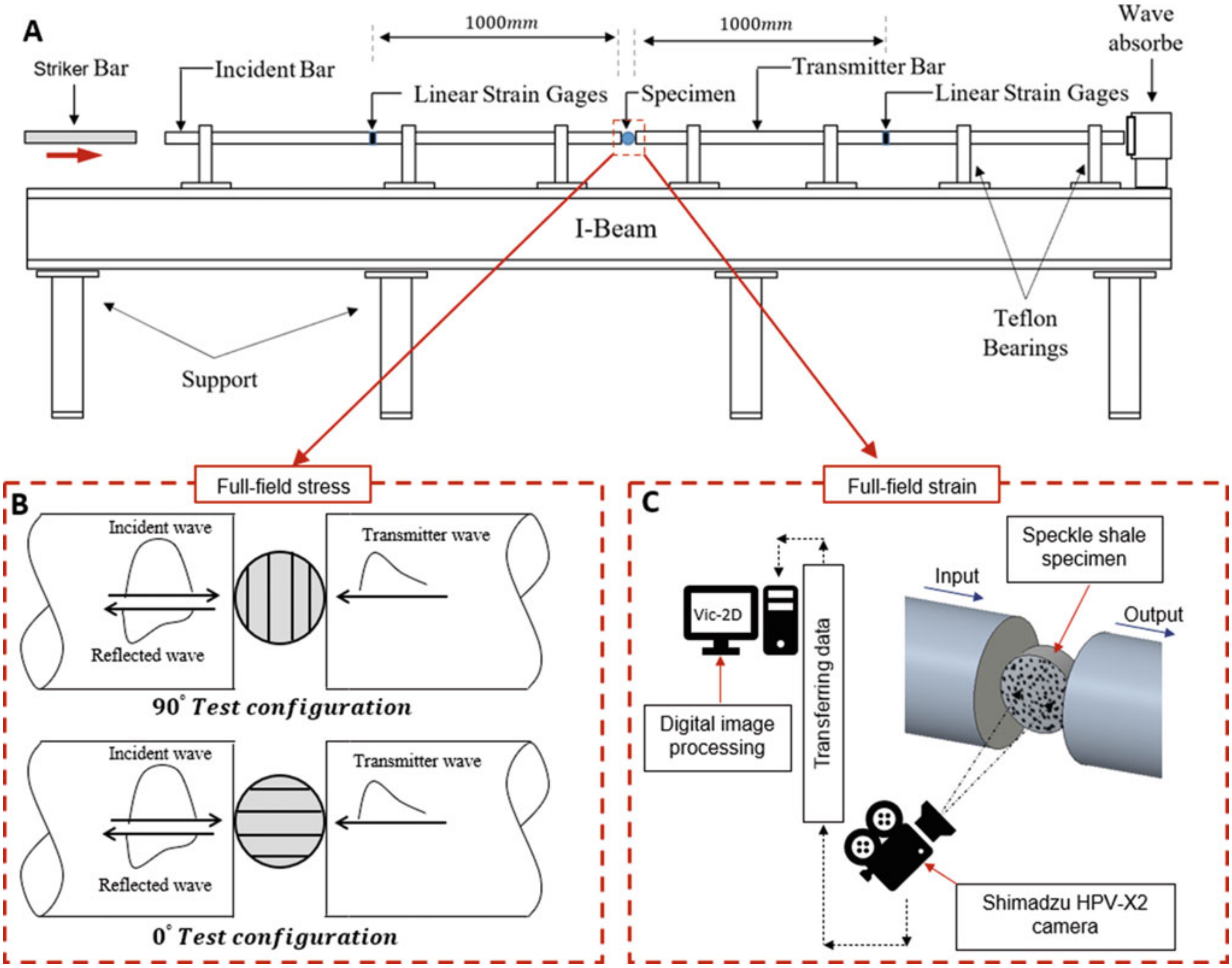

Fig. 7.2 Schematic of overall experimental setup. (**a**) Split Hopkinson pressure bar, SHPB; (**b**) Brazilian disc-loading configuration; (**c**) 2D-Digital image correlation method

$$P_1(t) = A_b E_b(\varepsilon_i(t) + \varepsilon_r(t))\text{and } P_2(t) = A_b E_b \varepsilon_t(t) \tag{7.1}$$

Thus, the average effective loading wave, P_{eff} on the specimen is,

$$P_{\mathrm{eff}}(t) = \frac{P_1(t) + P_2(t)}{2} \tag{7.2}$$

Where A_b is the cross-sectional area of the bar; E_b is the elastic modulus of the bar; $\varepsilon_i(t)$, $\varepsilon_r(t)$, and $\varepsilon_t(t)$ are the incident, reflected, and transmitted strain wave, respectively. The dimensions of the specimen and the effective loading wave, Eq. (7.1), are used as input to the Muskhelishvili formula to calculate the full-field stress, $\sigma_{ij} = f(P_{eff}, D, t, x, y)$ [16].

Full-field strain: Digital image correlation (DIC) method was used to measure the full-field deformation and strain, Fig. 7.2. The details of the specimen preparation, testing procedure, and cameras set up for DIC measurement can be found in [17–21].

7.3 Dynamic Damage Methodology, D(t)

The effect of pre-damage on the dynamic behavior of shale can be estimated by monitoring the macro-mechanical properties of shale (the elastic modulus, shear modulus, and Poisson's ratio) [22, 23]. Thus, the dynamic damage can be a part of the dynamic stress and dynamic strain data through the bi-modulus constitutive formula as follows:

$$e_{ij} = \frac{-\nu^o_{jk} D^\nu}{E^o_{kk} D^E}\sigma_{kk} + \frac{1+\nu^o_{ij} D^\nu}{E^o_{ij} D^E}\sigma_{ij} \tag{7.3}$$

Where the index notation, $i, j,$ and $k = x, y$.

Equation (7.3) is used with two different loading configurations to estimate the damage progress of the shale, see Fig. 7.2. The D^E and D^ν are the scalar damage related to the elastic modulus and Poisson ratio, respectively. E^o and ν^o are the dynamic initiation elastic mechanical properties of the virgin shale [17]. The ratio of ν^o/E^o, unaffected by damage growth, then only E_{ij} can be related to the damage growth, i.e., the D^ν can be neglected [6]. Thus, in a dynamic case and under equilibrium assumption, Eq. 7.3 can be rewritten for two dimensions, (x, y), as:

$$e_{xx}(t) = \frac{\sigma_{xx}(t)}{E^o_{xx} D^E_{xx}(t)} - \frac{\nu^o_{yx}}{E^o_{yy} D^E_{yy}(t)}\sigma_{yy}(t) \tag{7.4}$$

$$e_{yy}(t) = \frac{\sigma_{yy}(t)}{E^o_{yy} D^E_{yy}(t)} - \frac{\nu^o_{xy}}{E^o_{xx} D^E_{xx}(t)}\sigma_{xx}(t) \tag{7.5}$$

7.4 Results and Discussion

A typical load-deformation fitting curve of experimental data is shown in Fig. 7.3. This figure shows that the time from the initial loading up to full damage and fragmentation is too short and less than 25 μs. Furthermore, the specimen shows four stages of damage progress to failure (i) deform-undamaged, (ii) in-plane 1D-damage, (iii) increase density-damage, and finally (iv) in-plane branches damage and failure. In a short word, the load starts to propagate into the microstructure through the links between the porosity without any plastic deformation or damage. In stage two, the links are carried the maximum load and start damage and microcrack growth in the plane parallel to the crack face. In stage three, more nucleation shows up and

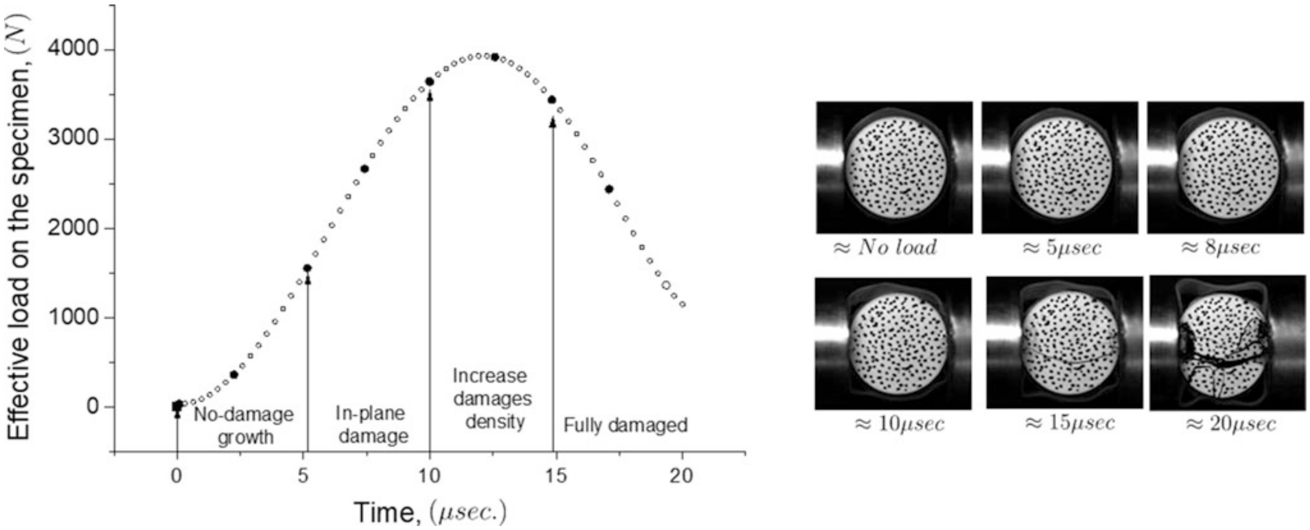

Fig. 7.3 A typical dynamic deformation field of Brazilian disc (Rother's shale). (i) Right: surface deformation during the loading wave; (ii) Left: fitting experimental data of effective load vs time up to 20 μs

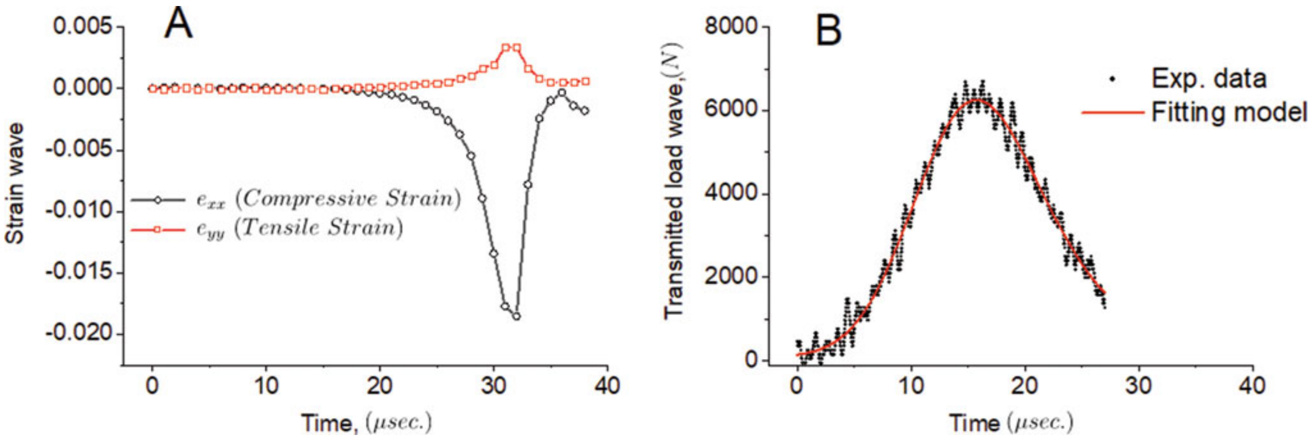

Fig. 7.4 A typical dynamic test of Rother's shale. (**a**) Compressive and tensile strain at the center point of the disc, (**b**) The effective load on the specimen

grow. In stage four, the microcrack grows faster and merges with a neighbor in a different plane (branches) up the failure. Stages two and four are essential to identify the initiation damage D^{o} and maximum damage $D^{\max}$ parameters.

The stress-strain during these stages are measured and used to fill-out and solve the constitutive equations. Thus, the incident, transmitted, and reflected waves are used as an input to calculate the effective load, Eq. 7.2, on the specimen, Fig. 7.4b. Then, the effective load and the specimen geometry are used as input to Muskhelishvili formula as mentioned above to estimate the stress distribution, $\sigma_{ij}(t)$ on the specimen surface. The full-field strain, $\varepsilon_{ij}(t)$ are measured by the 2D-DIC. Figure 7.4a shows the strain data at the center point of the specimen. The specimen is subjected to compressive strain 3X more than tensile strain. These data are utilized as a reference to identify the starting point of loading and merge the stress and strain waves.

Dynamic damage behavior of shale is obtained by solving Eq. (7.4) and Eq. (7.5). Figure 7.5 shows a complete picture to understand the damage, D and dynamic failure behavior of shale in two different material-loading configurations under compressive and tension stress wave.

1. Longitudinal material direction, Fig. 7.5a and c: The damage mechanisms in tension case are different than in compressive loading case. In the tension case, the microcrack starts breathing up to 13 μs, which is almost 50% of the maximum load, stage one and two of damage progress. Then, the crack initiates and propagates at the maximum damage $D^{\max} = 15.00$. The opening and closing of the microcrack activate local plastic deformation and that creates quasi-brittle damage, Fig. 7.5c. However, in the compressive loading condition, the damage is increasing rapidly where the crack is an initiation in less than 1.5 μs, and the maximum damage is $D^{\max} = 16.2$. In this direction, more fragmentation can be seen, brittle-damage, Fig. 7.5a.
2. Transverse material direction, Fig. 7.5b and d: Under tension stress wave, Fig. 7.5b, the micro-damage is an initiation; then, it is increasing fast up to maximum damage, $D^{\max} = 8.5$, then the crack grows slowly for 4 μs. Finally, the specimen failed and started to fragment. In a compressive loading case, Fig. 7.5d, there is no damage developed for the first 5 μs. The microcrack starts initiation and breathing up to 15 μs. After this point, the crack is propagated fast at the damage $D^{\max} = 49.7$, quasi-brittle damage.

Thus, in general, the dynamic damage behavior of shale can be listed as:

1. In the longitudinal-tension and transverse-compressive loading configuration, most of the loading wave is absorbed when the crack breathes. The damage is quasi-brittle damage and the shale fragments into large pieces, Fig. 7.5c and d. This observation is well matched with the Grady and Kipp result [13].
2. In the longitudinal-compressive and transverse-tension loading configuration, the damage is brittle and the shale fragments into smaller pieces, Fig. 7.5a and b.
3. The maximum dynamic damage in transverse-compressive setup is 3X higher than the damage in transverse-tension direction, see Fig. 7.5b and d, respectively.

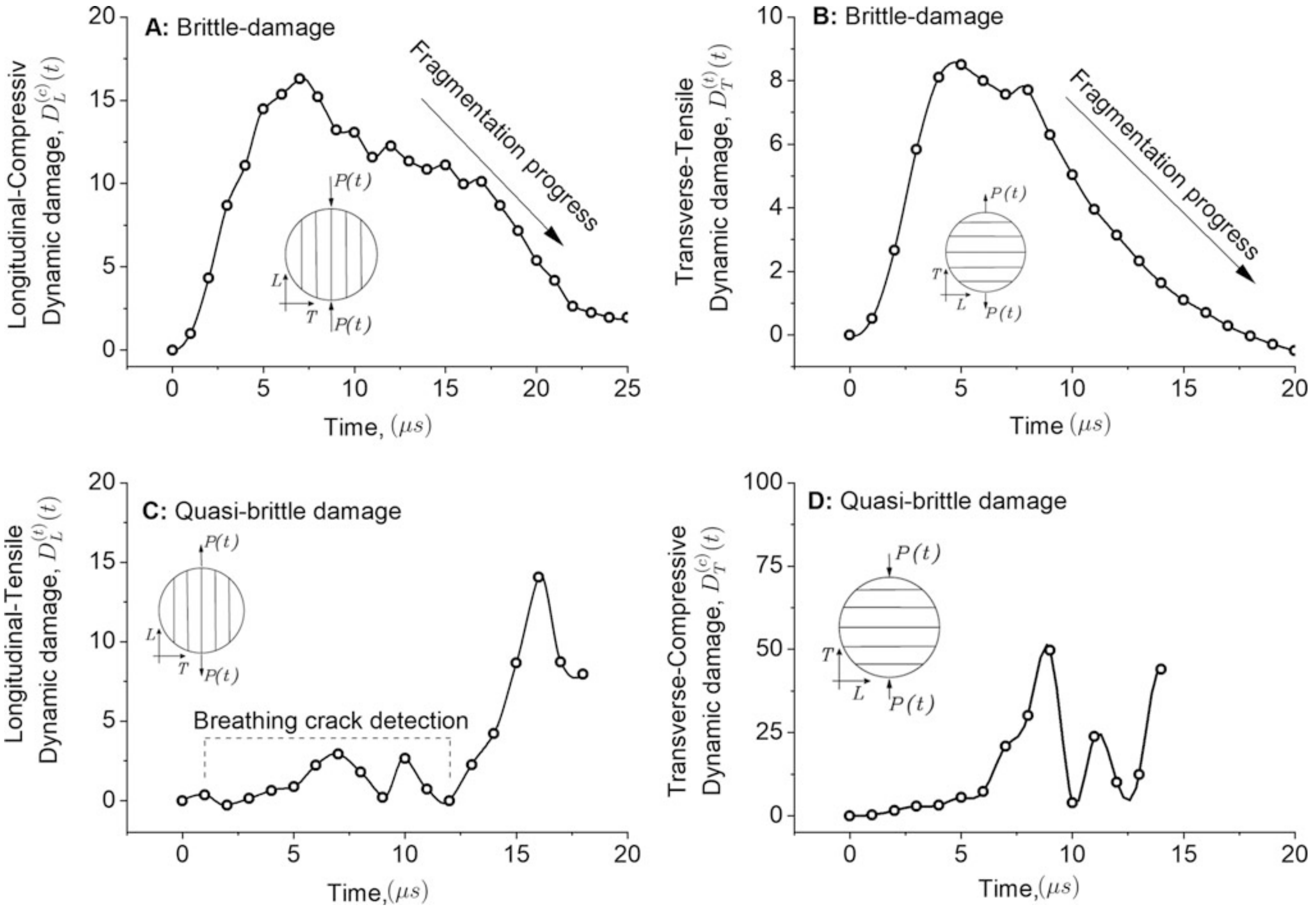

Fig. 7.5 A typical dynamic damage results of Rother's shale. (**a** and **b**) from zero-configuration setup, **c** and **d** from 90 configuration setup. (**a**) Damage in longitudinal under compressive stress, (**b**) Damage in transverse tensile stress, (**c**) Damage in longitudinal under tensile stress, (**d**) Damage in transverse under compressive stress

Table 7.1 The dynamic physical elastic properties and initial dynamic damage of Rother's shale that are measured experimentally

Property	Magnitude
Longitudinal tensile modulus, E_L^o (GPa)	04.02
Longitudinal compressive modulus, E_L^o (GPa)	69.16
Transverse tensile modulus, E_T^o (GPa)	20.36
Transverse compressive modulus, E_T^o (GPa)	08.60
Poisson's Ratio, ν_{LT}^o	00.34
Poisson's Ratio, ν_{LT}^o	00.23
Longitudinal-compressive max. dynamic damage	16.20
Longitudinal-tensile max. dynamic damage	15.00
Transverse-tensile max. dynamic damage	08.50
Transverse-compressive max. dynamic damage	49.70

Table 7.1 listed the physical elastic properties of shale specimen [17], and the dynamic damage initiation for different direction. This work is still in progress and more experimental work has to be done to fully understand the dynamic damage of shale with different orientations and loading rates.

7.5 Conclusion

This work presented a new experimental–analytical approach to understand and evaluate shale damage under dynamic loading conditions. Experimentally, the Split Hopkinson Pressure Bar (SHPB) is used to test circular disk specimens under a compressive stress wave. The samples were tested with different bedding orientations, parallel and perpendicular to the material bedding's direction. The full-field strain and surface damage progress are monitored by using 2D-DIC. The experimental data, far-field load, and local strain field were used as input to the bi-modulus constitutive macro-damage formula. The results show that the dynamic damage and fragmentation are functions of bedding direction and loading conditions (tension or compressive). As seen so far, more fragments can be achieved by passing the tension wave perpendicular to the bedding or apply a compressive loading wave parallel to the bedding layers.

Acknowledgments This material is based upon work supported by the Department of Energy under Award Number DE-FE0031777. This report was prepared as an account of work sponsored by an agency of the US Government. Neither the US Government nor any agency thereof, nor any of their employees, makes any warranty, express or implied, or assumes any legal liability or responsibility for the accuracy, completeness, or usefulness of any information, apparatus, product, or process disclosed, or represents that its use would not infringe privately owned rights. Reference herein to any specific commercial product, process, or service by trade name, trademark, manufacturer, or otherwise does not necessarily constitute or imply its endorsement, recommendation, or favoring by the US Government or any agency thereof. The views and opinions of authors expressed herein do not necessarily state or reflect those of the US Government or any agency thereof.

References

1. Liu, L., Katsabanis, P.D.: Development of a continuum damage model for blasting analysis. Int. J. Rock Mechan. Mining Sci. Geomechan. Abstr. **34**(2), 217–231 (1997)
2. Zhang, Y.Q., Hao, H., Lu, Y.: Anisotropic dynamic damage and fragmentation of rock materials under explosive loading. Int. J. Eng. Sci. **41**(9), 917–929 (2003)
3. W. Zhang and Y. Cai. Continuum Damage Mechanics and Numerical Applications. Springer-Verlag Berlin Heidelberg, China (2010)
4. Okeke, O.C., Okogbue, C.O.: Shales: a review of their classifications, properties and importance to the petroleum industry. Glob. J. Geol. Sci. **9** (1), 75–83 (2011)
5. Ma, S., Gutierrez, M., Hou, Z.: Coupled plasticity and damage constitutive model considering residual shear strength for shales. Int. J. Geomech. **20**(8), 1–8 (2020)
6. Costin, L.S.: A microcrack model for the deformation and failure of brittle rock. J. Geophys. Res. **88**(B11), 9485–9492 (1983)
7. Ashby, C., Sammis, M.F.: The damage mechanics of brittle solids in compression. Pure Appl. Geophys. **133**(3), 489–521 (1990)
8. Baˇzant, Z.P., Caner, F.C.: Impact comminution of solids due to local kinetic energy of high shears train rate: I. Continuum theory and turbulence analogy. J. Mech. Phys. Solids. **64**(1), 223–235 (2014)
9. Baˇzant, Z.P., Caner, F.C.: Comminution of solids caused by kinetic energy of high shear strain rate, with implications for impact, shock, and shale fracturing. Proc. Natl. Acad. Sci. U. S. A. **110**(48), 19291–19294 (2013)
10. Caner, F.C., Baˇzant, Z.P.: Impact comminution of solids due to local kinetic energy of high shears train rate: II-Micro plane model and verification. J. Mech. Phys. Solids. **64**(1), 236–248 (2014)
11. Chen, W., Maurel, O., Reess, T., De Ferron, A.S., La Borderie, C., Pijaudier-Cabot, G., Rey-Bethbeder, F., Jacques, A.: Experimental study on an alternative oil stimulation technique for tight gas reservoirs based on dynamic shock waves generated by pulsed arc electrohydraulic discharges. J. Pet. Sci. Eng. **88-89**, 67–74 (2012)
12. Murakami, S.: Damage mechanics. **185** (2012)
13. Grady, D.E., Kipp, M.E.: Continuum modelling of explosive fracture in oil shale. Int. J. Rock Mech. Mining Sci. **17**(3), 147–157 (1980)
14. Taylor, L.M., Chen, E.P., Kuszmaul, J.S.: Microcrack-induced damage accumulation in brittle rock under dynamic loading. Comput. Methods Appl. Mech. Eng. **55**(3), 301–320 (1986)
15. Chen, W., Bo, S.: Split Hopkinson (Kolsky) Bar Design, Testing and Application, Springer, New York (2011)
16. Muskhelishvili, N.I.: Some Basic Problems of the Mathematical Theory of Elasticity, 4th edn. Springer, Dordrecht (1977)
17. Fahem, A., Tg, A., Singh, R. P.: A novel method to evaluate elastic properties of heterogeneous, orthotropic and bi-modulus materials with applications to shale. in preparation, pp. 1–32, 2020
18. A. F. Fahem, A. Kidane, and M. A. Sutton. A novel method to determine the mixed mode (i/iii) dynamic fracture initiation toughness of materials. Int. Fract. Mech., 2020. https://doi.org/10.1007/s10704-020-00445-3
19. Fahem, A., Kidane, A.: A general approach to evaluate the dynamic fracture toughness of materials. Dynamic behavior of materials. Conf. Proc. Soc. Exp. Appl. Mech. **1**, 185–194 (2017). https://doi.org/10.1007/978-3-319-41132-3_26
20. Fahem, A., Kidane, A., Sutton, M.A.: Mode-I dynamic fracture initiation toughness using torsion load. Eng. Fract. Mech. **213**(3), 53–71 (2019). https://doi.org/10.1016/j.engfracmech.2019.03.039
21. Sutton, M.A., Orteu, J.J., Schreier, H.W.: Image correlation for shape, motion and deformation measurements- basic concepts, theory and applications, p. 341. Image, Rochester, NY (2009)
22. G. Z. Voyiadjis. Handbook of Damage Mechanics. Springer, New York (2020)
23. Nemat-Nasser, S.: Plasticity – a Treatise on Finite Deformation of Heterogeneous Inelastic Materials. Cambridge Cambridge University Press, Cambridge (2004)

Chapter 8
Probing Inertial Cavitation Damage in Viscoelastic Hydrogels Using Dynamic Bubble Pairs

Jin Yang, Harry C. Cramer III, Selda Buyukozturk, and Christian Franck

Abstract Inertial cavitation is a common phenomenon in nature, which is also similarly present in many engineering and medical applications including laser eye surgery and lithotripsy procedures. In a recent study, we showed experimentally that violently collapsing bubbles, i.e., material Mach numbers that exceed a critical value of 0.1 with respect to the longitudinal material wave speed, can significantly damage the surrounding hydrogel material. Here, we quantitatively characterize the change in mechanical properties of the surrounding material following a violent bubble collapse. To accomplish this, we introduce a second bubble in the vicinity of the violently collapsed bubble to re-initiate its growth and cavitation cycle through propagating pressure fields. By studying the secondary Bjerknes interaction force between these two bubbles, we find that the viscosity of the damaged material is reduced to the viscosity of the solvent (water) whose value is one order smaller than the undamaged polyacrylamide hydrogel, with the pre-determined bulk shear modulus of the initial bubble being essentially unaltered. In addition, we also estimate the magnitude of the re-initiating pressure wave that drives the regrowth of the first bubble. We anticipate that this work also paves the way for a fundamental understanding of bubble pair and bubble cloud interactions in compliant hydrogels and soft polymers.

Key words Inertial cavitation · high strain-rate · viscoelasticity · material damage · bubble pair interaction

8.1 Introduction

Cavitation is a common phenomenon in many biological systems and medical applications [1, 2]. Laser or ultrasound-induced inertial cavitation can be useful in many surgical and medical procedures, such as cataract laser surgery, lithotripsy, and histotripsy applications [3]. Yet, well-controlled laser or ultrasound-induced cavitation can provide an effective method for characterizing soft material viscoelastic properties at extremely high strain-rates on the order of $O(10^3) - O(10^8)$ s^{-1} [4–7]. However, cavitation can also cause serious damage to surrounding soft material and bio-tissues [8–10]. Recently, by analyzing laser induced violently cavitation bubbles, we have experimentally demonstrated that the surrounding soft material can accumulate significant inelastic damage when the material Mach number exceeds a critical value of 0.1 [11]. This cavitation-induced material damage can further cause bubble wall surface instabilities [12–14], as well as material fracture and/or fatigue accumulation [15].

Here, we have developed a new experimental method for characterizing the mechanical properties of the locally damaged surrounding material. To achieve this, we introduce a second bubble in the vicinity of the first bubble to re-initiate its growth and cavitation cycle. Using high speed video recording of the double-bubble dynamics, we conducted a combined

---

J. Yang (✉) · C. Franck
Department of Mechanical Engineering, University of Wisconsin, Madison, WI, USA
e-mail: jyang526@wisc.edu

H. C. Cramer III
Center for Biomedical Engineering, Brown University, Providence, RI, USA

Department of Mechanical Engineering, University of Wisconsin, Madison, WI, USA

School of Engineering, Brown University, Providence, RI, USA

S. Buyukozturk
Department of Mechanical Engineering, University of Wisconsin, Madison, WI, USA

School of Engineering, Brown University, Providence, RI, USA

S. Mates, V. Eliasson (eds.), *Dynamic Behavior of Materials, Volume 1*, Conference Proceedings of the Society for Experimental Mechanics Series, https://doi.org/10.1007/978-3-030-86562-7_8

experimental and theoretical investigation of the secondary Bjerknes interaction [16, 17], where the sustained material cavitation damage can be measured quantitatively.

8.2 Material Preparation

In our experiments, stiff polyacrylamide (PA) hydrogel samples were prepared from 40.0% acrylamide solution and 2.0% bis solution (Bio-Rad, Hercules, CA) mixed to a final concentration of 8.0% / 0.08% Acrylamide/Bis (v/v) in deionized water and crosslinked with 0.5% APS (ThermoFisher Scientific, USA) and 1.25% TEMED (ThermoFisher Scientific, USA). Once mixed, PA samples were completely submersed in deionized water for 24 h to allow for complete swelling. The quasistatic shear modulus, G_∞, of the prepared stiff PA is 2.77 kPa. Stiff PA has also been found to show strain stiffening effects during our previous inertial cavitation experiments and is quantitatively characterized by a quadratic law Kelvin-Voigt (qKV) viscoelastic material model with a strain stiffening parameter $\alpha = 0.48 \pm 0.014$, and viscosity $\mu = 0.186 \pm 0.194$ Pa·s [11].

8.3 Experimental Setup

The experimental setup in this study is adapted from our previous studies [11, 12], as shown in Fig. 8.1a, where the first single cavitation bubble was generated through a single pulse from an adjustable 1–25 mJ Q-switched Nd:YAG Minilite II (Continuum, Milpitas, CA) laser platform frequency doubled to 532 nm (cf. Fig. 8.1b-i). After a 20s interval, we introduced a second bubble in the vicinity of the first remaining bubble to re-initiate its growth and cavitation cycle, as shown in Fig. 8.1b-ii. After another 20s, we photographed both bubbles' stress-free equilibrium states, as shown in Fig. 8.1b-iii. In each laser-induced cavitation event, a single laser pulse was expanded to fill the back aperture of a Nikon Plan Fluor 20X/0.5 NA imaging objective and was aligned through the back port of a Nikon Ti:Eclipse microscope (Nikon Instruments, Long Island, NY). Pulses were reflected off a 532 nm notch dichroic mirror (Semrock, Rochester, NY) to the rear aperture of the imaging objective. Cavitation bubbles were recorded at one million fps with a Hyper Vision HPV-X2 high speed camera (Shimadzu), with triggered full-field illumination from an SILUX640 laser illumination system (Specialized Imaging, Pitstone, United Kingdom). Samples were imaged in 25 mm Chamlide magnetic chambers (Live Cell Instrument, Seoul, South Korea) in all tests. Output TTL signals from the camera aligned image acquisition with the laser pulse and illumination pulses. An exposure time of 500 ns and an illumination pulse width of 250 ns were used to maximize illumination and minimize image ghosting in all samples at 400 × 250 pixels at FP mode (128 acquisition frames). Cavitation events were generated 600 μm above the bottom surface to ensure boundary effects remained negligible.

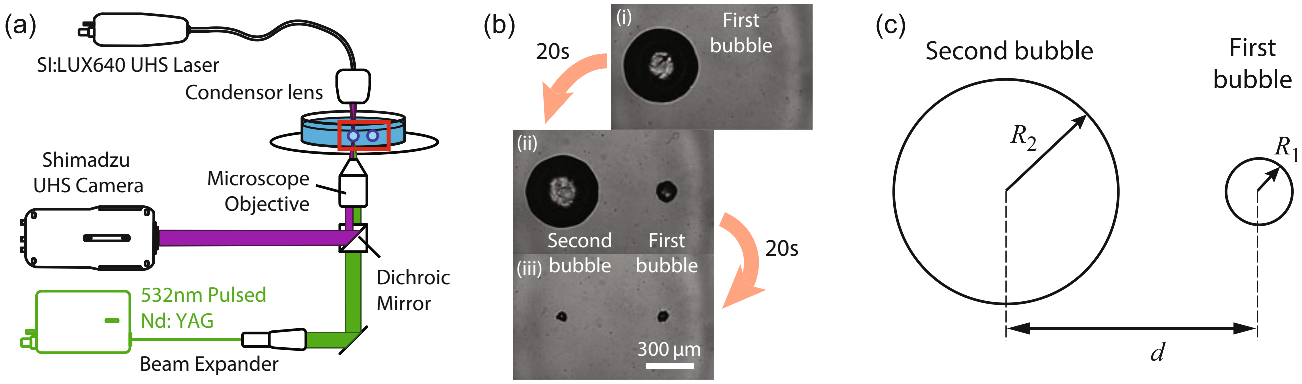

Fig. 8.1 (**a**) Experimental setup of the laser-induced inertial micro-cavitation (modified based on Yang, et al. [11]). (**b**) After the first cavitation bubble was generated, the laser focus was shifted by a distance *d*, and a second bubble was cavitated after 20s. After another 20s, both bubbles were recorded again to measure their stress-free equilibrium states. (**c**) Schematic diagram of the double bubble experiment

8.4 Results and Discussions

Using ultra-high-speed videography, we captured the dynamic process of the two bubbles interacting with each other. Each individual frame was analyzed to fit the bubble radius using a custom-written MATLAB script. All the measured experimental parameters are summarized in Table 8.1 where we denote two bubbles' time-dependent radii as $R_1(t)$ and $R_2(t)$, respectively. The final equilibrium radii of the two bubbles, $R_{1\infty}$ and $R_{2\infty}$, were both around 30–40 μm where we assumed that they reached their stress-free states. The maximum radius of the second bubble $R_{2\max}$ was about 320–370 μm, and a maximum radial stretch ratio was about 8–10. In our experiments, we tested three different distances between two bubbles, where d ranging from 450 μm to 840 μm. Bubble radii and the distance between the two bubbles were normalized by $R_{2\max}$ such that $R^*_i = R_i/R_{2\max}(\mathrm{i} = 1, 2)$, $d^* = d/R_{2\max}$. We also defined the normalized time $t^* = t\,(p_\infty/\rho)^{1/2}\,/R_{2\max}$, where p_∞ is the atmospheric pressure, and ρ is the medium density. All the normalized bubble radii vs. normalized time curves are plotted in Fig. 8.2., where the non-dimensional distance d* equals (a)1.29 ± 0.06, (b)1.85 ± 0.28, and (c)2.50 ± 0.29, respectively

Next, we introduce a theoretical model of the secondary Bjerknes interaction force between these two bubbles [16, 17]. In the vicinity of an oscillating bubble, we assume that the surrounding material is incompressible, and the velocity field is:

$$v = \frac{R^2\dot{R}}{r^2}. \tag{8.1}$$

The equation of motion satisfies the Euler equation:

$$\rho\frac{\partial v}{\partial t} + \frac{\partial p}{\partial r} = 0, \tag{8.2}$$

where we have omitted the nonlinear convective term $v\,(\partial v/\partial r) \sim O(r^{-5})$ since $O(d^{-5})$ is a small value in our experiments. The Bjerknes pressure of the second bubble acting on the first bubble at distance d is:

$$\delta p_{21} = \frac{\rho}{d}\frac{d}{dt}\left(R_2^2\dot{R}_2\right) \tag{8.3}$$

Similarly, the Bjerknes pressure of the first bubble acting on the second bubble at distance d is:

$$\delta p_{12} = \frac{\rho}{d}\frac{d}{dt}\left(R_1^2\dot{R}_1\right) \tag{8.4}$$

Table 8.1 Summary of bubble radii and the distance between two bubbles

Distance	$d1$	$d2$	$d3$
$R_{2\max}$ (μm)	348.2 ± 15.7	345.9 ± 19.3	334.8 ± 13.2
$R_{2\infty}$ (μm)	34.0 ± 2.0	35.8 ± 4.3	35.2 ± 2.4
$R_{1\infty}$ (μm)	38.5 ± 2.8	37.3 ± 3.0	36.5 ± 3.5
d (μm)	447.2 ± 2.3	639.0 ± 3.6	836.8 ± 8.8
d^*	1.29 ± 0.06	1.85 ± 0.28	2.50 ± 0.29

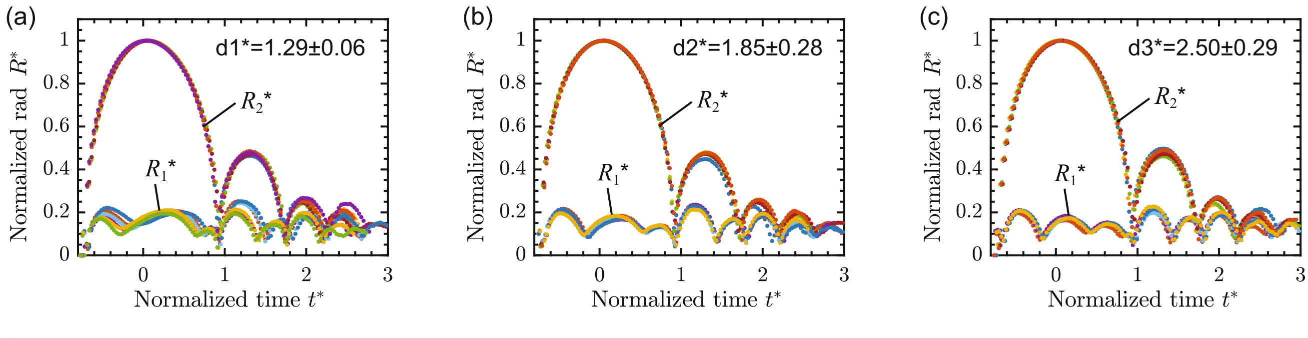

Fig. 8.2 Normalized bubble radii vs. normalized time curves in our experiments with three different bubble distances, where the non-dimensional distance d* equals (**a**)1.29 ± 0.06, (**b**)1.85 ± 0.28, and (**c**)2.50 ± 0.29, respectively

Following [16, 17], assuming that the two bubbles both remain spherical, the dynamics of their effective radii can be described by the following coupled Keller-Miksis equations:

$$\begin{cases} \left(1-\frac{\dot{R}_1}{c}\right)R_1\ddot{R}_1+\frac{3}{2}\left(1-\frac{\dot{R}_1}{3c}\right)\dot{R}_1^2=\frac{1}{\rho}\left(1+\frac{\dot{R}_1}{c}+\frac{R_1}{c}\frac{d}{dt}\right)\left(p_{b1}-p_\infty+S_1-\frac{2\gamma}{R_1}\right)-\frac{1}{d}\left(R_2^2\ddot{R}_2+2R_2\dot{R}_2^2\right) \\ \left(1-\frac{\dot{R}_2}{c}\right)R_2\ddot{R}_2+\frac{3}{2}\left(1-\frac{\dot{R}_2}{3c}\right)\dot{R}_2^2=\frac{1}{\rho}\left(1+\frac{\dot{R}_2}{c}+\frac{R_2}{c}\frac{d}{dt}\right)\left(p_{b2}-p_\infty+S_2-\frac{2\gamma}{R_2}\right)-\frac{1}{d}\left(R_1^2\ddot{R}_1+2R_1\dot{R}_1^2\right) \end{cases} \tag{8.5}$$

where overdots denote derivatives with respect to time; ρ is the mass density of the surrounding material; c is the longitudinal wave speed in the surrounding material and is assumed to be constant in our tests [11]; γ is the surface tension between gaseous bubble contents and the surrounding material; S_1 and S_2 are stress integrals of the deviatoric Cauchy stress as shown in (8.6):

$$\begin{cases} S_1=\frac{(3\alpha_1-1)G_{1\infty}}{2}\left[5-\left(\frac{R_{1\infty}}{R_1}\right)^4-\frac{4R_{1\infty}}{R_1}\right]-\frac{4\mu_1\dot{R}_1}{R_1}+2\alpha_1G_{1\infty}\left[\frac{27}{40}+\frac{1}{8}\left(\frac{R_{1\infty}}{R_1}\right)^8+\frac{1}{5}\left(\frac{R_{1\infty}}{R_1}\right)^5+\left(\frac{R_{1\infty}}{R_1}\right)^2-\frac{2R_1}{R_{1\infty}}\right] \\ S_2=\frac{(3\alpha_2-1)G_{2\infty}}{2}\left[5-\left(\frac{R_{2\infty}}{R_2}\right)^4-\frac{4R_{2\infty}}{R_2}\right]-\frac{4\mu_2\dot{R}_2}{R_2}+2\alpha_2G_{2\infty}\left[\frac{27}{40}+\frac{1}{8}\left(\frac{R_{2\infty}}{R_2}\right)^8+\frac{1}{5}\left(\frac{R_{2\infty}}{R_2}\right)^5+\left(\frac{R_{2\infty}}{R_2}\right)^2-\frac{2R_2}{R_{2\infty}}\right] \end{cases} \tag{8.6}$$

where the surrounding material of the second bubble is modelled as an undamaged, isotropic material whose material properties were characterized in our previous studies (quasistatic shear modulus $G_{2\infty}=2.77$ kPa, strain stiffening parameter $\alpha_2=0.48\pm0.14$, and viscosity $\mu_2=0.186\pm0.194$ Pa·s) [11]. We also model the damaged material near the first bubble as an isotropic material with the unknown shear modulus $G_{1\infty}$ and viscosity μ_1. The strain stiffening parameter was assumed to be unchanged such that $\alpha_1\approx\alpha_2$.

The internal pressure in the first and second bubbles are denoted as p_{b1} and p_{b2}, respectively; p_∞ is the far-field pressure assumed to be atmospheric. For the simplest case of an isothermal bubble filled with a mixture of water vapor and non-condensable gas, which was assumed to be homobaric and follow the ideal gas law, we have:

$$\begin{cases} p_{b1}=\left(p_\infty+\frac{2\gamma}{R_{1\infty}}\right)\left(\frac{R_{1\infty}}{R_1}\right)^3 \\ p_{b2}=\left(p_\infty+\frac{2\gamma}{R_{2\infty}}\right)\left(\frac{R_{2\infty}}{R_2}\right)^3 \end{cases} \tag{8.7}$$

Boundary conditions. Following Estrada et al. [4], we assume that the heat and mass transfer inside two bubbles follow Fourier's law and Fick's law, respectively. At the bubble wall, we assume that the surrounding material remains isothermal with a constant room temperature. Across the bubble wall, there was mass transfer of the water vapor, but we approximate that there was no mass transfer of the condensable gas.

Initial conditions. We set the second bubble nucleation as the starting time point, and the initial conditions of the first bubble were $R_{10}=R_{1\infty}$, $\dot{R}_{10}=0$. We applied the experimentally measured $R_2(t)$ as a known variable, so there was no initial condition needed for R_2. During the nucleation of the second bubble, the expansion pressure wave was released, thus changing the internal pressure in the first bubble by an effective pressure drop Δp_b.

Fitting process. Following [4], a fifth-order explicit Dormand-Prince Runge-Kutta method with adaptive step-size control is used to evolve the governing Eqs. (8.5), (8.6), and (8.7) forward in time where $\{G_{1\infty}, \mu_1, \Delta p_\mathrm{b}\}$ are unknown variables. The least squares (LSQ) error is defined as the L_2 norm of the difference between experimental R_1 data points and the numerical simulations in the second bubble's first expansion-collapse cycle. A global optimization technique, "pattern search" [18], was applied to look for a global minimum of LSQ error and the optimization relative tolerance was set to be 10^{-2}. Three representative best fit R_1 vs. time curves of each distance case are overlaid with the experimentally measured results in Fig. 8.3. (a-c), where the non-dimensional distance d* equals 1.29 ± 0.06, 1.85 ± 0.28, and 2.50 ± 0.29, respectively. All the fitted variables and LSQ errors are further summarized in Fig. 8.4.

From Figs. 8.3a, b and 8.4a, we find that the best-fit LSQ error has a smaller value for a larger distance d, and the variance for other fitted variables is also smaller. This is because, as d increases, the nonlinear convective term $v\,(\partial v/\partial r)-O(d^{-5})$ has a smaller value, and both the first and second bubble will maintain their spherical shape when d is large. Therefore, our theoretical model of the double-bubble interaction has higher accuracy. We also find that the viscosity of the damaged

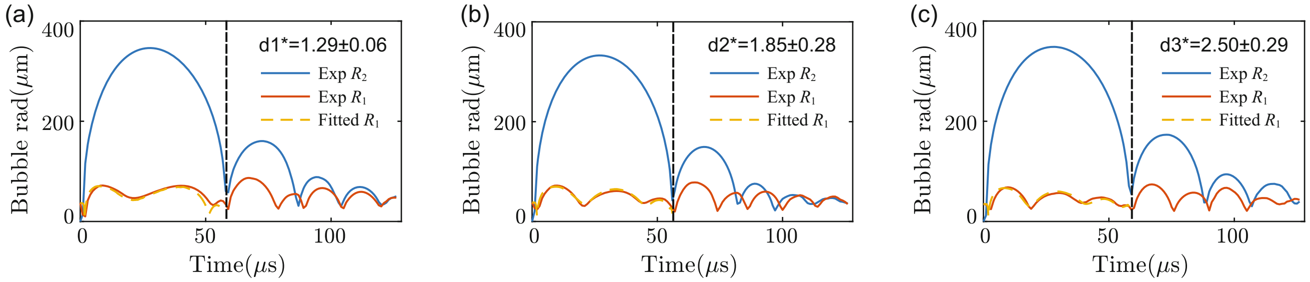

Fig. 8.3 Three representative best fit R_1 vs. time curves are overlaid with experimental measurements, where the non-dimensional distance d* = (**a**) 1.29 ± 0.06, (**b**)1.85 ± 0.28, and (**c**)2.50 ± 0.29, respectively (The vertical dashed lines indicate the duration of the second bubble's first expansion-collapse cycle)

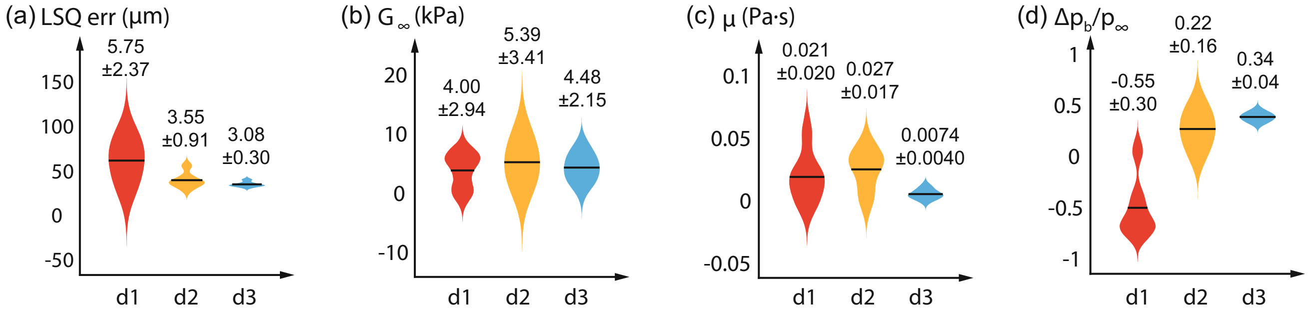

Fig. 8.4 Statistics of the best fit (**a**) LSQ err, (**b**, **c**) shear modulus and viscosity of the damaged material, and (**d**) magnitude of the re-initiating pressure wave during the second bubble's nucleation that drives the regrowth of the first bubble

surrounding material is reduced to the viscosity of the solvent (water), whose value ($\mu_1 = 0.0074 \pm 0.0040$ Pa·s) is one order smaller than the undamaged polyacrylamide hydrogel ($\mu_2 = 0.186 \pm 0.194$ Pa·s). The pre-determined bulk shear modulus was essentially unaltered ($G_{1\infty} = 4.48 \pm 2.15$ kPa, $G_{2\infty} = 2.77$ kPa). The viscosity is reduced since the gel's microstructure has been significantly damaged locally at the bubble wall where the material strains are the highest [15]. However, the apparent bulk shear modulus of the gel, $G_{1\infty}$ remains intact since any change in the apparent shear modulus close to the wall would be negligible when averaged across the bulk of the sample when computed from the stress integrals S_1 and S_2 in (8.6). Our conclusion that material damage leads to viscosity reduction is consistent with previous assumptions in [7, 15], and as far as we know, this is the first time that quantitative experimental evidence has been provided to substantiate this assertion.

In addition, we also estimate the magnitude of the pressure wave released from the second bubble's nucleation that drove the regrowth of the first bubble, as shown in Fig. 8.4d. The value of this pressure wave is negative when the distance is close, but the result is positive in the far-field. This may be because the surrounding gel is a global system, and the near-field negative pressure induces positive pressure in the far-field. However, a full understanding of this phenomenon still remains an open question.

8.5 Conclusions

In this chapter, we have developed a novel experimental approach for characterizing the change in mechanical properties of the surrounding material following a violent bubble collapse, where we introduce a second bubble in the vicinity of the first, violently collapsed bubble by re-initiating its growth and cavitation cycle through propagating pressure fields. From studying this double-bubble interaction, we find that the viscosity of the damaged material is reduced to the viscosity of the solvent while its bulk shear modulus is essentially unchanged. In addition, we estimate the magnitude of the pressure wave during laser-induced cavitation nucleation in viscoelastic hydrogels. We expect that this work will pave the way for a fundamental understanding of bubble pair and bubble cloud interactions in compliant hydrogels and soft tissues. Our findings may also have implications from laser eye treatment to lithotripsy for better quantitative guiding and minimizing tissue damage in these medical technologies.

Acknowledgments We gratefully acknowledge funding support from the Office of Naval Research (Dr. Timothy Bentley) under grants N00014-17-1-2058, N00014-18-1-2625 and N00014-20-1-2408.

References

1. Brennen, C.E.: Cavitation and Bubble Dynamics. Cambridge University Press, New York (2014)
2. Wan, M., Feng, Y., ter Haar, G.: Cavitation in biomedicine. Springer, Dordrecht (2015)
3. Bailey, M.R., Khokhlova, V.A., Sapozhnikov, O.A., Kargl, S.G., Crum, L.A.: Physical mechanisms of the therapeutic effect of ultrasound (a review). Acoust. Phys. **49**, 369–388 (2003)
4. Estrada, J.B., Barajas, C., Henann, D.L., Johnsen, E., Franck, C.: High strain-rate soft material characterization via inertial cavitation. J. Mech. Phys. Solids. **112**, 291–317 (2018)
5. Yang, J., Franck, C.: Strain stiffening effects of soft viscoelastic materials in inertial microcavitation. Dynamic Behavior of Materials in Conference Proceedings of the Society for Experimental Mechanics, Vol. 1, 2020
6. Mancia, L., Yang, J., Spratt, J.S., Sukovich, J.R., Xu, Z., Colonius, T., Franck, C., Johnsen, E.: Acoustic cavitation rheometry. Soft Matter. **17** (10), 2931–2941 (2021)
7. Spratt, J.S., Rogriguez, M., Schmidmayer, K., Bryngelson, S.H., Yang, J., Franck, C., Colonius, T.: Characterizing viscoelastic materials via ensemble-based data assimilation of bubble collapse observations. J. Mech. Phys. Solids. **152**, 104455 (2021)
8. Maxwell, A.D., Wang, T.-Y., Yuan, L., Duryea, A.P., Xu, Z., Cain, C.A.: A tissue phantom for visualization and measurement of ultrasound-induced cavitation damage. Ultrasound Med. Biol. **36**, 2132–2143 (2010)
9. Mancia, L., Vlaisavljevich, E., Yousefi, N., Rodriguez, M., Ziemlewicz, T.J., Lee Jr., F.T., Henann, D., Franck, C., Xu, Z., Johnsen, E.: Modeling tissue selective cavitation damage. Phys. Med. Biol. (2019)
10. Estrada, J.B., Cramer, H.C., Scimone, M.T., Buyukozturk S., Franck, C.: Neural cell injury pathology due to high-rate mechanical loading. Brain Multiphysics. **2**, 100034 (2021)
11. Yang, J., Cramer III, H.C., Franck, C.: Extracting non-linear viscoelastic material properties from violently-collapsing cavitation bubbles. Extreme Mechan. Lett. **39**, 100839 (2020)
12. Yang, J., Cramer III, H. C., Franck, C.. Dynamic rugae strain localizations and instabilities in soft viscoelastic materials during inertial microcavitation. Dynamic Behavior of Materials in Conference Proceedings of the Society for Experimental Mechanics, Vol. 1, 2021
13. Yang, J., Tzoumaka, A., Murakami, K., Johnsen, E., Henann, D., Franck, C.: Predicting complex nonspherical instability shapes of inertial cavitation bubbles in viscoelastic soft matter. Phys. Rev. E. In press (2021)
14. Yang, J., Yin, Y., Cramer, III H.C., Franck, C.; The penetration dynamics of a violent cavitation bubble through a hydrogel-water interface. Dynamic Behavior of Materials in Conference Proceedings of the Society for Experimental Mechanics, Vol. 1, 2022
15. Movahed, P., Kreider, W., Maxwell, A.D., Hutchens, S.B., Freund, J.B.: Cavitation-induced damage of soft materials by focused ultrasound bursts: a fracture-based bubble dynamics model. J. Acoust. Soc. Am. **140**(2), 1374–1386 (2016)
16. Mettin, R., Akhatov, I., Parlitz, U., Ohl, C.D., Lauterborn, W.: Bjerknes forces between small cavitation bubbles in a strong acoustic field. Phys. Rev. E. **56**, 2924 (1997)
17. Pelekasis, N.A., Gaki, A., Doinikov, A., Tsamopoulos, J.A.: Secondary Bjerknes forces between two bubbles and the phenomenon of acoustic streamers. J. Fluid Mech. **500**, 313–347 (2004)
18. Audet, C., Dennis Jr., J.E.: Analysis of generalized pattern searches. SIAM J. Optim. **13**, 889–903 (2003)

Chapter 9
A Simple Data-Rich IBII Test for Identifying All Orthotropic Stiffness Components at High Strain Rates

Lloyd Fletcher and Fabrice Pierron

Abstract This work focuses on the development of a new simple IBII test configuration that is designed to maximize identifiability of all four orthotropic stiffness components for bone and glass fiber-reinforced polymer (GFRP) composites. A limitation of current ultra-high speed camera technology is the spatial resolution so it is desirable to explore test configurations that do not require the use of geometrical stress concentrators. Here, the heterogeneity of the kinematics is increased using three parameters: (1) impacting over a percentage of the sample's height, (2) changing the angle of the input loading pulse, and (3) changing the material orthotropy angle relative to the specimen edges. Two identification strategies based on the virtual fields method are explored including the generalized stress–strain curves and the special optimized virtual fields. This chapter focuses on the presentation of the image deformation simulations used to find optimal test configurations.

Key words High strain rate testing · Full-field measurements · Image-based inertial impact test · Cortical bone

9.1 Introduction

The rate-dependent properties of orthotropic materials such as bone and glass fiber-reinforced polymer (GFRP) composites are of interest for understanding bone fracture or for designing impact resistant structures. The current test technique for obtaining high strain rate material properties is the split Hopkinson pressure bar (SHPB). This technique relies on several assumptions including that the sample must be in a state of quasi-static equilibrium and that the sample undergoes uniform 1D deformation [1]. These assumptions limit the ability of the SHPB technique to accurately extract a single stiffness component let alone identify multiple orthotropic stiffness components in a single test. Therefore, there is a clear need for new test methods that can extract more information from a single test at high strain rates.

Recently, the Image-Based Inertial Impact (IBII) test has emerged as an alternative technique that does not rely on the assumptions of quasi-static equilibrium or 1D deformation. In fact, the use of image-based measurements allows for deformation that is intentionally inhomogeneous providing a large database of points for material property identification. Thus far applications of the IBII test have shown that it is possible to extract the transverse and shear moduli for a carbon fiber in-plane and through-thickness [2–4]. However, for other orthotropic materials such as bone and GFRP the rate dependency of the longitudinal modulus and Poisson's ratio are also of interest. This chapter presents the development of a new "simple" IBII test configuration that enhances heterogeneity without the use of geometric stress concentrators. Increased heterogeneity is achieved by combining an off-axis test sample with an impact over a portion of the sample height (as shown in Fig. 9.1). The results of image deformation simulations are presented here as part of the test design process. In the future, the optimal configurations will be used to obtain experimental data.

L. Fletcher (✉)
Aeronautical & Astronautical Engineering, Faculty of Engineering & Physical Sciences, University of Southampton, Southampton, UK
e-mail: L.C.Fletcher@soton.ac.uk

F. Pierron
Mechanical Engineering, Faculty of Engineering & Physical Sciences, University of Southampton, Southampton, UK

S. Mates, V. Eliasson (eds.), *Dynamic Behavior of Materials, Volume 1*, Conference Proceedings of the Society for Experimental Mechanics Series, https://doi.org/10.1007/978-3-030-86562-7_9

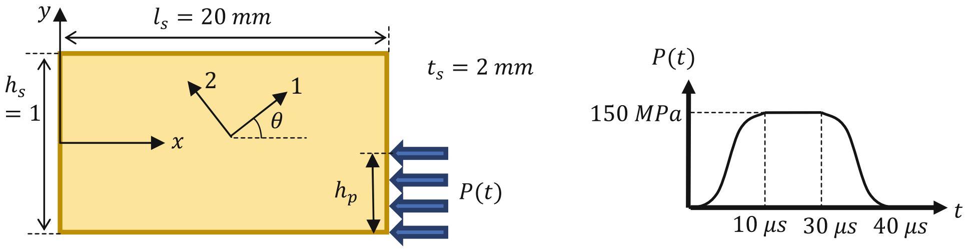

Fig. 9.1 Schematic of an IBII test on an orthotropic cortical bone sample, note that the material 1 axis is aligned with the long axis of the bone

9.2 The IBII Test: Background and Theory

The IBII test uses a thin plate-like specimen that is impacted in an edge-on configuration as shown in Fig. 9.1. Throughout the test full-field displacement measurements are taken on the sample's surface using an ultra-high speed camera. From the displacement fields the strain fields are obtained by spatial differentiation and the acceleration fields are obtained by double temporal differentiation. The resulting kinematics is then combined using the virtual fields method to extract material model parameters. Conceptually, the acceleration fields can be thought to act as an embedded load cell through Newton's second law. In this study, two different approaches were used to identify all four orthotropic stiffness components. This includes the special optimized virtual fields [4, 5] and generalized stress–strain curves [6]. Both of these methods rely on the principle of virtual work. For the IBII test configuration considered here, a number of simplifying assumptions are made, (1) the sample thickness is constant, (2) the sample is in a state of plane stress, and (3) the kinematic fields are uniform through the sample thickness. Applying these assumptions and neglecting body forces gives the principle of virtual work as:

$$\int_S \boldsymbol{\sigma} : \boldsymbol{\varepsilon}^*\, dS - \int_l \boldsymbol{T} \cdot \boldsymbol{u}^*\, dl + \rho \int_S \boldsymbol{a} \cdot \boldsymbol{u}^*\, dS = 0 \tag{9.1}$$

where $\boldsymbol{\sigma}$ is the stress tensor, $\boldsymbol{T}$ is the traction vector, and $\boldsymbol{u}^*$is the virtual displacement vector which is used to derive the virtual strain tensor $\boldsymbol{\varepsilon}^*$. The acceleration vector is given by $\boldsymbol{a}$, the density of the material is given by ρ, and perimeter of the sample is denoted by l with the surface area being given by S. The first term of Eq. (9.1) is the internal virtual work, the second term is the external virtual work, and the third is the acceleration virtual work. Here, we identify a linear elastic orthotropic constitutive law that is described by four stiffness components: Q_{11}, Q_{22}, Q_{12}, Q_{66}. For the case of the special optimized virtual fields, virtual fields are selected such that the contribution of the impact pulse (external virtual work term) is cancelled leaving the internal virtual work and acceleration virtual work terms. Substituting the linear elastic orthotropic constitutive law for the stress tensor in the internal virtual work term yields a series of linear equations which are solved to find the four orthotropic stiffness components. Further details on the application of the special optimized virtual fields to the IBII test can be found in [4, 5, 7]. For the generalized stress–strain curves rigid body virtual fields are substituted into Eq. (9.1) such that the internal virtual work term cancels due to the null virtual strains. This gives a series of equations that allow a combination of spatial averages of the acceleration and spatial averages of the strain to be plotted against each other with the resulting relationship being linear with a slope equal to one of the desired orthotropic stiffness components. Full details of the generalized stress–strain curves can be found in [6].

9.3 Finite Element Model and Image Deformation Method

A finite element model of the test configuration shown in Fig. 9.1 was constructed using ABAQUS/explicit. All modelling was done in 2D using CPS4R elements (4-node, plane-stress, reduced integration). A parametric sweep was used to determine the optimal mesh size (0.1 mm) and time step ($0.8t_{\text{crit}}$). The specimen was modelled as linear elastic and orthotropic with the nominal properties of cortical as: $\rho = 2000$ kg/m^3, $E_{11} = 20\ GPa$, $E_{22} = 10$ GPa, $\nu_{12} = 0.3$, and $G_{12} = 5$ GPa. The material angle was varied between $-80^\circ < \theta \leq 90^\circ$ in steps of 5°. A pressure pulse shown in Fig. 9.1 was applied over different portions of the sample height from $h_p = 0.3h_s$ to $h_p = h_s$ in steps of $0.05h_s$. The simulated camera frame rate was set at 5 Mfps and a total of 128 steps were extracted to replicate the number of frames available on the Shimadzu HPV-X camera. The displacement fields were then used to synthetically deform grid images using the image deformation procedure described in [7]. The parameters of the synthetic images were also set to replicate the experimental conditions (400 × 250 pixels, grid pitch of 0.337 mm, grid sampling of 6 pixels/period, etc.). Here, the first pass of the design sweep was based on identifying the configurations with the lowest systematic error without noise or smoothing applied (Err^0_{sys}).

9.4 Image Deformation Results

In order to identify potential configurations, the systematic error for each stiffness component was analyzed for the generalized stress–strain curves (GSSC) and special optimized virtual fields (VFO). To ensure identifiability of all stiffness components the sum of the percentage systematic error on all stiffness components was plotted as a function of the test configuration (impact height "h_p" and material angle "θ"). The sum of the systematic errors on all stiffness components for the special optimized virtual fields is shown in Fig. 9.2. Here, we observe strong sensitivity to the material angle with poor results near 0 and 90 as expected. The most stable region where the error is low is in the bottom right section of the plot for relatively high material angles combined with an impact pulse applied over 50% of the height or more.

The sum of the systematic error on each combination of identified stiffnesses with the GSSCs is shown in Fig. 9.3. For the GSSCs, it is possible to take an angled slice along the material 1 axis or perpendicular to this axis with each slice yielding a different combination of stiffness parameters (i.e., Q_{11}, Q_{12}, Q_{66} for a slice across the material 1 direction, given as S1 in the figure below). As the angled slices were taken from the top corner of the sample and must not intersect the impact edge, only a certain range of material angles are possible for each slice (hence the missing data for certain angles in each plot). Additionally, data with a combined error above 50% has been excluded for clarity. These results show that impacting over some portion of the height provides more significant heterogeneity enabling the different terms in GSSCs to be activated and that there is a reasonable region over which the combined error is less than 1% for each stiffness component.

Combining the results in Figs. 9.2 and 9.3 shows that the configurations that result in minimum systematic error do not coincide for all methods. In fact, it is not possible to apply the GSSCs to both slices for angles outside of $|40| < \theta < |50|$ due to geometric constraints. The configuration which yields the minimum systematic error for all methods has a pulse height of $h_p = 0.4h_s$ and a material angle of $\theta = 40^{\circ}$. For this configuration, the sum of all systematic errors across all methods is 4.6% (4 identified using the VFO, 3 from GSSCs, S1 and 3 from GSSCs, S2). This gives an average systematic error of 0.46% per stiffness identified. This is extremely low considering the limited spatial resolution of current ultra-high speed cameras.

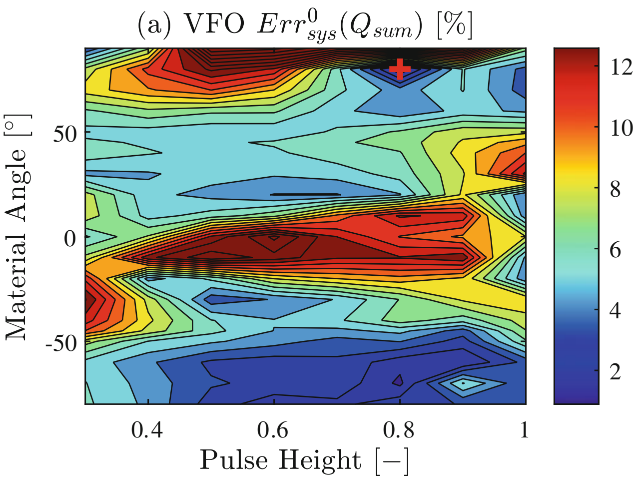

Fig. 9.2 Sum of the percentage systematic errors for all four stiffness parameters when the identification is performed using the special optimized virtual fields (VFO). The error is plotted as a function of the test design parameters, the material angle, and the pulse height. The overall minimum is shown with a red cross

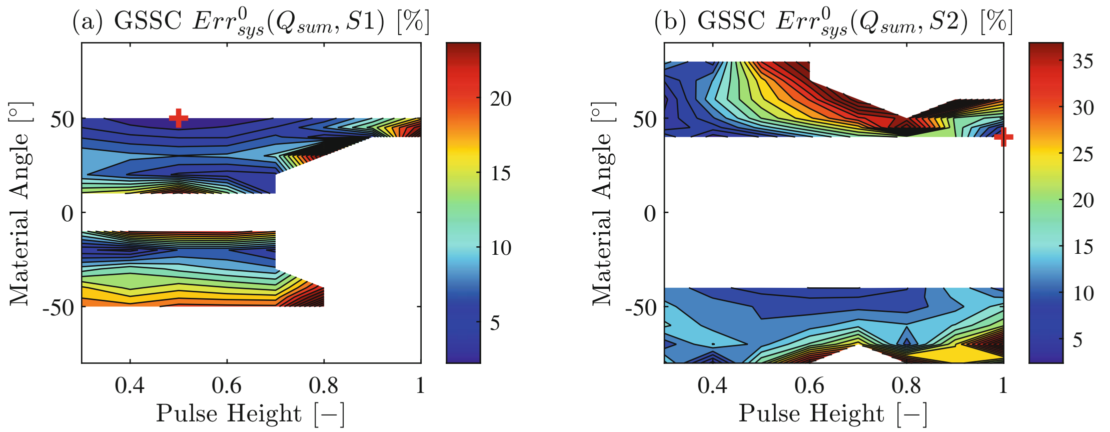

Fig. 9.3 Sum of the percentage systematic errors for all four stiffness parameters when the identification is performed using the generalized stress–strain curves (GSSC). The error is plotted as a function of the test design parameters, the material angle, and the pulse height. (**a**) shows the error for slice 1 identifying Q_{11}, Q_{12}, Q_{66} and (**b**) shows the error for slice two identifying Q_{22}, Q_{12}, Q_{66}. The overall minimum is shown with a red cross

9.5 Conclusion

The results of this study show that it is possible to design a simple IBII test configuration that encodes enough kinematic information to identify all four orthotropic stiffness components with a low systematic error. This was achieved without the use of geometric stress concentrators by varying the portion of the sample that was impacted and the material angle. The optimal test configuration over all methods was shown to be an impact over 40% of the specimen height with a material angle of 40°. This gave an average systematic error of less than 1% on all identified stiffness components. Future work will include performing additional image deformation simulations on the selected test configuration to specify smoothing parameters that give an optimal compromise between random and systematic errors. Additionally, the optimal test configuration will be analyzed experimentally.

Acknowledgments LF gratefully acknowledges support from the Leverhulme Trust as an Early Career Research Fellow through grant ECF-2018-212. LF and FP also acknowledge support from EPSRC through grant number EP/L02690/1.

References

1. Lopatnikov, S.L., Gama, B.A., Krauthouser, K., Gillespie, J.W.: Applicability of the classical analysis of experiments with split Hopkins pressure bar. Tech. Phys. Lett. **30**, 102–105 (2004). https://doi.org/10.1134/1.1666953
2. Parry, S., Fletcher, L., Pierron, F.: The off-axis IBII test for composites. J. Dyn. Behav. Mater. **7**(1), 127–155 (2021). https://doi.org/10.1007/s40870-020-00271-7
3. Van Blitterswyk, J., Fletcher, L., Pierron, F.: Image-based inertial impact (IBII) tests for measuring the interlaminar shear moduli of composites. J. Dyn. Behav. Mater. **6**, 373–398 (2020). https://doi.org/10.1007/s40870-020-00258-4
4. Fletcher, L., Van-Blitterswyk, J., Pierron, F.: A novel image-based inertial impact test (IBII) for the transverse properties of composites at high strain rates. J. Dyn. Behav. Mater. **5**, 65–92 (2019). https://doi.org/10.1007/s40870-019-00186-y
5. Pierron, F., Grédiac, M.: The Virtual Fields Method: Extracting Constitutive Mechanical Parameters from Full-Field Deformation Measurements. Springer, New York (2012)
6. Pierron, F., Fletcher, L.: Generalized stress–strain curves for IBII tests on isotropic and orthotropic materials. J. Dyn. Behav. Mater. **5**, 180–193 (2019). https://doi.org/10.1007/s40870-019-00197-9
7. Fletcher, L., Van Blitterswyk, J., Pierron, F.; A manual for conducting image-based inertial impact (IBII) tests. https://eprints.soton.ac.uk/433431/ (2019). Accessed 7 Oct 2019

Chapter 10
Comparison of the High Strain Rate Response of Boron/Silicon Carbide and MAX Phase Ceramics Using the Image-Based Inertial Impact Test

Lloyd Fletcher, Logan Shannahan, and Fabrice Pierron

Abstract The high strain rate material behaviour of armour ceramics is important for the design of armour systems. The current standard test technique for obtaining high strain rate material properties is the split Hopkinson pressure bar (SHPB). This technique relies on several assumptions including that the sample must be in a state of quasi-static equilibrium and that the sample undergoes uniform 1D deformation. These assumptions limit the ability of the SHPB technique to accurately identify the high strain rate response of ceramics because they fail at extremely low strains, especially when under tensile loading.

Recently, the Image-Based Inertial Impact (IBII) test has emerged as an alternative technique that does not rely on the assumption of quasi-static equilibrium and is specifically designed to obtain the high strain rate tensile strength of brittle materials. Therefore, this work focuses on the application of the IBII test to obtain the high strain rate properties of several armour materials including: boron carbide, silicon carbide and the recently developed MAX phase ceramics. Results for the boron and silicon carbide show that there is no rate sensitivity on the identified elastic properties (modulus and Poisson's ratio) at strain rates on the order of 1000/s. Additionally, results for the tensile strength of boron and silicon carbide compare well with quasi-static values despite exhibiting high scatter. The MAX phase ceramics will be tested in the future and the results will be presented at the conference.

Key words Armour ceramics · MAX phases · High strain rate testing · Image-based inertial impact test

10.1 Introduction

Ceramics such as boron and silicon carbide are commonly used in armour applications. More recently, MAX Phase ceramics have been proposed as a new potential armour material with beneficial properties of both metals and ceramics. Therefore, there is a strong need to study the response of these materials at high strain rates. Traditionally high strain rate material data is obtained using the split Hopkinson pressure bar (SHPB) [1]. However, it is difficult to apply this technique to ceramics due to their low strain to failure and brittle failure mode. A key assumption of the SHPB analysis is that the sample is in state of quasi-static equilibrium such that all inertial effects have fully damped out [2]. This problem is more pronounced when loading ceramics in tension because the failure strain is low, and therefore it is unlikely that quasi-static equilibrium is achieved prior to sample failure. Another difficulty when testing brittle samples in tension with the SHPB is the need to grip the sample. This requires the use of longer samples which increases difficulties with achieving quasi-static equilibrium and susceptibility to the effects of parasitic bending.

Thus, there is a need for new test methods that do not require the assumption of quasi-static equilibrium. Recently, ultra-high speed imaging technology has become readily available with sensor sizes and image quality capable of performing full-

---

L. Fletcher (✉)
Aeronautical & Astronautical Engineering, Faculty of Engineering & Physical Sciences, University of Southampton, Southampton, UK
e-mail: L.C.Fletcher@soton.ac.uk

L. Shannahan
CCDC, Army Research Laboratory, Aberdeen Proving Ground, MD, USA

F. Pierron
Mechanical Engineering, Faculty of Engineering & Physical Sciences, University of Southampton, Southampton, UK

S. Mates, V. Eliasson (eds.), *Dynamic Behavior of Materials, Volume 1*, Conference Proceedings of the Society for Experimental Mechanics Series, https://doi.org/10.1007/978-3-030-86562-7_10

field measurements at millions of frames per second. This frame rate is high enough to resolve elastic wave propagation in materials and creates new opportunities for test development. A new test method that has been shown to be particularly well suited to brittle and quasi-brittle materials is the Image-Based Inertial Impact (IBII) test. The IBII test has been successfully used to obtain the high strain rate tensile strength of tungsten carbide cermets in [3]. Therefore, the purpose of this study is to use the IBII test method to investigate the high strain rate response of a range of armour ceramics including: boron/silicon carbide and MAX Phase ceramics. This extended abstract presents preliminary data on a boron carbide sample to illustrate the methodology.

10.2 Background and Theory

The IBII test uses a thin rectangular plate-like test sample that is impacted in an edge-on configuration. A schematic of the main components of the IBII test setup is shown in Fig. 10.1. Here, we observe a thin plate-like sample which is bonded to a cylindrical waveguide. The wave guide acts as a kind of specimen holder and aids in alignment with the projectile that is used to produce the impact loading pulse. Throughout the test full-field displacement measurements are taken over the whole surface of the sample using an ultra-high speed camera. Taking the second temporal derivative of the displacement fields yields the acceleration fields while the first spatial derivative of the displacement fields gives the strain. The derived kinematic fields are then used with an inverse identification procedure (in this case the virtual fields method) to obtain the desired material properties. Intuitively, one can think of combining the acceleration fields with Newton's second law to produce a kind of embedded dynamic load cell. More formally, the IBII test data can be analyzed using the 'stress-gauge' equation (as in [3, 4]):

$$\overline{\sigma_{xx}}^{y} = \rho x_0 \overline{a_x}^{S} \tag{10.1}$$

where $\overline{\sigma_{xx}}^{y}$is the average axial stress over the line at x_0, $\overline{a_x}^{S}$is the surface average of the acceleration field over the area S (from the free edge to x_0) and ρ is the density of the material. Equation (10.1) above can be derived using the principle of virtual work and applying a virtual field that describes a rigid body translation in the 'x' direction (see [3]). The stress-gauge equation is useful for extracting the elastic modulus but for tensile failure stress identification a more local approximation of the tensile stress is required. In this case, a linear approximation of the stress distribution can be obtained by combining the results from three rigid body virtual fields (translation in x, y and a rigid rotation), as described in [3]:

$$\sigma_{xx}(LSG) = \rho x_0 \overline{a_x}^{S} + \frac{12 \rho x_0 y}{h^2}\left(\overline{a_x y}^{S} - \overline{a_y x}^{S} + x_0\, \overline{a_y}^{S}\right) \tag{10.2}$$

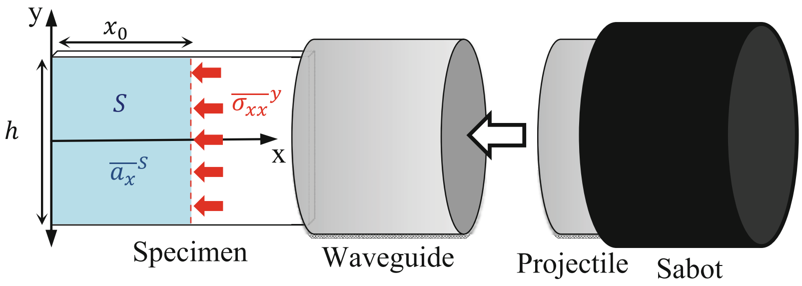

Fig. 10.1 Schematic of the IBII test showing the main components and the key terms from Eq. 10.1

where σ_{xx}^{LSG} denotes the linear stress-gauge (LSG) which gives the axial stress as a function of horizontal 'x_0' and vertical position 'y' on the sample from the free edge. The height of the sample is given by h and the remaining terms are weighted spatial averages of the x and y acceleration over the surface S.

Table 10.1 Summary of imaging and full-field measurement parameters for the IBII tests

Camera	Shimadzu HPV-X	Measurement technique	Grid method [5]
Pixel array size	400 × 250	Grid pitch	0.7 mm
Dynamic range	10 bits	Grid sampling (pxpp)	5 px/period
Frame rate	Five million fps	Window type	Bi-triangular
Integration time	110 ns	Window width	2pxpp-1
Total images	128	Displacement calculation	Iterative [5]
Lens	Sigma 105 mm	Spatial smoothing	Gaussian over 61 × 61 px
Field of view	56 × 35 mm	Temporal smoothing	3rd order Savitsky-Golay over 13 frames

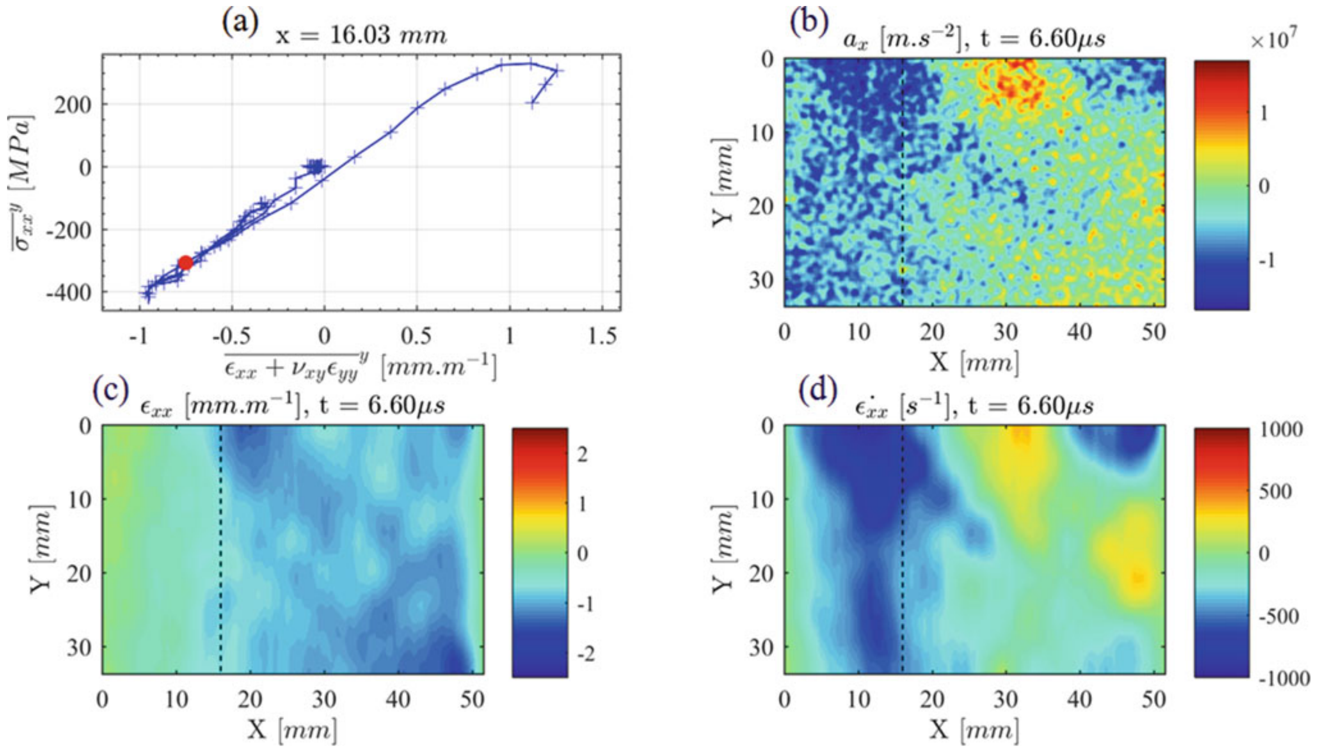

Fig. 10.2 The stress–strain curve at $x = 16$ mm from the free edge is shown in (**a**) as indicated by the dashed black line on the kinematic fields, the red dot indicates the time step shown in the fields. The axial acceleration field is shown in (**b**), the axial strain field is shown in (**c**) and the axial strain rate field is shown in (**d**)

10.3 Experimental Method

The IBII tests were conducted using the procedure outlined in the IBII test manual which can be found in [4]. The IBII samples were spray painted with a thin coat of white paint followed by directly printing a grid onto the surface of the paint as described in [4]. The projectile and waveguide were made from maraging steel and a nominal impact speed of 50 m/s was used. The relevant imaging and full-field measurement parameters are summarized in Table 10.1. The results presented here are for a single boron carbide sample with dimensions 54 × 34 × 4 mm and a density of 2508 kg. m^{-3}.

10.4 Results and Discussion

The kinematics derived from the grid method displacements for the tested boron carbide sample are shown in Fig. 10.2 along with a representative stress–strain curve. This data shows that the accelerations reach peak magnitudes on the order of 1×10^7m. s^{-2} while the axial strain are only a few milli-strain. The strain rate field is heterogenous with peaks on the order of

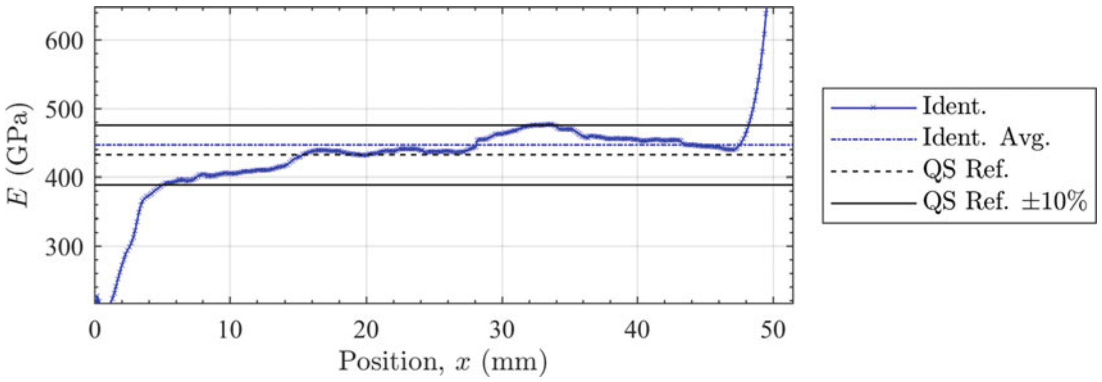

Fig. 10.3 Elastic modulus obtained by linearly fitting the stress–strain curves as a function of position from the free edge for the tested boron carbide sample

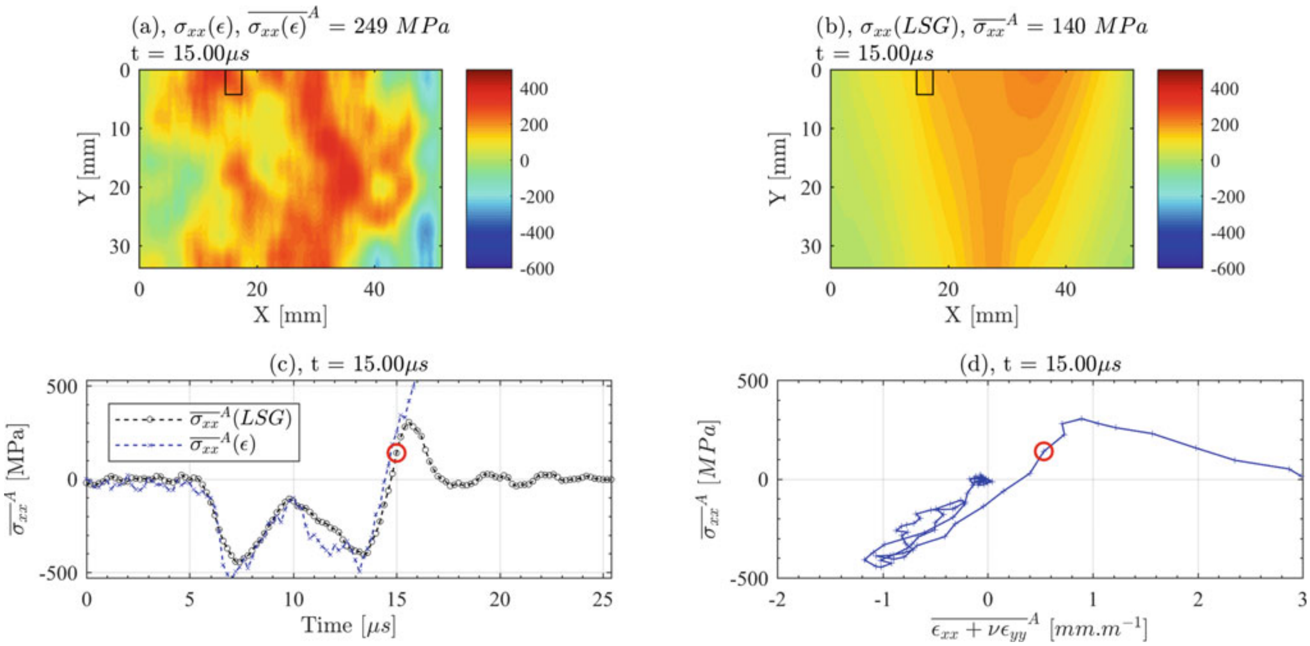

Fig. 10.4 Tensile failure stress diagnostics for the tested boron carbide sample. (**a**) shows the stress field calculated from the strains and identified stiffness parameters. (**b**) shows the stress field calculated using the linear stress-gauge equation (Eq. 10.2). (**c**) shows the agreement between these two stress measures over the virtual gauge region where the first crack forms. (**d**) shows the local stress–strain curve over the virtual gauge region

1000s^{-1}. Observation of the stress–strain curves shows the compressive response remains linear elastic before unloading and eventually failing in tension.

All the stress–strain curves along the specimen from the free edge to the impact edge were linearly fitted to obtain the elastic modulus. Figure 10.3 shows the identified elastic modulus as a function of position for the tested boron carbide sample. Near the free edge the stress is low resulting in poor identification and on both the free and impact edge of the sample the data is corrupted by spatial smoothing edge effects. Taking the stable portion in the middle of the sample, it can be seen that the modulus is stable and compares well to the quasi-static value expected for boron carbide [6]. The overall average modulus was taken over the middle 50% of the sample and was found to be 446 GPa.

The tensile failure stress was also analysed using the linear stress-gauge equation. The resulting kinematics at the time of fracture is shown in Fig. 10.4. Taking the peak value of the linear stress-gauge as the tensile failure stress gives 305 MPa which compares well to previous shock spall studies on boron carbide [6].

10.5 Conclusion

The results of this study show that the IBII test method is a useful tool for analysing the high strain rate response of armour ceramics. Here, we analysed preliminary data for a boron carbide sample to demonstrate the efficacy of the method. The elastic modulus was identified as 446 GPa which closely matched the quasi-static modulus. The tensile failure stress was 305 MPa which compared well to previous shock spall studies on a similar material. Future work will include performing IBII tests on MAX Phase ceramic samples and comparing these to six boron carbide and six silicon carbide samples.

Acknowledgements Funding from EPSRC is acknowledged by Professor Pierron and Dr. Fletcher (Grant EP/L026910/1).

References

1. Field, J.E., Walley, S.M., Proud, W.G., Goldrein, H.T., Siviour, C.R.: Review of experimental techniques for high rate deformation and shock studies. Int. J. Impact Eng. **30**, 725–775 (2004). https://doi.org/10.1016/j.ijimpeng.2004.03.005
2. Lopatnikov, S.L., Gama, B.A., Krauthouser, K., Gillespie, J.W.: Applicability of the classical analysis of experiments with split Hopkins pressure bar. Tech. Phys. Lett. **30**, 102–105 (2004). https://doi.org/10.1134/1.1666953
3. Fletcher, L., Pierron, F.: An image-based inertial impact (IBII) test for tungsten carbide cermets. J. Dyn. Behav. Mater. **4**, 481–504 (2018). https://doi.org/10.1007/s40870-018-0172-4
4. Fletcher, L., Van Blitterswyk, J., Pierron, F.: A manual for conducting image-based inertial impact (IBII) tests. https://eprints.soton.ac.uk/433431/ (2019). Accessed 7 Oct 2019
5. Grédiac, M., Sur, F., Blaysat, B.: The grid method for in-plane displacement and strain measurement: a review and analysis. Strain. **52**, 205–243 (2016). https://doi.org/10.1111/str.12182
6. Dandekar, D.P.: Shock response of boron carbide, Army Research Lab Aberdeen Proving Ground MD. https://apps.dtic.mil/sti/citations/ADA389400 (2001) Accessed 17 Feb 2021

Chapter 11
High-Rate Indentation Using Miniature Kolsky Bar Methods

Daniel T. Casem, John J. Pittari III, and Jeffrey J. Swab

Abstract A Kolsky Bar method for high-rate indentation is being developed. Samples are adhered to the end of the input bar and the indenter is mounted directly on the end of the output bar. When the input pulse reaches the sample, the sample is driven into the output bar and loaded. By carefully choosing the lengths and impedances of the bars and striker, the maximum load and loading duration can be reliably controlled. It can furthermore be ensured that the sample is only subjected to a single loading, i.e., the sample is not reloaded due to later stress-wave reverberations in the bars even though a momentum trap is not used. Depending on the sample and desired indentation load, very small output bars may be needed. For this reason, the output bar is instrumented with a normal displacement interferometer on the free-end. This choice of instrumentation is highly sensitive and also can be used to verify that the sample only experiences a single loading cycle. The current study is preliminary and focuses on Vickers indentation of OFHC Cu. However, the method is applicable to a wide range of materials and has the potential for loading times less than 5 μs, about a factor of 20 shorter than the current state of the art.

Key words Indentation · Split Hopkinson pressure bar · High strain-rate · Plasticity

11.1 Introduction

Indentation tests are performed to determine the hardness of materials. An indenter, typically diamond, is pressed into a sample at a known force and the size of the resulting indentation is used to calculate a hardness value for that indenter type and that specific load. There are standards for hardness testing, see for example [1, 2] for Knoop and Vickers hardness testing of ceramics. It is a useful test because it is fast, inexpensive, and essentially non-destructive. Although it is an indirect measure, hardness is related to the mechanical properties of the material, and a considerable amount of information can potentially be obtained from a simple experiment; see for example [3].

Conventional hardness testing is done with loading times on the order of tens of seconds. Because mechanical properties are often rate sensitive, there is an interest in developing high rate hardness testing methods. To address this need, [4, 5] developed a modified Kolsky bar (Split Hopkinson Pressure Bar) to perform hardness tests with indentation times in the range of 100–500 μs. In this configuration, the indenter is mounted at the end of an input bar. The sample is mounted on a fixed base that incorporates a load cell. A striker impact drives the indenter tip into the sample and the indention force is measured by the load cell. A momentum trap on a flanged input bar is used to ensure the sample is only loaded once. The indentation size is measured directly from the recovered sample providing the information needed to determine a hardness value. The objective of the present work is to develop a miniature Kolsky bar method that can provide even shorter loading times (<5 μs) to complement existing capabilities.

The basic arrangement is shown in Fig. 11.1. A striker bar impacts the end of the input bar; a pulse shaper may be used if necessary. The input bar is standard, with no flange or momentum trap, and is instrumented with strain gages at the mid-point. If the input bar is small enough, an interferometer can be used instead. This could be a Transverse Displacement Interferometer (TDI) [6, 7] or a Photon Doppler Velocimeter (PDV) [8, 9]. The sample is glued or in some other way fastened to the

---

D. T. Casem (✉)
US Army Research Laboratory, FCDD-RLW-TC, Aberdeen Proving Ground, MD, United States
e-mail: daniel.t.casem.civ@mail.mil

J. J. Pittari III
US Army Research Laboratory, FCDD-RLW-MB, Aberdeen Proving Ground, MD, United States

J. J. Swab
US Army Research Laboratory, FCDD-RLW-ME, Aberdeen Proving Ground, MD, USA

S. Mates, V. Eliasson (eds.), *Dynamic Behavior of Materials, Volume 1*, Conference Proceedings of the Society for Experimental Mechanics Series, https://doi.org/10.1007/978-3-030-86562-7_11

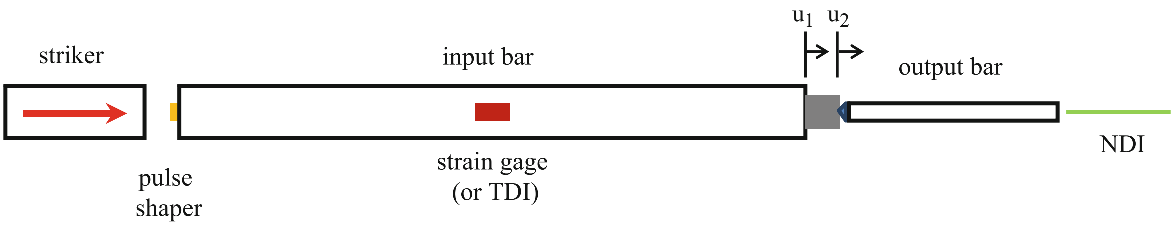

Fig. 11.1 A Kolsky bar used for high rate indentation

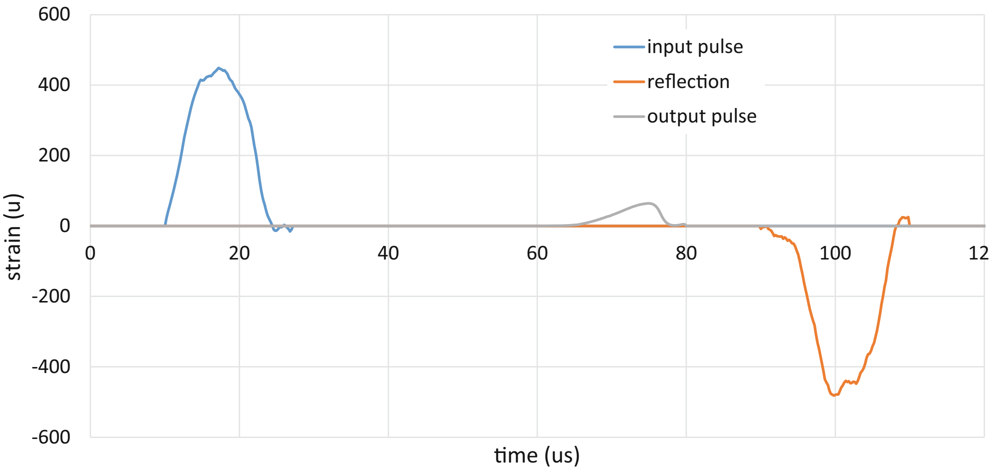

Fig. 11.2 Stress waves from an indentation into OFHC Cu

end of the input bar. Its dimensions are small but large enough that the resulting indentation is free from edge effects. A small gap may be left between the sample and the indenter tip to prevent premature loading during set up. When the input pulse reaches the sample, it is driven into the indenter tip. The pulse transmitted into the output bar reflects from the free-end and back to the sample. If the bar geometry and materials are chosen carefully, the indenter will separate from the sample and travel downrange without re-loading the sample. This will typically require a very low-impedance output bar (low density, low wave speed, and/or small diameter). The sample can then be removed from the bar and the indentation analyzed post-mortem. The advantage of this approach is that various stop rings and momentum traps are not needed to control the sample loading. This makes it easy to use small diameter bars. Since small diameter bars have short rise-times, higher loading rates can be obtained.

11.2 Example

An application is now presented with a Vickers indent into OFHC Cu. The copper sample is cylindrical with $L = D = 3.18$ mm. It is glued to the end of 3.18 mm diameter steel input bar, 405 mm long. The striker is 25 mm long, 3.18 mm diameter, and a small amount of vacuum grease is used as a pulse shaper. The output bar is 40 mm long and 1.59 mm diameter. The indenter is embedded in the end of a 3.18 mm. The input bar is instrumented with strain gages, and the output bar with an NDI. The pulses are shown in Fig. 11.2. The NDI measures displacement, but it can be related to the traditional strain measurement using standard equations [7].

The input pulse is rounded due to the pulse shaper. The output pulse is small, but easily measured by the highly sensitive NDI. The load vs. indentation depth curve, calculated from a standard analysis, is shown in Fig. 11.3. The peak force is 25 N and the maximum indentation depth is 38 μm. The loading time is about 10 μs. The indentation rate is not constant, reaching a peak of about 4 m/s. It could be made more constant by appropriate pulse shaping.

That the sample is not reloaded can be deduced from the relative magnitudes of the signals shown in Fig. 11.2. If each end of the two bars remain free after the experiment, the reflection and the output pulse will continue to reverberate in the input and output bars, respectively, long after the sample has been loaded. The reflection will act at the sample periodically, separated by

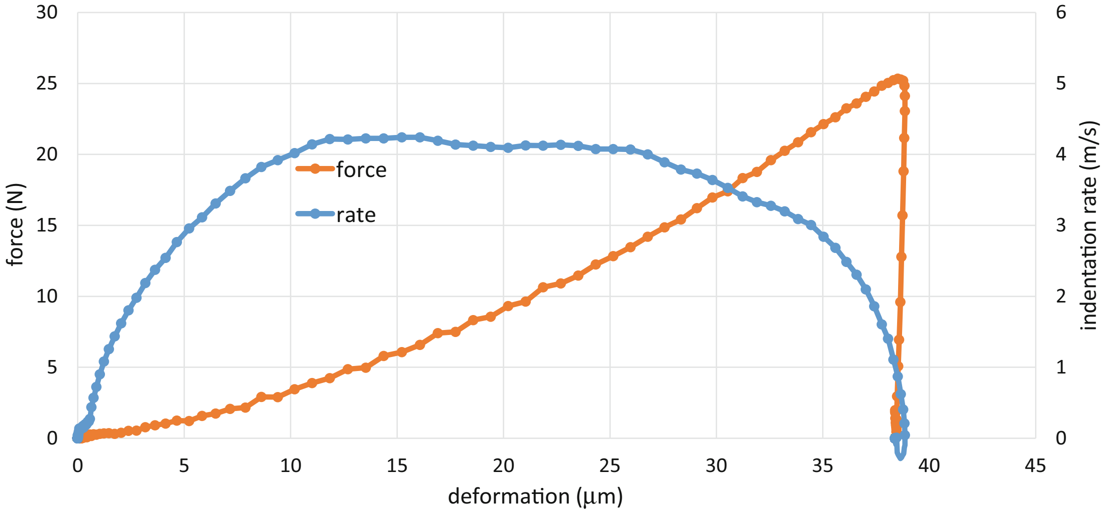

Fig. 11.3 Force vs. Vickers indentation depth for OFHC Cu, along with the loading rate (rate of indentation depth)

the time needed to travel the length of the input bar and back to the sample. Each time this occurs, the end of the sample will move towards the indenter by an amount proportional to the area under the reflected pulse, in this case 38 µm. Similarly, each time the reflection of the output pulse acts at the indenter tip, it moves away from the specimen 4.4 µm. Based on this, one might expect reloading to occur, but since the input bar is considerably longer than the output bar, reverberations in the output bar occur 10 times as frequently as those in the input bar, and the sample is not reloaded.

1.6 mm diameter steel bars can typically resolve events at frequencies as high as 3 MHz, thus very high loading rates can potentially be obtained. Further reducing bar size can be used for faster events, provided indenters can be mounted. For example, the markers in Fig. 11.3 are at time intervals of 0.2 µs. The sharp temporal resolution at the point of peak stress and as the sample unloads is notable and greatly exceeds the capabilities of commercially available load cells.

11.3 Conclusion

A high rate indentation method is under development which has the potential for loading times under 5 µs. This will permit hardness testing at rates at least an order of magnitude higher than currently used methods. A key feature is the use of bars that are tailored to the sample to achieve the desired indentation load and rate. This typically requires small, low-impedance bars, which has the added benefit of increasing the sensitivity of the force and displacement measurements both in time and magnitude. An example was given for a Vickers indentation into copper. Application of the method to other materials and indenter shapes seems straightforward.

References

1. ASTM C1326-13: Standard Test Method for Knoop Indentation Hardness of Advanced Ceramics. ASTM, West Conshohocken, PA (2018)
2. ASTM C1327-15: Standard Test Method for Vickers Indentation Hardness of Advanced Ceramics. ASTM, West Conshohocken, PA (2019)
3. Kalidindi, S.R., Pathak, S.: Determination of the effective zero-point and the extraction of spherical nanoindentation stress-strain curve. Acta Mater. **56**(14), 3523–3532 (2008)
4. Subhash, G., Koeppel, B.J., Chandra, A.: Dynamic indentation hardness and rate sensitivity in metals. ASME J. Eng. Mater. Technol. **121**, 257–263 (1999)
5. Koeppel, B.J., Subhash, G.: Characteristics of residual plastic zone under static and dynamic Vickers indentations. Wear. **224**, 56–67 (1999)
6. Kim, K.S., Clifton, R.J., Kumar, P.: Combined normal-displacement and transverse-displacement interferometer with an application to impact of y-cut quartz. J. App. Phys. **48**(10), 4132–4139 (1977)
7. Casem, D.T., Grunschel, S.E., Schuster, B.E.: Normal and transverse displacement interferometers applied to small diameter Kolsky bars. Exp. Mech. **52**(2), 173–184 (2012)
8. Strand, O.T., Goosman, D.R., Martinez, C., Whitworth, T.L.: Compact system for high-speed velocimetry using heterodyne techniques. Rev. Sci. Instr. **77**, 083108 (2006)
9. Avinadav, C., Ashuach, Y., Kreif, R.: Interferometry-based Kolsky bar apparatus. Rev. Sci. Instrum. **82**, 073908 (2011)

Chapter 12
Ultrasonic Guided Waves Generated by Parametrized Novel Mini Impactor with Application to a Composite Structure

Benjamin J. Katko, Hyungsuk Eric Kim, Alexander Westra, Janelle Dela-Cueva, and Hyonny Kim

Abstract Nondestructive structural interrogation using guided waves for damage detection is an established engineering assessment technique. In this research, a novel composite mini impactor tool is presented as an excitation source for the use in the evaluation of composite structures. Nondestructive evaluation (NDE) of aerospace composite structures is critical since non-visible internal damage, such as barely visible impact damage (BVID), can affect the safety of the structure. Traditional impact hammers have been used in NDE of composite structures, but the excitation frequency range produced is limited (less than 40 kHz). A unidirectional carbon/epoxy mini impactor device was designed to excite a frequency range between 40 and 500 kHz. Parameterization of the device was performed to define its operational domain and underlying physics. The effect of varying the mini impactor stiffness and total impactor mass, which includes an aluminum tip (i.e., tip + beam), was evaluated for time-domain features, frequency content, and amplitude ranges. During the parameterization, different waveguide materials (flat plates) were explored, which included both isotropic and anisotropic materials, thereby allowing for a mapping of structural response to the waveguide's density, stiffness properties, and thickness. The parametrized mini impactor data were captured using piezoelectric acoustic contact sensors for structural response to the mini impactor. High-speed imagery was used to directly observe the physical motion of the mini impactor.

Key words Aerospace composites · Nondestructive evaluation · Mini impactor · Ultrasonic guided waves · Damage detection

12.1 Introduction

Ultrasonic guided wave (UGW) transmission across pristine laminates and metals was parameterized to establish a baseline for damage assessment. Mini impactor beams of varying lengths and thicknesses were designed to deliver high energy impulses of short durations, with frequencies in the ultrasonic range. Impulse duration brevity is proportional to impactor tip hardness, and inversely proportional to impactor beam weight [1]. For this reason, the mini impactors consist of thin flat aluminum tips affixed to carbon/epoxy beams of varying sizes. The parametrization of the mini impactor device was performed to define the operational domain and underlying physics affecting the subsequent excitation characteristics of the waveguides. Four plate types were investigated: 6061-T6 aluminum, mild steel, plain woven carbon fiber (style 282 weave) epoxy composite, and 8 harness satin fiberglass (style 7781 weave) epoxy composite.

Throughout experimentation, the mini impactor data were captured using piezoelectric acoustic contact sensors (R15s, Mistras) with a resonant frequency of 150 kHz. This sensor type was successful in UGW detection for damaged aerospace structures [2]. Also utilized was a Phantom v7.3 high-speed camera for observing the beam impact-contact interaction, dynamics, and contact duration. The R15s sensors were excited primarily by longitudinal and shear stress waves and perform adequately when compared to the R15s sensor transfer functions via thin glass tube and pencil lead break tests [3]. High-speed imagery captured the tip location and beam shape as a function of time providing key information of the beam dynamics and the contact force model estimation. The mini impactor produces an excitation with usable frequency ranging between 40 and 500 kHz within the plate, and the intensity of the received signals is high enough to not require amplification of the R15s output. In total, approximately 850 experiments were conducted, with many more performed to establish and calibrate the experimental methodology. Parallel to the experimentation was finite element modeling using Abaqus finite element analysis (FEA). The goal of the FEA is to model the mini impactor, the impact event, and excitation of guided waves into the wave

---

B. J. Katko (✉) · H. E. Kim · A. Westra · J. Dela-Cueva · H. Kim
Department of Structural Engineering, Jacobs School of Engineering, University of California—San Diego, La Jolla, CA, USA
e-mail: bkatko@eng.ucsd.edu

S. Mates, V. Eliasson (eds.), *Dynamic Behavior of Materials, Volume 1*, Conference Proceedings of the Society for Experimental Mechanics Series, https://doi.org/10.1007/978-3-030-86562-7_12

guide, and thereby gain more detailed insight into the physics of the response. The 0.8 mm thick 6061-T6 plate and 4 ply, 38 mm mini impactor were chosen as the baseline models for calibration due to aluminum's well-known UGW behavior.

12.2 Background

12.2.1 Experimental Methodology

A mini impactor is a carbon fiber beam with aluminum shims adhered distally and proximally on the beam. Each beam is constructed of T800/3900-2 unidirectional, pre-impregnated carbon fiber epoxy composite. The mini impactor is cantilevered above the plate with the goal of the small, flat impactor tip striking flat upon the waveguide surface, see Fig. 12.1. Maintaining a lightweight yet stiff beam motivated the mini impactor beam design, and Table 12.1 summarizes the mini impactor beams used in experimentation.

The waveguides include two isotropic and two anisotropic plate types. Of interest were materials and thicknesses pertinent to aerospace structures. Three plate thicknesses were identified: nominally 0.8, 1.5, and 6 mms. The isotropic plates were 6061-T6 aluminum and heat-treated mild steel. The anisotropic plates were composite laminates, the first being a plain-woven carbon fiber Type 282 3 K and an E-Glass 7781 8H. The carbon/epoxy layup were: $[0]_4$, $[0]_{6,}$ and $[0]_{22}$. While the glass/epoxy layups were $[0]_4$, $[0]_{6,}$ and $[0]_{24}$. The composite laminates were infused with Kaneka GR6862 epoxy resin via the vacuum-assisted resin transfer molding (VARTM) method. The plates were simply supported and padded with foam to mitigate any boundary condition induced guided wave behavior during experimentation, as shown schematically in Fig. 12.1.

Capturing the impact event was performed via two different methodologies depending on data desired. The UGW propagation was captured using two R15s sensors. The R15s sensors were coupled to the plates with gel couplant and spring-loaded hold-downs. The first sensor is located at 100 mm from the impact event, and the second sensor is located at 65 mm from the first. Ten replicate experiments were performed for each of the 72 possible experimental combinations. The power spectral density (PSD) was calculated for each of the 720 experiments and averaged to produce 72 PSD plots to present. Approximately 130 high speed videos were captured and analyzed to measure tip displacement. The purpose of capturing tip displacement during the impact event was for the estimation of the velocity profile at the impactor tip. As a first assumption, linear impact impulse-momentum theory was applied to obtain an estimate of average contact force during the impact event. The estimated average forces ranged between 3 and 20 N depending on beam and contact duration. To ensure proper on-time triggering, a simple switch circuit was used to begin the data acquisition process. At contact, the switch (mini impactor) was closed thus completing the circuit on the waveguide surface, this was monitored by the oscilloscope and provided insight to the contact duration. Fig. 12.1 highlights the basic mini impactor, waveguide, and piezoelectric sensor arrangement.

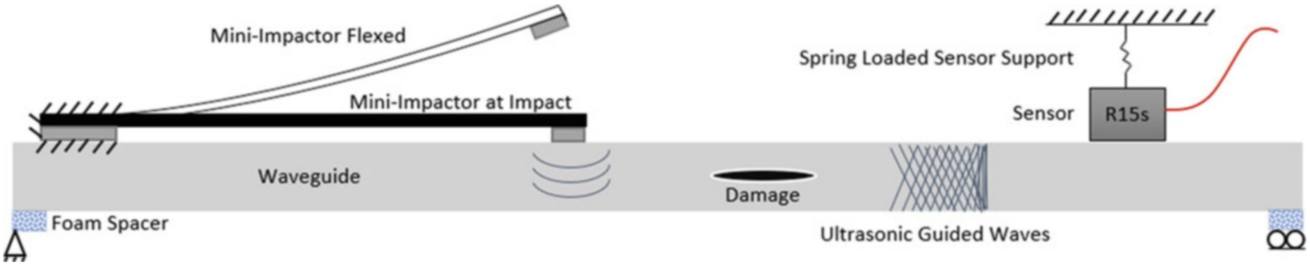

Fig. 12.1 Mini impactor, waveguide, and sensor arrangement. Waveguide nominal thickness ranged from 0.8 mm to 6 mm and the mini impactor beam thickness and lengths varied producing different stiffness and masses

Table 12.1 Summary of mini impactor beam properties

# of plies per beam	4	4	6	6	8	8
Cantilever length (mm)	38.10	44.45	57.15	69.85	76.20	88.90
Width (mm)	6.13	6.10	6.68	6.88	6.58	6.84
Thickness (mm)	0.74	0.73	1.17	1.18	1.58	1.50
Beam + tip mass (g)	0.110	0.114	0.203	0.253	0.337	0.382
Stiffness (N/m)	1682	999.7	2121	1227	2170	1216
1st natural frequency (Hz)	642.1	476.6	494.3	338.5	390.4	277.1

12.2.2 *Simulation Methodology*

The mini impactor and aluminum plates were modeled in FEA with 8-node hexahedral continuum shell elements (SC8R in Abaqus). The mini impactor was idealized as a cantilever beam with fixed boundary conditions and an initial displacement boundary condition of 6.35 mm. The Aluminum 6061-T6 plates were meshed with 109,509 SC8R elements with a maximum element size of 0.50 mm, which provides 10 nodes per smallest wavelength of interest [4]. The impact phenomenon was modeled as a two-step explicit dynamic analysis. The initial displacement was prescribed on the mini impactor tip in the first step and then released in the second step to replicate the impact experiments. The impactor to waveguide plate interactions were modeled using the General Contact formulation in Abaqus. The R15s sensor was modeled on the 6061-T6 aluminum plate as a surface-adjacent point node at 100 mm from the impact tip strike point, replicating the experimental setup. Displacement quantities (U11, U22, and U33) measured at 100 mm and 165 mm for the duration of the simulation. Displacement quantities were recorded at time increments of 10 μs. This timestep was used to determine if the longitudinal and shear stress wave packets arrive on time. Mesh and timestep refinements will enhance the displacement and frequency content capable of being observed during simulation.

12.3 Analysis

12.3.1 *Experimental Results*

Timeseries data recorded via the R15s contact sensors was transformed into the frequency domain and presented as a PSD graph. Fig. 12.2 highlights the timeseries response for nominal 6 mm thick carbon fiber wave guide.

The PSD was normalized by the respective impacting beam's first natural frequency and thus the units are db/Hz^2. An unnormalized power spectral density is a statement about the squared variance of the signal at that frequency bin. In this case, the squared variance is represented as squared voltage and multiplied by $10\log_{10}$ to convert to decibels (db). Using db to represent the PSD was chosen as an intuitive representation of the PSD as it can be related to loudness of a sound, which is usually represented in decibels (e.g., consider the db level of a jet engine versus a bird chirp). Normalizing the PSD by the impacting beam's natural frequency was found to condense all the raw PSD graphs. Figures 12.3, 12.4, and 12.5 represent the normalized mean PSD performed on different thickness waveguides. The legends in Figs. 12.3, 12.4, and 12.5 are an

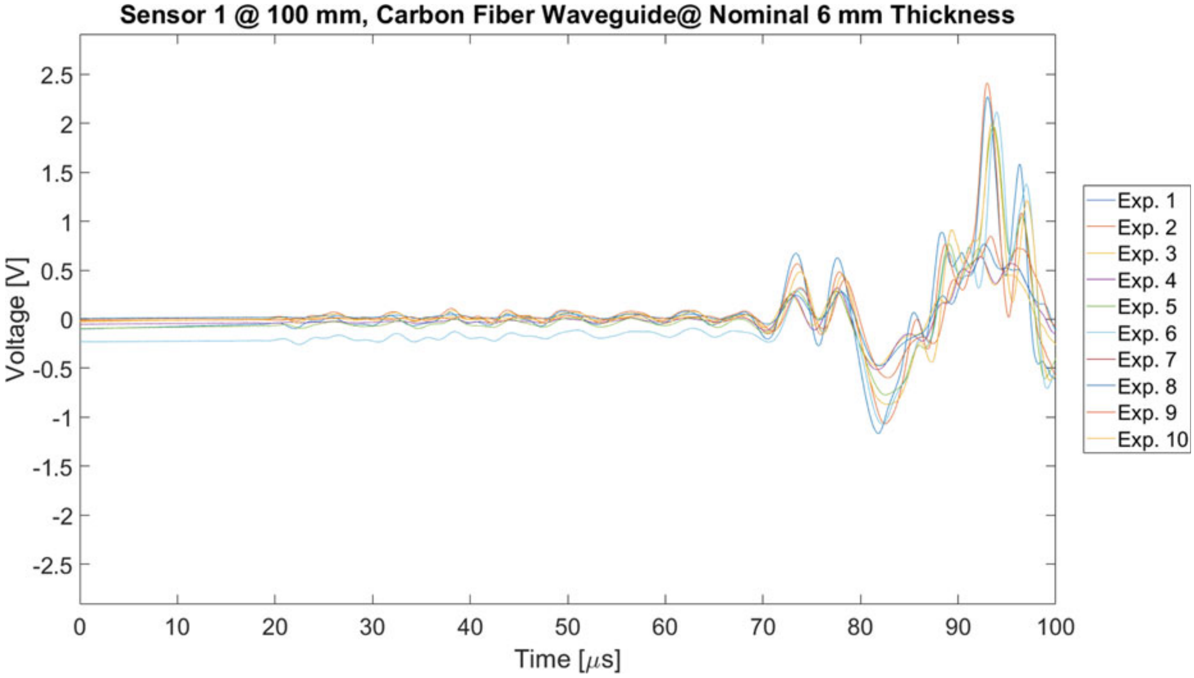

Fig. 12.2 Ten R15s sensor experiment timeseries responses to 6 ply, 57 mm mini impactor

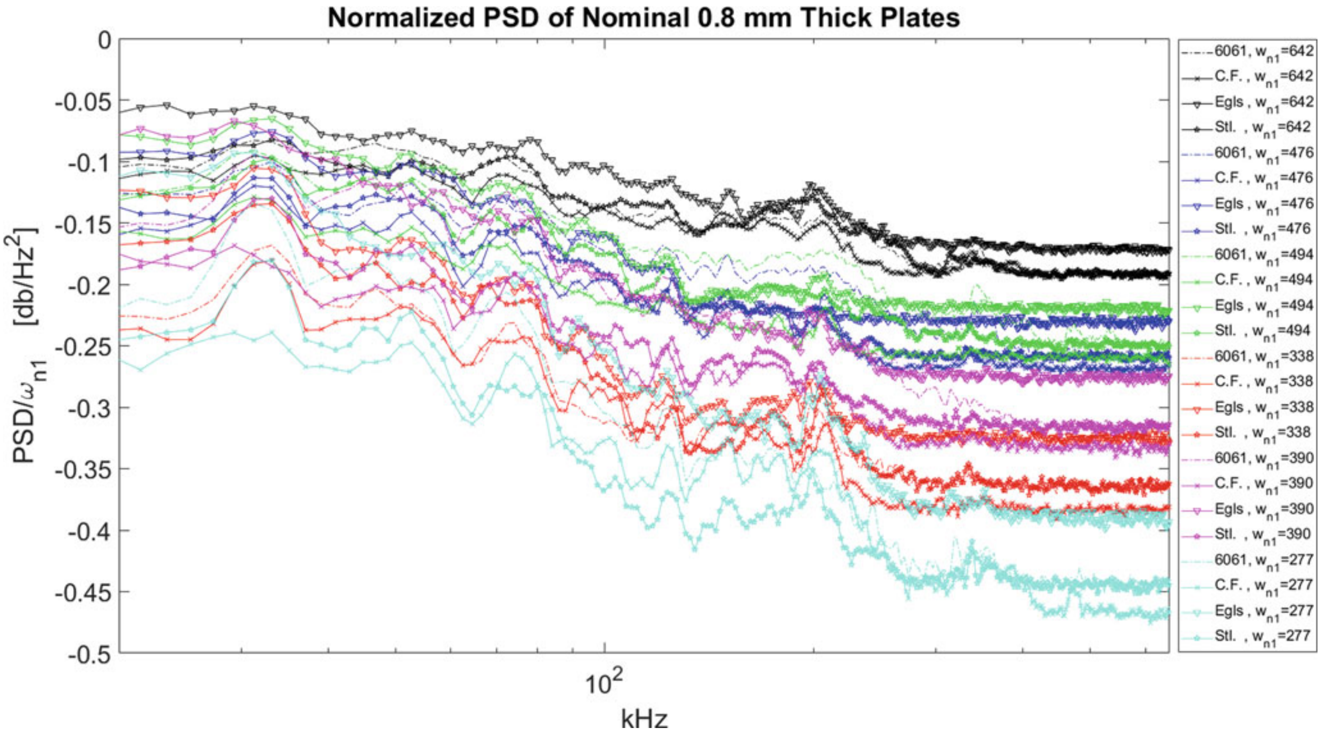

Fig. 12.3 Normalized PSD for all impactors generating guided waves on the 0.8 mm thick (nominal) plates

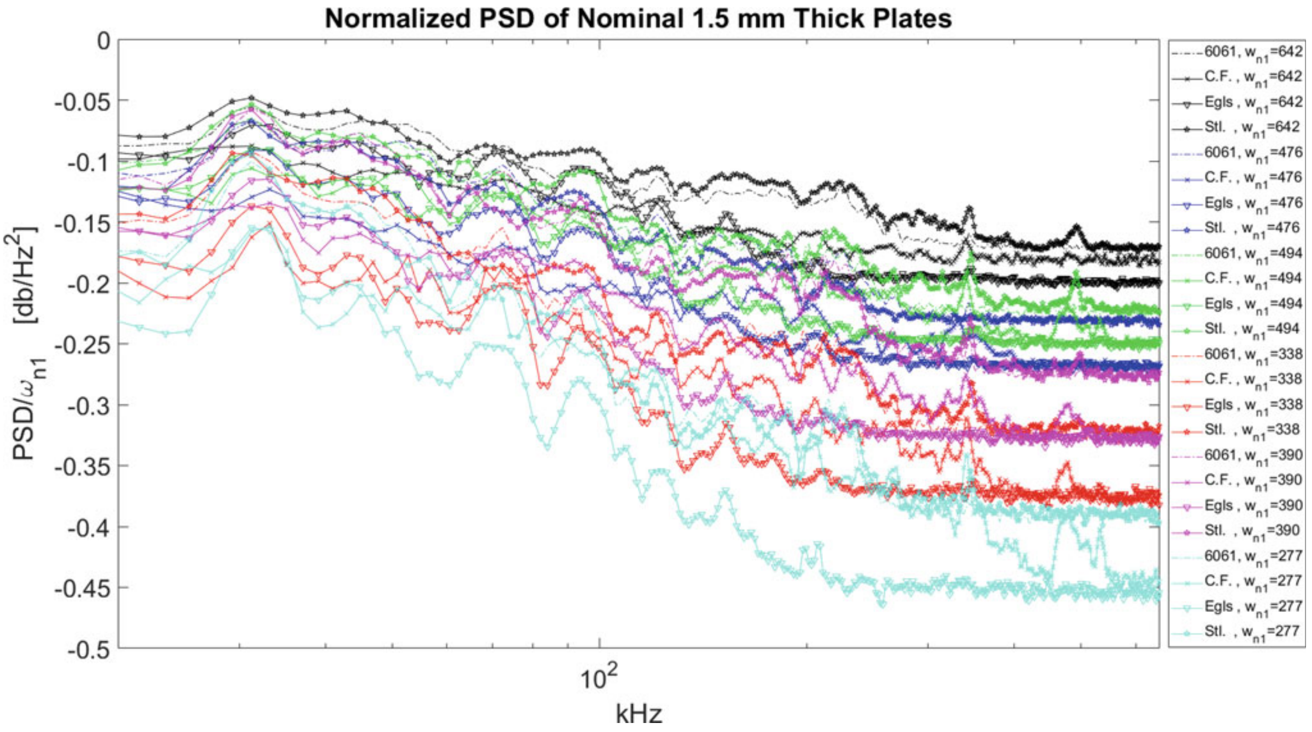

Fig. 12.4 Normalized PSD for all impactors generating guided waves on the 1.5 mm thick (nominal) plates

abbreviation of the waveguide material type together with the accompanying mini impactor first natural frequency. Each mini impactor type (different natural frequencies) is grouped by color and varying line symbols.

The nominally 0.8 mm thickness plates show strong frequency response to 350 kHz, before turning into white noise dominated power content.

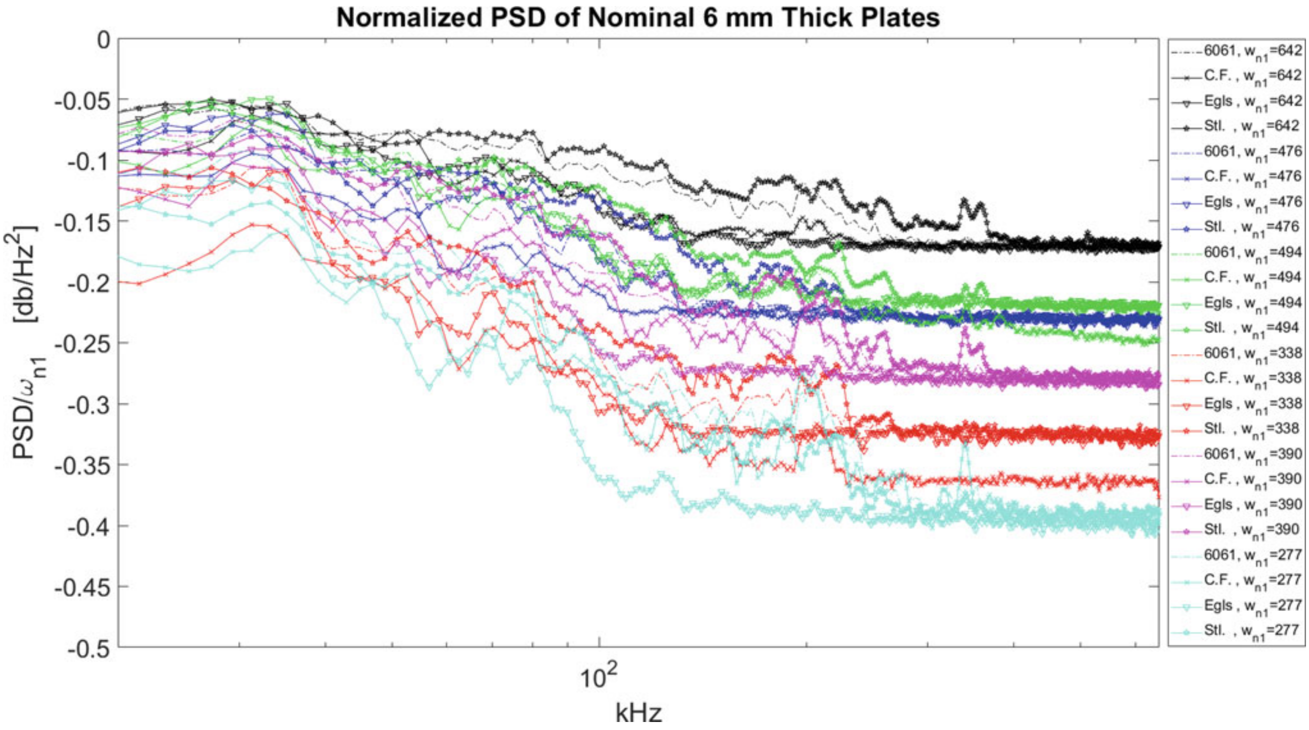

Fig. 12.5 Normalized PSD for all impactors generating guided waves on the 6 mm thick (nominal) plates

The steel and carbon fiber plates of nominally 1.5 mm thickness show strong power density up to approximately 500 kHz, whereas the 6061-T6 and 7781 EGlass power density does not have significant content beyond 400 kHz.

In general, the non-steel 6 mm thickness plates did transmit significant power beyond 250 kHz. The exception being carbon fiber plate excited by the 8 ply, 89 mm long beam.

12.3.2 *Simulation Results*

To ensure that the modeling of the mini impactor-induced UGW were performed accurately, the 4 ply, 38 mm length beam impacting the 0.8 mm thick aluminum plate was modeled. The experimental timeseries responses are shown and overlaid with the corresponding FEA simulation in Fig. 12.6. Of major importance was identifying if the wave packets characterized by the longitudinal and shear stress waves were passing by the first sensors location at the expected time.

The triggering mechanism employed during physical experimentation allowed the alignment of the signals. This known zero became a common zero between simulations and experiments. The significance of Fig. 12.6 indicates that both stress wave packets are arriving on time. These simulations are ongoing, and the future goal is to extend this capability to accurately capture the UGW behavior in general composite plates for various mini impactor types.

12.4 Conclusion

In general, presence of damage compromises an aerospace structure. Nondestructive evaluation is necessary to assess non-visible damage to aircraft, with respect to their damage tolerance. Damage exceeding the aircraft's allowable limit (dictated by FAA Advisory Circular 20-107B guidelines) [5] must be detected, evaluated, and repaired. Transmission of UGW across potentially damaged laminates can be used for damage detection and characterization. A novel impactor device has been created and parameterized to identify the operable domain within common aerospace composite materials. Plotting the PSD of all the plates excited by all the beams was initially performed, then normalized by each respective beams first natural frequency producing a normalized, mean PSD figure. Looking at expected frequency characteristics observed the

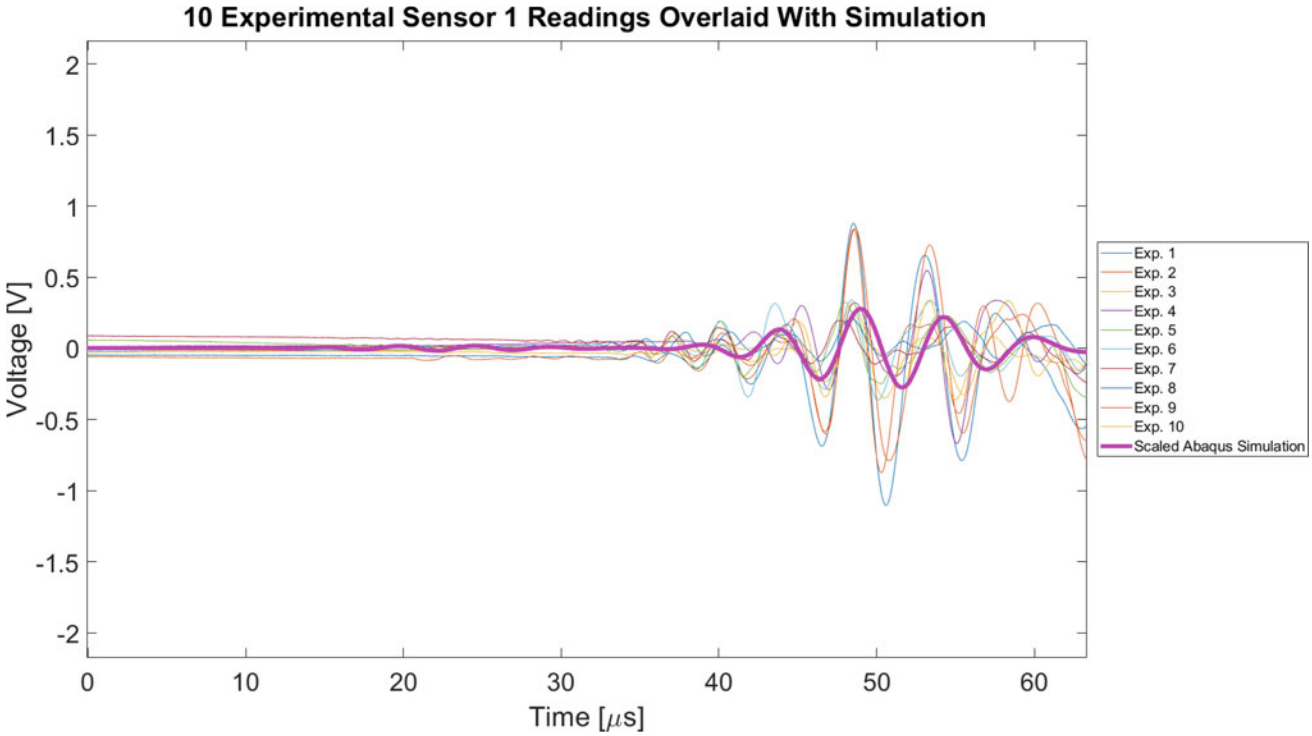

Fig. 12.6 Experimental timeseries transducer readings at 100 mm from the impact location overlaid with the scaled Abaqus nodal displacement estimates

R15s transfer functions identified by Ono et al. [3], the mini impactor is a suitable excitation source. From the waveguide perspective, all the beams excited steel commonly across all waveguide thicknesses. The 1.5 mm thick carbon fiber plate had a common power response 100–200 kHz more than that of the 0.8 and 6 mm thick plates. E-Glass plates attenuated the transmitted ultrasonic guided waves, and this is realized by the absence of power at the higher frequencies.

References

1. Halvorsen, W.G., Brown, D.L.: Impulse technique for structural frequency response testing. Sound Vib. **11**(11), 8–21 (1977)
2. Capriotti, M., et al.: Non-destructive inspection of impact damage in composite aircraft panels by ultrasonic guided waves and statistical processing. Materials. **10**(6), 616 (2017)
3. Ono, K., Cho, H., Matsuo, T.: Transfer functions of acoustic emission sensors. J. Acoust. Emission. **26**, 72–90 (2008)
4. ABAQUS: ABAQUS Analysis User's Manual, Version 6.13, Dassault Systemes Simulia Corp (2013)
5. Federal Aviation Administration: Composite aircraft structure. Advisory Circular (AC) 20-107B, Change 1, 2010. https://www.faa.gov/documentLibrary/media/Advisory_Circular/AC20-107B.pdf

Chapter 13
Effect of Impact Velocity on Dynamic Response of Polymeric Foams

Vijendra Gupta, Chizoba Onwuka, Addis Kidane, and Michael Sutton

Abstract The deformation characteristics of polymeric foams, when subjected to high-speed impacts are highly dependent on the impact velocity. At low impact velocities, the deformation is homogeneous. In contrast, at high impact velocities, the deformation is highly localized with the occurrence of progressive cell crushing initiated from the impact end. This leads to a "shock wave" like propagation of the deformation. In this study, the dynamic deformation behavior of a low-density rigid polyurethane foam material is investigated through high-speed impact experiments. Cylindrical polycarbonate projectiles are fired on the foam specimens at velocities ranging from 40 m/s to 120 m/s using a gas gun setup. The images of the deforming specimen are captured with a high-speed camera and processed using digital image correlation to obtain full-field deformation. It is shown through experiments that the deformation behavior at high impact velocities is significantly different from the response at low impact velocities. It is found that the strain behind the shock front significantly increases with the impact velocity.

Key words Critical velocity · Shock strength · Rigid polyurethane · Shock response · Digital image correlation

13.1 Introduction

Polymeric foams, belonging to the class of cellular foam materials, have remarkable impact resistance and energy absorption capability under high-speed impacts [1]. This is due to their distinct deformation behavior when subjected to high impact velocities. The material compacts locally near the impact end, and this compaction is propagated in the direction of the impact [2]. This leads to high energy absorption and low force transmission to the supporting structure. The mechanism of deformation is governed by the mesoscale structure of the foam that consists of a congregation of cells with connected faces. It is also dependent on the material properties of the cell wall material. Particularly, in rigid polymer foams, the cells collapse through brittle fracture mechanism at high loading rates [3]. Unlike shock in dense solids, shock in cellular materials is usually concerned with the structural collapse of cells in a sequential manner. The critical velocity of shock initiation is used to categorize the high impact velocity response (or shock mode) and the low impact velocity response (or transitional mode) [4]. The literature for the dynamic behavior of cellular materials in compression has been reviewed in detail in [5]. Extensive numerical studies have also been done to understand the dynamic behavior of foam. The microstructure is typically modeled using a Voronoi diagram in finite element analysis to study the dynamic response of foam [6–8]. The shock response of open-celled aluminum foam was examined using direct impact experiments [9]. More recently, an experimental study investigated the compaction wave propagation in polymeric foams using high-speed digital image correlation (DIC) [10]. The experimental studies, however, are limited and demand more attention.

In the present study, our objective is to examine the effect of impact velocity on the nature of the deformation using impact experiments. This study will guide in understanding the dynamic deformation features in polyurethane foam. Furthermore, it will help in the design of foam material for high-speed impact applications. To this end, the full-field response is obtained with the help of DIC and a high-speed camera. Specifically, the strain fields are studied to understand the fundamental difference in response at low and high impact velocities.

V. Gupta (✉) · C. Onwuka · A. Kidane · M. Sutton
Department of Mechanical Engineering, University of South Carolina, Columbia, SC, USA
e-mail: vijendra@email.sc.edu

S. Mates, V. Eliasson (eds.), *Dynamic Behavior of Materials, Volume 1*, Conference Proceedings of the Society for Experimental Mechanics Series, https://doi.org/10.1007/978-3-030-86562-7_13

13.2 Materials and Methods

Foam specimens were cut from a LAST-A-FOAM® FR-7106 rigid polyurethane foam board obtained from General Plastics Manufacturing Company. Cuboid specimens of 30 × 14 × 12.8 mm^3 were machined using an end mill cutter on a vertical milling machine. The specimen surface with the largest surface area was speckled using commercially available spray paints to get a sharp contrast coat for DIC. The specimen photographed before and after speckling is inset in Fig. 13.1. The foam specimens were prepared from the same batch of foam boards that were used in our previous study [11]. Thus, the actual measured density of 93.3 kg/m^3 for the foam was taken from the previous study. The nominal density specified as 96 kg/m^3 by the manufacturer differed only slightly from the actual density. The relative density was obtained to be 7.8% from the density of the parent material taken to be 1200 kg/m^3.

The schematic of the experimental setup is shown in Fig. 13.1. The specimen is impacted with cylindrical polycarbonate projectile accelerated using a gas gun setup. The impact velocities exercised in the experiments are mentioned in Table 13.1. The right end of the specimen is held stationary using rigid support. A lithium-based grease is used to hold the specimen in place on the rigid support while also helping to reduce the friction. The grease is also applied to the impact end of the specimen for the same purpose. The projectile velocity attained just before impact is measured using a laser emitter and detector setup. A pair of vent holes on the barrel is used to allow a laser beam to pass through them. Then, the average velocity of the projectile before impact is computed by knowing the time and distance traveled between the projectile crossing the laser beam and striking the specimen. The time when the projectile crosses the laser beam is recorded using a digital oscilloscope (not shown in the figure) whereas the time when the projectile impacts the specimen is acquired from the camera that is triggered using the same oscilloscope. The images are captured using HPV-X2, a high-speed camera from Shimadzu. Different framing rates are used depending on the impact velocity and are given in Table 13.1. High-speed imaging stipulates high-intensity light due to a limitation on exposure time. Hence, a high flash power lamp supplied from Photogenic Professional Lighting is used to illuminate the specimen in synchronization with the camera.

The captured images were processed using VIC-2D from Correlated Solutions Inc. to extract the full-field deformation in the specimen. Based on the speckle size, the subset size and step size were taken to be 25 and 2, respectively. An incremental

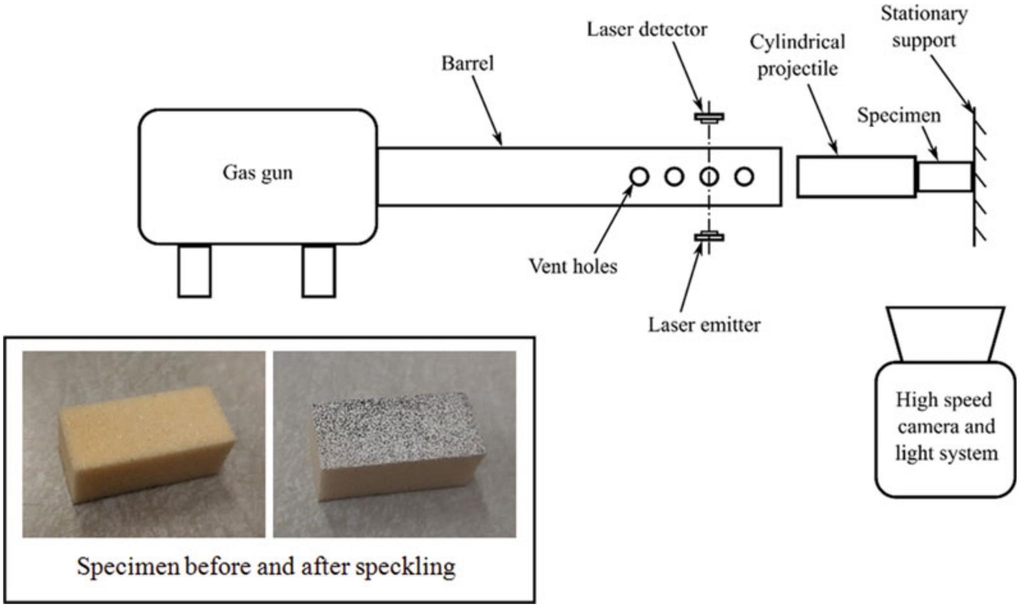

Fig. 13.1 Schematic of the experimental setup and specimen photographs

Table 13.1 Framing rates

Impact velocity (m/s)	Framing rate (10^3 frames/s)
41	100
60	100
79	200
116	500

correlation was employed to address the excessive deformation seen in the specimen. Zero-normalized squared differences correlation criterion was used to nullify the effect caused due to slight changes in the lighting conditions. The deformation in the specimen is expected to be predominantly uniaxial if the heterogeneity because of variations in the cell geometry at the mesoscale is ignored. The effects of wave reflections from the top and bottom surfaces of the specimen were also considered to be negligible. Thus, the two-dimensional field data obtained from DIC were averaged along Y-direction to focus on the uniaxial deformation features. Note that the data on the boundaries of the specimen surface is unavailable due to the finite size of the subset used in DIC.

13.3 Results and Discussion

The axial strain (e_{xx}) contour plots corresponding to different impact velocities are shown in Fig. 13.2. As mentioned before, the data on thin strips (<2 mm) on either end of the specimen is not available. The strain response at an impact velocity of 116 m/s is noticeably different from the response at 41 m/s. However, a gradual transition in response is seen at the intermediate impact velocities of 60 m/s and 79 m/s. At an impact velocity of 41 m/s, the strain remains low in the beginning period with high strains observed in isolation at multiple locations at a later period. The mesoscale structure can be used to

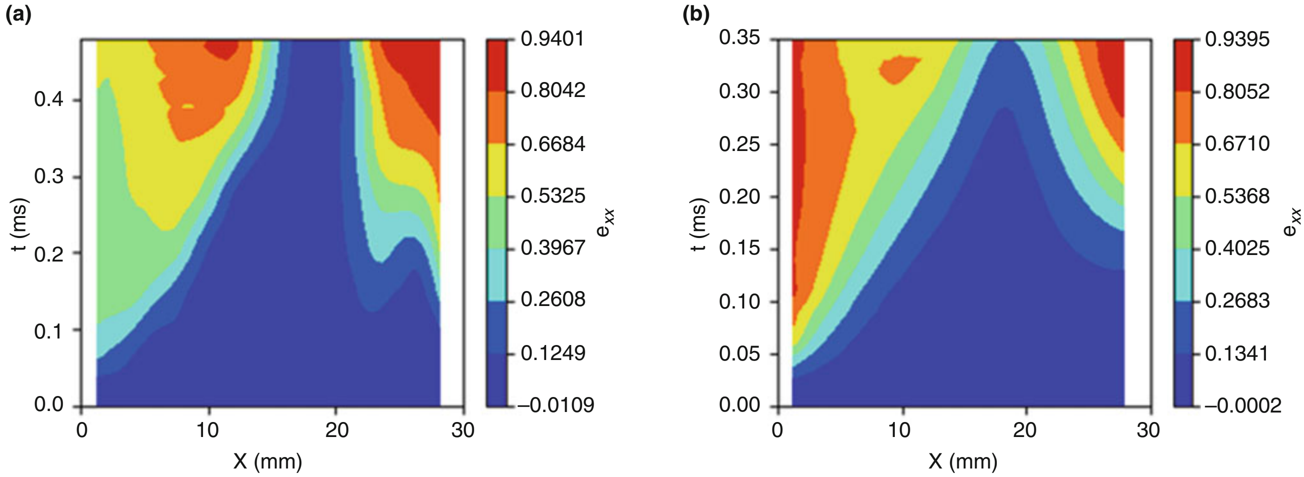

impact velocity = 41 m/s

impact velocity = 60 m/s

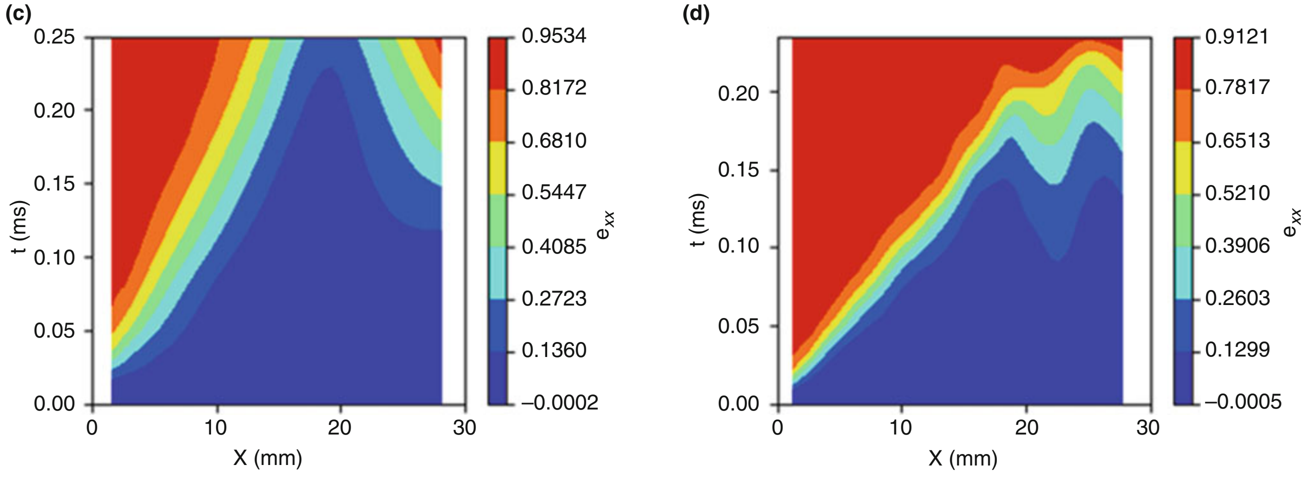

impact velocity = 79 m/s

impact velocity = 116 m/s

Fig. 13.2 Axial strain contour plots at various impact velocities. (**a**) impact velocity = 41 m/s. (**b**) impact velocity = 60 m/s. (**c**) impact velocity = 79 m/s. (**d**) impact velocity = 116 m/s explain this phenomenon. High strains are caused due to the collapse of weaker bands of cells in the specimen. However, the overall magnitude of strain does not increase beyond 80% until about 0.35 ms. At an impact velocity of 116 m/s, high strains exceeding 80% are observed at about 0.03 ms but only near the impact end while the strain remains low in the rest of the specimen. This is because of the sequential crushing of cells initiated from the impact end. This results in a "shock wave"-like propagation. Interestingly, at all impact velocities, deformation tends to localize at the ends of the specimen. It is possibly due to the crushing of open boundary cells that are comparatively weaker than the interior cells that are mostly closed and connected to other cells.

Figure 13.3 shows the evolution of spatial profiles of axial strain and particle velocity in the beginning period of deformation for the impact velocity of 116 m/s. The shock wave propagation is evident in both Fig. 13.3a, b. The strain ahead of the shock is relatively low as compared to the strain behind the shock. On the other hand, though the particle velocity ahead of shock is low compared to the velocity behind the shock, it is not close to zero. This is reasonable as the material is stiffer in the beginning period of the linear elastic region, and the material exhibits lower strains and higher stresses. Therefore, particle velocities are a little high as they are proportional to stresses in elastic waves. To study further, the time (t^*), when the particle velocity at the left end reaches the imposed impact velocity of 116 m/s, is determined. It is assumed that at this time the shock is fully developed. As seen in Fig. 13.3b, the particle velocity at the left end reaches the impact velocity of 116 m/s at 40 μs and remains at that level afterwards.

The strain evolution from 40 μs to 200 μs is shown in Fig. 13.4. It is observed that the strong shock, in the beginning, weakens later. The strain ahead of the shock increases and the development of strain localization is observed. The beginning and the end of the shock front are located to compute the average value of strain behind and ahead of the shock. These

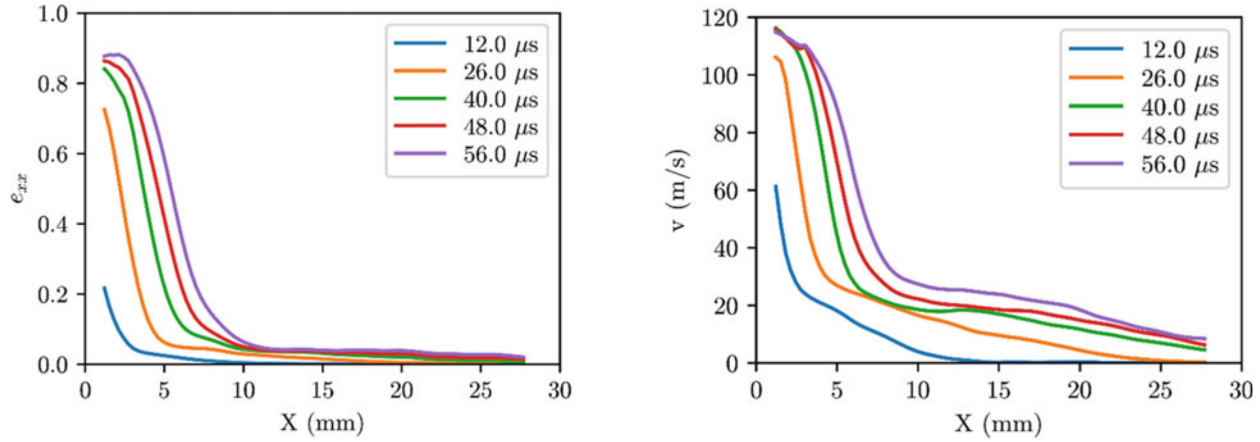

Fig. 13.3 Spatial profile of (**a**) axial strain and (**b**) particle velocity corresponding to impact velocity of 116 m/s in the beginning period

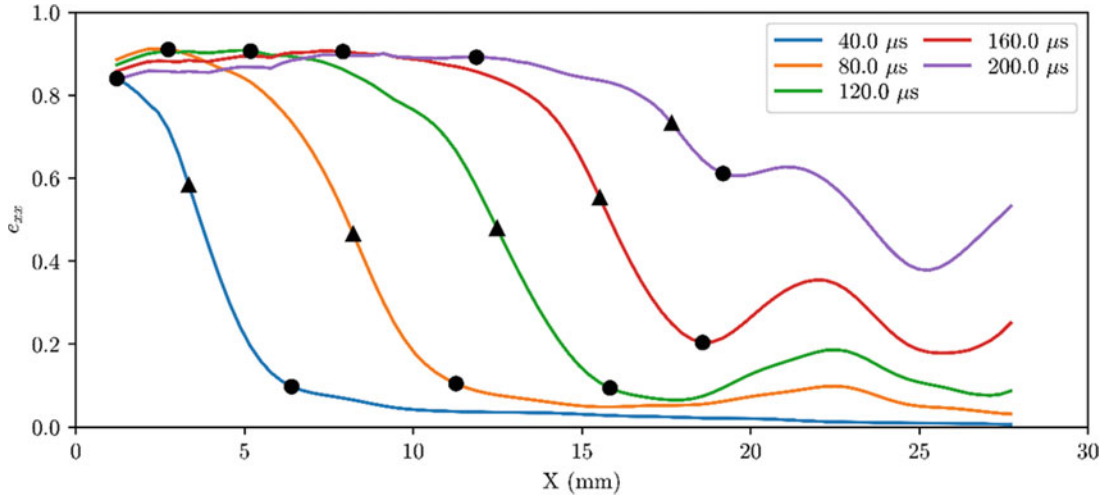

Fig. 13.4 Spatial axial strain profile corresponding to impact velocity of 116 m/s

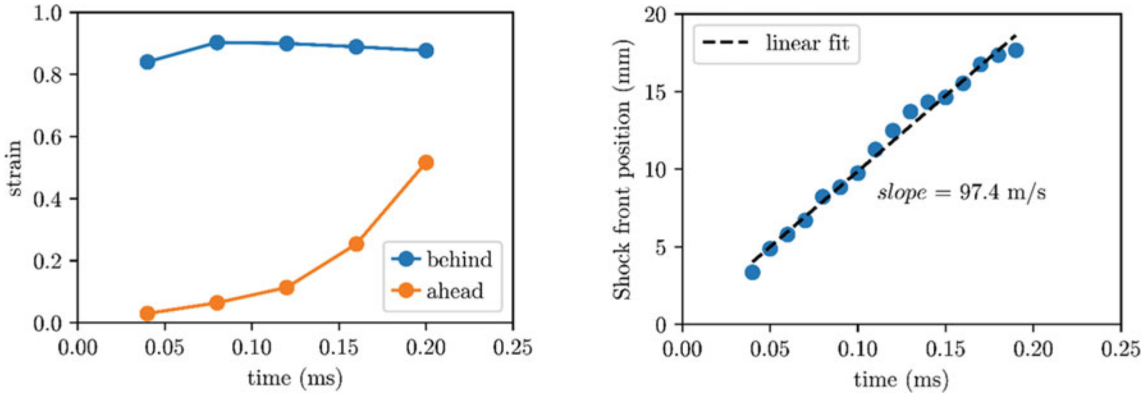

Fig. 13.5 (**a**) Average strain behind and ahead of shock front corresponding to impact velocity of 116 m/s and (**b**) Lagrangian shock position with time

Fig. 13.6 Variation of average strain behind and ahead of shock front with impact velocity

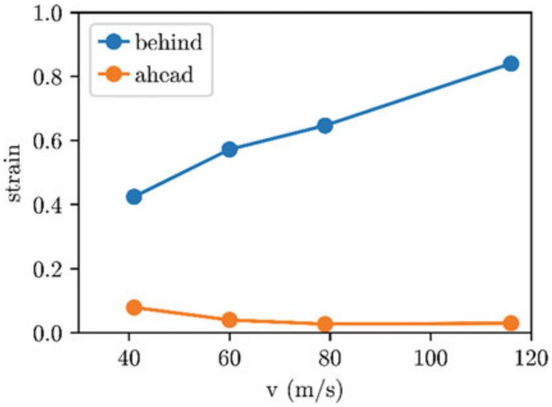

locations are highlighted using solid black circles in the figure. The shock front location is also estimated by finding the location corresponding to $\max|\partial e_{xx}/\partial X|$ and is shown in the figure using solid triangles.

The average value of the strain behind and ahead of the shock is shown in Fig. 13.5a. It is seen that the average strain ahead of the shock front increases significantly beyond 0.12 ms. This is likely because of multiple reflections of elastic waves between the shock front and the stationary support. On the other hand, the average value of strain behind the shock front roughly stays constant. The shock front position in undeformed coordinates is shown in Fig. 13.5b. The Lagrangian shock velocity (V_s) is computed to be 97 m/s from the slope of the data. The shock velocity can be obtained from continuum-based shock theory [12] and is given by the following equation:

$$V_s = \frac{V_i}{e_b} \tag{13.1}$$

where V_i is the impact velocity and e_b is the strain behind the shock. Considering the average value of strain behind the shock between 0.04 ms and 0.2 ms as 0.882 from Fig. 13.5a, V_s can be calculated as 132 m/s. This value is relatively higher than the 97 m/s obtained from the experiments. The primary cause for this is the disintegration of material while getting crushed by the projectile. Material fragmentation invalidates the fundamental assumption of mass conservation in continuum-based shock models.

To compare the strains behind and ahead of shock at different velocities, time, t^*, is identified for all the impact velocities. As previously explained, this is the time when the particle velocity reaches the impact velocity. Figure 13.6 shows the variation of average value of strain behind and ahead of shock front with impact velocity. It is seen that strain behind the shock increases sharply with impact velocity but the decrease in strain ahead of the shock is insignificant. This is because of a larger jump in strain resulting from a stronger shock associated with higher impact velocity.

13.4 Conclusions

The effect of impact velocity on the deformation response of a low-density polyurethane foam is explored in this study. It is shown that the deformation characteristics significantly differ depending on the magnitude of impact velocity. It is observed that the average strain behind the shock front substantially increases with the impact velocity. It is also observed that even at high impact velocities the average strain ahead of the shock front can increase appreciably over time. The theoretical shock velocity over predicted the shock velocity computed from the experiments because of assumptions in continuum-based shock models. Impact experiments done with the specimen in confinement will have better agreement with shock theory since the conservation of mass is obeyed.

Acknowledgments The funding from the US Army Research Office via grant W911NF-18-1-0023 is gratefully acknowledged.

Appendix

The axial strain referred in this chapter is the engineering strain. This strain should not be confused with the component of the Lagrangian strain tensor. The axial Lagrangian strain component (E_{11}) can be obtained from engineering strain (e_{xx}) by using the following equation:

$$e_{xx} = 1 - \sqrt{(1 + 2E_{11})} \tag{13.A.1}$$

It is noteworthy that e_{xx} is considered positive in compression.

References

1. Gibson, L.J., Ashby, M.F.: Cellular Solids: Structure and Properties, Second edn. Cambridge University Press, New York (1997)
2. Tan, P.J., Reid, S.R., Harrigan, J.J., Zou, Z., Li, S.: Dynamic compressive strength properties of aluminium foams. Part I - experimental data and observations. J. Mech. Phys. Solids. **53**(10), 2174–2205 (2005). https://doi.org/10.1016/j.jmps.2005.05.007
3. Koohbor, B., Ravindran, S., Kidane, A.: Effects of cell-wall instability and local failure on the response of closed-cell polymeric foams subjected to dynamic loading. Mech. Mater. **116**, 67–76 (2018). https://doi.org/10.1016/j.mechmat.2017.03.017
4. Zheng, Z., Liu, Y., Yu, J., Reid, S.R.: Dynamic crushing of cellular materials: continuum-based wave models for the transitional and shock modes. Int. J. Impact Eng. **42**, 66–79 (2012). https://doi.org/10.1016/j.ijimpeng.2011.09.009
5. Y. Sun and Q. M. Li, "Dynamic compressive behaviour of cellular materials: A review of phenomenon, mechanism and modelling," *Int. J. Impact Eng.*, vol. 112, no. pp. 74–115, 2018, doi: https://doi.org/10.1016/j.ijimpeng.2017.10.006
6. Ajdari, A., Nayeb-Hashemi, H., Vaziri, A.: Dynamic crushing and energy absorption of regular, irregular and functionally graded cellular structures. Int. J. Solids Struct. **48**(3–4), 506–516 (2011). https://doi.org/10.1016/j.ijsolstr.2010.10.018
7. Wang, S., Ding, Y., Wang, C., Zheng, Z., Yu, J.: Dynamic material parameters of closed-cell foams under high-velocity impact. Int. J. Impact Eng. **99**, 111–121 (2017). https://doi.org/10.1016/j.ijimpeng.2016.09.013
8. Gupta, V., Miller, D., Kidane, A.: Numerical and Experimental Investigation of Density Graded Foams Subjected to Impact Loading, pp. 31–35 (2020). https://doi.org/10.1007/978-3-030-30021-0_6
9. Barnes, A.T., Ravi-Chandar, K., Kyriakides, S., Gaitanaros, S.: Dynamic crushing of aluminum foams: part i - experiments. Int. J. Solids Struct. **51**(9), 1631–1645 (2014). https://doi.org/10.1016/j.ijsolstr.2013.11.019
10. Ravindran, S., Koohbor, B., Malchow, P., Kidane, A.: Experimental characterization of compaction wave propagation in cellular polymers. Int. J. Solids Struct. **139–140**, 270–282 (2018). https://doi.org/10.1016/j.ijsolstr.2018.02.003
11. V. Gupta, D. Miller, A. Kidane, and M. Sutton, "Optimization for Improved Energy Absorption and the Effect of Density Gradation in Cellular Materials," 2021. https://doi.org/10.1007/978-3-030-59765-8_4
12. Zheng, Z., Wang, C., Yu, J., Reid, S.R., Harrigan, J.J.: Dynamic stress-strain states for metal foams using a 3D cellular model. J. Mech. Phys. Solids. **72**, 93–114 (2014). https://doi.org/10.1016/j.jmps.2014.07.013

Chapter 14
The Form and Function of the Kolsky Bar for Dynamic Three-Point Bending

Shane Paulson, Cody Kirk, Jinling Gao, and Wayne Chen

Abstract With a wide variety of applications, fiber-reinforced plastic composite materials experience a wide range of loading conditions which span the entire spectrum of strain rates. Patch repairs on roadways and bridges experience long-term fatigue and environmental loading. Such repair jobs can experience pure compressive or tensile stresses, while others experience large shear and bending stresses. The same is true for composite armors, which can experience high-velocity piercing impact events or large-scale blast pressures. With such a variety of conditions, experimental methods must have the capability to replicate these conditions. The three-point bending test is one of the standard methods for evaluating the flexural performance of a material or structure at quasi-static loading rates. The adaptation of this standard method to high loading rates requires a careful balance of replicating standard geometries and simplifying the data reduction process. The current study employs a custom shaped loading bar attached to the end of the incident bar in a conventional Kolsky bar apparatus. This loading bar transitions the incident bar geometry from a circular cross-section to that of a superellipse. This end shape evenly distributes the applied load across the width of the beam sample, while minimizing the reflections of the incident wave prior to contact with the bar-sample interface. To evaluate this geometry, beam samples were cast using Pro-Set INF114 epoxy resin. This method was evaluated with a bar-end velocity of 4 m/s, and a comparison was made between the superellipse shape and an unchanged bar geometry. For each case, the strain signals, local damage, and global failure modes were compared.

Key words Dynamic behavior · Adhesive · Interface · Fracture

14.1 Introduction

The growth of the composite materials industry has resulted in a cornucopia of applications for these novel materials. While a carbon fiber composite material was once used only for high-end military or sporting equipment, such materials can now be found in phone cases and automotive components. With this rapid growth in use comes a more diverse profile of loading conditions. The performance of a material under a given condition can be as trivial as the protection of a consumer cell phone or as critical as major structural repair in buildings and bridges.

For simple loading conditions, it is often simple to obtain a stress–strain relation for a material for a range of strain rates, from creep and quasi-static to impact and shock loads. Techniques such as the split-Hopkinson pressure bar, or Kolsky bar, have vastly simplified this process for uniaxial compression and tension [1]. However, the simplicity of the Kolsky bar is built around a uniaxial load condition and simple 1-D wave propagation [1]. If the bending properties of a material are to be evaluated at a high strain rate, these simplifications cause some issues for the experimenter.

For quasi-static evaluation, ASTM has long-used standards for three-point bending. These standards can be found for a wide variety of materials, including fiber-reinforced composite materials [2]. In these standards, the loading device is shaped to provide a uniform load distribution across the width of a beam sample, which most often results in a rectangular footprint on the sample. This gives the first roadblock when implementing a three-point bend condition with a Kolsky bar, as cylindrical bars are used for their simple analysis and implementation. The goal of this work is to examine this geometric issue in order to simplify the use of the Kolsky bar in three-point bending.

S. Paulson (✉) · C. Kirk · J. Gao
Department of Aeronautics and Astronautics Engineering, College of Engineering, Purdue University, West Lafayette, IN, USA
e-mail: paulsons@purdue.edu

W. Chen
Department of Aeronautics and Astronautics Engineering, College of Engineering, Purdue University, West Lafayette, IN, USA

Department of Materials Engineering, College of Engineering, Purdue University, West Lafayette, IN, USA

S. Mates, V. Eliasson (eds.), *Dynamic Behavior of Materials, Volume 1*, Conference Proceedings of the Society for Experimental Mechanics Series, https://doi.org/10.1007/978-3-030-86562-7_14

14.2 Methodology

When using a Kolsky bar for impact experiments, careful attention must always be paid to the mathematics of wave propagation, even in 1-D experiments. For traditional compression experiments, this process is quite simple, and the stresses and strains in the sample can be calculated rather easily [1]. If a square or rectangular loading footprint is desired; however, there will be some change in geometry required between the end of an incident bar and a three-point bending sample. With this change in geometry comes added complexity to account for the added interfaces which contribute to more wave reflections in the incident bar and the device used to make this change in shape.

For this work, a modified Kolsky bar system was used, composed of a striker bar (19.00 mm diameter, 610 mm length), incident bar (19.00 mm diameter, 3.67 m length), and a transmission bar (19.00 mm diameter, 1.83 m length). Each bar was composed of 7075-T6 aluminum. The incident bar was modified with a female ½″-20 thread, 25 mm deep, and the transmission bar was modified with a male ½″-20 thread, 19 mm long. A supporting structure was machined from 7075-T6 aluminum, with dimensions shown in Fig. 14.1, and was attached to the transmission bar.

At the incident bar end, two loading devices were machined from 7075-T6 aluminum. The first device provided a baseline and was machined to a 19.00 mm diameter to match the incident bar and a length of 75 mm. This control device ensures minimal wave reflections and dispersion by matching the incident bar geometry. The second device is a prototype for a constant impedance loading bar. This prototype makes use of the superellipse geometry to generate a smooth transition from a circular cross-section to a nearly square cross-section. This device has a circular section at the threaded end with a length of 15 mm. After this circular section is a transition region, with a length of 50 mm. In this transition region, the cross-section maintains a constant area while changing into a superellipse shape. Lastly, the device has a third superellipse region with a constant cross-section over a length of 10 mm.

This superellipse geometry was generated using Eq. (14.1). In this equation, n determines the order of the superellipse, where the special case $n = 2$ generates a circle with radius r. For this study, the final shape is a superellipse with an order of 20. For a constant impedance, a constant cross-sectional area is required. The area of a superellipse defined by Eq. 1 can be found using Eq. 2. By setting a constant area constraint, the radius of the superellipse can be found using Eq. (14.2). For the transition region, Eq. (14.3) was used to vary the order of the superellipse shape through the length of the region. Here, the order varies along the length of the region, z, with its maximum value of $L = 50$. In Eq. (14.3), n_m denotes the maximum order of the superellipse.

$$x^n + y^n = r^n \tag{14.1}$$

$$A = \frac{4^{1-\frac{1}{n}} \cdot r^2 \cdot \sqrt{\pi} \cdot \Gamma\left(1 + \frac{1}{n}\right)}{\Gamma\left(\frac{1}{2} + \frac{1}{n}\right)} \tag{14.2}$$

$$n(z) = \frac{2 - n_m}{2} \cdot \cos\frac{z\pi}{L} + \left(\frac{n_m - 2}{2} + 2\right) \tag{14.3}$$

These loading devices were used for three-point bending of epoxy beam samples. Samples were made of Pro-Set INF114 epoxy resin (16.48 mm width, 11.37 mm height, and 59.18 mm length). The sample configuration is shown in Fig. 14.2 below with the control loading device attached to the incident bar. The superellipse device is shown attached to the incident bar in Fig. 14.3.

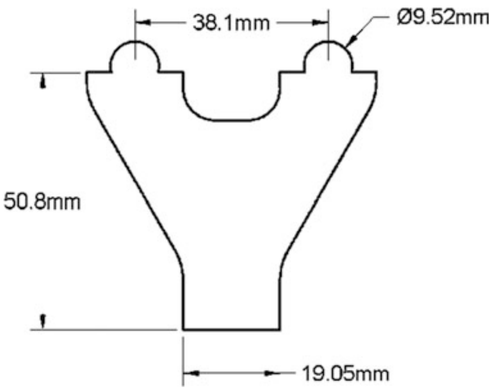

Fig. 14.1 Three-point bending support device

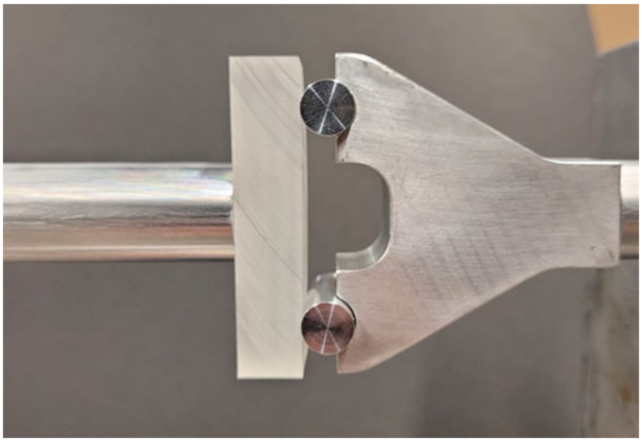

Fig. 14.2 Three-point bending configuration with control loading device

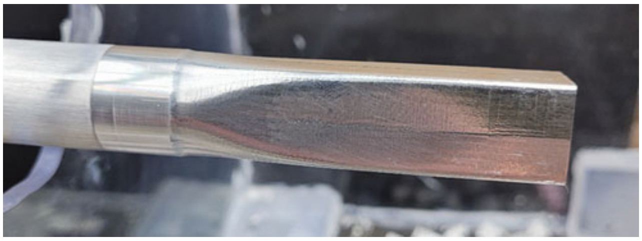

Fig. 14.3 Constant impedance superellipse loading device

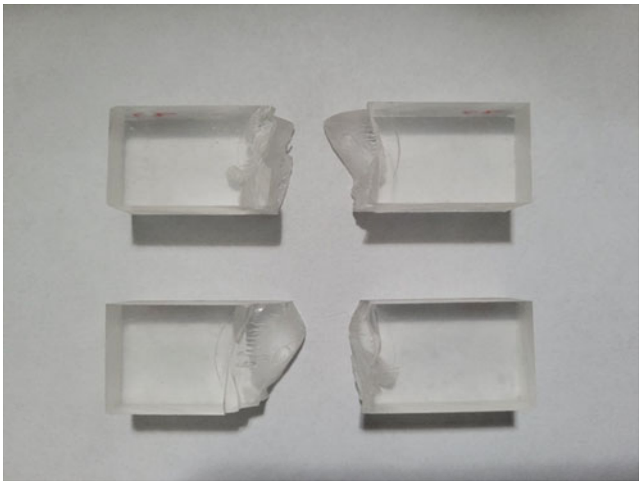

Fig. 14.4 Epoxy samples after impact from control loading device

14.3 Results

Three epoxy beam samples were impacted with each loading device, and their conditions after impact were noted. Two broken samples from the control group are shown in Fig. 14.4, and two broken samples from the superellipse group are shown in Fig. 14.5. From a visual inspection, there is no clear difference in the mode of failure between the two groups of samples. In the images provided, there are clear marks from the loading device visible on the sample surface. These marks give a clear indication of the area subjected to the impact load, which is dependent entirely on the shape of the loading device used.

Fig. 14.5 Epoxy samples after impact from prototype loading device

14.4 Conclusion

This preliminary study designed a prototype loading device to be used for three-point bending experiments using a Kolsky bar. This device was designed and manufactured for a constant 1-D impedance and compared with a cylindrical loading device. When used to impact epoxy beam samples, the two loading devices did not produce an obvious difference in failure mode in the samples. The samples did exhibit clear marks left by the loading device, indicating the shape of the load applied to the sample. Additional experimentation is necessary to further evaluate sample failure modes as well as the wave propagation in the prototype loading device.

Acknowledgments The authors would like to thank their colleagues from the Impact Science Laboratory at Purdue University for their assistance and support in understanding and improving this work.

References

1. Chen, W., Song, B.: Split Hopkinson (Kolsky) Bar Design, Testing and Applications. Springer, New York (2011)
2. ASTM: Standard C393, Standard Test Method for Core Shear Properties of Sandwich Constructions by Beam Flexure. ASTM International, West Conshohocken, PA (2016). https://doi.org/10.1520/C0393_C0393M-16

Chapter 15
Additional Study of the Explosively Driven Expanding Ring Tension Test

Brady Aydelotte, Paul Hibner, B. Daniel Brown, William Fuger, Colter Angell, and Warren Jones

Abstract The explosively driven expanding ring tension test is a method for loading a sample ring of material in dynamic tension that avoids some issues associated with other dynamic tension methods. In this work, we build on previously reported work and our own modeling and simulation efforts to improve the geometry and material selection for the driver and the explosive. We modeled two of the many geometric variables in the explosively driven expanding ring test: charge size and buffer ring geometry. We tested two different explosives and several different heat treatments. Through our modeling efforts, we found larger buffer rings increased sample ring velocity. Testing revealed that the maraging 350 steel drivers required careful heat treatment or driver failure during the test would result. Some additional candidate driver materials, 300M and HY 100, are examined and appear to be reasonable alternatives.

Key words Tension · Dynamic · Explosive · Strength · High Strain Rate

15.1 Introduction

Dynamic materials property characterization is important for automotive safety, shock mitigation, and other areas. Many dynamic materials characterization techniques such as the Split Hopkinson Pressure Bar [1] or shock compression [2] measure properties in compression or where the initial load is applied in compression, such as in shock-induced spallation [3]. A number of tension-based techniques have been developed based on the Hopkinson bar as well [1]. These techniques are popular and well established but suffer from difficulties due to the dispersive nature of elastic-plastic waves and their low velocity in uniaxial stress loading conditions.

An alternative, or perhaps supplement, to these approaches is the explosively driven expanding ring tension test, where symmetric expansion can avoid some wave propagation issues. The expanding ring tension test is also advantageous because it allows large plastic strains. This method was proposed by Johnson, Stein, and Davis [4], who used explosives to place a sample ring into tension. Their approach was further developed by Perrone [5] and Hoggatt and Recht [6]. Warnes et al. [7] utilized VISAR [8] to measure the ring surface velocity, a major improvement which avoided some of the data reduction problems experienced previously. Warnes et al. [9] developed an improved experimental geometry and explored the effect of shock hardening.

In this work, we continue prior efforts [10] to explore different configurations of this experiment. Aydelotte [10] developed an experimental configuration derived from Warnes et al. [7] which resulted in a similar experimental geometry to that shown in Warnes et al. [9]. We used hydrocode modeling to explore using different heights of buffer rings to dampen vibration in the sample ring and studied two different explosive column heights. In addition to the modeling, we built and fired multiple test articles. Fracture of the drivers led us to examine different heat treatments of maraging 350 steel and to vary the charge. We also explored two additional material choices for the driver 300M and HY 100.

B. Aydelotte (✉) · P. Hibner · B. D. Brown · W. Fuger · C. Angell · W. Jones
Idaho National Laboratory, Idaho Falls, ID, USA
e-mail: brady.aydelotte@inl.gov

S. Mates, V. Eliasson (eds.), *Dynamic Behavior of Materials, Volume 1*, Conference Proceedings of the Society for Experimental Mechanics Series, https://doi.org/10.1007/978-3-030-86562-7_15

15.2 Modeling and Simulation Setup and Results

We explored two issues via modeling and simulation: the height of buffer rings above and below the sample ring and the length of the explosive column.

Following Aydelotte [10], we used the ALEGRA hydrocode [11] to conduct 2D axisymmetric simulations. The Johnson Cook strength and fracture models [12] were used for all materials except the copper tube and maraging 350 steel driver, which were modeled using the Steinberg-Guinan-Lund [13] constitutive model and the Johnson Cook fracture model. The sleeve containing the explosive was modeled as acrylic. The sample and buffer rings were modeled as OFHC copper. Element size was held constant at 0.125 mm on an edge.

A Jones-Wilkins-Lee [11] equation of state model was used to model the explosive C4; no strength model was used. Sesame tables, provided with the ALEGRA distribution, were used for equations of state for the other materials except the acrylic which was modeled using a Mie-Grüneisen [11] equation of state. Model constants were taken from the provided library of values. Please consult the ALEGRA [11] documentation for further details.

An example of one simulation geometry is shown in Fig. 15.1. The motion of the sample ring was driven by the detonation of a small column of explosives in the center of the geometry. A shockwave passes through the explosive sleeve, the air, the copper tube, the steel driver, and then the sample ring, imparting a radial velocity.

We studied the effect of buffer ring size by modeling buffer rings from 1 mm to 6 mm tall, in 1 mm increments. The sample ring was modeled as 1.5 mm tall and 1.5 mm thick and the charge was 20 mm tall with an outer diameter (OD) of 15.88 mm. The ring internal diameter (ID) was fixed at 50.8 mm. The copper tube thickness was kept constant at 1.651 mm. The results of this study are displayed in Fig. 15.2a.

The model predicted that adding side buffer rings increased the radial ring velocity. Generally, increasing buffer ring height increased ring velocity. All buffer ring heights reduced the time between the initial velocity spike and the steady deceleration phase of the ring expansion, where stress and strain data can be readily extracted.

We also examined the effect of two different explosive column heights, 20 mm and 40 mm for 6 mm tall buffer rings and 1.5 mm × 1.5 mm sample ring. Initial experiments showed that 40 mm tall explosive columns ruptured the Cu tubes, so we

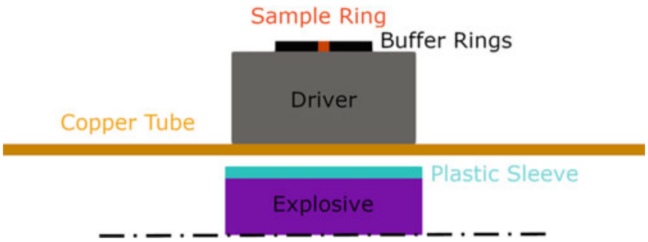

Fig. 15.1 A representative modeling geometry, with the center line at the bottom of the image. The copper tube is intended to direct explosive gases laterally. The explosive drives a load into the driver which transmits the load to the sample ring (sandwiched between two buffer rings of the same material), propelling it radially outward. In this figure, the direction the sample ring moves is upward. The explosive is detonated from both left and right simultaneously at the center line

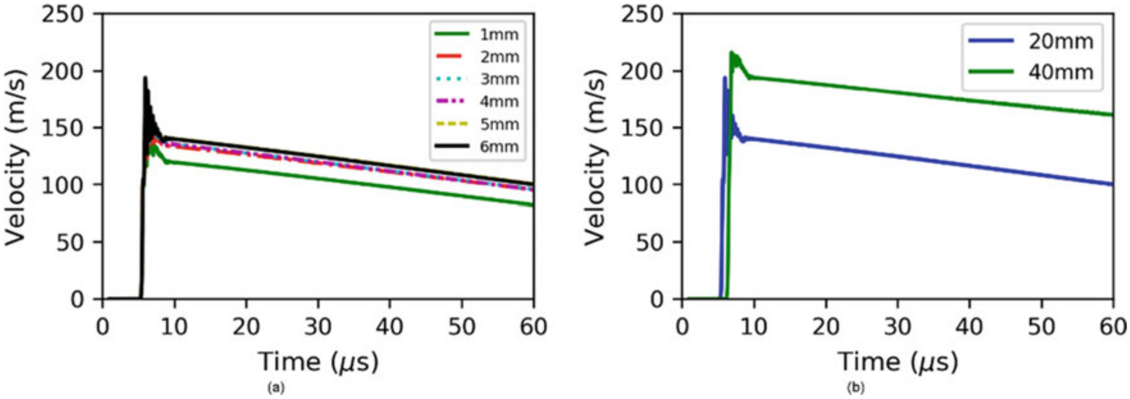

Fig. 15.2 (**a**) The effect of different buffer ring heights. (**b**) The effect of an explosive column of the same diameter but two different heights

explored using 20 mm tall explosive columns. The results are shown in Fig. 15.2b. Reducing the explosive column volume by half did not halve the ring velocity.

15.3 Experimental Setup and Results

We constructed several sample experimental setups following Fig. 15.3. The first attempts involved aging the maraging 350 steel drivers for 4 h at 493 C and cooling the samples on a wire rack in air to achieve maximum strength. We used commercial-grade 25.4 mm OD, 22.23 mm ID copper 122 tubing. Explosive charges of different sizes and compositions were hand-packed into an acrylic tube which was centered within the assembly using machined foam inserts, which also positioned the detonators. The explosive train consisted of one Teledyne RP-1 exploding bridgewire detonator on either side of the explosive column and C4 or Primasheet 1000 explosive. The charges were detonated with an FS-17 firing set. Unfortunately, our PDV was not available for use with these tests. The initial tests were proof-of-concept tests only.

We found that three of four drivers ruptured when in this heat treatment as shown in Fig. 15.4. Reducing the charge length in shot 3 fractured the driver but preserved the sample ring, which developed at least 5 necks and an average engineering strain of 0.1. Changing to Primasheet 1000 and reducing the diameter of the charge prevented the driver from failing and resulted in a sample ring with at least 4 necks and an average engineering strain of 0.09.

To identify a better heat treatment for the maraging 350 steel drivers, we aged the drivers in 1 h increments and found that the as-received and the driver aged 1 h exhibited no external damage when subjected to the force applied by Primasheet 1000 charges 20 mm × 15.88 mm OD in size, see Table 15.1. The driver aged 2 h fractured, though the driver aged 3 h did not. It was decided to utilize as-received maraging 350 steel drivers with no additional heat treatment.

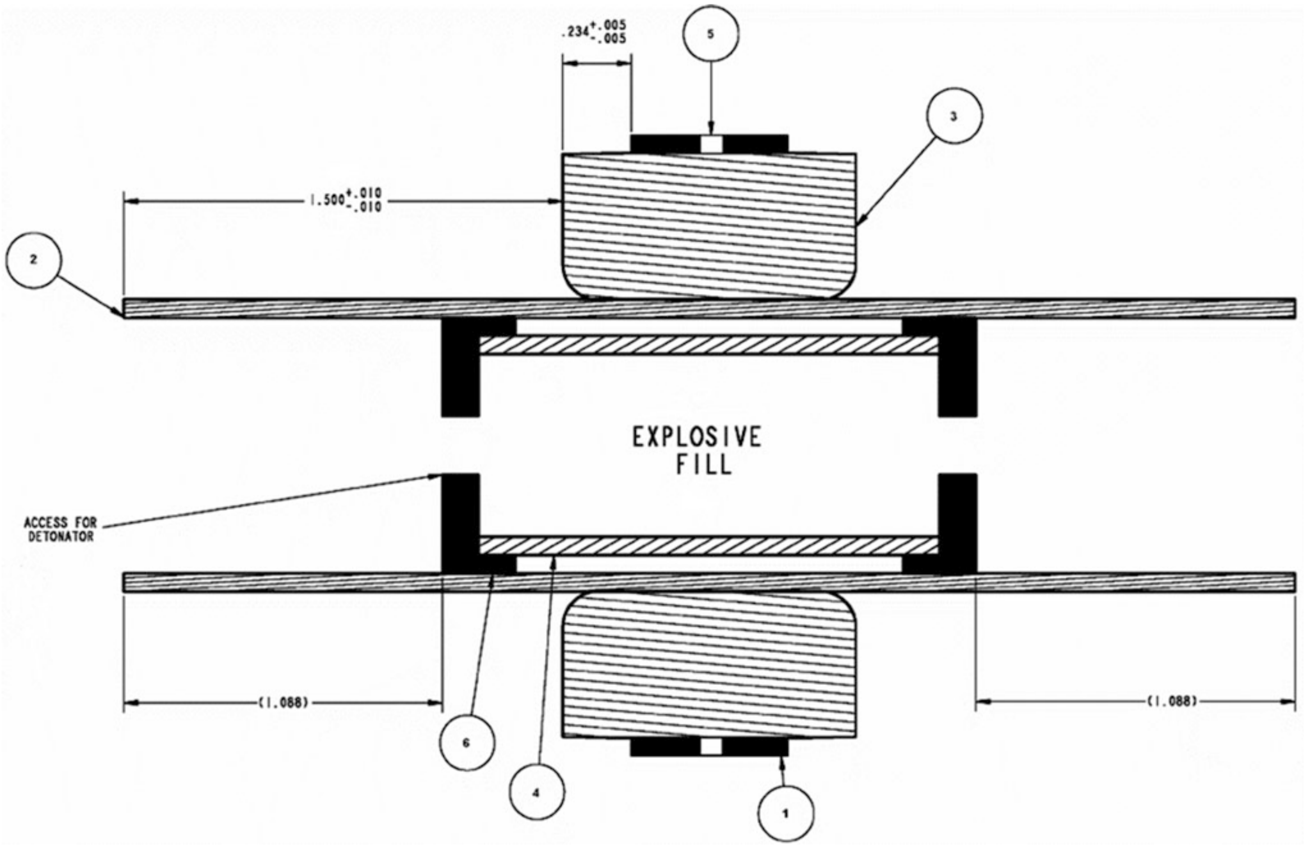

Fig. 15.3 A diagram example of the experimental assembly for the expanding ring experiment. (1) Buffer rings, (2) Copper tube, (3) maraging 350 steel driver, (4) Plastic tube, (5) Sample ring, (6) Foam caps to position the explosive and detonators

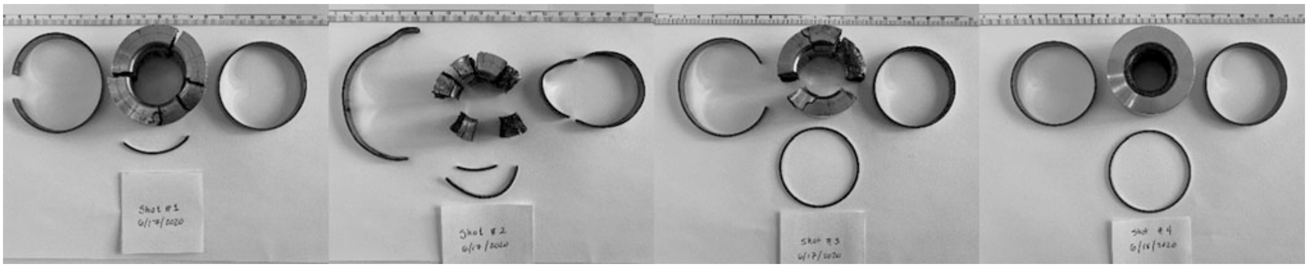

Fig. 15.4 Results of our first proof-of-concept tests. The drivers fractured in three of four cases

Table 15.1 Charge sizes and composition for proof-of-concept tests

	Shot 1	Shot 2	Shot 3	Shot 4
Charge size (mm)	40.0 × 15.88 OD	40.0 × 15.88 OD	27.3 × 15.88 OD	40.0 × 12.7 OD
Explosive	C4	C4	C4	Primasheet 1000

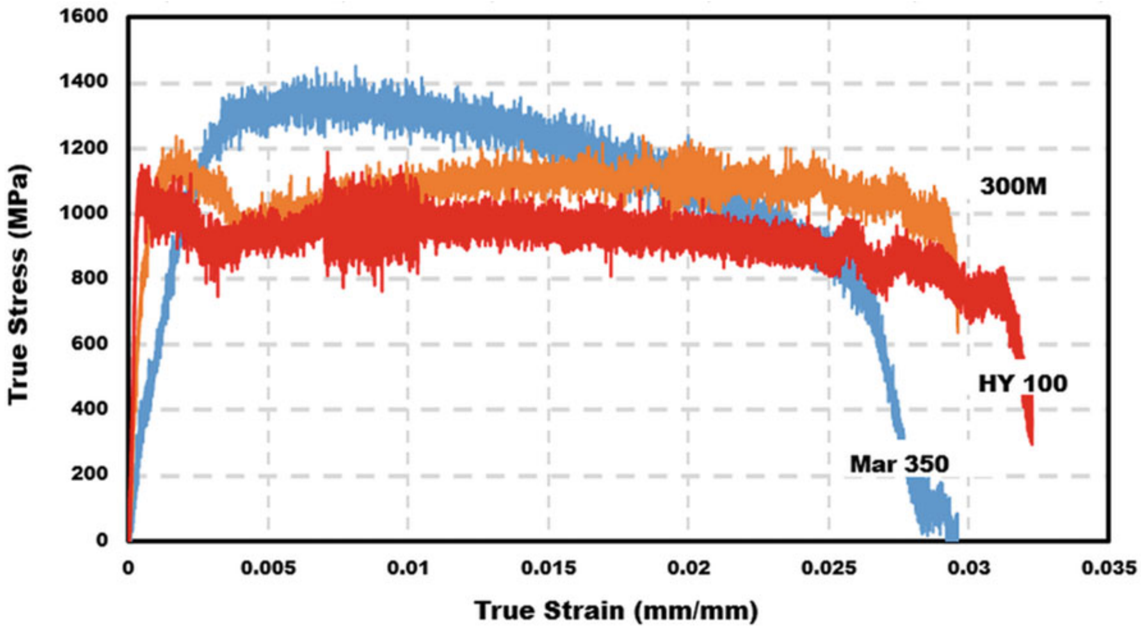

Fig. 15.5 Tension data for two alternate candidate materials for the driver ring

In addition to maraging 350 steel, a number of other steel alloys appear to be suitable for use in the driver. Tensile Split Hopkinson Pressure Bar data for as-received 300M, HY 100, and maraging 350 steel are shown in Fig. 15.5. In their as-received condition, 300M and HY 100 both exhibited similar strength and ductility to solution-annealed maraging 350 steel.

15.4 Conclusion

The explosively driven variant of the expanding ring tension test was introduced by Johnson et al. [4] in 1963. While not without limitations, this test has utility in testing materials in tension, particularly at high strain rates that Split Hopkinson Pressure bars typically have difficulty reaching without very small samples, and where uniaxial strain spall strength may not provide the desired information. We examined two of the many geometric variables in the explosively driven expanding ring test: charge size and buffer ring geometry. Each of these can influence the ring velocity. This study found that the buffer rings should be present and that their height should be greater than the sample ring; however, any height buffer ring appears to be better than none at all.

We also found that the driver material required sufficient ductility to function properly and tolerate the loading from the explosives. We achieved acceptable results using solution-annealed maraging 350 steel drivers. It appears that some other high strength steels would work as well.

Acknowledgments We would like to acknowledge a grant of time on the INL HPC systems, the assistance of the ALEGRA development team at Sandia National Laboratory, and the staff who operate the INL National Security Test Range. The views and opinions expressed herein do not necessarily state or reflect those of the US Government or any agency thereof.

References

1. Gama, B.A., Lopatnikov, S.L., Gillespie Jr., J.W.: Hopkinson bar experimental technique: a critical review. Appl. Mech. Rev. **57**(4), 223–250 (2004). https://doi.org/10.1115/1.1704626
2. Marsh, S.P. (ed.): LASL Shock Hugoniot Data. University of California Press, Berkely/Los Angeles, CA (1980)
3. Antoun, T., Seaman, L., Curran, D.R., Kanel, G.I., Razorenov, S.V., Utkin, A.V.: *Spall Fracture*, 1st edn. Springer, New York (2003)
4. Johnson, P., Stein, B., Davis, R.: Measurement of dynamic plastic flow properties under uniform stress. Presented at the Symposium on Dynamic Behavior of Materials, 1963
5. Perrone, N.: On the use of the ring test for determining rate-sensitive material constants. Exp. Mech. **8**(5), 232–236 (May 1968). https://doi.org/10.1007/BF02326281
6. Hoggatt, C.R., Recht, R.F.: Stress-strain data obtained at high rates using an expanding ring. Exp. Mech. **9**(10), 441–448 (Oct. 1969). https://doi.org/10.1007/BF02410405
7. Warnes, R.H., Duffey, T.A., Karpp, R.R., Carden, A.E.: An improved technique for determining dynamic material properties using the expanding ring. In: Meyers, M.A., Murr, L.E. (eds.) Shock Waves and High-Strain-Rate Phenomena in Metals: Concepts and Applications, pp. 23–36. Springer US, Boston, MA (1981)
8. Barker, L.M.: Laser interferometer for measuring high velocities of any reflecting surface. *J. Appl. Phys.* **43**(11), 4669 (1972). https://doi.org/10.1063/1.1660986
9. Warnes, R.H., Karpp, R.R., Follansbee, P.S.: The freely expanding ring test - a test to determine material strength at high strain rates. *J. Phys. Colloq.* **46**(C5), C5–583–C5–590 (1985). https://doi.org/10.1051/jphyscol:1985575
10. Aydelotte, B.B.: Analysis of the explosively driven expanding ring tension test. In: Dynamic Behavior of Materials (2021)
11. Bova, S.W., et al.: ALEGRA User Manual. Sandia National Laboratory, Albuquerque, NM, SAND2020-DRAFT (2020)
12. Johnson, G.R., Holmquist, T.J.: Test Data and Computational Strength and Fracture Model Constants for 23 Materials Subjected to Large Strains, High Strain Rates, and High Temperatures. Los Alamos National Lab, Los Alamos, NM, Technical LA-11463-MS (1988)
13. Steinberg, D.J., Lund, C.M.: A constitutive model for strain rates from 10–4 to 106 s−1. *J. Appl. Phys.* **65**(4), 1528 (1989). https://doi.org/10.1063/1.342968

Chapter 16

Ballistic Performance Evaluation of Carbon Graphite Foam (CGF) and Nanoparticle-Kevlar (SNK) Composites Using Compressed-Air Guns

Muhammad Ali Bablu and James M. Manimala

Abstract Owing to their exceptional thermal and mechanical properties, materials such as Carbon Graphite Foam (CGF) and silica Nanoparticle-Treated Kevlar (SNK) are of interest in many multifunctional applications. It is therefore desirable to evaluate their ballistic performance in comparison to baseline foams or untreated Kevlar, for instance. In this study, we evaluate CGF and SNK composite samples using compressed-air guns (CAG). Two CAGs are used in this study, a large-bore (2.5″) and a small-bore (0.357″) CAG. Firstly, an improved analytical model was developed to predict the projectile's velocities for the CAGs. This Loss-Compensated Model (LCM) builds upon existing analytical models such as the Adiabatic, Lagrange, and the Pidduck and Kent models by incorporating clearance leakage, improved surface friction, and air drag effects. The CAGs were calibrated using projectiles of multiple weights in order to establish the cylinder pressure versus projectile velocity characteristics. Velocity measurement was accomplished using a high-speed camera. Correlation with predictions from analytical models demonstrates that the LCM gives excellent agreement with the high-speed camera (HSC) measurements in comparison to the other models. For CAGs with a higher degree of losses due to projectile or barrel imperfections, the LCM provides a significant improvement in projectile velocity prediction. After achieving confidence on velocity measurement by HSC via LCM model, ballistic tests are performed on CGF and SNK. CGF composite samples were constructed from modular foam blocks with aluminum face sheets bonded together using an epoxy adhesive. Baseline aluminum foam composite samples were also constructed using the same procedure. For the SNK samples, a multistep treatment process was established that allows for a more uniform distribution of the nanoparticle in the fabric. Neat Kevlar K745 fabric was considered as the baseline. 10%, 30%, and 40% by weight of silica nanoparticle addition using an 80–100 nm particle size, water-based colloidal solution were considered for the SNK samples. Multiple samples were made and tested for the same test case. Both non-penetrative and penetrative test cases were considered. For the CGF, the depth of backing signature measurement as per NIJ Standard 0101.06 is considered as the performance parameter. A plasticine clay witness block was used as the backing material. For the SNK testing, the projectile's kinetic energy reduction is used as the performance metric as per NIJ Standard 0108.01. Custom boundary fixtures were constructed, and consistent sample holding procedures were implemented to minimize any influence of boundary imperfections. The test and baseline samples were evaluated under the same conditions for all cases. The results show that the CGF composite absorbs nearly double the amount of energy as the baseline aluminum foam composite. The failure mode and mechanisms were identified and contrasted using high-speed camera footage. For the SNK cases, it was seen that the addition of nanoparticles improved the fabric's ballistic performance by providing a 20% mass advantage (due to three less layers) for the 40 wt.% SNK vis-à-vis neat Kevlar for the non-penetrative case. This improvement in specific ballistic performance is attributable to the enhanced frictional mechanisms and shear rigidity for SNK fabric. In conjunction with current additive and hybrid fabrication processes, materials such as CGF and SNK present strong potential to enable multifunctional structural solutions for emerging engineering challenges.

Key words Ballistics · Modeling · Nano-silica · Kevlar · Carbon graphite foam

Nomenclature

μ_k	Coefficient of kinetic friction
γ	Ratio of specific heats
ρ	Density of air

M. A. Bablu (✉) · J. M. Manimala
Oklahoma State University, Stillwater, OK, USA
e-mail: mbablu@okstate.edu

S. Mates, V. Eliasson (eds.), *Dynamic Behavior of Materials, Volume 1*, Conference Proceedings of the Society for Experimental Mechanics Series, https://doi.org/10.1007/978-3-030-86562-7_16

i	The cross-sectional area of the barrel
A_b	Considered equal area of breech and bore
A_c	Cross-sectional area of cylinder
A_e	Effective area of release for air
A_l	Leakage area
a_0	Speed of sound in a gas
$\widetilde{a}_0$	Non-dimensional factor
C	Coefficient of flow
c_d	Coefficient of drag
f	Frictional force
G	Mass of the gas
KE_f	Kinetic energy lost due to friction
KE_g	Kinetic energy of gas
KE_l	Kinetic energy lost due to gas leakage
KE_p	Kinetic energy of projectile
L	Length of the barrel
L_b	Breach length
L_c	Length of the cylinder
L_e	Effective length
m	Mass of the projectile
$\dot{m}_{\mathrm{out}}$	Rate of decrease in mass
$\dot{m}_{\mathrm{flux}}$	Outward mass flux
M	Molar mass
$\dot{M}_l$	Leakage mass flow rate
P	Pressure acting on the projectile
P_0	Average pressure
P_f	Final pressure
P_i	Initial pressure
R	Ideal gas constant
S	Surface bounded by gas volume
T	Temperature
t	Time taken for expansion of gas
v	Velocity of the projectile
v_i	Initial velocity of the projectile
v_r	Residual velocity of the projectile
V	Volume behind the projectile containing gas
V_c	Volume of the container
V_f	Final volume of compressed air
V_i	Initial volume of compressed air
$\dot{V}_{li}$	Initial volumetric flow rate of gas leakage
$\dot{V}_{lf}$	Volumetric flow rate of gas leakage
$\dot{\Lambda}_{xg}$	Outward volume flux per unit area in the direction of the barrel axis
W_d	Work done against air drag
W_f	Work done against friction
W_g	Pressure work done by gas on projectile
x	Distance traveled by projectile
$\bar{x}_p$	Non-dimensional gun barrel length (P_0AL/ma_0^2)
x_g	Length of barrel behind the projectile at any time

16.1 Introduction

In practice, compressed-air or gas-guns which are used for ballistic evaluation of structural materials can exhibit various losses not captured by classical velocity-pressure models [1, 2]. Building upon the classical models, an improved model for the prediction of the projectile's velocity as a function of the cylinder pressure could be developed by accounting for the common mechanisms of losses in compressed-air/gas-guns. Such a Loss Compensated Model (LCM) is of interest in developing simple methodologies for analysis in various application scenarios.

Ballistic characteristics for two hybrid structural composites—carbon graphite foam composites and silica nanoparticle-treated Kevlar fabric composites with potential multifunctional applications are examined via impact tests using compressed-air guns. Carbon Graphite Foam (CGF) is a composite foam of graphitized carbon and various inorganic additives that have excellent performance in challenging applications in either wet or dry conditions. Because of their particular combination of characteristics [3, 4], like having high thermal conductivity, low coefficient of thermal expansion, high electrical conductivity, high strength at elevated temperatures, chemical resistance, oxidation resistance, lightweight, and relatively inexpensive, CGF is being considered for several different applications instead of metallic foam. Moreover, their thermal and mechanical properties can be tailored by controlling the graphitization process [5]. According to their microstructure, metal foams may undergo major deformations at almost constant, the so-called plateau stress [6, 7]. That is why, metal foams are used as energy absorbers in the case of ballistic impacts and blast loading in the form of space debris shields [8], claddings [9], and armor systems for automotive, military, and civilian structures [10, 11]. Mainly, aluminum foam core fiber-metal sandwich structures are being used because of their higher perforation energy than the same non-foam core composites [12]. Hou et al. [13] investigated the ballistic performance of closed-cell aluminum foam core metallic sandwich structures as an energy absorber to shield the impact and found out that higher foam core offers higher ballistic limit. Hanssen et al. [14] carried out tests on open-cell aluminum foams. In studies and numerical simulations of bird strikes on sandwich panels, they illustrated the beneficial effect of aluminum foam core sandwich panels. Destefanis et al. [8] examined open-cell aluminum foam composite sandwich plates, Kevlar, and high-strength aluminum alloy face sheets to use them as a Whipple shield against the thread of high-speed space debris impacts on manned spacecraft. Aluminum foam as the core for sandwich panels with aluminum face sheets guarantees good lightweight strength, rigidity, and ballistic output. However, the metal foam has some limitations in a highly corrosive, heated environment, and it is comparatively more expensive. CGF could potentially provide an alternative to metal foams as a ballistic protection material in certain multifunctional applications. In the first part of this study, a comparative investigation of ballistic performance between CGF and mass equivalent aluminum foam (ALF) composites is carried out using a Large Bore Compressed-Air Gun (LBG). The LBG used for this experiment is a one-stage light-gas gun. It has a charge chamber, an inlet valve to admit a charge of compressed air to the charge chamber, and a barrel, which communicates at its breech end with the charge chamber via a quick-release valve-like system based on a perforated piston when the gun is fired.

In the next part of this study, the improvement of Kevlar fabric's ballistic performance resulting from the addition of silica nanoparticles is investigated using a Small Bore Compressed-Air Gun (SBG). There have been extensive studies on the performance enhancement of various kinds of lightweight personal armor and protective structures. Aramid fabrics such as Kevlar play a crucial role in making modern protective structures and armor systems much more lightweight and better performing than previous versions. High strength to weight ratio, improved mobility, environment resistance, and high impact strength are the main reasons for applying fiber-based material for armor applications. Under high-velocity projectile impact, several ballistic tears arise in woven fabrics such as Kevlar due to strain or localized compressive loading and yarn uncurling, followed by fiber plastic deformation and breakage [15–17]. At comparatively lower velocities of projectiles, fabric damage is mainly attributed to yarn pull out [18]. The performance of the ballistic fabric is affected by the type of weave and fibers [19], boundary conditions [20], inter-yarn friction [21–23], fabric-projectile friction, and projectile's geometry [20] among which inter-yarn friction plays a key role [24]. The aforementioned studies indicate that the higher the inter-yarn friction, the higher the capacity of energy absorption and thus the superior the ballistic performance is. This has motivated the treatment of Kevlar with shear thickness fluids to enhance the friction of the yarns during impact [25, 26]. Previously, considerable research has been done on stab resistance and ballistic performance of Shear Thickening Fluid (STF) impregnated fabric composites. Khodadadi et al. [27] used high-velocity impact tests to study the behavior of two and four layers of neat and STF/Kevlar composites containing 15 to 45 wt.% of Nano-Silica in a polyethylene glycol (PEG) medium. It was concluded that the impregnation process increases the amount of energy absorbed by the Kevlar and for an optimum amount of loading, energy absorption is maximized. Dong et al. [28] investigated the effect of nano-silica impregnation on the mechanical properties of Kevlar, showing that a dry nano-silica impregnation process increases the friction between adjacent and cross yarns. Thus, the nanoparticle impregnated Kevlar can withstand a much higher loading and displays better shear rigidity [28]. Depending on the fineness of the weave versus the projectile size, failure under transverse deformation due to yarn breakage is also possible

[28, 29]. Several layers of Kevlar fabric are usually used to achieve improved ballistic protection in soft body armor. The primary goal of evaluating Silica Nanoparticle-Treated Kevlar (SNK) is to examine their potential to deliver better specific ballistic performance and to understand the mechanisms involved. In conjunction with current additive and hybrid fabrication processes, materials such as CGF and SNK present strong potential to enable multifunctional structural solutions for emerging engineering challenges.

16.2 Theoretical Model

16.2.1 Classical Models

There are several classical pressure-velocity models [27] to predict the muzzle (or exit) velocity of a projectile fired from a compressed-gas gun. These models are useful to estimate the velocity of the projectile for impact test scenarios. In this study, the newly developed Loss-Compensated Model (LCM) is compared against existing models as well as experiments. Most of the existing models assume an ideal gas relation so that gas properties remain uniform both behind the sabot of the projectile and throughout its progression through the breech and barrel.

The Isobaric model, which is also the simplest of the models, is first among the models considered. In this model, the pressure behind the projectile is deemed constant [1, 2]. According to this model, the projectile's velocity is

$$v = \sqrt{\frac{2L(P_iA - f)}{m}} \tag{16.1}$$

However, this equation is found to be insufficient for realistic cases in terms of desired precision. In particular, it should be remembered that as it moves along the barrel, the initial amount of gas contained within the starting volume will have to expand to fill the growing volume behind the projectile [27].

Next, one might examine an isothermal model. An isothermal formulation makes it possible to adjust the pressure behind the projectile. However, the temperature change encountered by the gas molecules does not account for it. As the gas chamber empties, the gas temperature decreases, according to the Joule-Thompson effect. A reversible adiabatic state, indicating an isentropic expansion of gas, is, therefore more appropriate [1]. Thus, an adiabatic model can be proposed with the projectile velocity given by

$$v = \sqrt{\frac{2P_f V_i^{\gamma}\left(V_f^{1-\gamma} - V_i^{1-\gamma}\right)}{m(1-\gamma)} - \frac{2fL}{m}} \tag{16.2}$$

Also, by approximating the gradient of state properties within the breech and the barrel as a Lagrangian using the Lagrange method, an enhanced model can be postulated [1, 2]. The projectile velocity accordingly to this model, known as the Lagrange's model can be expressed as

$$v = \sqrt{\frac{2RTG}{(1-\gamma)\left(\frac{G}{3}+m\right)}\left[\frac{(L_b+L)^{1-\gamma}}{(L_b)^{1-\gamma}} - 1\right] - \frac{2fL}{\frac{G}{3}+m}} \tag{16.3}$$

Later on, the Lagrange model was expanded to account for the region of vacuum produced by the moving gas, as it continues. The state parameters of the compressed gas, such as pressure, volume, and density are changed as it takes time to pass from the front of the breach to the rear of the projectile. This leads to the Pidduck and Kent model [1, 2] which predicts a projectile velocity given by

$$v = \sqrt{a_0^2 \frac{\widetilde{a}_0}{(\gamma-1)^2}\left[1 - \left(\frac{1 + \frac{\gamma(P_iAL)^{\gamma}}{ma_0^2}}{\frac{G}{m}}\right)^{1-\gamma}\right]} \tag{16.4}$$

where $\widetilde{a}_0$ can be derived from,

$$\frac{G}{m} = \frac{2\gamma}{\gamma - 1}\widetilde{a_0}\left(1 - \widetilde{a_0}\right)^{-\frac{\gamma}{\gamma-1}}\int_0^1 \left(1 - \widetilde{a_0}\,\mu^2\right)d \tag{16.5}$$

For small *G/m* ratios [2] which have been considered in this study:

$$v = \frac{2a_0\sqrt{\widetilde{a_0}}}{\gamma - 1}\sqrt{\left[1 - \left(1 + \frac{\gamma\overline{x}_p}{\frac{G}{m}}\right)^{1-\gamma}\right]} \tag{16.6}$$

where $\widetilde{a_0}$ can be approximated as

$$\widetilde{a_0} = \frac{G(\gamma - 1)}{m(2\gamma)}\left\{1 - \frac{3\gamma - 1}{6\gamma}\frac{G}{m} + \left[\frac{1}{4} - \frac{1}{12\gamma} + \frac{1}{180\gamma^2}\right]\left(\frac{G}{m}\right)^2 + \ldots\right\} \tag{16.7}$$

16.2.2 Loss-Compensated Model (LCM)

While the classical models for compressed-air/gas-gun projectile velocity prediction capture the assumptions under ideal working conditions, it is desirable to incorporate specific practical thermo-mechanical losses which, obviously are expected to vary between individual gas-guns. Therefore, a Loss-Compensated Model (LCM) is proposed that accounts for some of the major mechanisms of loss in gas-guns. To begin with, the control volume of the gas behind the sabot can be expressed as

$$V = \dot{\Lambda}_{xg}At \tag{16.8}$$

This volume can be assumed to be bounded by a surface, *S* and the mass inside can be expressed by

$$G = \int_{\dot{\Lambda}_{xg}} \rho At d\dot{\Lambda}_{xg} \tag{16.9}$$

Therefore, the rate of decrease in mass from this control volume is

$$\dot{m}_{out} = -\frac{d}{dt}\int_{\dot{\Lambda}_{xg}} \rho At d\dot{\Lambda}_{xg} \tag{16.10}$$

As mass is conserved in this system, the above equation represents the mass flux rate out of the control volume after the exit valve is released. The rate of outward mass flux across any small element *dS* of the surface *S* is $\rho tA\dot{\Lambda}_{xg}dS$ [1]. Integrating over the entire surface yields the mass flux as

$$\dot{m}_{flux} = \int_S \rho At\dot{\Lambda}_{xg}dS = \int_{\dot{\Lambda}_{xg}} \nabla\left(\rho\dot{\Lambda}_{xg}\right)Atd\dot{\Lambda}_{xg} \tag{16.11}$$

As the direction of mass flux is only outward along the axis of the barrel,

$$\dot{m}_{flux} = \int_{\dot{\Lambda}_{xg}} \frac{\delta}{\delta x_g}\left(\rho At\dot{\Lambda}_{xg}\right)d\dot{\Lambda}_{xg} \tag{16.12}$$

For mass to be conserved, the rate of decrease of mass in the control volume and rate of mass flux out must be equal throughout the motion of the projectile [27, 28] and so we get

$$\frac{\delta\rho}{\delta t} + \left[\dot{\Lambda}_{xg}\frac{\delta\rho}{\delta x_g} + \rho\frac{\delta\dot{\Lambda}_{xg}}{\delta x_g}\right] = 0 \tag{16.13}$$

Since there is no density gradient assumed along the outward direction of the barrel that term is removed to obtain

$$\frac{1}{\rho}\frac{\delta\rho}{\delta t} = -\frac{\delta\dot{\Lambda}_{xg}}{\delta x_g} \tag{16.14}$$

If the base of the projectile has moved a distance, x and the bore area is A, then the volume behind the projectile occupied by the gas is

$$V(t) = Ax(t) \tag{16.15a}$$

$$\delta\dot{\Lambda}_{xg} = \frac{1}{x}\frac{dx}{dt}\delta x_g \tag{16.15b}$$

Now, integrating over x_g and using the condition that at $x_g = 0$, $\dot{\Lambda}_{xg} = 0$, and noting that x is the position of the base of the projectile and *dx/dt* is the velocity of the projectile at time *t*, we can write

$$\frac{1}{x}v\int_0^{x_g}\partial x_g = \int_0^{\dot{\Lambda}_{xg}}\partial\dot{\Lambda}_{xg} \tag{16.16a}$$

$$\dot{\Lambda}_{xg} = x_g\,\frac{v}{x} \tag{16.16b}$$

This means that the velocity of the gas-particle varies linearly from the breech to the projectile's base and is a fundamental aspect of Lagrange's approximation [2]. The kinetic energy of the gas stream can be written as

$$KE_g = \frac{1}{2}G\dot{\Lambda}_{xg}^2 \tag{16.17}$$

Noting that the mass of the gas is its density times the volume it occupies at any time, *t* and therefore

$$KE_g = \int_0^x \frac{1}{2}\rho A x_g^2\,\frac{v^2}{x^2}dx_g \tag{16.18a}$$

$$KE_g = \frac{1}{6}Gv^2 \tag{16.18b}$$

Now, considering the ratio of specific heats, γ, initial pressure, P_i, final pressure, P_f, initial volume, V_i, final volume, V_f, and breech length, L_b, and assuming the breech and bore are of the same cross-sectional area, A_b, one can state [1, 2],

$$P_iV_i^\gamma = P_fV_f^\gamma \tag{16.19a}$$

$$\frac{P_f}{P_i} = \left(\frac{(L_e+L)A_b}{(L_e)A_b}\right)^{-\gamma} = \left(\frac{(L_e+L)}{(L_e)}\right)^{-\gamma} \tag{16.19b}$$

With the adiabatic condition, the pressure work acting on the rear surface of the projectile can be expressed as

$$W_g = \int_0^L P_f(t)A_e dx \tag{16.20a}$$

$$W_g = A_eP_iL_e\frac{(L_e+L)^{1-\gamma} - (L_e)^{1-\gamma}}{(1-\gamma)\;(L_e)^{1-\gamma}} \tag{16.20b}$$

The effective length, L_e can be calculated using the relation

$$A_cL_c = A_bL_e \tag{16.21}$$

To account for the leakage of compressed air around the sabot, one can make use of Moss's Eq. (16.22) [30], which states

$$\dot{M}_l = 0.5303 \frac{A_l C P_f}{\sqrt{T_f}} \tag{16.22}$$

where P_f is pressure ahead of projectile that can be considered as the atmospheric pressure in psi, T_f is the temperature in $^\circ R$. $\dot{M}_l$ will be obtained in lbs./s. After converting this value to kg/s, one can use the following formula to calculate the volumetric flow rate:

$$\dot{V}_{lf} = \dot{M}_l \frac{P_f}{R T_f} \tag{16.23}$$

where $R = 287$ J/kg/k. Now from the adiabatic condition, we can find that

$$\dot{V}_{li} = \left[\frac{P_f \dot{V}_{lf}^{\gamma}}{P_i}\right]^{\frac{1}{\gamma}} \tag{16.24}$$

Thus, the loss of kinetic energy due to leakage around the projectile is

$$KE_l = \frac{1}{6} \dot{M}_l \frac{\dot{V}_{li}}{\dot{\Lambda}_{xg}} v^2 \tag{16.25}$$

This resultant kinetic energy lost due to leakage can be inserted into an energy balance relationship, accounting for the kinetic energy of the gas, the kinetic energy lost from frictional resistance and drag resistance of the air inside the containing box, the correction for leakage around the surface of the projectile and the kinetic energy of the projectile as follows:

$$KE_g + KE_p + W_f + KE_l + W_d = W_g \tag{16.26a}$$

$$KE_g = \frac{1}{6} G v^2 \tag{16.26b}$$

$$KE_p = \frac{1}{2} m v^2 \tag{16.26c}$$

$$W_f = \mu_k m g L \tag{16.26d}$$

$$KE_l = \frac{1}{6} \dot{M}_l \frac{V_{li}}{\dot{\Lambda}_{xg}} v^2 \tag{16.26e}$$

$$W_d = \frac{1}{2} c_d \rho A_e v^2 L \tag{16.26f}$$

$$W_g = A_e L_e P_i \frac{(L + L_e)^{1-\gamma} - L_e^{1-\gamma}}{(1-\gamma)(L_e)^{1-\gamma}} \tag{16.26g}$$

After simplifying, the projectile velocity as per this loss-compensated model can be extracted and expressed as

$$v = \sqrt{C_1 - C_2} \tag{16.27}$$

$$C_1 = \frac{2RTG\left[\frac{(L_e+L)^{1-\gamma}}{(L_e)^{1-\gamma}} - 1\right]}{(1-\gamma)\left(m + \frac{G}{3} + C_d \rho A L + \frac{1}{3} \dot{M}_l \frac{\dot{V}_{li}}{\dot{\Lambda}_{xg}}\right)} \tag{16.28}$$

$$C_2 = \frac{\mu_k m g L}{\left(m + \frac{G}{3} + C_d \rho A L + \frac{1}{3} \dot{M}_l \frac{V_l}{\dot{\Lambda}_{xg}}\right)} \tag{16.29}$$

Utilizing these models, comparisons can be made to experimental velocity for the compressed-air guns used in this study. The Large-Bore Gun (LBG) consists of a compressed-air cylinder coupled to a 2.5-in. bore barrel that can be used to fire various projectiles carried in nylon sabots. Three projectiles of different masses are used for the LBG. These three projectiles are named Projectile-A, which has a mass of 110 g, Projectile B, which has a mass of 220 g, and Projectile-C, which has a mass of 395 g. As for the Small-Bore Gun (SBG), a 0.357 Cal, 127 gr (8.23 g), flat-point, cast bullet is used as the projectile. The projectiles are fired at different cylinder pressure settings and the velocity is recorded and analyzed using high-speed camera footage. Figure 16.1 shows the comparison of theoretical velocity as per the different models with experimentally measured velocity. From these comparisons, it can be seen that the Loss-Compensated Model (LCM) predicts much better

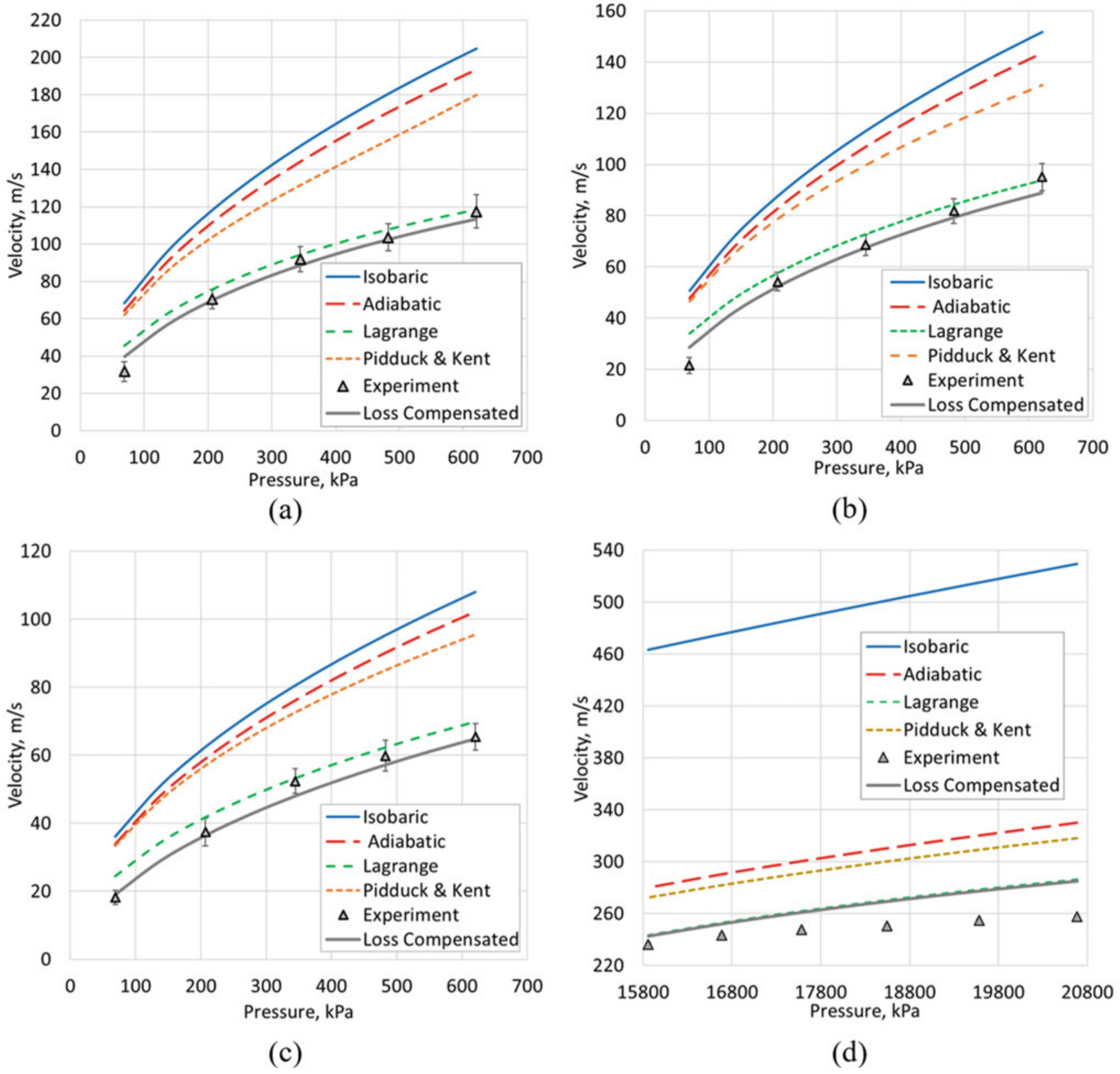

Fig. 16.1 Comparison of measured projectile velocity versus cylinder pressure with various theoretical model predictions for the large-bore gun for projectiles of mass (**a**) 110 g, (**b**) 220 g, and (**c**) 395 g and (**d**) for the small-bore gun for a projectile of mass 8.1 g

agreement with the measured velocity for all projectile in comparison to the other models since it considers compensation for lost energy due to multiple loss mechanisms. For an SBG, although the model gives slightly better accuracy, deviations are notable at higher pressures, likely due to certain unaccounted loss mechanisms such as in the release value of the trigger mechanism and due to the rifled barrel, which needs to be explored further.

16.3 Ballistic Testing of Carbon-Graphite Foam Composite

After the calibration of the large-bore gas-gun, a set of impact tests on Carbon-Graphite Foam (CGF) composite samples was carried out to determine their ballistic performance vis-à-vis baseline aluminum foam composite samples.

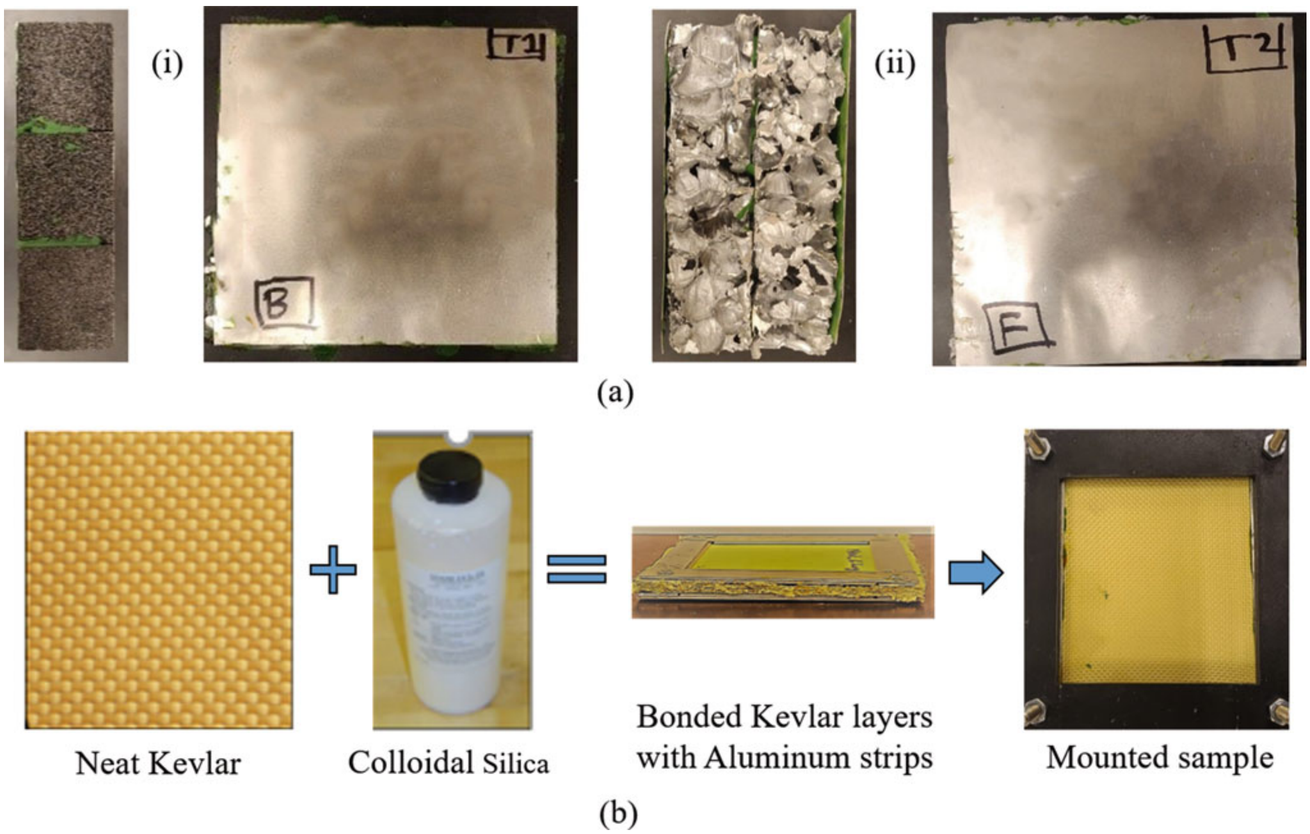

Fig. 16.2 (**a**) (i) carbon-graphite foam, (ii) aluminum foam test articles, and (**b**) sample preparation process for the silica-nanoparticle treated Kevlar fabric.

16.3.1 *Sample Preparation*

CGF composite samples consist of two layers of 0.3 mm thick, 152.4 mm × 152.4 mm aluminum face sheets with nine, 50.8 mm × 50.8 mm × 50.8 mm CGF cubes arrayed and sandwiched between them by bonding them together with Loctite EA 9359.3 Aero epoxy. The bonded components were allowed to cure for 24 h under pressure at a temperature of 180 °F using a hot press. A similar procedure was used to make the baseline aluminum foam composite samples. While the CGF samples were made in a modular fashion, the baseline foam composite sample was constructed from two layers of 43.2 mm-thick, aluminum-metallic foam sandwiched between three layers of aluminum face sheets and bonded together such that it had the same overall mass as the CGF samples. The curing time and processing procedure for the aluminum foam samples were the same as that for the CGF samples. Figure 16.2a shows photographs of the fabricated CGF and aluminum foam composite samples.

16.3.2 *Test Procedure*

The gun was sighted on the target center, and the impact velocity was calibrated by adjusting the pneumatic pressure. The impact velocity of each projectile was measured using a high-speed camera throughout the impact event. The 395-g, Projectile-C which is made of steel and has a hemispherical tip of 1inch diameter was used in all cases. The target was placed against a clay witness (Roma Plastilina No. 1 clay) under consistent pressure in order to measure the depth of back-face signature as per NIJ Standard 0101.06. The projectile's energy absorbed (or dissipated) through the impact event can be computed as

$$E = \frac{1}{2} m \left(v_r^2 - v_i^2 \right) \tag{16.30}$$

To relate the depth of back-face signature (BFS) to the projectile's residual velocity (v_r), a series of impact tests were also performed on the clay witness without a test article as prescribed by the NIJ standard. The BFS was measured with the help of a digital Vernier caliper and a depth gauge for all cases. The projectile velocity versus BFS data for the clay alone can then be used to determine the residual velocity of the projectile by measuring the BFS for the impact on the CGF and ALF test article. In the case of both the CGF and ALF test articles, an operating pressure of 20 psi was used during testing. The impact event was recorded using a high-speed camera and the initial velocity before the impact was measured. Subsequently, after obtaining the initial velocity before impact and residual velocity after impact, the energy absorbed or dissipated by the test article under impact is calculated using Eq. (16.30) and can serve as an indicator of the ballistic performance of the CGF and baseline test articles.

16.4 Ballistic Testing of Silica Nanoparticle-Impregnated Kevlar Fabric

16.4.1 Materials

Colloidal Silica

Colloidal silica has many applications related to paper, fibers, steel, and as a catalyst. Snowtex ST-ZL from Nissan Chemical which is water-based colloidal silica is used to impregnate the Kevlar fabrics with nanoparticles in this study. It has the following properties and composition (Table 16.1).

Kevlar Fabric

Kevlar 29 style 745, a medium-sized yarn, the plain-woven fabric is used across all test samples in this study. It has an areal density of 0.48 kg/m^2, a fabric thickness of 0.61 mm with a yarn count of 17 per inch. This style of Kevlar is commonly used in flexible body armor applications due to its excellent strength to weight ratio and relatively good flexibility.

16.4.2 Sample Preparation

The Kevlar fabric was first cut into rectangular-shaped swatches and weighed using a precision balance. The swatches were then dried in an oven at 80 °C for 30 min to remove any moisture and weighed again. Next, the swatches were treated with measured quantities of the colloidal silica solution to impregnate them with the appropriate percentage by weight of nanoparticles. After treatment with the colloidal silica solution, fabric swatches were dried in the oven at 80 °C for 30 min to remove the water. Once again, the sample's weight was measured and compared to that of the targeted 10%, 30%, or 40% by weight of addition for the silica nanoparticle-treated Kevlar (SNK) composite samples to check if the targeted weight has been achieved with sufficient accuracy. Next, the samples are affixed with aluminum tabs and mounted onto the test fixture. Figure 16.2b depicts the sample preparation process for SNK.

Table 16.1 Properties of colloidal silica

Composition/property	Value
SiO_2 (wt.%)	40–41
Na_2O (wt.%)	<0.07
Particle shape	Spherical
Particle size (nm)	70–100
Viscosity (mPa.s at 25 °C)	<5
Specific gravity (25 °C)	1.29–1.32

16.4.3 Test Procedure

High-velocity impact tests were carried out using an AIRFORCE model R1401 air gun on neat Kevlar fabric and Silica Nanoparticle-Kevlar (SNK) composite samples at three different levels of silica nanoparticle addition by weight: 10, 30, and 40 wt.% in a velocity range of 230–285 ms^{-1}. Two tests were carried out for each case (number layer of the neat Kevlar/SNK). The gun is sighted more or less on the target center. The velocities of each projectile before and after impact were measured with a high-speed camera with a frame rate of 50,000 frames per second immediately before and after impacting the target. The projectile is 357 Cal, 127 gr, flat point bullets. Then the absorbed kinetic energy by a projectile was calculated using Eq. (16.30) for the penetrative cases. The coefficient of restitution (COR) as specified by NIJ Standard 0108.01 was calculated using Eq. (16.31).

$$\text{COR} = \frac{v_r}{v_i} \tag{16.31}$$

To maintain a uniform boundary condition throughout all the tests, first, the Kevlar specimen was cut according to the size of the fixture (4″ × 4″). The fixture used in this setup has two square mounting frames and four independent metal cross bars of the same width. After cutting, epoxy is applied to bond the four edges of the Kevlar fabric layers together and with the aluminum tabs. The tabbed samples are attached to the mounting fixture utilizing four bolts under consistent torque to allow them to be held firmly in place. No slippage of the boundary attachment was noticed in any of the tests.

16.5 Discussion of Results

16.5.1 Carbon-Graphite Foam Composite

Firstly, from the impact tests done on the clay witness alone, a linear relationship was established between the measured BFS as a function of projectile velocity as shown in Fig. 16.3a. This relationship is then used to extract the residual projectile velocity after penetration in the impact tests with the test articles from the measured BFS. Thus, using the relationship between BFS depth and projectile velocity relationship established previously using impact test on the clay witness alone, the residual velocity of the projectile after the penetration of the test samples was estimated.

It was observed that complete penetration occurred predominantly due to the shear failure of samples. In the case of the CGF samples, a brittle fracture-dominated "punch-through" type failure mode is noticed whereas for the aluminum foam samples a ductile "pull-through" type failure is noticed. A comparison of the absorbed energies is shown in Fig. 16.3b. It can be seen that the initial velocity was kept about the same for all tests. The average absorbed energy for the CGF composite samples was about 194 J, whereas that for the ALF composite samples was about 101 J, indicating that the CGF absorbs nearly double the energy absorbed by the mass-equivalent baseline ALF samples. More investigation is required to ascertain further mechanisms involved in energy absorption for CGF composites.

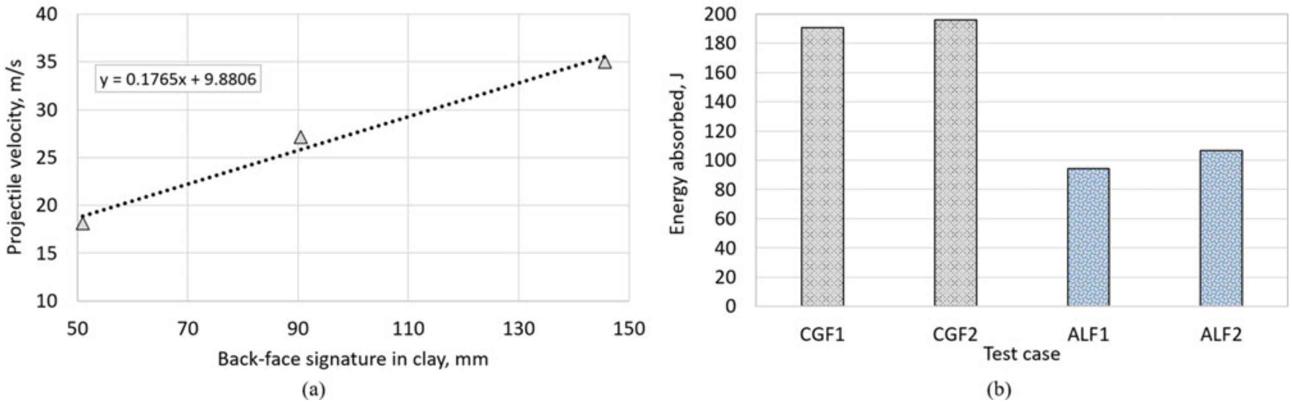

Fig. 16.3 (**a**) Projectile's velocity of impact versus depth of back-face signature in the clay witness alone and (**b**) impact energy absorbed by carbon-graphite foam (CGF) and aluminum foam (ALF) test articles

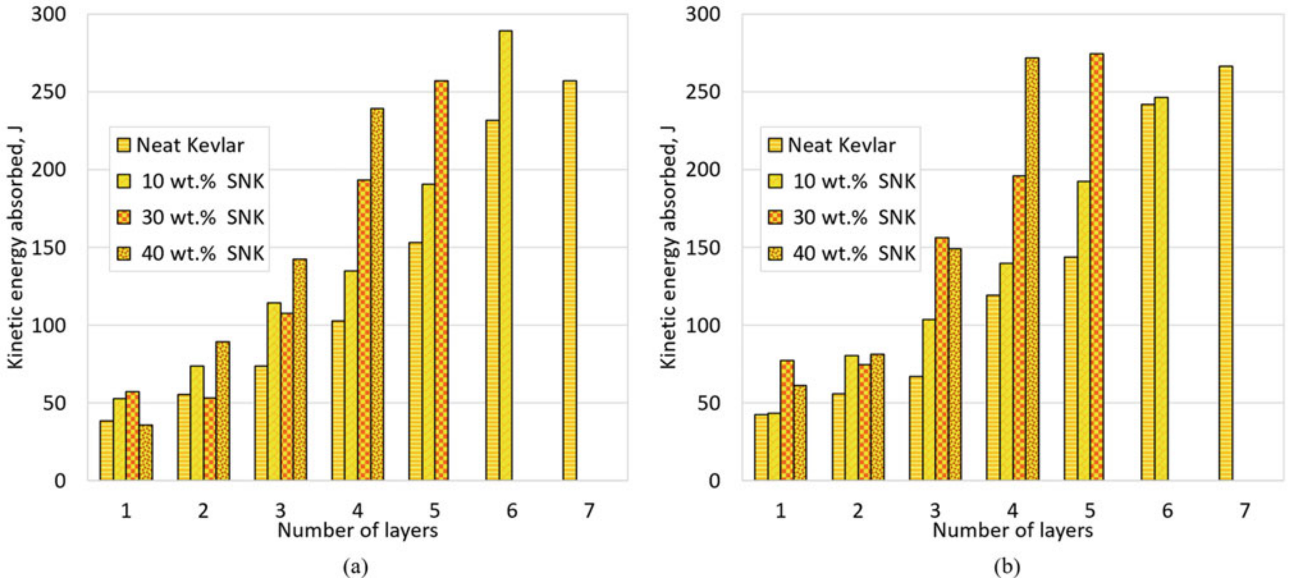

Fig. 16.4 Kinetic energy absorbed versus the number of layers of neat and silica nanoparticle treated Kevlar fabric for (**a**) test set-1 and (**b**) test set-2

16.5.2 Silica Nanoparticle-Impregnated Kevlar

The test results for the Kevlar samples showed that it took seven neat Kevlar layers to fully prevent the high-speed projectile from penetrating through. However, for the Kevlar impregnated with silica nanoparticles at 10, 30, and 40 wt.%, the projectile penetration was prevented by six, five, and four layers, respectively. This implies that there is a notable increase in the ballistic performance of Kevlar when treated. It is noted that the addition of nanoparticles to the Kevlar fabric is also found to reduce its flexibility to some degree which would be important to quantify for certain applications. The kinetic energy absorbed in the two sets of impact tests is detailed in Fig. 16.4. In this figure, the improvement of energy absorbed by the different numbers of layers with an increase in the level of nano-silica impregnation becomes evident.

It can be seen that there is a notable increase in the absorbed energy for the SNK cases compared to the neat sample, depending on the level of treatment, though for some cases with a lower number of layers, exceptions are observed. This could be attributed to the potential non-uniform impregnation of silica nanoparticles in some samples, despite the best efforts to accomplish homogeneity throughout the process. Fig. 16.5 shows curve fits for kinetic energy absorbed versus the number of layers of neat and treated Kevlar. The trends are captured well using quadratic curve fits for all cases. It is noted that the rate of increase of energy absorbed with the increasing number of layers is steeper as the wt.% of nanoparticle addition to Kevlar increases. This indicates that with the increase in the level of treatment, the energy absorption capacity increases more rapidly.

Figure 16.6 shows the plots of the coefficient of restitution versus the number of layers for neat and SNK samples computed as per NIJ Standard 0108.01. The coefficient of restitution is the measure of the residual velocity of the projectile after impact. These curves show a downward concavity. This reiterates the observation that having multiple layers provides better energy absorption than the summation of the energy absorbed by a single layer for neat and treated cases. The rate of increase of negative slope towards the higher degree of treatment also shows that the residual velocity decreases more rapidly for a higher level of treatment. It is possible that the energy absorbed by the Kevlar samples in the event of complete blockage of the projectile does not necessarily indicate the maximum energy that it can absorb. If this maximum energy is to be determined, a test procedure where the projectile velocity is gradually increased needs to be followed and the transition from non-penetrative to the penetrative case must be identified.

Figure 16.7 shows photos of perforated (in case of penetrative cases) or deformed (in case of non-penetrative cases) rear face of samples for neat, 10, 30, and 40 wt.% SNK cases after high-speed impact tests. As can be seen, the local fabric structure in the impact region of the impregnated fabric of the SNK is slightly better well preserved compared to the neat fabric. Furthermore, in some cases, when the projectile penetrates the neat fabric, the yarns are pushed aside within the fabric without significant fiber breakage. Although the primary cross yarns at the center of the impact point are strained in the neat fabric sample, the secondary yarns in the rest of the neat fabric sample continue to remain just about unperturbed. As the secondary yarn does not contribute, the energy dissipation and consequently the resistance to impact tends to remains lower in the case of neat Kevlar. The yarn pull-out is not seen as much in SNK fabrics, and the core impact zone is much smaller. The

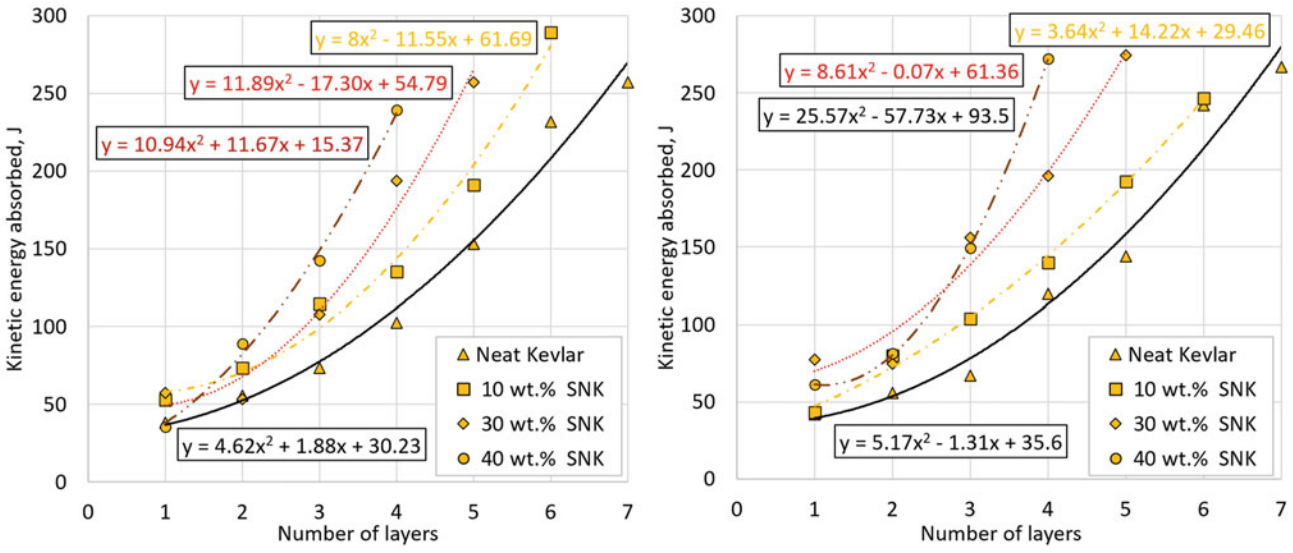

(a) (b)

Fig. 16.5 Quadratic curve fits for kinetic energy absorbed versus the number of layers of neat and silica nanoparticle treated Kevlar fabric for (**a**) test set-1 and (**b**) test set-2

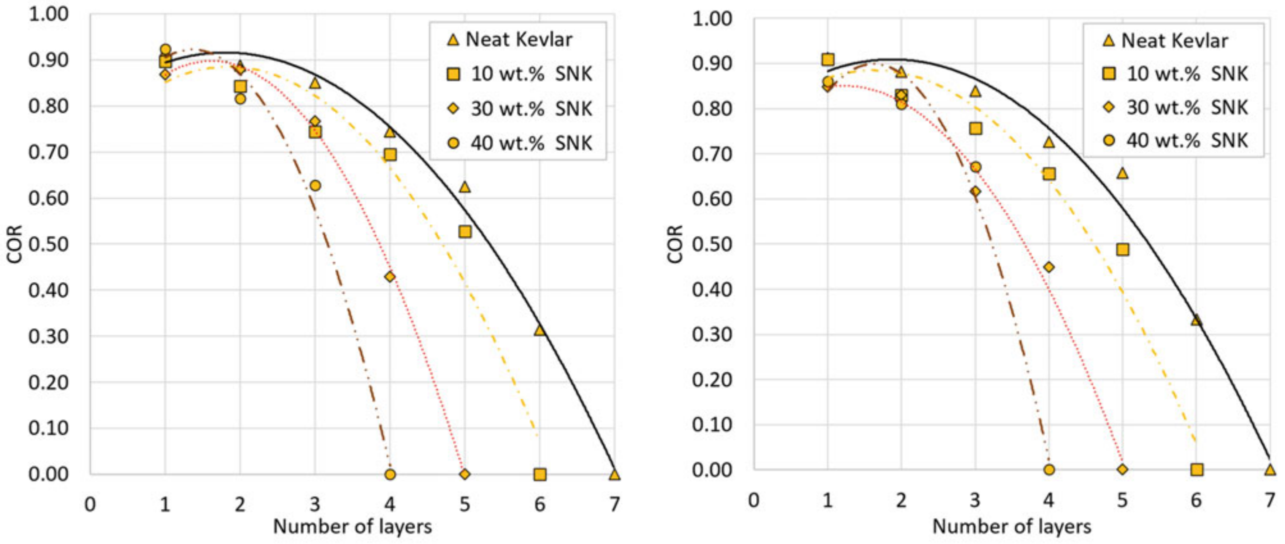

(a) (b)

Fig. 16.6 Coefficient of Restitution (COR) versus the number of layers of neat and silica nanoparticle treated Kevlar fabric for (**a**) test set-1 and (**b**) test set-2

higher frictional properties induced by the silica nanoparticles impregnated in the inter-yarn and inter-fiber interstices limits the local movement and pull-through of the yarns and allows adjacent yarns to participate in preventing the penetration of the projectile.

From the damage analysis using the photos shown in Fig. 16.8a, it is found that the projectile was stopped after penetrating all layers before the last one and was stopped by the last layer in the case of neat Kevlar. As for the 10 wt.% cases, the back-face impact pattern shows more damage to the last layers. In the case of 30 and 40 wt.% treatments, the penetration was prevented well without any significant signature to the rear face of the sample. Part of the kinetic energy of a high-speed projectile was also absorbed by the deformation of the projectile (Fig. 16.8b). The rest of the energy is absorbed by the Kevlar sample. It can be observed that in terms of percentage mass advantage for the non-penetrative cases with the addition of

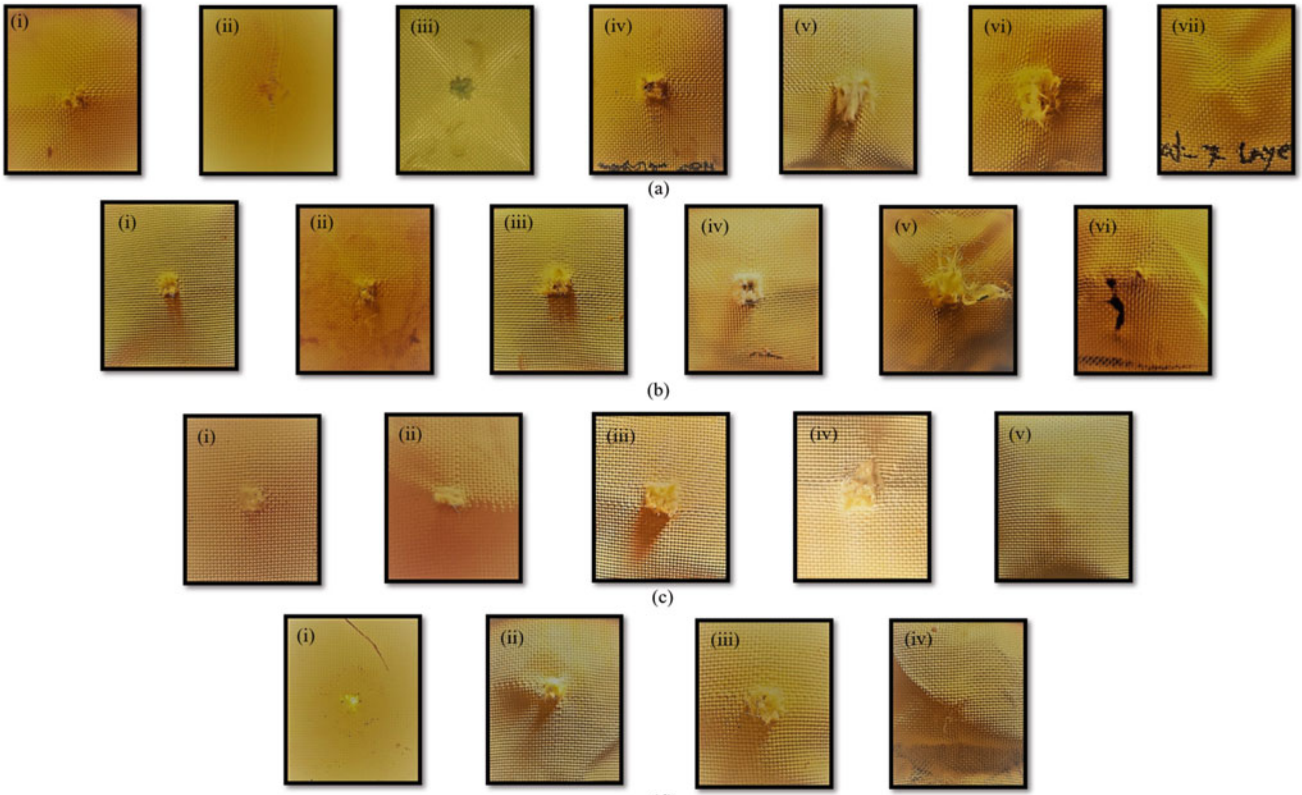

Fig. 16.7 Rear face of (**a**) neat, (**b**) 10 wt.%, (**c**) 30 wt.%, and (**d**) 40 wt.% silica nanoparticle treated Kevlar samples after impact for (i) one, (ii) two, (iii) three, (iv) four, (v) five, (vi) six, and (vii) seven layers, as the case may be

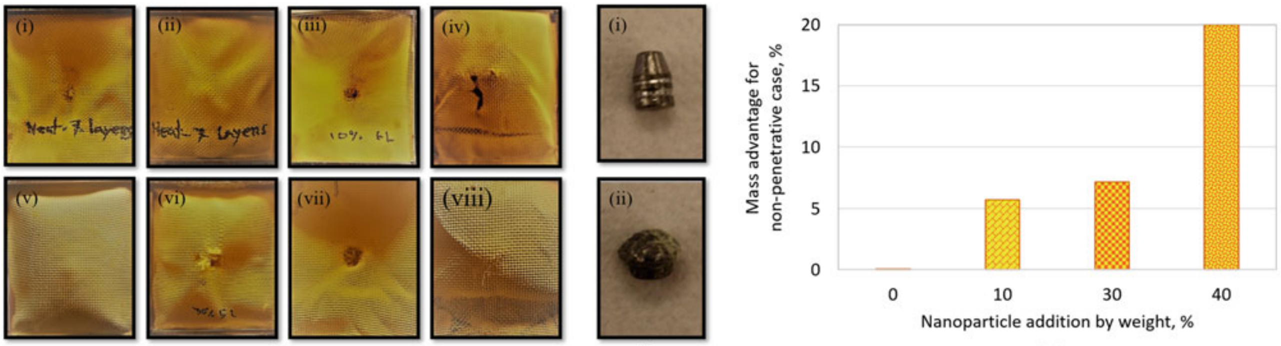

(a) (b) (c)

Fig. 16.8 (**a**) Front and rear face of neat and silica nanoparticle treated Kevlar samples for non-penetrative cases: (i) Neat–front and (ii) rear faces, (iii) 10 wt.% – front and (iv) rear faces, (v) 30 wt.% – rear and (vi) front faces, and (vii) 40 wt.%–front and (iv) rear faces; (**b**) (i) pristine and (ii) deformed state of the projectile; and (**c**) Percentage mass advantage for the non-penetrative case achievable by treatment of 10, 30, and 40 wt.% of silica nanoparticles in comparison to neat Kevlar

10, 30, and 40 wt.% of silica nanoparticles versus the neat non-penetrative case (Fig. 16.8c), a significant improvement can be obtained with the 40 wt.% addition case as only four layers (versus 7 for the neat case) are needed to prevent penetration, which is desirable in the construction more lightweight armors. These experiments could also be used to calibrate an empirical model for such hybrid composites to predict the projectile's exit velocity in terms of the entry velocity, number of layers, and the wt.% of nanoparticle treatment.

16.6 Conclusion

A loss compensated model was developed to predict the projectile velocity for compressed-air/gas-guns. This model builds upon the classical Lagrange model by including clearance leakage, improved surface friction, and air drag effects. Comparisons with experiments using a large-bore compressed-air gun for projectiles of various masses show that the loss compensated model can predict the velocities with excellent accuracy compared to other classical models. For a small-bore compressed-air gun, although the model gives better accuracy, deviations are notable at higher pressures, likely due to certain unaccounted loss mechanisms. Ballistic characterization tests were conducted on two types of composite structural materials with potential for multifunctional applications. First, Carbon-Graphite Foam (CGF) composite samples are evaluated versus mass-equivalent Aluminum Foam (ALF) composite samples using the large bore gun as per NIJ Standard 0101.06. The results show that the average absorbed energy for the CGF composite samples was about 194 J, whereas that for the ALF composite samples was about 101 J, indicating that the CGF absorbs nearly double the energy absorbed by the mass-equivalent, baseline ALF samples. Next, silica nanoparticle-treated Kevlar (SNK) fabric was tested and compared to their neat counterpart using a small-bore gun. 10, 30, and 40 wt.% of nanoparticle addition were considered. It is found that having multiple layers provides better energy absorption than the summation of the energy absorbed by a single layer for neat and treated cases. It is observed from the post-impact inspection of the neat and treated Kevlar samples that the SNK engages more secondary yarns (other than the primary cross yarns at the impact location) to mitigate the impact likely due to improved inter-yarn and inter-fiber friction although the treated fabrics could be less flexible. A significant improvement (20%) in terms of percentage mass advantage for the non-penetrative cases can be obtained with 40 wt.% addition for SNK as only four layers (versus 7 for the neat case) are needed to prevent penetration, which is desirable in the construction more lightweight armors.

Acknowledgments Support for this work from the Ray and Linda Booker Fellowship is gratefully acknowledged. Thanks are due to the undergraduate student, Zack Krawczyk for help with the experiments.

References

1. Helminiak, N.S.: Construction and Characterization of a Single Stage Dual Diaphragm Gas Gun. Master's Theses, Marquette University, Milwaukee, WI (2017)
2. Seigel, A. E.: Performance calculations and optimization of gas guns. U.S. Army Electronics Research and Development Command, HDL-CR-81-723-1 (1981)
3. Inagaki, M., Qiu, J., Guo, Q.: Carbon foam: preparation and application. Carbon. **87**, 128–152 (2015)
4. Manylov, M.S., Filimonov, S.V., Shornikova, O.N., Malakho, A.P., Avdeev, V.V.: Thermophysical properties of carbon-carbon materials based on graphite foam. Refract. Ind. Ceram. **58**(1), 113–116 (2017)
5. Zhu, J., Wang, X., Guo, L., Wang, Y.I., Wang, Y.A., Yu, M., Lau, K.: A graphite foam reinforced by graphite particles. Carbon. **45**(13), 2547–2550 (2007)
6. Ashby, M.F., Mehl Medalist, R.F.: Mechanical properties of cellular solids. Metallurgical Trans. AIME. **14**, 1755–1769 (1983)
7. Ashby, M., Evans, T., Fleck, N.A., Hutchinson, J.W., Wadley, H.N.J., Gibson, L.J.: Metal Foams: A Design Guide. Butterworth-Heinemann, Oxford (2000)
8. Destefanis, R., Schäfer, F., Lambert, M., Faraud, M.: Selecting enhanced space debris shields for manned spacecraft. Int. J. Impact Eng. **33** (1–12), 219–230 (2006)
9. Ma, G.W., Ye, Z.Q.: Energy absorption of double-layer foam cladding for blast alleviation. Int. J. Impact Eng. **34**(2), 329–347 (2007)
10. Hanssen, A.G., Enstoc, L.K., Langseth, M.: Close-range blast loading of aluminum foam panels. Int. J. Impact Eng. **27**(6), 593–618 (2002)
11. Wadley, H.N.G., Dharmasena, K., He, M.Y., McMeeking, R.M., Evans, A.G., Bui-Thanh, T., Radovitzky, R.: An active concept for limiting injuries caused by air blasts. Int. J. Impact Eng. **37**(3), 317–323 (2010)
12. Reyes-Villanueva, G., Cantwell, W.J.: The high velocity impact response of composite and FML reinforced sandwich structures. Compos. Sci. Technol. **64**(1), 35–54 (2004)
13. Hou, W., Zhu, F., Lu, G., Fang, D.-N.: Ballistic impact experiments of metallic sandwich panels with aluminum foam core. Int. J. Impact Eng. **37** (10), 1045–1055 (2010)
14. Hanssen, A.G., Girard, Y., Olovsson, L., Berstad, T., Langseth, M.: A numerical model for bird strike of aluminum foam-based sandwich panels. Int. J. Impact Eng. **32**(7), 1127–1144 (2006)
15. Cheeseman, B.A., Bogetti, T.A.: Ballistic impact into the fabric and compliant composite laminates. Compos. Struct. **61**(1–2), 161–173 (2003)
16. Shim, V.P.W., Tan, V.B.C., Tay, T.E.: Modeling deformation and damage characteristics of woven fabric under small projectile impact. Int. J. Impact Eng. **16**(4), 585–605 (1995)
17. Lim, C.T., Tan, V.B.C., Cheong, C.H.: Perforation of high-strength double-ply fabric system by vary shaped projectiles. Int. J. Impact Eng. **27** (6), 577–591 (2002)
18. Kirkwood, K.M., Kirkwood, J.E., Lee, Y.S., Egres, R.G., Wagner, N.J.: Yarn pull-out as a mechanism for dissipating ballistic impact energy in Kevlar KM-2 fabric – part I: quasi-static characterization of yarn pull-out. Text. Res. J. **74**(10), 920–928 (2004)

19. Tan, V.B.C., Tay, T.E., Teo, W.K.: Strengthening fabric Armour with silica colloidal suspensions. Int. J. Solids Struct. **42**(5–6), 1561–1576 (2005)
20. Zeng, X.S., Shim, V.P.W., Tan, V.B.C.: Influence of boundary conditions on the ballistic performance of high-strength fabric targets. Int. J. Impact Eng. **32**(1–4), 631–642 (2005)
21. Nadler, B., Steigmann, D.J.: A model for frictional slip in woven fabrics. C. R. Méc. **331**(12), 794–804 (2003)
22. Zeng, X.S., Tan, V.B.C., Shim, V.P.W.: Modeling inter-yarn friction in woven fabric Armour. Int. J. Numer. Methods Eng. **66**(8), 1309–1330 (2006)
23. Duan, Y., Keefe, M., Bogetti, T.A., Cheeseman, B.A.: Modeling the role of friction during ballistic impact of a high-strength plain-weave fabric. Compos. Struct. **68**(3), 331–337 (2005)
24. Briscoe, B.J., Motamedi, F.: The ballistic impact characteristics of aramid fabrics: the influence of interface friction. Wear. **158**(1–2), 229–247 (1992)
25. Bender, J., Wagner, N.J.: Reversible shear thickening in monodisperse and bidisperse colloidal dispersions. J. Rheol. **40**(5), 899–916 (1996)
26. Lee, Y.S., Wagner, N.J.: Dynamic properties of shear thickening colloidal suspensions. Rheol. Acta. **42**(3), 199–208 (2003)
27. Khodadadi, A., Liaghat, G., Vahid, S., Sabet, A.R., Hadavinia, H.: Ballistic performance of Kevlar fabric impregnated with nanosilica/PEG shear thickening fluid. Compos. Part B. **162**, 643–652 (2019). https://doi.org/10.1016/j.compositesb.2018.12.121
28. Dong, Z., Manimala, J.M., Sun, C.T.: Mechanical behavior of silica nanoparticle-impregnated Kevlar fabrics. J. Mech. Mater. Struct. **5**(4), 529–554 (2010)
29. Manimala, J.M., Sun, C.T.: Investigation of failure in Kevlar fabric under transverse indentation using a homogenized continuum constitutive model. Text. Res. J. **84**, 399–410 (2014)
30. Moss, S.A.: Flow of air and other gases with special reference to small differences in pressure. Am. Mach. **29**, 368–407 (1906)

Chapter 17
Shear Damage Model Identification for Off-axis IBII Composites Specimen Loaded and Unloaded at High Strain Rates

Fabrice Pierron, Samuel Parry, and Lloyd Fletcher

Abstract Testing polymer matrix composites in shear at high strain rates is a difficult task using standard test methods like the Kolsky bar because of the low wave speed and low strain to failure. Moreover, it is well known that such composites exhibit a non- linear response in shear generally attributed to a combination of damage and matrix plasticity. In quasi-static conditions, such models are generally identified by performing cycles of loading and unloading to discriminate damage from plasticity.

However, current high strain rate test methods are unable to do this. The present paper details how the new Image-Based Inertial Impact (IBII) test naturally provides loading/unloading and how a damage model can be identified using the Virtual Fields Method from full-field strain and acceleration maps.

Key words IBII test · High strain rate · Composite · Shear damage

17.1 Introduction

The rate dependent properties of orthotropic materials such as Carbon Reinforced Fibre Composites (CFRP) composites are important to simulate events like bird-strike or general third body impact. The current test technique for obtaining high strain rate material properties is the split Hopkinson (or Kolsky) bar (SHB). This technique relies on several assumptions including that the sample must be in a state of quasi-static equilibrium and that the sample undergoes uniform 1D deformation. These assumptions limit the ability of the SHB technique to accurately extract a single stiffness component let alone identify multiple orthotropic stiffness components in a single test.

Recently, the Image-Based Inertial Impact (IBII) test has emerged as an alternative technique that does not rely on the assumptions of quasi-static equilibrium or 1D deformation. In fact, the use of image-based measurements allows for deformation that is intentionally inhomogeneous providing a large database of points for material property identification. Thus far, applications of the IBII test have shown that it was possible to extract the transverse and shear moduli for a carbon fibre in-plane and through-thickness [1–3].

However, as is well known for such composites, the shear behaviour exhibits a non-linear response generally attributed to either diffuse damage (matrix micro-cracks) [4] and/or matrix plasticity [5]. In quasi-static conditions, this behaviour is generally characterized by cyclic loadings/unloadings for which modulus decrease is evaluated from the different unloading slopes, and plasticity identified through the permanent strain at zero stress. However, at high strain rates, such cyclic loadings have so far eluded experimentalists, the best achievable being interrupted loadings [6], and at limited strain rates (a few 100s of s^{-1}). The IBII test provides a unique opportunity to perform one loading/unloading cycle at strain rates on the order of 1000 s^{-1}. This paper presents the inverse identification of a shear damage model based on IBII test data (full-fields kinematic measurements at 2 Mfps with a Shimadzu HPV-X camera and inverse identification with the Virtual Fields Method).

F. Pierron (✉) · S. Parry · L. Fletcher
School of Engineering, Faculty of Engineering and Physical Sciences, University of Southampton, Southampton, UK
e-mail: F.Pierron@soton.ac.uk

S. Mates, V. Eliasson (eds.), *Dynamic Behavior of Materials, Volume 1*, Conference Proceedings of the Society for Experimental Mechanics Series, https://doi.org/10.1007/978-3-030-86562-7_17

17.2 Experimental Methodology

The IBII test consists in inertially impacting a thin rectangular specimen on one of its edges, as represented in Figs. 17.1 and 17.2. This is achieved by a cylindrical projectile sitting in a nylon sabot, fired by a custom-designed gas gun at velocities of a few tens of m.s^{-1}. The full procedure is provided in the open access IBII test manual, available online [7].

The material considered in this study is a 12-ply unidirectional laminate made from Hexply M21/35%/268/T700GC UD. It is the same material as tested in [8]. The specimens were cut to the dimensions reported in Figure 17.2. The material's density was measured to be 1575 ± 17 kg.m^{-3}. To measure the specimens' deformations, the grid method was used [9]. A black on white grid of pitch 0.9 mm was printed using a flatbed printer, see procedure in [7]. A Shimadzu HPX-X camera was used to record images of the deforming specimens, at 2 MHz. 128 images were recorded during the test, using copper wires bonded onto the wave guide to create a trigger signal, which was delayed by the time for the wave to propagate along the wave guide. A flashlight was triggered off light gates positioned at the end of the barrel to account for the 100 μs rise time of the flash. A thorough alignment procedure allows for accurate alignment of the wave guide and the impactor [10]. Once the images have been captured, displacements are obtained through spatial phase shifting with the grid method algorithm published in [9]. Strains are obtained through spatial differentiation after spatial smoothing, and acceleration through double temporal differentiation after temporal smoothing. The parameters and their optimization are detailed in [1] and will not be recalled here.

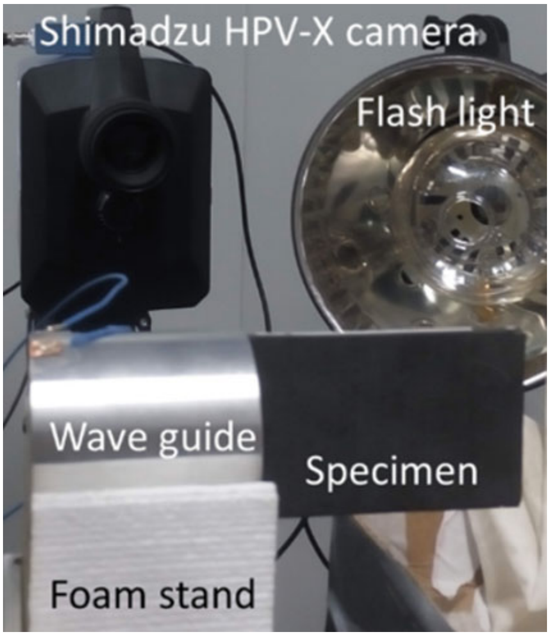

Fig. 17.1 Specimen in the test chamber

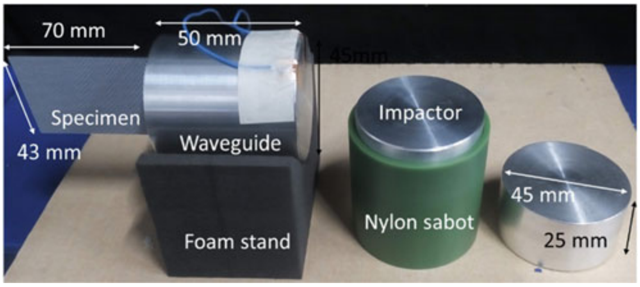

Fig. 17.2 Specimen, waveguide, and impactor

17.3 Identification Procedure

The identification procedure relies on the calculation of an average stress along an angled slice from acceleration data, as detailed in [1]. The process will only be briefly outlined her. Let us consider an angled cross-section along the fibre direction, as sketched in Fig. 17.3. Writing the equilibrium of the downstream part of the specimen (in blue), the following relationships are obtained:

$$\overline{\sigma_6}^{1} = \frac{S}{1}\overline{a_1}^{s}\ ;\ \overline{\sigma_2}^{1} = \frac{S}{1}\overline{a_2}^{s} \tag{17.1}$$

where σ_6 is the shear stress and σ_2 the transverse stress in the angled coordinate system, a_1 and a_2 are the two components of acceleration in the angled coordinate system and the overbar indicates spatial average over the slice of width l for stress, and over the surface S for acceleration (see Fig. 17.3). S is the area of the blue part of the specimen, and l the length of the angled slice. The acceleration averages can be calculated from experimental data, as well as the strain averages over the angled slice, using appropriate interpolation routines as detailed in [1]. In the case where the material is purely linear elastic, it is possible to plot stress–strain curves and identify both shear and transverse modulus simultaneously. However, as seen in Fig. 17.4, looking at slice #170, the shear strain is far from uniform along its length. While some points at the top of the slice will remain in the linear domain (the start of non-linearity can be estimated to be around 1% of strain following results in [8]), the bottom part will be well in the non-linear regime. As a result, the shear stress–strain curve in Fig. 17.5 is smeared and identifying a stiffness directly from this curve leads to a bias.

To bring the analysis one step further from [1], a shear damage model is considered here. This model is the same as already identified under quasi-static conditions in [11]. The model is provided in Eq. (17.2).

$$\begin{array}{ll} \sigma_6 = G_{12}^0[1-d(\varepsilon_6)]\varepsilon_6 & \begin{cases} <|\varepsilon_6|-\varepsilon_6^0>^+=0 & \text{if} |\varepsilon_6|<\varepsilon_6^0 \\ <|\varepsilon_6|-\varepsilon_6^0>^+=|\varepsilon_6|-\varepsilon_6^0 & \text{if} |\varepsilon_6|>\varepsilon_6^0 \end{cases} \\ d(\varepsilon_6)=\frac{K}{G_{12}^0}<\varepsilon_6-\varepsilon_6^0>^+ & \end{array} \tag{17.2}$$

where G_{12}^0 is the linear elastic (undamaged) shear modulus, d is the scalar shear damage variable, ε_6^0 is the (positive) engineering shear strain elastic limit (or damage threshold), and K is the parameter driving the evolution of damage.

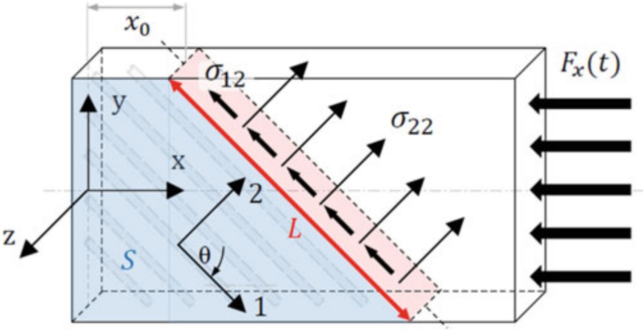

Fig. 17.3 Schematic of the off-axis IBII test specimen

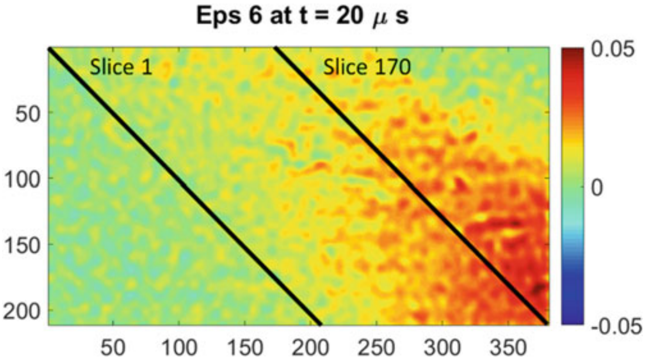

Fig. 17.4 Engineering shear strain at maximum loading, with the two slices defining the range of processed slices

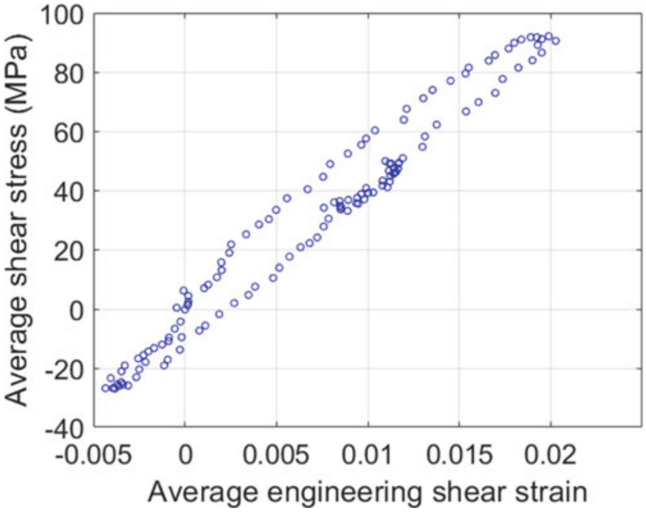

Fig. 17.5 Average stress vs average strain, slice 170

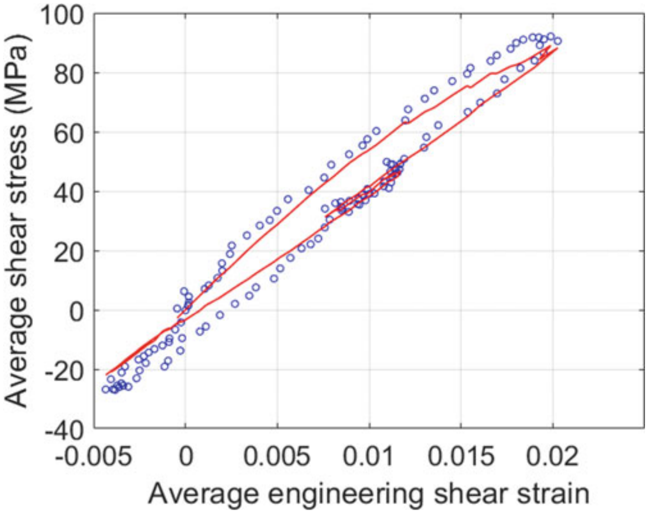

Fig. 17.6 Average stress vs average strain, slice 170, with fitted damage model (in red)

Therefore, the model has three parameters to be identified:G_{12}^0, ε_6^0, and K. To identify these parameters, the expression of the average shear stress over a slice from Eq. (17.1) is used in conjunction with the stress obtained from strain and the damage model. The cost function used is as follows:

$$\varphi\left(G_{12}^0, \varepsilon_6^0, K\right) = \sum_{t=0}^{64\mu s} \sum_{s=1}^{170} \left(\overline{\sigma_6}^1 (a)_{t,s} - \overline{\sigma_6}^1 (\varepsilon)_{t,s}\right)^2 \tag{17.3}$$

where $\overline{\sigma_6}^1 (a)_{t,s}$ is the stress calculated from acceleration for each angled slice and each time (according to Eq. 17.1), and $\overline{\sigma_6}^1 (\varepsilon)_{t,s}$ is the stress calculated from strain and the damage model, for each angled slice and each time. As seen in Fig. 17.3, 170 slices have been considered, and 128 times steps covering 64 μs at 2 Mfps. The non-linear optimization problem was solved using the *fminunc* function in Matlab™, which is a second order Quasi-Newton method. The initial values of the parameters were selected as $G_{12}^0 = 5.8$ GPa, $\varepsilon_6^0 = 0.01$ and $K = 100$ MPa. The problem converged towards the following solution:

$G_{12}^0 = 6.2$ GPa, $\varepsilon_6^0 = 0.004$ and $K = 90$ MPa. Figure 17.6 shows the model fit (in red) and the experimental data in blue.

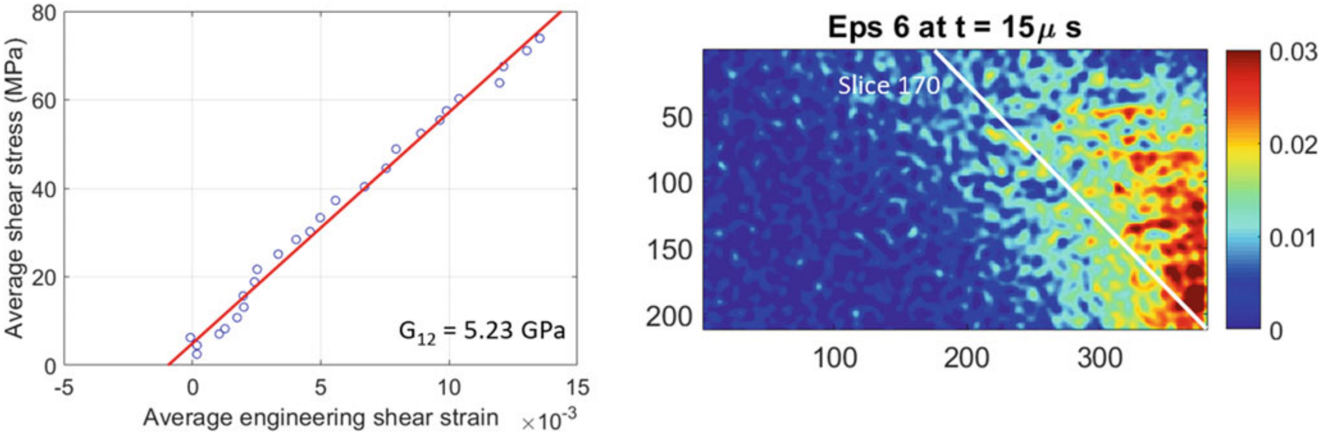

Fig. 17.7 Average shear stress vs average engineering shear strain for slice 170 up to $t = 15$ μs, and corresponding engineering shear strain map (in the material coordinate system at 45°)

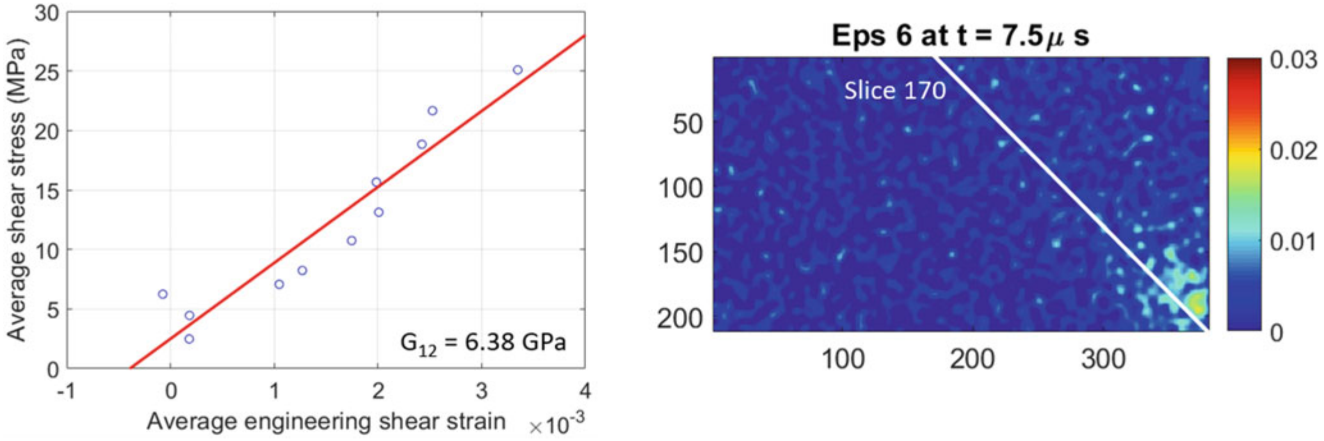

Fig. 17.8 Average shear stress vs average engineering shear strain for slice 170 up to $t = 7.5$ μs, and corresponding engineering shear strain map (in the material coordinate system at 45°)

One can see that the model does a decent job at reproducing the non-linear behaviour, though the fit is not perfect. The stress is underestimated at the top of the loading curve, and the damaged modulus seems to be underestimated (or damage is over- estimated). Of particular interest however is the value of the initial (undamaged) shear modulus. In [1], this specimen (UD45-7 in Table 6) yielded a shear modulus of 5.44 GPa by fitting a straight line to points up to an average shear strain of 15.10^{-3} and averaging over all 170 slices. Selecting only slice 170 as shown on Fig. 17.7, and restricting the data to the first 15 μs to reach a maximum engineering shear strain of 15.10^{-3}, a modulus of 5.23 GPa is obtained. What can be seen on the strain map also provided in the figure is that at the bottom right of the specimen, the strain is much larger than 15.10^{-3} and non-linear behaviour is expected to be already significant there. This will therefore lead to an underestimation of the shear modulus. It must also be noted that ‘visually,’ the response does look reasonably linear, and this is a consequence of the smearing effect when averaging over the slice. To test this further, the modulus was identified by gradually decreasing the interval of time.

For 12.5 μs, the modulus is identified to be 5.52 GPa; 5.94 GPa for 10 μs and 6.38 GPa for 7.5 μs. The data for this time interval is represented in Fig. 17.8. One can see that the maximum local strain is now about 15.10^{-3} and non-linear effects are mitigated. The value of the modulus here is very similar to that identified with the damage model using all slices, which reinforces the conclusion that the shear moduli as obtained in [1] are most probably underestimated.

Finally, Fig. 17.9 shows a map of the damage parameter d at the end of the test. The distribution is consistent with the test kinematics with a concentration at the bottom right corner, but the values are unrealistically large, illustrating the limitations of the model.

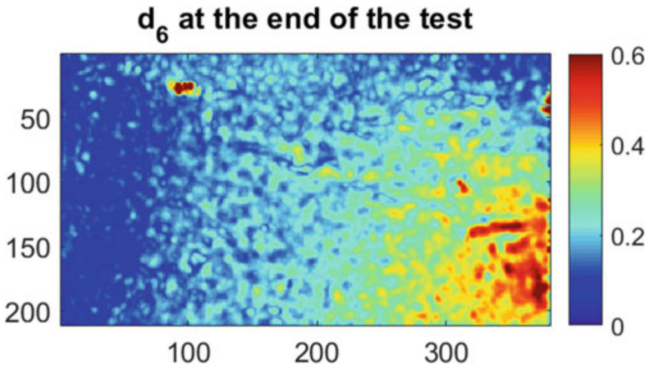

Fig. 17.9 Shear damage parameter map at the end of the test

17.4 Conclusion

This work presents some preliminary results concerning the identification of a non-linear shear damage model to describe the behaviour of off-axis 45° UD composite IBII tests. This test has the unique feature of providing a cycle of loading/unloading at strain rates on the order of 1000 s^{-1}, which provides an opportunity to have a better understanding of the non-linear shear behaviour of composites at such strain rates.

The main conclusion from this preliminary study is that the non-linear model is essential to identify representative elastic modulus values as the strain distributions over the angled slices are far from uniform. However, the simple damage model considered here needs to be improved to better describe the observed behaviour. There are several potential pathways to follow for this. First, a higher order damage model (instead of a linear one) may help improve the description of the damage part of the process. It seems clear from the global curve in Fig. 17.5 that the unloading occurs linearly along a line of shallower slope, which is typical of damage processes. However, from the same figure, it looks like some permanent strain exists at zero stress. This may be non-recoverable (plasticity) or recoverable (viscous effects), the current experiments do not allow this ambiguity to be cleared. Recovering the impacted specimens after the test and imaging the grid at rest may be a route to test this. Finally, to get a better temporal description of the damage process, higher frame rate should be used. Going to the full capacity of the Shimadzu HPV-X camera used here, a 5 Mfps frame rate would provide more than double the number of points in the early part of the test, which is essential to obtain the initial shear modulus in an accurate manner.

Acknowledgements The authors would like to thank Dr Julien Berthe at ONERA in Lille, France, for supplying the composite plates used for the specimens evaluated in this study. Thanks are also given to Dr Jared Van Blitterswyk and Dr Xavier Régal for their help conducting the IBII tests. Funding from EPSRC is acknowledged by Professor Pierron and Dr Fletcher (Grant EP/L026910/1) and by Mr Parry (PhD studentship).

References

1. Parry, S., Fletcher, L., Pierron, F.: The off-Axis IBII Test for Composites., Journal of Dynamic Behavior of Materials (2021). https://doi.org/10.1007/s40870-020-00271-7
2. Van Blitterswyk, J., Fletcher, L., Pierron, F.: Image-based inertial impact (IBII) tests for measuring the interlaminar shear moduli of composites. Journal of Dynamic Behavior of Materials. **6**(3), 373–398 (2020)
3. Van Blitterswyk, J., Fletcher, L., Pierron, F.: Image-based inertial impact test for composite interlaminar tensile properties. Journal of Dynamic Behavior of Materials. **4**, 543–572 (2018)
4. Ladeveze, P., LeDantec, E.: Damage modelling of the elementary ply for laminated composites. Compos. Sci. Technol. **43**(3), 257–267 (1992)
5. Sun, C.T., Chen, J.L.: A simple flow rule for characterizing nonlinear behavior of fiber composites. J. Compos. Mater. **23**(10), 1009–1020 (1989)
6. Fitoussi, J., et al.: Experimental methodology for high strain-rates tensile behaviour analysis of polymer matrix composites. Compos. Sci. Technol. **65**(14), 2174–2188 (2005)
7. Fletcher, L., Van Blitterswyk, J., Pierron, F.: A manual for conducting image-based inertial impact (IBII) tests. Southampton. https://doi.org/10.5258/SOTON/P0015

8. Castres, M., et al.: Experimental evaluation of the elastic limit of carbon-fibre reinforced epoxy composites under a large range of strain rate and temperature conditions. Strain. **53**(6), e12248 (2017)
9. Grédiac, M., Sur, F., Blaysat, B.: The grid method for in-plane displacement and strain measurement: a review and analysis. Strain. **52**(3), 205–243 (2016)
10. Van Blitterswyk, J., Fletcher, L., Pierron, F.: Investigation of the 2D assumption in the image-based inertial impact test. Strain. **57**(1), e12369 (2021)
11. Chalal, H., et al.: Experimental identification of a nonlinear model for composites using the grid technique coupled to the virtual fields method. Compos. A: Appl. Sci. Manuf. **37**(2), 315–325 (2006)